

# Valley physics and disorder phenomena in 2D materials

PhD Thesis

Johannes H. J. Martiny  
February, 2020





## Valley physics and disorder phenomena in 2D materials

PhD Thesis  
February, 2020

By  
Johannes H. J. Martiny  
johmar@dtu.dk

Supervisor: Antti-Pekka Jauho  
Co-supervisor: Kristen Kaasbjerg

Copyright:      Reproduction of this publication in whole or in part must include the customary bibliographic citation, including author attribution, report title, etc.

Cover photo:    Vibeke Hempler, 2012

Published by:   DTU, Department of Physics, Fysikvej, Building 311, 2800 Kgs. Lyngby Denmark  
[www.fysik.dtu.dk](http://www.fysik.dtu.dk)

## Preface

This thesis is submitted in candidacy for the Ph.D. degree at the Technical University of Denmark (DTU). The work has been carried out between February 2017 and February 2020, initially at DTU Nanotech (February 2017 - January 2019), and later at DTU Physics (January 2019 - February 2020), and is jointly funded by the Center for Nanostructured Graphene (CNG), sponsored by the Danish National Research Foundation (Project DNRF103), and DTU. The Ph.D. project has been supervised by Prof. Antti-Pekka Jauho and co-supervised by Dr. Kristen Kaasbjerg. I have personally performed all numerical calculations and simulations detailed in the thesis in Matlab or Python unless otherwise explicitly stated.

I would like to thank Antti and Kristen for many interesting discussions, a lot of helpful feedback, and for motivating a wide scope for the research activities. I would also like to thank current as well as former members of the groups of Prof. Antti-Pekka Jauho and Prof. Mads Brandbyge for providing a great local research environment. Outside of DTU I would like to thank my collaborators on the research into superconductors, Brian M. Andersen at the Niels Bohr Institute, Copenhagen University, and Andreas Kreisel at the Faculty of Physics and Earth Sciences, Leipzig University. A special thank you to Prof. Stephan Roche and the members of his research group at ICN2, Autonomous University of Barcelona, for providing a scientifically interesting and enjoyable external research stay. I am particularly grateful to Jose H. Garcia for his help implementing the large scale numerical method.

Finally, my sincerest thanks to my family and in particular my wife, Christine, for their help and support throughout my Ph.D. studies.

Thank you,

Johannes H. J. Martiny

## Abstract

The successful isolation in 2004 of the first 2D material graphene, a single layer of carbon atoms, has opened up new pathways for both fundamental research into condensed matter at the nanoscale and the development of entirely new technologies. Among these new possibilities is the option of transferring information using a degree of freedom other than the electron charge, and in this manner redefining conventional electronics. In graphene such a degree of freedom exists in the form of distinct momentum states of electrons in two unique "valleys" of the electronic band structure. Electrons in graphene can thus be distinguished by their so-called valley index. Storing and transferring information can be accomplished by selective manipulation of electrons based on their valley index, setting up currents, not of charge, but of valley polarization. Such currents are expected to be protected from the effects of most common sources of disorder in the nanoscale system, a major advantage over conventional charge-based electronics.

In this thesis we consider how the valley degree of freedom can be manipulated in graphene through engineering of the nanoscale system. We suggest an approach to inducing currents of valley polarization in the graphene sheet which can be controlled by an external potential, and demonstrate how such tunability of the resulting tunable filtering of electrons based on their valley index predicts a clear signature in experiment. We go on to discuss the effects of disorder in realistic nanostructured systems, outlining both the robustness of our results to moderate levels of imperfections and the possibility of new regimes of valley filtering in the strongly disordered system.

Furthermore, we extend our studies of disorder to include impurities on the surface of the high-temperature superconductor FeSe, wherein recent experimental evidence indicates that local magnetism can be nucleated around defect sites. We model such impurity-induced magnetism in a microscopic model of FeSe and predict the formation and underlying symmetries of the local magnetism. Finally, we derive the expected signature of these symmetries in experiment and compare our findings with recent scanning tunneling microscopy measurements.

## Resumé

I 2004 blev det første 2D materiale, grafen, isoleret som et enkelt lag af karbon atomer. Dette har åbnet nye muligheder for både grundforskning i faststoffysik på nanoskala, og forbedring af eksisterende eller opfindelse af helt nye teknologier. Blandt disse muligheder er en metode til at overføre information ved brug af en frihedsgrad forskellig fra elektronens ladning, og på denne måde redefinere konventionel elektronik. I grafen eksisterer en sådan frihedsgrad i form af forskellige impuls-tilstande i to unikke dale eller "valleys" i den elektroniske båndstruktur. Elektroner i grafen kan derfor opdeles efter deres såkaldte valley-indeks. Opbevaring og overførsel af information kan opnås inden for denne teknologi ved selektiv manipulation af elektroner baseret på deres valley-indeks, hvorved der opnås strømme, ikke af ladning, men af valley polarisering. Disse strømme forventes at være beskyttede over for effekterne af de mest almindelige kilder til uorden i nano-systemer - en stor fordel over traditionel ladnings-baseret elektronik.

I første del af denne afhandling undersøger vi hvordan valley-frihedsgraden kan manipuleres i grafen gennem nano-strukturering af det omkringliggende system. Vi foreslår en fremgangsmåde til at inducere strømme af valley-polarisering i et grafen lag, hvor strømmen kan kontrolleres af et eksternt potentiale. Denne kontrol over valley-filtrering i grafen-laget gør os i stand til at forudsige en tydelig signatur af effekten i eksperimenter. Derudover diskuterer vi indflydelsen af uorden i realistiske nanostrukturerede systemer, og demonstrerer både stabiliteten af vores resultater i disse systemer samt muligheden for at opnå nye regimer af valley filtrering i det stærkt uordnede system.

I anden del af afhandlingen udvider vi vores studier af uorden til også at inkludere urenheder på overfladen af højtemperatur-superlederen FeSe, hvor nylig eksperimentel evidens indikerer at lokal magnetisme kan opstå omkring defekter i krystallen. Vi modellerer denne urenheds-inducerede magnetisme ved hjælp af en mikroskopisk model for FeSe, og forudsiger formations-mekanismen for, samt den underliggende symmetri af, den lokale magnetisme. Til slut udleder vi den forventede signatur af disse symmetrier i eksperimenter, og sammenligner vores teoretiske slutninger med nylige målinger foretaget ved skannings-tunnelerings-mikroskopi.

## List of publications

Paper I: (attached)

**Symmetry-forbidden intervalley scattering by atomic defects in monolayer transition-metal dichalcogenides**

Kristen Kaasbjerg, Johannes H. J. Martiny, Tony Low, and Antti-Pekka Jauho  
*Physical Review B* **96** (24), 241411(R) (2017)

Paper II: (attached)

**Theoretical study of impurity-induced magnetism in FeSe**

Johannes H. J. Martiny, Andreas Kreisel, Brian M. Andersen  
*Physical Review B* **99** (1), 014509 (2018)

Paper III: (attached)

**Tunable valley Hall effect in graphene superlattices**

Johannes H. J. Martiny, Kristen Kaasbjerg, and Antti-Pekka Jauho  
*Physical Review B* **00**, 005400 (2019)

Paper IV: (attached)

**Quantum phase transition of iron-based superconductivity in  $\text{LiFe}_{1-x}\text{Co}_x\text{As}$**

J.-X. Yin, S. S. Zhang, G. Dai, Y. Zhao, A. Kreisel, G. Macan, X. Wu, H. Miao, Z.-Q. Huang, Johannes H. J. Martiny, B. M. Andersen, N. Shumiya, D. Multer, M. Litskevich, Z. Cheng, X. Yang, T. A. Cochran, G. Chang, I. Belopolski, L. Xing, X. Wang, Y. Gao, F.-G. Chuang, H. Lin, Z. Wang, C. Jin, Y. Bang, and M. Z. Hasan  
*Physical Review Letters* **123**, 217004 (2019)

Paper V: (attached)

**Visualization of local magnetic moments emerging from impurities in the Hund's metal states of FeSe**

S. Y. Song, Johannes H. J. Martiny, A. Kreisel, B. M. Andersen, J. Seo  
*Currently under review*  
*Preprint: arXiv:1909.13515*

Paper VI: (not attached)

**Extrinsic contributions to the valley Hall effect in gated graphene superlattices**

Johannes H. J. Martiny, J. H. Garcia, K. Kaasbjerg, A.-P. Jauho, and S. Roche  
*In preparation*

## List of conference contributions

- Center for Nanostructured Graphene 1 Day Seminar (*Oral contribution*)  
Lyngby, Denmark  
Spring 2017
- Carbonhagen 2017 (*Poster contribution*)  
Copenhagen, Denmark  
Summer 2017
- Frontiers of Condensed Matter, Les Houches Doctoral Training Session (*Poster contribution*)  
Les Houches, France  
Fall 2017
- Two Dimensional Electronics Beyond Graphene (*Poster contribution*)  
Easton, MA, United States  
Summer 2018
- International Conference on Superlattices, Nanostructures, and Nanodevices (*Poster contribution*)  
Madrid, Spain  
Summer 2018
- Graphene 2019 (*Poster contribution*)  
Rome, Italy  
Summer 2019
- Carbonhagen 2019 (*Poster contribution*)  
Pi poster award winner  
Copenhagen, Denmark  
Summer 2019



# Contents

Preface . . . . .	i
Abstract . . . . .	ii
Resumé . . . . .	iii
List of publications . . . . .	iv
<b>1 Introduction</b>	<b>1</b>
1.1 Graphene electronics . . . . .	1
1.2 Valleytronics . . . . .	2
1.3 Nanostructuring graphene for novel applications . . . . .	3
1.4 Using disorder to probe the clean system . . . . .	4
1.5 Thesis outline . . . . .	4
<b>2 Topology and transport in graphene</b>	<b>7</b>
2.1 The Berry phase and wavepacket dynamics . . . . .	7
2.2 2D Transport phenomena . . . . .	11
2.3 The low energy model of graphene . . . . .	12
2.4 Valley Hall effect in the massive Dirac model . . . . .	13
2.5 Experimental signature of valley physics . . . . .	15
<b>3 Numerical methods</b>	<b>19</b>
3.1 Electronic structure . . . . .	19
3.2 Berry curvature in the tight-binding model . . . . .	20
3.3 Longitudinal conductivity from the Boltzmann equation . . . . .	23
3.4 Large scale methods using Chebyshev expansion of the Green's function . . . . .	24
3.5 Summary and comparison of methods . . . . .	31
<b>4 Valley Hall effect in gate-defined graphene superlattices</b>	<b>33</b>
4.1 A simple model . . . . .	34
4.2 Electronic structure of the superlattice . . . . .	35
4.3 Tunable valley Hall conductivity . . . . .	40
4.4 Robustness of results for realistic potentials and irregular gating . . . . .	42
4.5 Summary and outlook . . . . .	43
<b>5 Valley Hall effect in the disordered superlattice</b>	<b>45</b>
5.1 Intrinsic and extrinsic contributions to the valley Hall effect . . . . .	45
5.2 Electronic structure of the disordered superlattice . . . . .	49
5.3 Valley Hall conductivity in the disordered superlattice . . . . .	52
5.4 Summary and outlook . . . . .	53
<b>6 Impurity bound states and local magnetic order in the iron-based superconductor FeSe</b>	<b>55</b>

6.1	A brief introduction to FeSe . . . . .	55
6.2	Theoretical model of FeSe . . . . .	57
6.3	Local magnetic order nucleated on resonant states . . . . .	60
6.4	Recent evidence for impurity-nucleated local magnetic order in FeSe . . . . .	67
6.5	Summary . . . . .	72
<b>7</b>	<b>Summary and outlook</b>	<b>75</b>
	<b>Bibliography</b>	<b>77</b>
<b>A</b>	<b>Unfolding procedure</b>	<b>89</b>
<b>B</b>	<b>Profile of the superlattice potential</b>	<b>92</b>
<b>C</b>	<b>Chebyshev expansion details and derivations</b>	<b>94</b>
	<b>Attached Papers</b>	<b>97</b>
	Paper I . . . . .	97
	Paper I . . . . .	111
	Paper III . . . . .	122
	Paper IV . . . . .	135
	Paper V . . . . .	158

# Chapter 1

## Introduction

The historic quest for control over the structure of materials on the scale of the individual atom, so as to engineer their properties, has found a new pathway with the discovery of 2D materials [1–4]. Starting with the successful isolation of graphene in 2004 by Novoselov et al. [5] as a freestanding monolayer of carbon atoms, a multitude of 2D materials have been shown to be stable in atmospheric conditions [3, 6, 7]. Such "designer" materials open the door on a world where materials are created directly for a specific application, be it within high-performance electronics [8, 9], sensor development [10–12], or solar cells [13–15]. In this chapter we introduce the basic properties of graphene and pay special attention to the specific application of this material within modern electronics. We focus here entirely on graphene, and leave a corresponding introduction to our investigations of impurity effects in the iron-based superconductor FeSe to Chapter 6.

### 1.1 Graphene electronics

Low dimensional carbon structures exist in many forms, as evident in Fig. 1.1(a-d) where we show (a) monolayer graphene, (b) the layered structure of the parent compound graphite, (c) a carbon nanotube, and (d) the "buckyball"  $C_{60}$  fullerene. Mono and few-layer graphene samples were initially extracted as individual flakes by application of common adhesive tape to the parent compound graphite [5], but has since seen a dramatic development in modern methods for constructing both high-quality and well-isolated single flakes [17–19] and large-scale sheets suitable for industrial applications [20–22]. In addition, concurrent progress have been made in using another 2D material, hexagonal Boron Nitride (hBN), as either a substrate or for full encapsulation of graphene [17, 23]. This insulating material consisting of alternating Boron and Nitrogen atoms [as shown in the inset of Fig. 1.1(e)] has an almost perfectly matching lattice structure to graphene, and has allowed researchers to isolate graphene from the environment. Being all surface, the properties of graphene are highly susceptible to the effects of, e.g., charged impurities, and hence complete encapsulation is important if the intrinsic properties of graphene are to be probed [9]. The unique properties of graphene include high mechanical strength, exceptional carrier mobility, and outstanding thermal conductivity, making it an ideal candidate for use in future electronics [9, 24, 25] in applications such as high-frequency transistors [26] or Hall-effect based sensors [27].

A further development within the world of 2D materials is the inclusion of graphene and other 2D materials in stacked heterostructures, allowing for a "LEGO-like" control over material properties as shown schematically in Fig. 1.1(e). This stacking allows the construction of entirely new meta-materials, and opens pathways for further control using

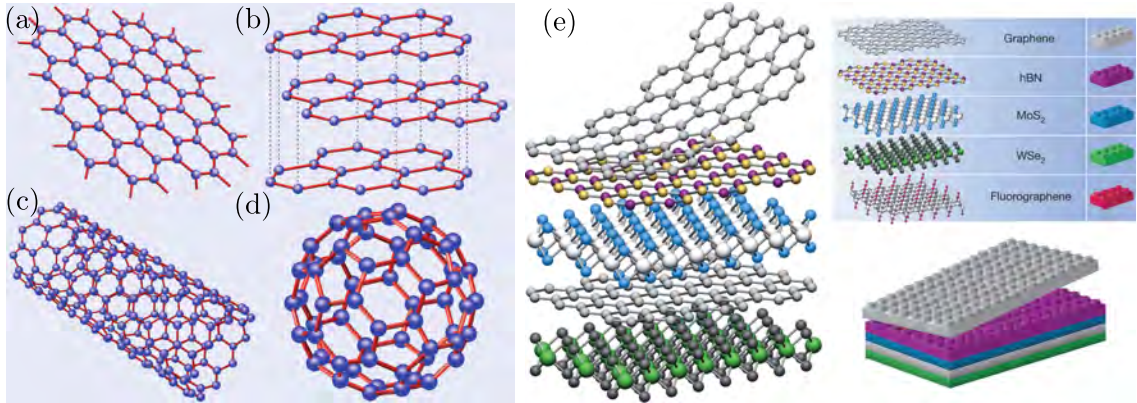


**Figure 1.1:** Carbon structures, showing (a) monolayer graphene, (b) the layered structure of the parent compound graphite, (c) a carbon nanotube, and (d) the "buckyball" C<sub>60</sub> fullerene. Reproduced from Castro Neto et al. [16]. (e) Schematic of 2D material heterostructures where individual layers are stacked like LEGO blocks to create designer materials with fine-tuned properties. Reproduced from Geim and Grigorieva [3].

nanostructuring techniques [28].

## 1.2 Valleytronics

Conventional electronics are defined by the electron charge degree of freedom, the control of which is accomplished through the application of electric fields to nanostructures. These charge-based electronics are inherently dissipative, causing an increase in power consumption and the possible loss of transferred information [29]. The energy dissipation is a major challenge within integrated electronics, limiting the performance of devices ranging from small mobile devices to large data centers [30].

A possible solution to this problem lies in utilizing a degree of freedom different from the electron charge for information processing, with an end goal of achieving almost dissipationless electronics. Spin electronics or *spintronics* have been a subject of intense study within this field [31]. Here, information is stored and transferred in the spin states of electrons. Nearly dissipationless currents of net spin polarization are induced through the spin Hall effect, in which an in-plane electric field induces a transverse spin current through extrinsic spin-dependent scattering on impurities or the intrinsic spin-orbit interaction in the sample [32–34]. Readout of the signal generated by such spin currents can be achieved through the inverse effect where the spin current generates a transverse electric field.

The electronic structure of graphene, hosting valleys which are degenerate in energy yet separated by a long distance in momentum space, suggests an entirely different approach using valley electronics or *valleytronics*. At low energies these valleys define a new degree of freedom through the valley polarization of a given state, essentially replacing the spin up or down labels of spintronics by the valley indexes  $K$  and  $K'$ . The huge momentum transfer required to scatter an electron between individual valleys indicates that this valley degree of freedom is protected from most sources of disorder unless the associated disorder potential is atomically sharp. Dissipationless currents of valley polarization can be induced through the valley Hall effect where an in-plane electric field drives a transverse valley current, thereby transferring a signal in the valley polarization. As we discuss in detail below, this valley-filtering effect appears in systems when inversion symmetry is broken in the lattice. The effect is linked to the topology of the electronic bands through the electronic Berry curvatures which adds a correction to the usual band velocity of

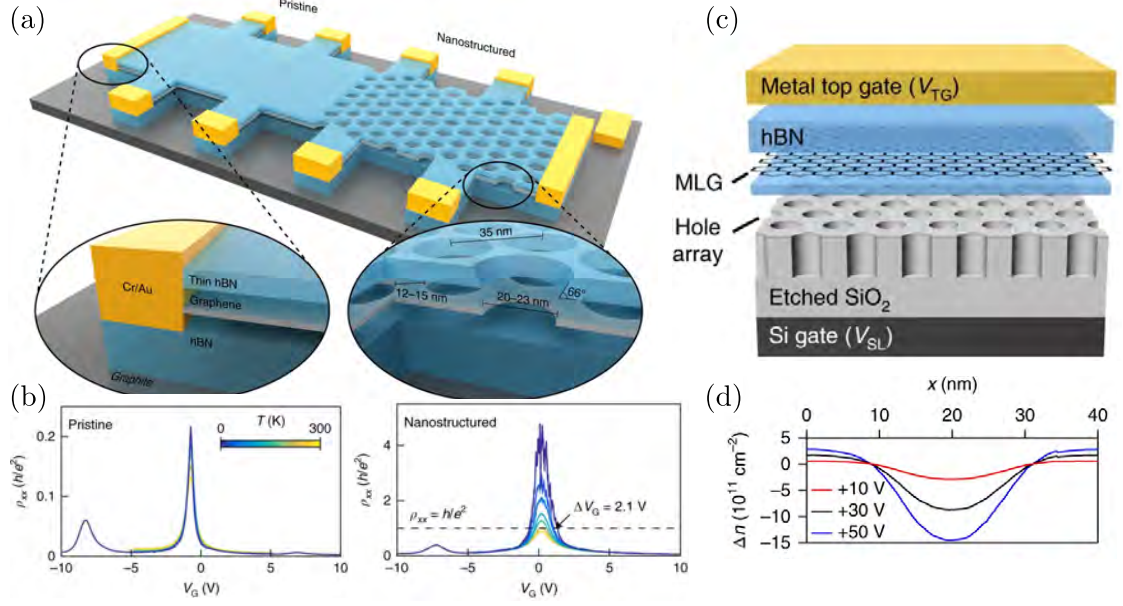


**Figure 1.2:** Examples of direct and indirect nanostructuring of graphene. (a) Direct nanostructuring of the graphene monolayer. (b) Resistivity spectra measured at a range of temperatures indicate that a band gap of  $2\Delta \approx 78$  meV is formed. Adapted from Jessen et al. [28]. (c) Indirect nanostructuring of the electronic properties of graphene. The graphene monolayer is pristine but is placed above a nanostructured dielectric (here:  $\text{SiO}_2$ ). The electronic density of the graphene sheet on top of the nanostructured region can be tuned by varying the bottom gate potential as shown in (d). This thesis includes a study of a similar system but considers a different shape of the induced potentials which locally breaks inversion symmetry. Adapted from Forsythe et al. [41].

the electronic state depending explicitly on the valley index [35]. While the study of valleytronics is not strictly limited to the world of 2D materials [36, 37], the high quality of available samples and the many ways of engineering their properties suggest them as natural platforms for such technology [38–40]. We outline the concept of band structure engineering in more detail in the following section.

### 1.3 Nanostructuring graphene for novel applications

While the properties of pristine graphene outlined above are interesting in their own right, a unique advantage of 2D materials over 3D materials is how these material properties can be selectively engineered for new applications. Techniques which would only provide a minor surface effect in layered bulk materials can instead dramatically change the electronic structure in the monolayer limit [28]. Examples of such engineering in graphene include approaches based on, e.g., strain [42–44], substrate-induced superlattice Moire effects [45–47], and top-down nanostructuring [28, 41, 48–51]. The latter approach can be loosely divided into two classes: (i) Direct nanostructuring where the graphene sheet itself is perturbed in a regular pattern, and (ii) indirect nanostructuring where the dielectric environment is modified instead [28]. An example of direct nanostructuring (i) is shown in Fig. 1.2(a) where a regular array holes have been created by Jessen et al. [28] in a graphene sheet by nanolithography, forming a so-called antidot lattice. The effects of quantum confinement in such structures have been suggested to induce the formation of band gaps in the initially metallic graphene [48, 52], an effect indicated when the thermal variation of the resistivity is compared in pristine and nanostructured parts of the sample

as shown in Fig. 1.2(b). While such direct nanostructuring provides a strong control over material properties, a major drawback in terms of valleytronic engineering lies in the creating of edge disorder by the lithographic procedure, which provides an additional source of intervalley scattering to the system.

Indirect nanostructuring, on the other hand, does not naturally lead to the formation of atomically sharp disorder detrimental to applications in valleytronics. Forsythe et al. [41] recently demonstrated a method for creating tunable band structure engineering in graphene. A schematic of their setup is displayed in Fig. 1.2(c), showing a hBN encapsulated graphene sheet placed on top of nanostructured dielectric consisting of  $\text{SiO}_2$  with cylindrical indentations. A superlattice is defined in the graphene layer by the regular structure of the induced potential through the nanostructured dielectric, a potential which can be tuned by the applied voltage to the bottom gate ( $V_{SL}$  in Fig. 1.2(c)). The result of a simulation of the density modulation underneath the superlattice potential is shown in Fig. 1.2(d), demonstrating the partial depletion of the density as the voltage controlling the superlattice potential is increased. The lack of intervalley scattering in this setup combined with an all-electrical method for tuning the superlattice potential suggests that this nanostructuring approach might be very well suited for applications in valleytronics. In the following chapters we investigate a similar system as a platform for tunable valleytronics where a reduction in the symmetry of the superlattice potential, removing the inversion center of the above disk-shapes, leads directly to the valley Hall effect.

## 1.4 Using disorder to probe the clean system

The work included in this thesis is multifaceted, but a unifying theme running throughout the chapters will be how the inclusion of disorder, be it single atomic vacancies, extended crystal boundaries, or imperfections in nanostructured samples, can be used to probe the properties of pristine system itself. Here, the inclusion of disorder can reveal information not available to measurement of the pristine sample, or even induce novel phenomena and suggest entirely new applications. Throughout the following chapters we will pay special attention to these effects and point out the potential benefits of such disorder to our understanding of the underlying systems.

## 1.5 Thesis outline

We have in the current chapter provided an introduction to the world of 2D materials and graphene in particular, with a strong focus on how the properties of graphene can be engineering through nanostructuring of the material itself or its dielectric environment. Following this, we present in **Chapter 2** the theoretical background needed to understand the interplay of topology and transport in graphene, including a simple picture of the valley Hall effect derived within the formalism of wave-packet dynamics. We also discuss the expected signature in transport measurement which will help guide our later investigations. In **Chapter 3** we provide an overview of the shared numerical methods employed throughout this thesis, including the calculation of the electronic Berry curvature describing the valley Hall effect within the tight-binding model, and a large-scale method based on polynomial expansion of the electronic Green's function. This large-scale method serves double duty, providing both disorder corrections to the conductivity in our investigations of the valley Hall effect in graphene, and a way of performing self-consistent mean field calculations of impurity-induced magnetism in a later study of the high-temperature superconductor FeSe.

With the motivation, theoretical framework, and numerical methods so established, we

proceed in **Chapter 4** with our investigations into the nanostructuring of graphene for valleytronics and the intrinsic contributions to the valley Hall effect. **Chapter 5** extends this investigation to include also extrinsic contributions from disorder by employing the large-scale polynomial expansion method.

Finally, in **Chapter 6** we shift our focus away from 2D materials and detail our investigations of impurity effects in the iron-based superconductor FeSe. We cover both our initial theoretical study of the formation of impurity-induced resonant states and the appearance of local magnetic order, and our contributions to a recent experimental paper where the signatures of such local magnetism in scanning tunneling microscopy (STM) have been investigated.



## Chapter 2

# Topology and transport in graphene

Historically, phase transitions in condensed matter systems were characterized in terms of the symmetries they spontaneously break [53]. Starting with the unexpected result of exactly quantized conductance in the quantum Hall effect [54], recent developments within the field have brought to light new phases of matter related to the concept of topological order, wherein band insulators can be classified as topologically equivalent only if they can be changed into each other by slowly changing the underlying Hamiltonian. The interplay between such topological ordering of the electronic ground state and the resulting unconventional transport phenomena appearing in nanostructures is a research topic of considerable interest in modern condensed matter physics [55–57].

In this chapter we introduce the basic theory underlying the phenomena investigated in the rest of the thesis. We begin by introducing the Berry phase and the framework of wave-packet dynamics, wherein superpositions of Bloch states allow us to formulate a simple equation of motion describing the so-called anomalous velocity contribution to electron dynamics. Using the concepts of this formalism, we then provide an outline of the family of Hall effects and their characteristics in electronic transport, culminating with the definition of the valley Hall effect studied in the first part of this thesis. Providing a short derivation of the low energy model of graphene, we study this effect within the massive Dirac model where simple analytical results can be obtained. This investigation will serve as a useful comparison point of our later studies of more complicated models. Finally, we cover the expected experimental signature of the valley Hall effect in nonlocal resistance measurements, and, based on the symmetry properties of the valley Hall effect, detail guidelines for nanostructuring graphene for valleytronics.

### 2.1 The Berry phase and wavepacket dynamics

In this section we cover definition of the Berry phase and associated Berry curvature, and examine their effects on the dynamics of wavepackets. Starting from the single-particle picture of quantum mechanics, we move onto the specific application of these concepts within crystalline solids described by periodic Bloch Hamiltonians. Our analysis is by necessity limited to the concepts relevant to our later studies of the valley Hall effect, and we refer the interested reader to the excellent reviews of Xiao et al. [35], Kane [53], and (from a large-scale modeling point of view) Gradhand et al. [58].

Consider a physical system described by a time dependent Hamiltonian  $H(\mathbf{R})$ , where the

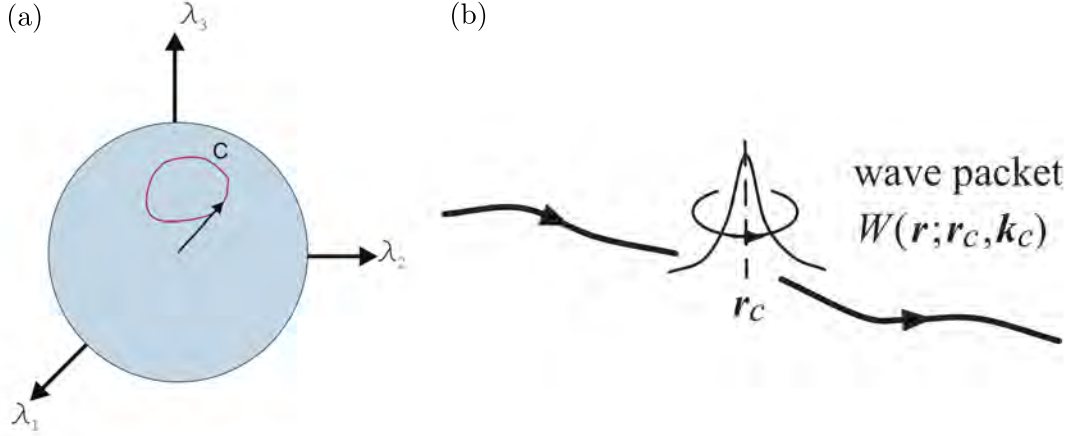


**Figure 2.1:** (a) A closed path in the three dimensional parameter space defined by  $\{\lambda_i\}_{i=1}^3$ . Adapted from Gradhand et al. [58]. (b) Illustration of a wave-packet constructed from a superposition of Bloch states. The wave-packet has a well-defined wavevector  $\mathbf{k}_c$  and center of mass  $\mathbf{r}_c$ . Adapted from Xiao et al. [35].

time dependence is absorbed into the variables  $R_i(t)$ . This Hamiltonian has associated instantaneous eigenstates at each time  $t$  given as the solution of the eigenvalue equation [35]

$$H |n(\mathbf{R})\rangle = \epsilon_n(\mathbf{R}) |n(\mathbf{R})\rangle. \quad (2.1)$$

These states are not uniquely defined by the above equation, as we can multiply by an arbitrary  $\mathbf{R}$  dependent phase factor (i.e. a choice of gauge). If the energy spectrum is non-degenerate the adiabatic theorem tells us that a system originally in an eigenstate  $|n(\mathbf{R}(t=0))\rangle$  will stay as an instantaneous eigenstate of  $H(\mathbf{R}(t))$  for all times  $t$ . A critical fact is that, during adiabatic evolution along a closed path  $\mathcal{C}$  in the parameter space (as indicated in Fig. 2.1(a)), the state not only picks up the conventional dynamic phase, but also acquires a geometric phase. This is the so-called Berry phase

$$\gamma_n = \oint_{\mathcal{C}} d\mathbf{R} \cdot \mathcal{A}_n(\mathbf{R}), \quad (2.2)$$

where

$$\mathcal{A}_n(\mathbf{R}) = i \langle n(\mathbf{R}) | \nabla_{\mathbf{R}} | n(\mathbf{R}) \rangle, \quad (2.3)$$

defines the Berry connection. Note that while this connection is gauge-dependent, the Berry phase itself becomes a gauge-independent (i.e. physical) quantity up to an integer multiple  $2\pi n$  specifically when the path  $\mathcal{C}$  is chosen closed.

We can rewrite the problem in terms of a local gauge-invariant quantity by defining the Berry curvature

$$\Omega_n(\mathbf{R}) = \nabla_{\mathbf{R}} \times i \langle n(\mathbf{R}) | \nabla_{\mathbf{R}} | n(\mathbf{R}) \rangle, \quad (2.4)$$

which (using Stokes theorem) yields the Berry phase as a surface integral

$$\gamma_n = \int_S d\mathbf{S} \cdot \Omega_n(\mathbf{R}), \quad (2.5)$$

with  $S$  the surface enclosed by the closed path  $\mathcal{C}$  in Fig. 2.1(a). Using the useful relation ( $n \neq m$ , for a derivation see Ralph [59])

$$\langle n(\mathbf{R}) | \nabla_{\mathbf{R}} | m(\mathbf{R}) \rangle = \frac{\langle n(\mathbf{R}) | \nabla_{\mathbf{R}} H(\mathbf{R}) | m(\mathbf{R}) \rangle}{\varepsilon_n(\mathbf{R}) - \varepsilon_m(\mathbf{R})} \quad (2.6)$$

the Berry curvature can also be written in an expanded form

$$\boldsymbol{\Omega}_n(\mathbf{R}) = \text{Im} \sum_{m \neq n} \frac{\langle n(\mathbf{R}) | \nabla_{\mathbf{R}} H(\mathbf{R}) | m(\mathbf{R}) \rangle \times \langle m(\mathbf{R}) | \nabla_{\mathbf{R}} H(\mathbf{R}) | n(\mathbf{R}) \rangle}{(\varepsilon_n(\mathbf{R}) - \varepsilon_m(\mathbf{R}))^2}, \quad (2.7)$$

where we have shifted the derivative from the eigenstates to the Hamiltonian itself. This way of rewriting our earlier expression of Eq. (2.4) will turn out to be an important step when we turn to our numerical implementations. There, the phases of the Hamiltonian eigenstates are in general made discontinuous by the numerical diagonalization procedure, precluding the taking of finite-element methods for the derivative. In contrast, the derivative of the Hamiltonian itself often can be obtained analytically, paving the way for a stable numerical procedure.

In a crystalline solid the eigenstates of the periodic Hamiltonian are Bloch states [53]

$$|\psi_{n\mathbf{k}}\rangle = e^{i\mathbf{k}\cdot\mathbf{r}} |u_{n\mathbf{k}}\rangle, \quad (2.8)$$

where  $|u_{n\mathbf{k}}\rangle$  is the cell-periodic part of the Bloch state. The periodic part is itself an eigenstate of the Bloch Hamiltonian  $H_{\mathbf{k}} = e^{-i\mathbf{k}\cdot\mathbf{r}} H e^{i\mathbf{k}\cdot\mathbf{r}}$ . The Bloch state can pick up a Berry phase when the wavevector  $\mathbf{k}$  is varied in a closed orbit in reciprocal space, something which can have a profound effect on, e.g., the anomalous form of graphene Landau levels and the experimental signature thereof in magnetotransport [60]. A Berry curvature in momentum space can be defined in similar fashion to the above

$$\boldsymbol{\Omega}_n(\mathbf{k}) = \nabla_{\mathbf{k}} \times i \langle u_{n\mathbf{k}} | \nabla_{\mathbf{k}} | u_{n\mathbf{k}} \rangle. \quad (2.9)$$

The Berry curvature is an intrinsic property of the crystal band structure since it only depends on the (periodic part) of the Bloch state itself, and is finite in a range of crystals with broken time-reversal or inversion symmetries [35]. Critically, the gauge invariance of this quantity implies that it can have an impact on electron dynamics even when electrons do not follow a closed path in momentum space, a fact which we shall elaborate in more detail when we investigate the consequences of nonzero local Berry curvature on transport properties.

Note that we have so far written the general 3D result - in the case of a 2D system the surface has normal  $\mathbf{n} = \hat{z}$ , in which case it turns out that we only need to consider the  $\Omega_z$  component of the Berry curvature to understand the dynamics of the system. This component is often written  $\Omega_{xy}$  within the literature, in analogy with the Hall conductivity  $\sigma_{xy}$ , since it involves the  $x, y$  components of the Berry connection. We adopt this notation in the following.

### 2.1.1 Equation of motion in wavepacket dynamics

The interplay between an applied E-field and the effects of finite Berry curvature can be captured in a semi-classical approach of wavepacket dynamics. The wave packet is constructed in the band in question as a superposition of Bloch states [35]

$$|W\rangle = \int d\mathbf{k} w(\mathbf{k}, t) |\psi_{n\mathbf{k}}\rangle, \quad (2.10)$$

with  $w(\mathbf{k}, t)$  the envelope function which is chosen such that the wavepacket can be said to have a definite wavevector (center of momentum)  $\mathbf{k}_c$ , while still retaining a well-defined center of mass  $\mathbf{r}_c$ . An illustration of such a wavepacket is shown in Fig. 2.1(b). The equations of motion of the wavepacket can be constructed by linearizing the perturbation around the wavepacket center  $\mathbf{r}_c$ . In the presence of an electric field, we obtain a modified version of the wavepacket velocity in the presence of finite Berry curvature [61]

$$\dot{\mathbf{r}} = \frac{1}{\hbar} \partial_{\mathbf{k}} \epsilon_n(\mathbf{k}) - e\mathbf{E} \times \boldsymbol{\Omega}_n(\mathbf{k}) \quad (2.11)$$

$$\equiv \mathbf{v}_n^0(\mathbf{k}) + \delta\mathbf{v}_n(\mathbf{k}), \quad (2.12)$$

with  $\mathbf{r}$  the wave-packet center in Fig. 2.1(b). Here, we recognize the usual band velocity as the first term, and defined the anomalous velocity  $\delta\mathbf{v}$  as the contribution relating to the electronic Berry curvature. If we consider a 2D material where  $\boldsymbol{\Omega}_n(\mathbf{k}) = \Omega_{xy,n}(\mathbf{k})\hat{\mathbf{z}}$  and assume an in-plane E-field  $\mathbf{E} = E\hat{\mathbf{x}}$ , we find the anomalous velocity to be perpendicular to the applied field

$$\delta\mathbf{v}_n(\mathbf{k}) = eE\Omega_{xy,n}(\mathbf{k})\hat{\mathbf{y}}. \quad (2.13)$$

We see that electron dynamics under the application of the in-plane electric field depend explicitly on the Berry curvature. As we show in the following section, this anomalous contribution can be used to characterize the multitude of different Hall effects. We note that the above wavepacket construction and the derived equation of motion is defined for a single band, and that if the wavepacket is constructed as superposition of Bloch states in multiple bands a generalized (non-Abelian) form of the Berry curvature enters the equation of motion instead [62].

For later use we also consider the symmetry properties of the Berry curvature. The above definitions lead to the following relations [35, 59]

$$\text{TR: } \Omega_{xy}(\mathbf{k}) = -\Omega_{xy}(-\mathbf{k}), \quad (2.14a)$$

$$\text{I: } \Omega_{xy}(\mathbf{k}) = \Omega_{xy}(-\mathbf{k}), \quad (2.14b)$$

i.e., the Berry curvature is odd in the presence of time-reversal symmetry, and even in the presence of inversion symmetry. In the presence of both symmetries the Berry curvature thus vanishes almost everywhere ( $\mathbf{k} = 0$  being the possible exception, as we shall see in pristine graphene).

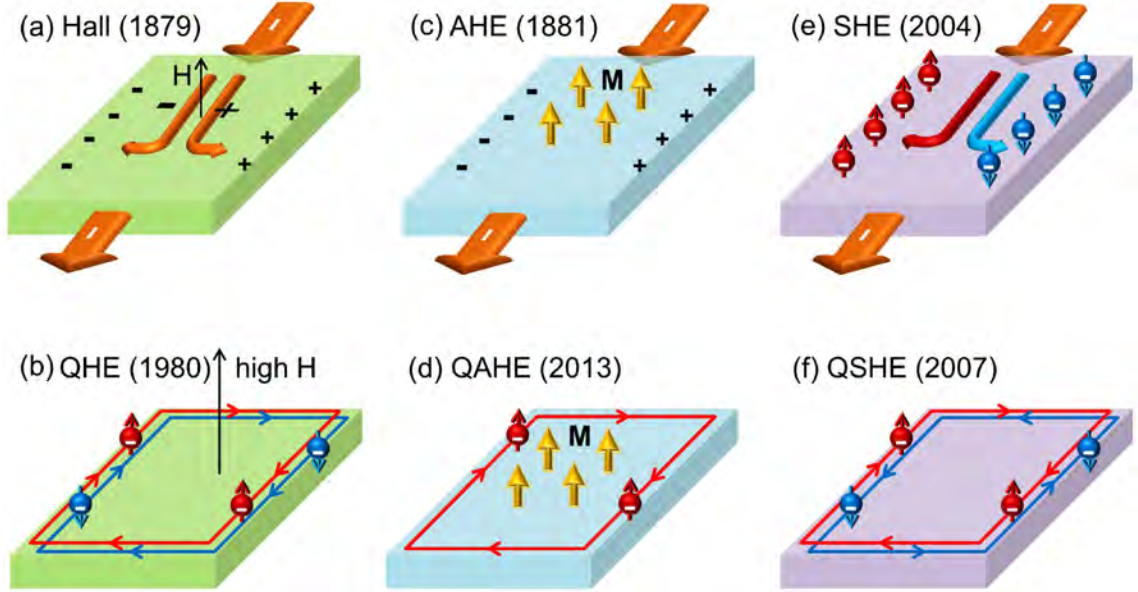


**Figure 2.2:** Transport phenomena and their dates of discovery. (a) The well-known Hall effect and its quantized counterpart of (b) the quantum Hall effect describing edge states in strong B-fields, have been supplemented by the discovery of (c) the anomalous Hall effect in ferromagnetic metals (M denoting the magnetization) and (d) its quantized form. Similar effect manifest for the electron spin in (e) the spin-orbit interaction driven spin Hall effect and (f) its quantized counterpart. Adapted from Chang and Li [63].

## 2.2 2D Transport phenomena

In Fig. 2.2 we show some of the members of the Hall effect family. The conventional Hall effect, where a voltage builds up across a sample under the application of an out of plane B-field, has a quantized counterpart in high B-fields in the *quantum Hall effect*. Here, the electronic density of states is split into distinct Landau levels related to quantized electron cyclotron orbits, yielding characteristic exactly quantized steps in the Hall conductivity as each level is filled. The formation of the quantum Hall effect can be understood using the concepts of band topology derived above. Constructing hybrid magneto-Bloch bands in a unit cell extended to include a magnetic flux quantum, it is possible to consider the system simply as two dimensional band insulator with nontrivial topology [53]. In particular, the quantized Hall conductivity follows from an integration of the anomalous velocity component of Eq. (2.13) summed over the number of filled bands [64]

$$\sigma_{xy}^{QHE} = \frac{e^2}{\hbar} \sum_{n \text{ filled}} \int_{BZ} \frac{d^2k}{2\pi} \Omega_{xy,n}(\mathbf{k}) \quad (2.15)$$

$$\equiv \frac{e^2}{\hbar} \sum_{n \text{ filled}} C_n, \quad (2.16)$$

where we defined in the second line the so-called Chern number

$$C_n = \frac{1}{2\pi} \int_{BZ} d^2k \Omega_{xy,n}(\mathbf{k}), \quad (2.17)$$

which is an integer describing the topology of the given band. Nonzero Chern numbers typically arise from the application of an external magnetic field breaking the time-reversal symmetry, but the quantum Hall effect can also occur in the absence of external fields in,

e.g., the Haldane model on the honeycomb lattice [65]. Since the insulating quantum Hall state is topologically nontrivial, it cannot be adiabatically deformed to a topologically trivial state without closing the band gap. This fact leads to the prediction of protected edge states at the interface to a trivial region as illustrated in Fig. 2.2(b), in the so-called *bulk-boundary correspondence*. The topological protection of these edge states towards localization is responsible for the robustness of the conductance quantization in the quantum Hall effect.

A non-quantized version of the quantum Hall effect can occur in systems with trivial band topology. Such a situation arises in the presence of spin-orbit coupling in ferromagnetic metals in the so-called *anomalous Hall effect* illustrated in Fig. 2.2(c). This effect arises from the presence of a locally nonzero Berry curvature in the partially filled band, yielding the intrinsic anomalous Hall conductivity

$$\sigma_{xy}^{AHE} = \frac{e^2}{\hbar} \int_{BZ} \frac{d^2k}{2\pi} f_{n\mathbf{k}} \Omega_{xy,n}(\mathbf{k}), \quad (2.18)$$

where  $f_{n\mathbf{k}} = [e^{(E_{n\mathbf{k}} - E_F)/k_B T} + 1]^{-1}$  is the Fermi Dirac distribution describing the occupation of the partially filled band, with  $E_F$  the Fermi level. As we cover in more detail in Chapter 5, extrinsic contributions to the anomalous Hall effect related to impurity scattering often mask the presence of the intrinsic contribution [66]. For nontrivial band topologies a quantized version of this result can also occur as illustrated in Fig. 2.2(d), the edge state now being spin polarized.

The above expressions for the quantum Hall and anomalous Hall effect have been used to model a variety of other transport phenomena. In the *spin Hall effect*, a similar expression to the anomalous Hall conductivity of Eq. (2.18) can be extracted, but now selective in the spin state. In short, the anomalous velocity becomes opposite for the two spin states, causing an effective filtering of electrons to the left and right parts of the Hall bar sample as illustrated in Fig. 2.2(d). The quantized counterpart shown in Fig. 2.2(f) supports pairs of counter-propagating edge states of opposite spin, defining a quantized spin current. As we shall see in the following, the *valley Hall effect* studied in the first part of this thesis can be described in a similar fashion. Before we turn to the derivation of this effect, however, we need to consider first the band structure and low energy model of graphene in more detail.

## 2.3 The low energy model of graphene

The hexagonal structure of the graphene lattice is shown in Fig. 2.3(a), with a unit cell consisting of two inequivalent carbons on the  $A$  (black disks) and  $B$  (white disks) sublattice sites. The conventional Brillouin zone of graphene is shown in Fig. 2.3(b), with several high-symmetry points labeled including the two inequivalent "valleys"  $K$  and  $K'$ . The electronic properties of graphene are exceptionally well-described by a simple tight-binding model containing nearest-neighbour couplings between the  $\pi$ -bonded  $2p_z$  orbital of each carbon site [67]

$$H = -t \sum_{\langle ij \rangle, \sigma} c_{i\sigma}^\dagger c_{j\sigma} + H.c., \quad (2.19)$$

where  $\langle ij \rangle$  indicate summation over nearest neighbors only, and  $t = 3.033$  eV sets the energy scale of the problem. The band structure is shown in Fig. 2.3(c) along the linecut through the symmetry points of Fig. 2.3(b) (orange dashed line). Two distinct "valleys" in the band structure can be observed at the  $K$  and  $K'$  points, with linear bands touching at the Fermi level in the center of each valley.

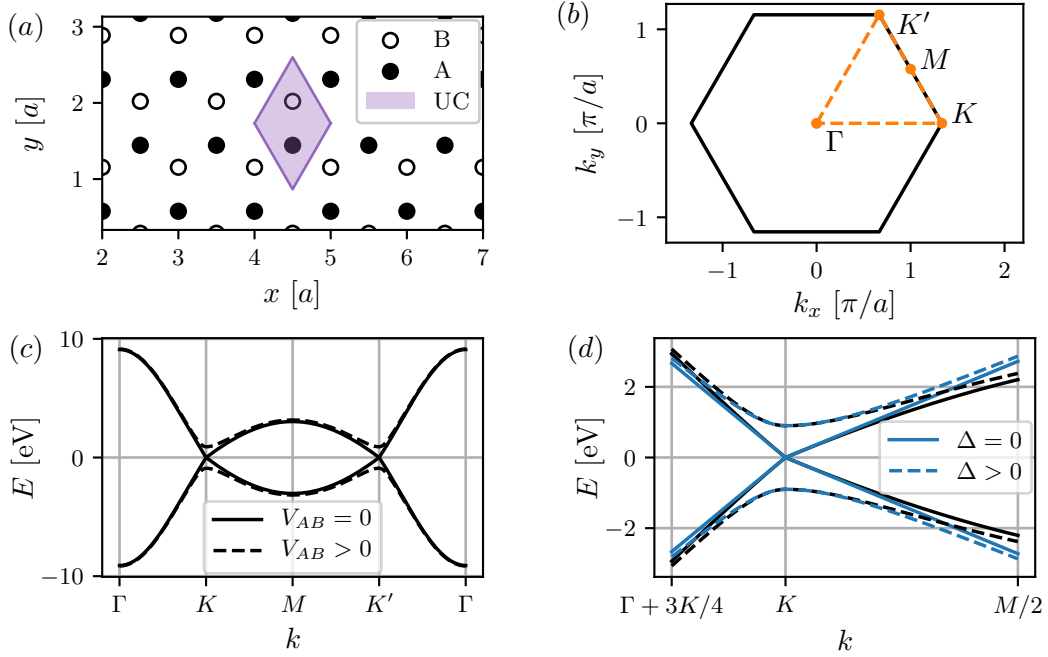


**Figure 2.3:** Graphene in the full tight-binding model and approximated by the Dirac model. (a) The graphene lattice, constructed from the A and B sublattices, with the unit cell indicated. (b) The graphene Brillouin zone with the high-symmetry points marked. (c) Band structure of graphene in the tight-binding model with (dashed lines) and without (full lines) an A/B staggered potential. The utilized linecut is shown in (a) by the dashed orange line. (d) Zoom of the band structure near the  $K$  point, showing also the Dirac model result with (dashed blue lines) and without (full blue lines) a mass term.

Fourier transforming the tight-binding model and considering the low energy limit for wavevectors close to the valley regions  $\mathbf{q} = \mathbf{k} - K_\tau$  ( $K_\tau \equiv \{K, K'\}$ ), we obtain the Dirac model

$$H_\tau(\mathbf{q}) = \hbar v_F (\tau q_x \sigma_x + q_y \sigma_y), \quad (2.20)$$

where we defined the Fermi velocity  $v_F = \sqrt{3}at/2\hbar \approx 1 \times 10^6$  m/s. Diagonalization of this low energy Hamiltonian yields the valence and conduction bands of the Dirac model  $E_\pm(\mathbf{q}) = \pm \hbar v_F q$ , with  $q = |\mathbf{q}|$ . In Fig. 2.3(d) we show these linear bands (blue full lines) compared with the tight-binding result in the  $K$  valley, demonstrating the close fit at low energies with a visible discrepancy only developing as the energy scale of the hopping  $t$  is reached.

Turning to the topology of these bands, we find that the Berry curvature has a monopole form in the symmetry points where the bands meet. Integrating the Berry curvature over a sphere containing this monopole, a Berry phase of  $\pm\pi$  is found in the Dirac model [35]. We can gain an intuitive understanding of this result by viewing the Dirac model as a specific limit result of the so-called massive Dirac model which we consider in the following section.

## 2.4 Valley Hall effect in the massive Dirac model

Graphene is a semi-metal with a vanishing density of states at the Fermi level in the undoped system. Much attention has been paid to engineering a gap in graphene [28, 50,

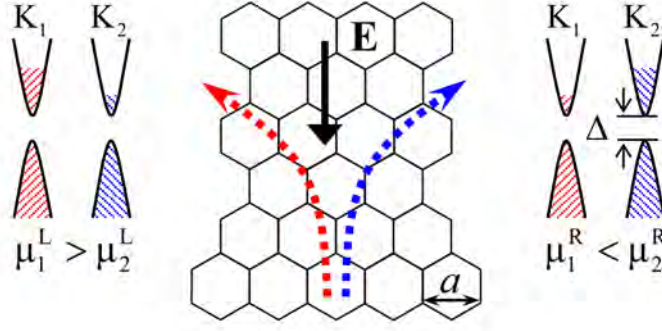


**Figure 2.4:** Schematic of the valley Hall effect. Under the effects of an in-plane electric field electrons in the  $K$  and  $K'$  valleys acquire opposite (anomalous) transverse velocities, causing a valley polarization to build up at the edges of the sample. Reproduced from Xiao et al. [61]

68], ideally creating a semiconductor which inherits the high mobility of graphene. Within the tight-binding model of graphene a band gap can be opened by breaking the sublattice symmetry,

$$H = -t \sum_{\langle ij \rangle} (a_i^\dagger b_j + H.c.) + V_{AB} \sum_i (a_i^\dagger a_i - b_i^\dagger b_i), \quad (2.21)$$

where we defined the creation and annihilation operators of the A/B sites, and  $V_{AB}$  is the magnitude of a sublattice asymmetric potential. The perfectly precise A/B asymmetry of this potential is of course an artificial construct which does not translate into something which can be engineered in the laboratory, although some suggestions do exist for inducing such a potential on graphene via, e.g., sublattice selective nitrogen doping [69, 70], and the model is often employed to describe the low energy band structure of the transition metal dichalcogenides where different atoms occupy the A/B sites of the honeycomb structure [71, 72]. The model is interesting for our purposes in the low energy limit where it serves as the generic model when perturbations break the sublattice symmetry in graphene. In this limit we obtain the so-called massive Dirac model

$$H_\tau(\mathbf{q}) = \hbar v_F (\tau q_x \sigma_x + q_y \sigma_y) + \Delta \sigma_z, \quad (2.22)$$

with mass term  $\Delta = V_{AB}$ , and eigenenergies in the valence and conduction bands

$$E_\pm(\mathbf{q}) = \pm \sqrt{\hbar^2 v_F^2 q^2 + \Delta^2}. \quad (2.23)$$

The resulting band gap of  $2\Delta$  is shown in Fig. 2.3(d) where we also compare this result with the tight-binding model including the A/B staggered potential. The bands are perturbed near the band edge, but recover their linear Dirac character as we move away from the band gap.

The Berry curvature can be calculated from the analytical eigenstates of the massive Dirac model, where we obtain

$$\Omega_{xy}^\pm(\mathbf{q}) = \mp \tau \frac{\Delta v_F^2 \hbar^2}{2(\Delta^2 + \hbar^2 v_F^2 q^2)^{3/2}}, \quad (2.24)$$

with  $\tau$  the valley index. We see that the Berry curvature peaks exactly at the symmetry points ( $q = 0$ ) with the width of the distribution determined by the mass. The presence of a finite Berry curvature of opposite sign in the valleys ( $K$  and  $K' = -K$ ), as required by the presence of time-reversal symmetry [see Eq. (2.14a)], indicates that electrons in each valley acquire opposite anomalous velocity components under the application of an in-plane E-field. The resulting valley Hall effect is shown schematically in Fig. 2.4, with a filtering of electrons diverting left or right based on the valley index taking place. In a finite sample this valley Hall effect will cause a buildup of polarization at the edges as indicated by shifted chemical potentials in each valley.

The resulting Hall conductivity of electrons in, e.g., the  $K$  valley can be found by integrating the anomalous velocity component of the single-valley Dirac model. We present this quantity here with the Fermi level placed in the conduction band

$$\sigma_{xy}^{0,K} = \frac{e^2 \Delta}{2h \sqrt{(v_F \hbar k_F)^2 + \Delta^2}}, \quad (2.25)$$

where the 0 superscript implies that this is an intrinsic contribution not related to impurity scattering effects, as we expand upon in Chapter 5. Inside the band gap (here:  $k_F \rightarrow 0$ ) we find  $\sigma_{xy}^{0,K} = \mp \text{sgn}(\Delta) e^2/h$  (including spin degeneracy) corresponding to a so-called half quantized valley Chern number,  $C_K = \mp \text{sgn}(\Delta) 1/2$ , of conduction and valence bands. The half quantized nature of this number is due to the decoupling of the graphene band into two distinct regions, and bulk-boundary correspondence implies that valley polarized edge states are expected when the sign of the mass term changes across an interface leading to an integer change in band topology [35]. The total Chern number of the graphene band decoupled in this fashion is  $C = C_K + C_{K'} = 0$  as required by time-reversal symmetry [Eq. (2.14a)].

The previous mass-less Dirac model can be viewed as the limit of this model as  $\Delta \rightarrow 0$ , causing a vanishing of the Berry curvature except at the  $K, K'$  points where it diverges towards  $\pm\infty$  depending on the sign of the mass term

$$\Omega_{\tau}^{\pm}(\mathbf{q}) \rightarrow \mp \tau \text{sgn}(\Delta) \begin{cases} 0 & \mathbf{q} \neq \mathbf{0} \\ \infty & \mathbf{q} = \mathbf{0} \end{cases}. \quad (2.26)$$

A signature of the resulting finite Berry phase in pristine graphene is seen in, e.g., the presence of a zeroth Landau in magnetotransport [60, 73]. For our purposes within valleytronics, however, pristine graphene is not of much use since the Berry curvature is finite only exactly at the Dirac point where the conduction and valence bands meet. This causes a cancellation of the anomalous velocity components at this filling and precludes any observation of valley filtering. Studies of the valley Hall effect in graphene thus play out in modified systems where perturbations break the inversion symmetry of the pristine graphene.

## 2.5 Experimental signature of valley physics

While the measurement of charge currents is well-developed, and spin currents can be accessed by coupling ferromagnetic leads to the sample [33], detecting valley currents in a simple fashion remains elusive [29]. Although valley filters do exist which could potentially be used to read out the incoming valley polarization [74], these filters rely on specific and complicated geometries themselves and are thus not yet mature enough as a technology to be used in this manner. In this section we are primarily concerned with the signature of the valley Hall effect in nonlocal resistance measurements where an all-electrical setup

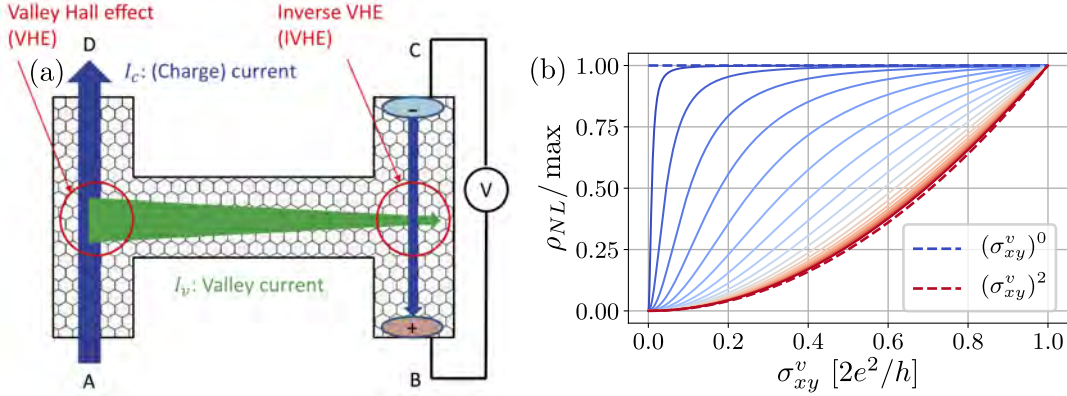


**Figure 2.5:** An experimental signature of valley physics. (a) Nonlocal resistance measurement schematic. A charge current between the A and D induces a transverse valley current which propagates to the C and B terminal side. The inverse valley Hall effect then creates a (nonlocal) voltage between terminals B and C. Adapted from Yamamoto et al. [29]. (b) Expected scaling of the normalized nonlocal resistivity with the valley Hall conductivity for varying values of  $\sigma_{xx} \in [0.01, 5] e^2/h$  (blue to red curves). The dashed flat and cubic curves show the limiting behavior for  $\sigma_{xx} \ll \sigma_{xy}^v$  and  $\sigma_{xx} \gg \sigma_{xy}^v$ , respectively.

provides a convenient framework for extracting also additional transport characteristics such as the intervalley scattering length. We note that valley polarization may also be detected by optical means through valley-selective excitation rules [71, 75, 76], and as the formation of topological boundary states between regions of opposite mass terms as predicted by bulk-boundary correspondence [77].

### 2.5.1 Nonlocal resistance

Using nonlocal resistance measurements to detect valley currents in a Hall bar geometry is a technique originally borrowed from spintronics [29]. A key advantage of this technique is an all-electrical setup for the measurement, promising straightforward integration into conventional electronics. We show the generic setup in Fig. 2.5(a). The technique relies on the generation of a transverse valley current through the valley Hall effect generated by a charge current between one pair of terminals, and the inverse effect occurring between a different set of terminals - the inverse valley Hall effect.

We can obtain a simple form of expected nonlocal signal using a heuristic argument [29]: An applied local voltage between terminal A and D induces a local electric field  $E_L$ . This is related to the local (between these terminals) current density through the longitudinal conductivity  $j_c^L = \sigma_{xx} E_L$ . The electric field in the presence of Berry curvature induces a transverse valley current along the Hall bar

$$j_v = \sigma_{xy}^v E_L \quad (2.27)$$

with the valley Hall conductivity  $\sigma_{xy}^v = \sigma_{xy}^K - \sigma_{xy}^{K'}$  as the proportionality constant. The valley current induces a valley gradient along the Hall bar. We associate a "valley field" to this gradient

$$E_v = \frac{1}{2e} \partial_x \delta \mu_v \quad (2.28)$$

with  $\delta \mu_v = \mu_K - \mu_{K'}$  the "valley potential" given by the accumulation of valley polarization across the Hall bar. Between a different set of terminals in the right-hand side of the Hall

bar [B and C in Fig. 2.5(a)], a conductance matrix relates the "nonlocal" (NL) charge and the transverse valley current to the electric and valley fields

$$\begin{pmatrix} j_c^{NL} \\ j_v \end{pmatrix} = \begin{pmatrix} \sigma_{xx} & -\sigma_{xy}^v \\ \sigma_{xy}^v & \sigma_{xx} \end{pmatrix} \begin{pmatrix} E_{NL} \\ E_v \end{pmatrix}, \quad (2.29)$$

or, inversely,

$$\begin{pmatrix} E_{NL} \\ E_v \end{pmatrix} = \frac{1}{(\sigma_{xx})^2 + (\sigma_{xy}^v)^2} \begin{pmatrix} \sigma_{xx} & \sigma_{xy}^v \\ -\sigma_{xy}^v & \sigma_{xx} \end{pmatrix} \begin{pmatrix} j_c^{NL} \\ j_v \end{pmatrix}. \quad (2.30)$$

Setting  $j_c^{NL} = 0$  in this expression, as expected if stray currents are negligible, we find the nonlocal electric field between the distant pair of terminals [C and B in Fig. 2.5(a)]

$$E_{NL} = \frac{\sigma_{xy}^v}{(\sigma_{xx})^2 + (\sigma_{xy}^v)^2} j_v \quad (2.31)$$

$$= \frac{\sigma_{xy}^v}{(\sigma_{xx})^2 + (\sigma_{xy}^v)^2} \sigma_{xy}^v E_L \quad (2.32)$$

$$= \frac{(\sigma_{xy}^v)^2}{(\sigma_{xx})^2 + (\sigma_{xy}^v)^2} \frac{1}{\sigma_{xx}} j_{c,L} \quad (2.33)$$

$$\equiv \rho_{NL} j_{c,L}, \quad (2.34)$$

where we have defined the nonlocal resistivity as the proportionality between the nonlocal E-field and the applied charge current

$$\rho_{NL} = \frac{(\sigma_{xy}^v)^2}{(\sigma_{xx})^2 + (\sigma_{xy}^v)^2} \rho_{xx}. \quad (2.35)$$

The nonlocal resistance, proportional to the above resistivity, then has the following limiting behavior

$$R_{NL} \propto \rho_{NL} \approx \begin{cases} (\sigma_{xy}^v)^2 \rho_{xx}^3, & \text{for } \sigma_{xx} \gg \sigma_{xy}^v \\ (\sigma_{xy}^v)^0 \rho_{xx}^1, & \text{for } \sigma_{xx} \ll \sigma_{xy}^v \end{cases}, \quad (2.36)$$

which we show as dashed lines in Fig. 2.5(b). The clearest signature of a nonzero valley Hall conductivity is found in the first of these regimes where the cubic scaling is retained, and consequently this expression has been used to fit a multitude of nonlocal measurements [38, 39, 78]. In the other regime a finite nonlocal current is still measured, but this is (nearly) independent of the valley Hall conductance corresponding to the upper blue curve in Fig. 2.5(b).

Beconcini et al. [79] obtained a similar result to the above by studying a diffusion equation in a strip geometry of width  $W$ . The nonlocal response is in this case written in terms of the valley Hall angle

$$\tan \theta_v = \frac{\sigma_{xy}^v}{\sigma_{xx}}, \quad (2.37)$$

which is often used as a figure of merit for the magnitude of the induced response in both valley and spin Hall effects [80]. In a sample with a long intervalley scattering length ( $l_v \gg W$ ) the expected nonlocal resistance measured at some distance  $d$  from the source of the local current is then found to be

$$\frac{\Delta R_{NL}(d)}{\rho_{xx}} = \frac{W}{2L_v} \frac{\tan^2 \theta_v}{1 + \tan^2 \theta_v} e^{-|d|/L_v} \quad (2.38)$$

with  $L_v = l_v \sqrt{1 + \tan^2 \theta_v}$  a renormalized valley diffusion length, and  $\Delta R_{NL}(d)$  the contribution to the nonlocal resistance not related to conventional stray current effects. Note that, apart from the geometrical factors related to the strip geometry and the addition of valley diffusion, this expression reproduces the result of our earlier heuristic argument [Eq. (2.35)].

### 2.5.2 Nonlocal resistance in the transport gap

The arguments given above for the expected signature of the valley Hall effect in nonlocal resistance measurements rely on the picture of bulk valley currents carried by subgap states through the bulk of the sample [79, 81], and is the usual interpretation given in measurements of nonlocal resistance peaks near the gapped region of perturbed graphene systems. This picture is well-defined for Fermi levels within, e.g., the valence band where current carrying states at the Fermi level coexist with the presence of finite and valley-dependent Berry curvature. The situation is, however, markedly different inside the bulk band gap. Landauer-Büttiker calculations with the Fermi level placed in the band gap do not find any such valley-Hall induced contributions to a nonlocal resistance [82], and these contributions only reappear as edge currents when detailed modeling of both electronic structure and edge geometry is included [83].

As pointed out recently by Shan and Xiao [84] this inconsistency stems from the artificial decoupling of the valleys of graphene under the assumption of vanishing intervalley scattering. This decoupling does not capture the global topology of the graphene band structure and allows for a possibly misleading interpretation of the valley Hall effect in terms of two copies of the anomalous Hall effects with opposite mass terms. Within this interpretation the Hall conductivity in the clean sample is given by an integration over the anomalous velocity of occupied states, which can be divided into two parts: (i) metallic edge states leading to quantized contributions to the Hall conductivity, and (ii) non-quantized contributions from partially filled bands which can be seen as Fermi surface property [85]. The graphene bands are topologically trivial, by which the in-gap quantized contribution (i) must be absent. The second contribution is trivially zero inside the band gap, leading to the vanishing of bulk valley currents when the Fermi level is placed in the gap, in contrast to the result of the decoupled (Dirac) model where the valley Hall conductivity peaks inside the gap. We note that metallic edge states may be recovered when the interaction between local edge geometry and substrate interactions are included [45].

Keeping this discussion in mind we thus limit our initial predictions (in Chapter 4) of the nonlocal response to the band edges where the picture of bulk valley currents is valid. We do however consider how a nonlocal response can be induced in an extended regions when the effects of disorder are considered in Chapter 5. Here, a lifting of the band gap can extend the Fermi surface contribution to cover an extended energy interval, providing a clear signature of the valley Hall effect in the measurement.

# Chapter 3

## Numerical methods

In this chapter we introduce the numerical methods which will be used throughout this thesis. This includes electronic structure calculations within the tight-binding approximation, as well as the two approaches to calculating the valley Hall conductivity: (i) from the electronic Berry curvature, which we met when discussing the anomalous velocity component of wavepackets in Section 2.1, and (ii) by the direct calculation of the linear response conductivity using an expansion of the Kubo-Bastin formula. As we will show in Chapter 4 and Chapter 5, these two methods lead to similar results yet each have their own advantages and drawbacks.

### 3.1 Electronic structure

We study tight-binding Hamiltonians on the form

$$H = \sum_{\langle ij \rangle, \sigma} t_{ij} c_{i\sigma}^\dagger c_{j\sigma}, \quad (3.1)$$

where  $i$  and  $j$  denote orbitals  $\phi$  in the given system, and  $t_{ij}$  are the tight-binding parameters. When studying graphene in the following chapters we restrict ourselves predominantly to the nearest neighbor interaction  $t_{ij} = -t\delta_{\langle ij \rangle}$ , with  $t = 3.033$  eV. When we study iron-based superconductors in a later chapter the above model will be extended to include the multi-orbital structure explicitly.

We define Bloch states as expansions of these local orbitals [86]

$$|\psi_{n\mathbf{k}}\rangle = \sum_i C_{in\mathbf{k}} |\chi_{i\mathbf{k}}\rangle \quad (3.2)$$

$$= \sum_{i\mathbf{R}} C_{in\mathbf{k}} e^{i\mathbf{k}\cdot(\mathbf{R}+\boldsymbol{\tau}_i)} |\phi_{i\mathbf{R}}\rangle, \quad (3.3)$$

describing localized orbitals  $|\phi_{i\mathbf{R}}\rangle$  at reciprocal lattice vectors  $\mathbf{R}$  with relative positions  $\boldsymbol{\tau}_i = \langle \phi_{i\mathbf{0}} | \hat{\mathbf{r}} | \phi_{i\mathbf{0}} \rangle$  in the unit cell. In the following we adopt the convenient shorthand notation where states are labeled by their indices only, e.g.,  $|\psi_{n\mathbf{k}}\rangle \equiv |n\mathbf{k}\rangle$ . The elements of the Bloch Hamiltonian are then

$$(H_{\mathbf{k}})_{ij} \equiv \langle i\mathbf{k} | \hat{H} | j\mathbf{k} \rangle = \sum_{\mathbf{R}} e^{i\mathbf{k}\cdot(\mathbf{R}-\boldsymbol{\tau}_i+\boldsymbol{\tau}_j)} \langle i\mathbf{R} | \hat{H} | j\mathbf{R} \rangle. \quad (3.4)$$

The expansion coefficients of the Bloch state  $C_{in\mathbf{k}}$  can be obtained by diagonalization of the Bloch Hamiltonian alongside the eigenvalues  $E_{n\mathbf{k}}$  defining the band structure of the

tight-binding model. Another quantity of interest will be the the band velocity [66]

$$\mathbf{v}_{n\mathbf{k}} = \frac{1}{\hbar} \langle n\mathbf{k} | \nabla_{\mathbf{k}} H_{\mathbf{k}} | n\mathbf{k} \rangle, \quad (3.5)$$

where  $\nabla_{\mathbf{k}}$  is the gradient operator with respect to the wavevector, and the derivative is calculated analytically from the definition of the Bloch Hamiltonian

$$(\nabla_{\mathbf{k}} H_{\mathbf{k}})_{ij} = i \sum_{\mathbf{R}} (\mathbf{R} - \boldsymbol{\tau}_i + \boldsymbol{\tau}_j) e^{i\mathbf{k} \cdot (\mathbf{R} - \boldsymbol{\tau}_i + \boldsymbol{\tau}_j)} \langle i\mathbf{R} | \hat{H} | j\mathbf{R} \rangle. \quad (3.6)$$

As we shall see in the following section, these matrix elements are also used in the calculation of the Berry curvature.

### 3.2 Berry curvature in the tight-binding model

In an earlier section we derived the semiclassical equation of motion of wavepackets [see Section 2.1.1], and found that several transport phenomena were linked to the electronic Berry curvature

$$\boldsymbol{\Omega}_n(\mathbf{k}) = \nabla_{\mathbf{k}} \times i \langle u_{n\mathbf{k}} | \nabla_{\mathbf{k}} | u_{n\mathbf{k}} \rangle, \quad (3.7)$$

defined in terms of the periodic part of the Bloch state,  $|u_{n\mathbf{k}}\rangle = e^{-i\mathbf{k}\mathbf{r}} |n\mathbf{k}\rangle$ . Several approaches to calculating this quantity exist within the literature [58, 87]. We outline here the calculation from the periodic part of the Bloch states. Direct evaluation of Eq. (3.7) using finite element methods for the derivative of the periodic part of the Bloch state suffers from issues due to the uncontrolled numerical phase of the eigenvectors in the diagonalization of the Hamiltonian. We instead insert a complete basis  $\sum_m |u_{m\mathbf{k}}\rangle \langle u_{m\mathbf{k}}|$  in Eq. (3.7) and apply the identity [66]

$$\langle u_{n\mathbf{k}} | \nabla_{\mathbf{k}} | u_{m\mathbf{k}} \rangle = \frac{\langle u_{n\mathbf{k}} | \nabla_{\mathbf{k}} H_{\mathbf{k}} | u_{m\mathbf{k}} \rangle}{E_{m\mathbf{k}} - E_{n\mathbf{k}}}, \quad (3.8)$$

which shifts the derivative to the Hamiltonian, as previously computed analytically in Eq. (3.6). We obtain an expression for the Berry curvature of the analytical derivatives and numerical eigenvalues of the Hamiltonian

$$\Omega_{xy,n}(\mathbf{k}) = i \sum_{m \neq n} \frac{\langle u_{n\mathbf{k}} | \nabla_x H_{\mathbf{k}} | u_{m\mathbf{k}} \rangle \langle u_{m\mathbf{k}} | \nabla_y H_{\mathbf{k}} | u_{n\mathbf{k}} \rangle}{(E_{m\mathbf{k}} - E_{n\mathbf{k}})^2}, \quad (3.9)$$

with  $\nabla_x \equiv \partial_{k_x}$ . Making the diagonal approximation for the positions  $\mathbf{r}_{ij\mathbf{R}} \equiv \langle i\mathbf{0} | \hat{\mathbf{r}} | j\mathbf{R} \rangle = \delta_{\mathbf{0}\mathbf{R}} \delta_{ij} \boldsymbol{\tau}_i$ , the somewhat complicated full result for the matrix elements appearing in Eq. (3.9) simplifies to [86]

$$\langle u_{n\mathbf{k}} | \nabla_{\mathbf{k}} H_{\mathbf{k}} | u_{m\mathbf{k}} \rangle = \sum_{ij} C_{im\mathbf{k}}^* C_{jn\mathbf{k}} (\nabla_{\mathbf{k}} H_{\mathbf{k}})_{ij}, \quad (3.10)$$

allowing for the numerical evaluation of the Berry curvature.

Using the Berry curvature obtained above, we calculate valley resolved conductivities as the integral over the anomalous velocity component

$$\sigma_{xy}^{K(K')}(E_F) = -\frac{2e^2}{h} \int_{K(K')} \frac{d^2k}{2\pi} \Omega_{xy}(\mathbf{k}, E_F). \quad (3.11)$$

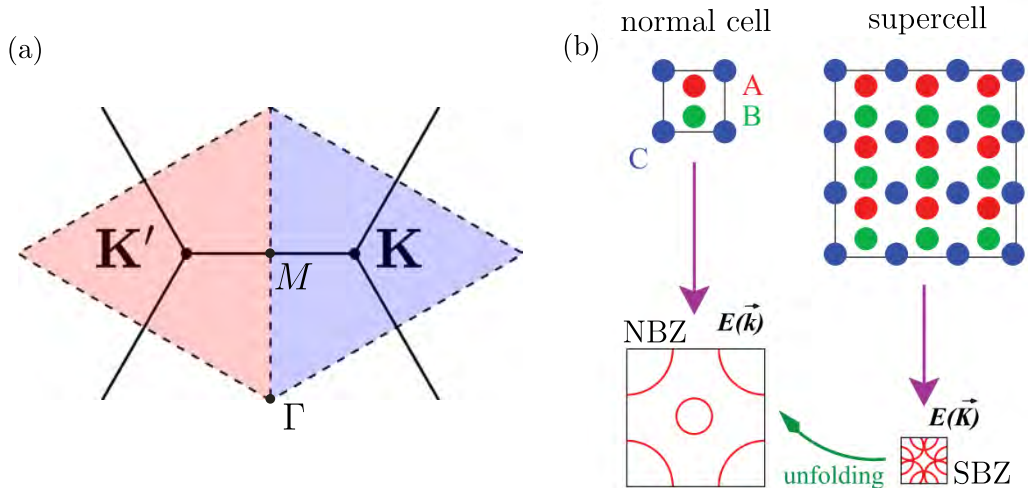


**Figure 3.1:** (a) The full valley regions used when calculating the valley Hall conductivity as the integral over the unfolded Berry curvature. The dashed lines indicate the  $\Gamma \leftrightarrow M$  lines where the Berry curvature vanishes in the presence of time-reversal symmetry. (b) Schematic of the unfolding procedure. A trivial extension of the pristine system yields a multitude of bands in the SBZ which are mapped to the original band structure in the NBZ by the unfolding procedure. Adapted from Popescu and Zunger [88].

Here, we have included spin degeneracy explicitly, and defined the Berry curvature of occupied states

$$\Omega_{xy}(\mathbf{k}, E_F) = \sum_n f_{nk} \Omega_{xy,n}(\mathbf{k}), \quad (3.12)$$

with  $f_{nk} = [e^{(E_{nk} - E_F)/k_B T} + 1]^{-1}$  the Fermi-Dirac distribution, in order to calculate valley Hall conductivities for any filling of the bands. The valley region in Eq. (3.11) is defined using the symmetry properties of the Berry curvature, which vanishes by symmetry on the  $\Gamma \leftrightarrow M$  lines in the Brillouin zone, enabling a consistent definition in terms of exactly half the Brillouin zone. This definition is illustrated in Fig. 3.1(a). An alternative definition based on the disk-shaped regions centered on the  $K$  and  $K'$  points is sometimes employed in the literature [34, 77], but then special attention must be paid to ensuring convergence in the disk radius as the Berry curvature distribution becomes delocalized from the  $K$  ( $K'$ ) point when the band gap widens. For this reason, we always use the full valley region in the following.

Finally, we define the valley Hall conductivity as the difference between valley resolved conductivities

$$\sigma_{xy}^v = \sigma_{xy}^K - \sigma_{xy}^{K'}. \quad (3.13)$$

When time-reversal symmetry is retained the valley resolved conductivities satisfy  $\sigma_{xy}^K = -\sigma_{xy}^{K'}$ , which follows directly from the symmetry properties of the Berry curvature [Eq. (2.14)] [35]. Hence, apart from initial tests and convergence analysis procedures, only half the Brillouin zone needs to be considered in the calculation since the valley Hall conductivity follows as  $\sigma_{xy}^v = 2\sigma_{xy}^K = -2\sigma_{xy}^{K'}$ .

### 3.2.1 Unfolding the supercell result

The technique derived above for calculating the valley Hall conductivity is based on the integration of the Berry curvature, as obtained from the tight-binding model, over the

valley region in the graphene Brillouin zone. If a graphene supercell is considered instead, the band structure and Berry curvature will be folded from the normal Brillouin zone (NBZ) into the smaller superlattice Brillouin zone (SBZ), and the definition of the valley regions for the integration procedure becomes unclear [see Fig. 3.1(a-b)]. We solve this issue by projecting or *unfolding* the Berry curvature calculated in the SBZ back into the NBZ, followed by an integration of the unfolded result over the valley region. This procedure has previously been used to study disorder contributions to both the anomalous Hall effect in "dirty" ferromagnetic metals [89] and to the valley Hall conductivity in transition metal dichalcogenides [86]. The unfolding procedure itself becomes quite extensive in full detail, and we provide here only an outline. The full calculation is included in Appendix A.

A superlattice is defined by the relation between the sets of basis vectors of the normal- and supercell in real space,  $\{\mathbf{a}\}_i, \{\mathbf{A}\}_i$ , and the corresponding relation between reciprocal lattice vectors,  $\{\mathbf{b}\}_i, \{\mathbf{B}\}_i$ , [88]

$$\begin{pmatrix} \mathbf{A}_1 \\ \mathbf{A}_2 \end{pmatrix} = \mathbf{M} \cdot \begin{pmatrix} \mathbf{a}_1 \\ \mathbf{a}_2 \end{pmatrix}, \quad (3.14)$$

$$\begin{pmatrix} \mathbf{B}_1 \\ \mathbf{B}_2 \end{pmatrix} = \mathbf{M}^{-1} \cdot \begin{pmatrix} \mathbf{b}_1 \\ \mathbf{b}_2 \end{pmatrix}, \quad (3.15)$$

$$(3.16)$$

with  $\mathbf{M}$  a matrix of integers, the determinant of which is the ratio of unit cell volumes,  $\det(\mathbf{M}) = \mathcal{V}_{SC}/\mathcal{V}_{NC}$ . In the following we denote quantities in the supercell by capital letters, e.g., the supercell Bloch state is  $|N\mathbf{K}\rangle$  with  $\mathbf{K} \in \text{SBZ}$ . A quantity defined in the SBZ can be unfolded using the overlap between the normal cell orbital  $|i\mathbf{k}\rangle$  and the supercell Bloch state  $|N\mathbf{K}\rangle$ ,

$$\lambda_{iN\mathbf{k}} = \langle i\mathbf{k} | N\mathbf{K} \rangle, \quad (3.17)$$

which can be derived analytically from our earlier Bloch state definitions (see Appendix A). We illustrate this unfolding procedure for the spectral weight of the superlattice system

$$A(\mathbf{K}, \epsilon) = \sum_{N\mathbf{K}} \frac{\eta/\pi}{(\epsilon - E_{N\mathbf{K}})^2 + \eta^2}, \quad (3.18)$$

where  $\eta$  is a numerical broadening. The corresponding unfolded spectral weight is obtained by convolution with the overlap

$$A^{(u)}(\mathbf{K}, \epsilon) = \sum_{N\mathbf{K}} \sum_i |\lambda_{iN\mathbf{k}}|^2 \frac{\eta/\pi}{(\epsilon - E_{N\mathbf{K}})^2 + \eta^2}, \quad (3.19)$$

where the sum over  $i$  spans the orbitals of the normal cell, in this case the  $A, B$  sites of graphene unit cell. The corresponding expression for the Berry curvature [Eq. (3.7)] is similar, but becomes more complicated due to the presence of derivatives in the definition, leading to gauge dependence if naive repetition of the above convolution is applied. An introduction to full result for the unfolded Berry curvature  $\Omega_{xy}^{(u)}(E_F)$  is presented in Appendix A. Once the unfolding has been performed for the Berry curvature, the valley resolved conductivities then follow by a simple application of Eq. (3.11).

We illustrate the unfolding procedure in Fig. 3.1(b) for a simple model where a square (normal) unit cell is repeated three times along each axis only, which in our notation is

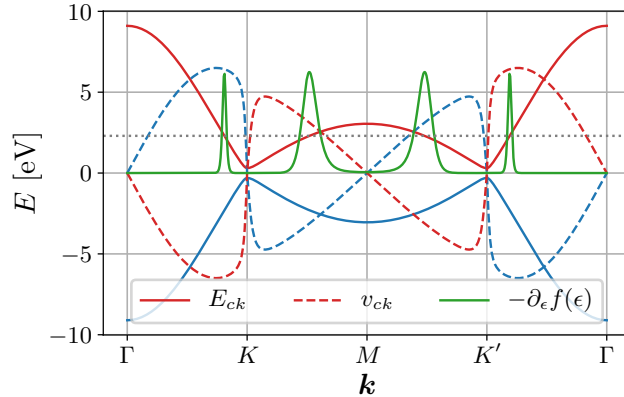


**Figure 3.2:** Components used in the calculation of the Boltzmann conductivity for a simple test model of graphene with a staggered potential  $V_{AB} = 0.1t$ . The band velocities are shown (dashed lines) next to the valence and conduction bands (full lines), alongside the Fermi window function (green line) evaluated at the Fermi level  $E_F = 2.3$  eV (indicated by the gray dotted line). The velocities and the Fermi window function are shown normalized to the same value for clarity.

captured by to the matrix

$$\mathbf{M} = \begin{pmatrix} 3 & 0 \\ 0 & 3 \end{pmatrix}, \quad (3.20)$$

as defined in Eq. (3.16). The corresponding superlattice Brillouin (SBZ) zone is  $\det\{\mathbf{M}\} = 9$  times smaller than the normal Brillouin zone (NBZ). In the pristine supercell the electronic bands  $E(\mathbf{k})$  of the NBZ are simply downfolded to the SBZ. By the reverse unfolding procedure, the original NBZ bands are recovered.

### 3.3 Longitudinal conductivity from the Boltzmann equation

As we saw earlier when discussing the measurement of the valley Hall effect in Sec. 2.5, a key figure of merit for dissipationless electronics applications of anomalous Hall effects is the (valley) Hall angle

$$\theta_v = \frac{\sigma_{xy}^v}{\sigma_{xx}}. \quad (3.21)$$

In addition to the valley Hall conductivity, which we calculate from the electronic Berry curvature, evaluation of the valley Hall angle requires a result for the longitudinal conductivity  $\sigma_{xx}$  close to the band edge of a gapped graphene system. We calculate the longitudinal conductivity from the DC Boltzmann equation approach in the relaxation time approximation [90]

$$\sigma_{xx} = \frac{2e^2}{\mathcal{V}} \sum_{n\mathbf{k}} \tau_{k_F} v_{n\mathbf{k},x}^2 \delta(E_F - E_{n\mathbf{k}}), \quad (3.22)$$

where  $\tau_{k_F}$  is the relaxation time and  $v_{n\mathbf{k},x}$  is the longitudinal component of the band velocity defined in Eq. (3.5). The components needed to calculate the Boltzmann conductivity are shown in Fig. 3.2 for the graphene tight-binding model with a staggered potential [Eq. (2.21)].

If we assume conduction to be limited by charged impurities, we find the relaxation time at the Fermi level [90]

$$\tau_{k_F} = \frac{\hbar}{n_{ci}} \left( \frac{e^2}{4\epsilon_0} \right)^{-2} (\sqrt{2} + q_0)^2 E_F \quad (3.23)$$

$$= C_{ci,\tau} E_F. \quad (3.24)$$

where we defined  $C_{ci,\tau} = \frac{\hbar}{n_{dis}} \left( \frac{e^2}{4\epsilon_0} \right)^{-2} (\sqrt{2} + q_0)^2$ , and  $q_0 = q_{TF}/k_F$  with  $q_{TF} = g_s g_\nu e^2 k_F / 4\pi\epsilon_0 \hbar v_F$  the Thomas Fermi wave vector. In this case the relaxation time varies linearly with the Fermi level. The conductivity can also be expressed via the mobility as  $\sigma_{xx} = ne\mu$  where  $n$  is the carrier density. We compare this with the known analytical result for the zero-temperature conductivity of graphene and extract the relaxation time [73, 90]

$$\sigma_{xx}(T=0) = \frac{e^2 v_F^2}{2} \rho(E_F) \tau_{k_F} = n(E_F) e \mu \quad (3.25)$$

$$\Rightarrow \tau_{k_F} = \frac{n(E_F) e \mu}{(e^2 v_F^2 / 2) \rho(E_F)} \quad (3.26)$$

$$= \frac{\mu}{e v_F^2} E_F, \quad (3.27)$$

with  $v_F \approx 10^6$  m/s. We can thus extract the proportionality constant as  $C_{ci,\tau} = \frac{\mu}{e v_F^2}$  by comparison with Eq. (3.24). The mobility of hBN encapsulated graphene is  $\mu \approx 10 \times 10^5$  cm<sup>2</sup> V<sup>-1</sup> s<sup>-1</sup> near the charge neutrality point, by which we set  $C_{ci,\tau} = 10$  ps/eV in the following, corresponding to a density of charged impurities of  $n_{ci} = 2.3 \times 10^{10}$  cm<sup>-2</sup>.

We note that the longitudinal conductivity thus obtained depends directly on a fitted parameter, an unavoidable assumption of our early studies which are limited to pristine superlattices. The specific value of this fitted parameter is of limited import to our initial predictions, since we are mostly interested in simply capturing the conductivity close to a gapped region qualitatively when computing the valley Hall angle as the superlattice potential is tuned. In a later section we will move beyond this assumption when studying large scale methods, which will allow us to describe the disordered superlattice in a quantitative manner and determine both components of the Hall angle from the same calculation.

### 3.4 Large scale methods using Chebyshev expansion of the Green's function

The previous method, where we quantified the valley Hall effect by calculating the electronic Berry curvature from the Bloch states, is not well suited for studies of disorder when large supercells are considered. Including disorder in the superlattice would necessitate the inclusion of multiple of these already extensive supercells in the tight-binding Hamiltonian, and the subsequent diagonalization of this matrix on a fine grid in reciprocal space, as required to converge the valley Hall conductivity, then becomes computationally unfeasible.

In this section we introduce instead an intrinsically real-space method based where disorder enters naturally into the calculation. The method is based on expansions of the Green's functions, which enter into our expressions for the DOS and linear response conductivity, in terms of orthogonal Chebyshev polynomials. As we shall see, this so-called kernel polynomial method (KPM) reproduces our earlier results for the valley Hall conductivity

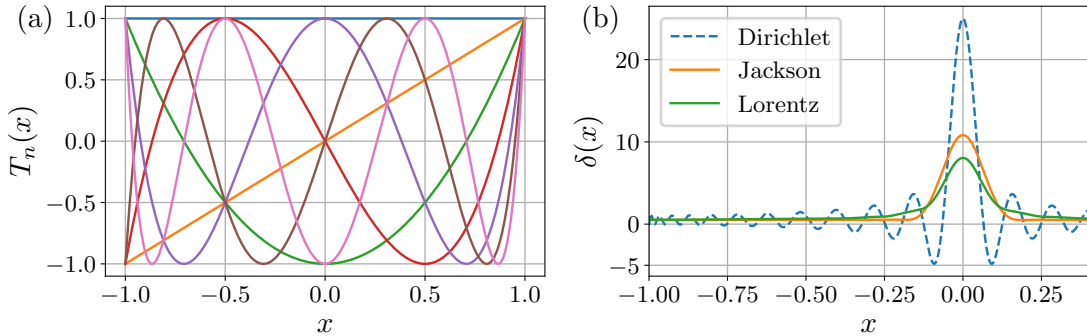


**Figure 3.3:** (a) The first seven Chebyshev polynomials  $T_n$  used in the expansion procedure. (b) Expansion of a delta function illustrating the effect of the kernel convolution for  $N = 50$ . The Dirichlet kernel is equivalent to a truncation of the series, leading to so-called Gibbs oscillations in the expanded quantity (dashed blue curve). Convolution of the delta function with the Jackson kernel yields a Gaussian (orange curve), while including the Lorentz kernel yields a Lorentzian (green curve). Reconstructed from Weiße et al. [91].

in the clean case, and the simultaneous calculation of both transverse valley-Hall and the longitudinal conductivities allows for a good definition of the Hall angle in the disordered case. In the following we provide a brief introduction to the KPM (we refer the interested reader to the excellent review by Weiße et al. [91]) before turning to the expanded form of the DOS and Kubo formulas. Note that while we initially use the method for transport calculations in Chapters 4 and 5, we will use the expansions once more when performing self-consistent mean field calculations in Chapter 6.

### 3.4.1 A short introduction to the kernel polynomial method

Consider the orthogonal family of Chebyshev polynomials of the second kind

$$T_n(x) = \cos[n \arccos(x)], \quad (3.28)$$

with domain on the interval  $x \in (-1, 1)$ . We show the first seven of these polynomials in Fig. 3.3(a). The polynomials satisfy the useful recursion relation

$$T_0(x) = 1, \quad (3.29a)$$

$$T_1(x) = x, \quad (3.29b)$$

$$T_{n+1}(x) = 2xT_n(x) - T_{n-1}(x), \quad (3.29c)$$

which will later enable us to avoid direct diagonalization of the tight-binding Hamiltonian, and instead use the sparsity of this matrix to perform efficient matrix-vector products recursively.

We can expand a given function  $f(x)$  in a series [91]

$$f(x) = \frac{2}{\pi\sqrt{1-x^2}} \sum_{n=0}^{\infty} \mu_n T_n(x), \quad (3.30)$$

in terms of the expansion moments  $\mu_n = 1/(\delta_{n0} + 1) \int_{-1}^1 dx f(x) T_n(x)$ . In our numerical evaluation we are of course forced to truncate this series at some finite order  $N$  ( $\sum_{n=0}^{\infty} \rightarrow \sum_{n=0}^N$ ), which often lead to so-called Gibbs oscillations in the expanded function. In Fig. 3.3(b) (blue dashed curve) we demonstrate this issue for an expansion of the Dirac-delta function. A naive expansion to order  $N = 50$  leads to oscillations in the expansion

(blue dashed line), and, critically, the delta function expansion is no longer strictly positive. This issue can be avoided by a so-called kernel convolution, which corresponds to including modified moments in the expansion

$$\mu_n \rightarrow \mu_n g_n, \quad (3.31)$$

where  $g_n$  is defined by the choice of kernel. The simplest kernel is the Dirichlet kernel, which simply corresponds to a truncation of the series in Eq. (3.30), yielding the Gibbs oscillations we saw in the delta function expansion in Fig. 3.3(b). In this thesis we consider two other kernels, the Jackson and Lorentz kernels

$$g_n^J = \frac{(N - n + 1) \cos\left(\frac{\pi n}{N+1}\right) + \sin\left(\frac{\pi n}{N+1}\right) \cot\left(\frac{\pi}{N+1}\right)}{N + 1}, \quad (3.32)$$

$$g_n^L = \frac{\sinh[\lambda(1 - n/N)]}{\sinh(\lambda)}, \quad (3.33)$$

where  $\lambda$  is a free parameter of the Lorentz kernel which we set to  $\lambda = 3$  for now, the meaning of which we return to in a later section. The effect of including these different kernels is shown in Fig. 3.3(b), where we see that the expanded delta function now becomes strictly positive in both cases. The difference between the two lies in the shape of the expanded function, the Jackson kernel yields a Gaussian approximation, while the Lorentz kernel yields a Lorentzian with width determined by the expansion order  $N$  and the free parameter  $\lambda$ . In the following we shall primarily use the Lorentz kernel when expanding Green's functions since this kernel expansion retains the functions' analytical properties. However, the Jackson kernel will turn out to be useful when expanding the DOS since the Gaussian approximation avoids a key issue of the Lorentz kernel: The long-tailed Lorentzian approximation for the delta functions entering into the definition of the DOS makes band gaps difficult to identify.

The Chebyshev expansion procedure outlined above is restricted to functions defined on the interval  $(-1, 1)$ . We can expand functions defined on domains exceeding this limit by performing a simple rescaling, which we now demonstrate for expansions involving the Hamiltonian. Given a Hamiltonian with either known or estimated bounds on the spectrum  $E_{min} < E_{nk} < E_{max}$ , we rescale

$$\tilde{H} = \frac{H - b}{a}, \quad (3.34)$$

$$\tilde{\epsilon} = \frac{\epsilon - b}{a}, \quad (3.35)$$

with  $a = (E_{max} - E_{min})/2$ , and  $b = (E_{max} + E_{min})/2$ . Since our later calculations do not involve highly asymmetric spectra, we choose  $E_{min} = \max(|E_{max}|, |E_{min}|)$  without loss of generality, and we can thus set  $b = 0$ . We define several rescaled quantities in the following by the notation  $\tilde{\mathcal{O}} = \mathcal{O}/a$ .

For our calculations of the linear response conductivity we require expansions of the spectral representation of retarded and advanced Green's functions, as well as the delta func-

tion. We expand these functions in the following manner [92]

$$G^{R/A}(\tilde{\epsilon}, \tilde{H}) = \frac{1}{\tilde{\epsilon} - \tilde{H} \pm i\eta} \quad (3.36)$$

$$= \mp \frac{2}{\pi\sqrt{1-\tilde{\epsilon}^2}} \sum_{n=0}^N g_n \frac{e^{\pm im \arccos(\tilde{\epsilon})}}{\delta_{n0} + 1} T_n(\tilde{H}) \quad (3.37)$$

$$\delta(\tilde{\epsilon} - \tilde{H}) = \frac{2}{\pi\sqrt{1-\tilde{\epsilon}^2}} \sum_{n=0}^N g_n \frac{T_n(\tilde{\epsilon})}{\delta_{n0} + 1} T_n(\tilde{H}), \quad (3.38)$$

where we have included the kernel coefficients  $g_n$  directly in the definition.

### 3.4.2 The Kubo-Bastin formula

We consider the linear response to a perturbation  $H'$  which is switched on adiabatically from  $t = -\infty$  to the current time  $t$  [80]

$$H \rightarrow H + \lim_{\tau_\phi \rightarrow \infty} e^{t/\tau_\phi} H', \quad (3.39)$$

where  $\tau_\phi$  is the characteristic time scale of the switching on of the perturbation.

Our starting point is the conductivity within linear response, given by the Kubo formula presented here in the zero frequency limit

$$\sigma_{\alpha\beta}(\omega = 0) = \mathcal{V} \lim_{\tau_\phi \rightarrow \infty} \int_0^\infty dt e^{it\tau_\phi/\hbar} \int_0^\beta d\lambda \text{Tr} \left[ \hat{\rho}_0 \hat{J}_\beta(0) \hat{J}_\alpha(t + i\hbar\lambda) \right], \quad (3.40)$$

written in terms of the inverse temperature  $\beta = 1/k_B T$  and the density matrix  $\hat{\rho}_0$  which enters into the correlation function of the time-dependent current operators. These operators are defined in the interaction picture as  $\hat{J}_\alpha(t) = e^{iHt/\hbar} \hat{J}_\alpha e^{-iHt/\hbar}$ . The result obtained by Bastin et al. [93] follows within the so-called independent electron approximation where the system is assumed noninteracting, i.e. representable by a Hamiltonian on the form  $H = \sum_n \epsilon_n c_n^\dagger c_n$  [80, 94]. We now outline the derivation of this result.

The time-dependent current operator can then be expressed in second quantized form as

$$\hat{J}_\alpha(t + i\hbar\lambda) = \sum_{p,q} e^{i(\epsilon_p - \epsilon_q)(t + i\hbar\lambda)/\hbar} c_p^\dagger c_q \langle p | \hat{J}_\alpha | q \rangle, \quad (3.41)$$

which, together with the identity [95]

$$\text{Tr} \left[ \hat{\rho}_0 c_m^\dagger c_n c_p^\dagger c_q \right] = \delta_{mn} \delta_{np} f(\epsilon_m) [1 - f(\epsilon_n)] + \delta_{mn} \delta_{pq} f(\epsilon_m) f(\epsilon_p), \quad (3.42)$$

leads to the single-particle Kubo formula [94]

$$\sigma_{\alpha\beta} = i\hbar \mathcal{V} \lim_{\tau_\phi \rightarrow \infty} \sum_{m,n} \frac{f(\epsilon_n) - f(\epsilon_m)}{(\epsilon_n - \epsilon_m)(\epsilon_n - \epsilon_m + i\hbar/\tau_\phi)} \langle m | \hat{J}_\beta | n \rangle \langle n | \hat{J}_\alpha | m \rangle. \quad (3.43)$$

We could now directly compute the conductivity from Eq. (3.43) in terms of the tight-binding Hamiltonian eigenvalues and eigenvectors, a procedure quite similar to our earlier calculations of the electronic Berry curvature. The implicit diagonalization of the Hamiltonian severely limits the scope of such calculations, however. These calculations would be restricted to quite small systems, precluding any studies of realistic disorder. Bastin et al. [93] solved this issue by rewriting Eq. (3.43) in terms of the Hamiltonian directly, at

the cost of an integration over energy. The full Kubo-Bastin result then becomes [80, 93, 94]

$$\sigma_{\alpha\beta} = i\hbar\mathcal{V} \int d\epsilon f(\epsilon) \text{Tr} \left[ \hat{J}_\alpha \delta(\epsilon - H) \hat{J}_\beta \frac{dG^R(\epsilon, H)}{d\epsilon} - \hat{J}_\alpha \frac{dG^A(\epsilon, H)}{d\epsilon} \hat{J}_\beta \delta(\epsilon - H) \right], \quad (3.44)$$

written in terms of the Green's functions defined in Eq. (3.37) with  $\eta = \hbar/\tau_\phi$ . At a first glance Eq. (3.44) does not provide any clear computational advantage over the earlier expression obtained in Eq. (3.43), trading diagonalization of the Hamiltonian for integration over the entire energy range. As we shall see, however, the sparsity of the tight-binding Hamiltonian combined with self-averaging properties of the trace enables an efficient computation of the both longitudinal and Hall components of the conductivity from this expression.

We now turn to the numerical implementation of the above result. Within tight binding we can express the current operator in terms of the analytically derived velocity operator,

$$\hat{\mathbf{J}} = q\hat{\mathbf{v}}/\mathcal{V} = -e\hat{\mathbf{v}}/\mathcal{V}, \quad (3.45)$$

$$\hat{\mathbf{v}} = \frac{i}{\hbar} [\hat{H}, \hat{\mathbf{r}}], \quad (3.46)$$

$$\Rightarrow \mathbf{v}_{ij} = \langle \mathbf{r}_i | \hat{\mathbf{v}} | \mathbf{r}_j \rangle = -\frac{i}{\hbar} t_{ij} (\mathbf{r}_i - \mathbf{r}_j), \quad (3.47)$$

where the final expression lists the matrix elements in the tight-binding real-space basis. We proceed by inserting the expansions of the spectral representations of the delta and Green's functions in the Kubo-Bastin formula of Eq. (3.44), and obtain our final result [92]

$$\sigma_{\alpha\beta}(E_F) = \frac{i\hbar e^2}{\mathcal{V}} \int d\epsilon f(\epsilon) \text{Tr} \left[ \hat{v}_\alpha \delta(\epsilon - H) \hat{v}_\beta \frac{dG^R}{d\epsilon} - \hat{v}_\alpha \frac{dG^A}{d\epsilon} \hat{v}_\beta \delta(\epsilon - H) \right] \quad (3.48)$$

$$\approx \frac{4\hbar e^2}{\pi\mathcal{V}} \int_{-1}^1 d\tilde{\epsilon} f(a\tilde{\epsilon}) \sum_{m,n}^N \Gamma_{mn}(\tilde{\epsilon}) \mu_{mn}^{\alpha\beta}, \quad (3.49)$$

where the dependence on the Fermi level is implicitly included through the Fermi function, and we defined

$$\Gamma_{mn}(\tilde{\epsilon}) = \frac{1}{a^2(1-\tilde{\epsilon}^2)(\delta_{m0}+1)(\delta_{n0}+1)} \times \left[ (\tilde{\epsilon} - in\sqrt{1-\tilde{\epsilon}^2}) e^{in \arccos(\tilde{\epsilon})} T_m(\tilde{\epsilon}) + (\tilde{\epsilon} + im\sqrt{1-\tilde{\epsilon}^2}) e^{-im \arccos(\tilde{\epsilon})} T_n(\tilde{\epsilon}) \right], \quad (3.50)$$

$$\mu_{mn}^{\alpha\beta} = g_n g_m \text{Tr} [\hat{v}_\alpha T_m(\tilde{H}) \hat{v}_\beta T_n(\tilde{H})]. \quad (3.51)$$

Here,  $\Gamma_{mn}$  collects all constant terms in the sum, while  $\mu_{mn}$  defines the expansion moments. Once these moments have been computed to the necessary order in  $N$  required to resolve all features, the full result for the conductivity for any values of filling and temperature then follow easily from evaluation of Eq. (3.49).

The calculation of the expansion proceeds as follows. Define a basis of real-space orbital states  $|i\rangle = c_i^\dagger |0\rangle$ , where  $|0\rangle$  is the Fermi sea with all states unoccupied. We evaluate the trace by formally splitting the moments in terms of left and right components

$$\mu_{mn}^{\alpha\beta} = \text{Tr} [\hat{v}_\alpha T_m(\tilde{H}) \hat{v}_\beta T_n(\tilde{H})] \quad (3.52)$$

$$= \sum_i \langle i | \hat{v}_\alpha T_m(\tilde{H}) \hat{v}_\beta T_n(\tilde{H}) | i \rangle \quad (3.53)$$

$$= \sum_i \langle L, i_m | \hat{v}_\beta | R, i_n \rangle, \quad (3.54)$$

where we defined the left- and righthand components

$$\langle L, i_m | = (\langle i | \hat{v}_\alpha) T_m(\tilde{H}), \quad (3.55)$$

$$|R, i_n\rangle = T_n(\tilde{H}) |i\rangle. \quad (3.56)$$

We proceed by computing these vectors one at a time to order  $N$  and then performing the required inner products which yield the expansion moments. Employing the recursion relations of Eq. (3.29), we can calculate the right-hand vector for all  $n$  using only an initial state  $|i\rangle$

$$|R, i_0\rangle = |i\rangle, \quad (3.57a)$$

$$|R, i_1\rangle = \tilde{H} |i\rangle, \quad (3.57b)$$

$$|R, i_{n+1}\rangle = 2\tilde{H} |R, i_n\rangle - |R, i_{n-1}\rangle, \quad (3.57c)$$

which can be iterated in linear time to any order  $N$ . The left-hand vector can be computed in a similar fashion by setting the initial state to  $|i'\rangle = (\hat{v}_\alpha^\dagger |i\rangle)$  and taking the Hermitian conjugate at the end of the recursion procedure. Once both independent recursions have been performed to order  $N$ , the expansion moments then follow from the inner product as defined in Eq. (3.54).

### 3.4.3 Including the valley projector

Studies of the valley Hall effect requires a decomposition of the full Hall conductivity into valley components, as we saw earlier when we considered the Berry curvature approach. In the KPM we study this effect through the valley projector [44, 80]

$$\hat{P}_{K(K')} = \sum_{\mathbf{k} \in K(K')} |\mathbf{k}\rangle\langle\mathbf{k}|, \quad (3.58)$$

where the  $K(K')$  subscript indicate projection to the same valley regions as defined previously in Fig. 3.1(a). Defining the valley current operator as  $\hat{J}_\beta^{K(K')} = \hat{P}_{K(K')} \hat{J}_\beta \hat{P}_{K(K')}$  and making the replacement  $\hat{J}_\beta \rightarrow \hat{J}_\beta^{K(K')}$  in the Kubo-Bastin formula of Eq. (3.44), we end up studying the valley resolved expansion moments

$$\mu_{mn}^{\alpha\beta, K(K')} = \text{Tr} \left[ \hat{v}_\alpha T_m(\tilde{H}) \left( \hat{P}_{K(K')} \hat{v}_\beta \hat{P}_{K(K')} \right) T_n(\tilde{H}) \right] \quad (3.59)$$

$$= \sum_i \langle L, i_m | \hat{P}_{K(K')} \hat{v}_\beta \hat{P}_{K(K')} |R, i_n\rangle. \quad (3.60)$$

Substitution of these moments in the Kubo-Bastin formula [Eq. (3.49)] allow us to compute valley resolved conductivities, and thus to obtain the full valley Hall conductivity defined in Eq. (3.13). Calculation of these valley resolved moments involves terms on the form  $\sum_{\mathbf{k} \in K(K')} |\mathbf{k}\rangle\langle\mathbf{k}|R, i_n\rangle$ , which can be efficiently computed in a three step process: (i) fast Fourier transform (FFT) of the real space vector to its representation in reciprocal space, (ii) projection to the valley region, and (iii) an inverse FFT back to real space before the final inner product yielding the valley resolved moment is performed. The efficient FFT-based approach to this projection ensures that the computational cost is negligible when compared to the sparse-matrix-vector products of the moment calculation.

### 3.4.4 Stochastic evaluation of the trace

Our expanded quantities involve a trace over all orbitals of the system, which, for the extremely large system sizes considered, can become computationally expensive. This

issue can be avoided by using the self-averaging properties of the expansion, leading to the following stochastic approximation to the trace [91]

$$\text{Tr} [\hat{\mathcal{O}}] = \sum_i \langle i | \hat{\mathcal{O}} | i \rangle \quad (3.61)$$

$$\approx \frac{1}{N_{rv}} \sum_{rv} \langle rv | \hat{\mathcal{O}} | rv \rangle, \quad (3.62)$$

where  $N_{rv}$  is the number of random vectors. Random vectors can be constructed as  $|rv\rangle = \sum_i \exp(2\pi i \phi_i) |i\rangle$ , where  $\{\phi_i\}_{i=1}^D$  is a set of random numbers drawn from a uniform distribution on the interval  $(0, 1)$ . The error in above approximation scales inverse with the product of the total dimension of the system (size of  $H$ ) and number of random vectors,  $err \propto (\sqrt{N_{rv}D})^{-1}$  [91], and hence only a small number of random vectors need to be considered when computing the trace in large systems. These random vector moments can be computed efficiently in parallel.

### 3.4.5 Numerical details and convergence

We set two broadenings in the calculation of the conductivity, the thermal broadening in the various Fermi functions, and the broadening inserted during the kernel convolution used to damp the Gibbs oscillations in the truncated Green's function expansion. The broadening of the latter depends on the choice of kernel and the number of moments in the expansion  $N$ . The broadenings are then

$$\tilde{\eta}_T = \frac{k_B T}{a}, \quad (3.63a)$$

$$\tilde{\eta}_\phi^J = \frac{\pi}{N}, \quad (3.63b)$$

$$\tilde{\eta}_\phi^L = \frac{\lambda}{N}. \quad (3.63c)$$

When selecting the number of energy points  $N_\varepsilon$  in the trapezoidal integration over the full scaled energy interval, we enforce the general procedure of covering the minimal broadening  $\tilde{\eta}_{min} = \min(\tilde{\eta}_T, \tilde{\eta}_\phi)$  with at least four points. This high number of points becomes especially important when calculating the Fermi surface contribution at low temperatures where the Fermi window function is sharply peaked. In terms of the reduced bandwidth  $\tilde{W} = 2$  (width of the Chebyshev domain) this criterion translates into a definite number of energy points  $N_\varepsilon = 4\tilde{W}/\tilde{\eta}_{min}$ , where the result is implicitly rounded to the nearest integer.

### 3.4.6 Convergence of the density of states

Having fixed a size of the real space system, the two main details to pay attention to when performing calculations within the Chebyshev expansion method is the number of moments in the expansion  $N$  and the number of random vectors  $N_{rv}$ . In Fig. 3.4(a-b) we illustrate the convergence of the density of states with these two variables for the tight-binding model of graphene under the A/B staggered potential introduced in Eq. (2.21), with  $V_{AB} = 0.45$  eV. The system consists of the graphene unit cell tiled in a  $600 \times 600$  grid, including  $2 \times 600^2 = 7.2 \times 10^5$  orbitals in the calculation.

We consider first in Fig. 3.4(a) the calculation without the random vector approximation, i.e., evaluating the trace in full, and different values of the expansion order  $N$  (the curves are shown with a small offstep for clarity). We see that the expansion order effectively sets the energy broadening of the calculation due to the inclusion of the Jackson kernel [Eq. (3.63b)]. In Fig. 3.4(b) we consider a different situation where the expansion order

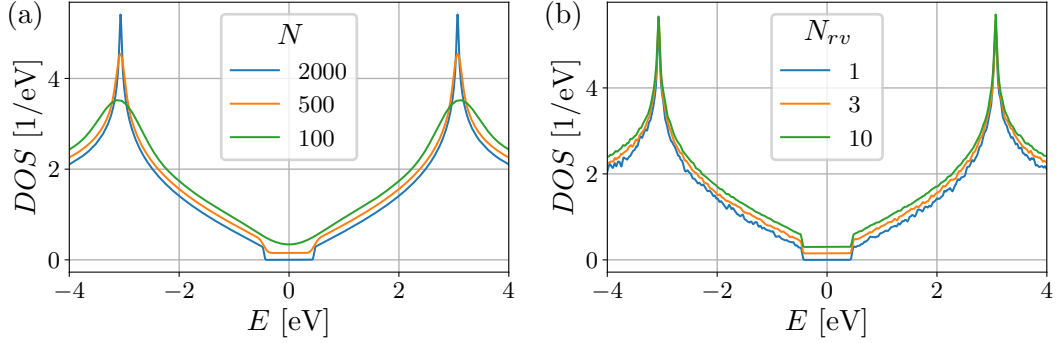


**Figure 3.4:** Convergence of the DOS as obtained in the large-scale Chebyshev expansion method. (a) DOS calculated for the tight-binding model of graphene with an A/B staggered potential, shown here without the random vector approximation and varied expansion order  $N$ . (b) Repeated calculation for fixed expansion order  $N = 2000$ , and a varied number of random vectors  $N_{rv}$ . Curves in both figures are shown with a small offstep for clarity.

$N = 2000$  is fixed while the number of random vectors is varied. The result illustrates why the random vector approximation must be applied with care - including too few random vectors introduces artificial features in the result, in this case the breaking of the particle hole symmetry of the underlying model for  $N_{rv} = 1, 3$ . As noted previously, however, the random vector approximation converges quickly to the full trace for large system sizes considered in this work.

### 3.5 Summary and comparison of methods

In this chapter we outlined the numerical methods which will be used throughout the thesis. We were mostly concerned with two different methods for the calculation of the valley Hall conductivity. In the first method we obtained directly the full distribution of electronic Berry curvature, the symmetry of which will be helpful to understand our results in later sections. In addition, the Berry curvature itself can become important in several predicted effects, such as the Berry curvature dipole mechanism in the nonlinear Hall effect [96] and for applications in current rectification [97]. A major drawback for studies of superlattices using this method is the required diagonalization of the tight-binding Hamiltonian, limiting the maximum system size.

In contrast, the second method based on Chebyshev expansion allows for the calculation of valley-Hall and longitudinal conductivities on the same level of approximation in large systems, leading to a well-defined expression for the valley Hall angle. A drawback is the lack of knowledge of the electronic Berry curvature, with the conductivity obtained directly using the valley projected current operator instead. The main advantage for our purposes is the linear scalability, which will enable us to study disorder corrections to the valley Hall conductivity. In addition, as we investigate in Chapter 5, an added benefit of the Kubo formalism is the possibility of decomposing the full conductivity into Fermi surface and Fermi sea components [80, 94, 98].



## Chapter 4

# Valley Hall effect in gate-defined graphene superlattices

*This chapter contains content published in Physical Review B 00, 005400 (2019).*

With the main numerical methods of the thesis developed, we now turn to the application of these techniques for studies of valleytronics in graphene superlattices. A multitude of solid state systems have been suggested as platforms for achieving dissipationless electronics using the valley Hall effect, including two dimensional platforms in, e.g., bilayer graphene under a transverse electric field [38, 99] and graphene aligned precisely to an underlying hBN substrate [39, 40]. In this chapter we introduce a novel system of this type, a monolayer graphene superlattice optimized for valleytronics where the valley Hall effect becomes directly tunable by an external potential. This allows for a smooth interpolation between the massless and massive Dirac fermions in the nanostructured system, providing a degree of control which enables predictions of unambiguous signatures in measurement. Our studied system is inspired by recent developments within the nanostructuring community where dielectric nanopatterning has been used to define gate-tunable superlattice potentials [41], as discussed in Section 1.3. In addition, as we shall see in the following chapter (Chapter 5), the engineering of the valley Hall effect by an external potential also provides an opportunity to study intrinsic and extrinsic contributions to the valley Hall effect.

We start off this chapter by summarizing some of our earlier discussion on the valley Hall effect in the well-known low energy model of massive Dirac electron we introduced in Section 2.4. We present the analytical predictions for the valley Hall effect in this simplified picture and quantify the region of validity of the model when moving beyond the idealized system by comparing the analytical results of the low energy model with the full tight-binding model of graphene under a staggered potential. We then turn to our study of the valley Hall effect in graphene superlattices defined by an external potential, where we demonstrate band gap formation as a universal feature in the superlattice system, a result also indicated by earlier studies of perturbations of  $C_3$  symmetry in graphene [100, 101]. Moving beyond our considerations of the electronic structure of the superlattice, we explain the symmetry and gate-tunability of the electronic Berry curvature in the superlattice Brillouin zone and demonstrate how the corresponding unfolded quantity indicates the presence of the valley Hall effect. We go on to quantify this effect by calculating the valley Hall conductivity as a function of the electronic filling in the superlattice system,

finding characteristic plateaus of the valley Hall conductivity in the gapped region with gate-tunable widths and positions. A figure of merit for the valley Hall effect is provided by calculation of the valley Hall angle relating the anomalous response to the longitudinal conductivity. Based on our results for this Hall angle we make initial qualitative predictions for the experimental signature of the valley Hall effects in these systems in nonlocal resistance experiments. Finally, the robustness of our results is demonstrated by including repeated irregularities in the superlattice potential and external potentials which decay realistically at the edges of the nanostructured regions.

## 4.1 A simple model

Prior to our analysis of the superlattice result we will investigate a simple model which has been studied in detail analytically [61]. This will prepare us to better understand features in the superlattice results, helping us in particular to isolate effects of the superlattice engineering from effects of the breakdown of the low energy model, i.e., the crossover to the full tight-binding result, with increasing potential magnitudes. We reiterate here some of the discussion of Section 2.4.

Consider the tight-binding model of graphene under a staggered perfectly A/B antisymmetric potential

$$H = -t \sum_{\langle ij \rangle} \left( a_i^\dagger b_j + H.c. \right) + V_{AB} \sum_i \left( a_i^\dagger a_i - b_i^\dagger b_i \right), \quad (4.1)$$

where we have defined the creation and annihilation operators of the graphene A and B sites. In the low energy approximation, and in the limit of vanishing intervalley scattering, the above model yields the massive Dirac model we studied in Section 2.4 with mass term  $\Delta = V_{AB}$ . In that model we previously found the Berry curvature of the conduction band in the  $K$  valley to be [Eq. (2.24)]

$$\Omega_{xy}(\mathbf{q}) = -\frac{\Delta v_F^2 \hbar^2}{2(\Delta^2 + \hbar^2 v_F^2 q^2)^{3/2}}, \quad (4.2)$$

with  $v_F = \sqrt{3}at/2\hbar$ , and a valley Hall conductivity of the fully filled valence band of  $2e^2/h$ . This latter result is derived under assumption of infinitely extending linear Dirac bands in the integration of the Berry curvature, an approximation which only applies exactly for graphene as the mass tends to zero and the Berry curvature becomes fully localized at the Dirac points [35]. We will now compare this idealized model with the full tight-binding result and demonstrate that, while a close resemblance is found at low energies, the applicability of the model is not only limited by the presence of intervalley scattering, but also by the fact that the two valleys share the same momentum space in the graphene Brillouin zone. The correction to the valley Hall conductivity associated with the latter approximation becomes increasingly important in tight-binding modeling as the width of the Berry curvature distribution increases beyond the narrowly defined valley region of the Dirac model.

In Fig. 4.1(a) we show the tight-binding Berry curvature (full lines) compared with the analytical result (dashed lines) evaluated on the same grid in reciprocal space for three different values of the staggered potential. As expected, the numerical result closely matches the analytical expression, but has a small deviation which increases as the staggered potential approaches the energy scale of the hopping  $t$ . This discrepancy is clearly expressed at the edge of the BZ valley region, where the Berry curvature must change sign under time-reversal symmetry (see Eq. (2.14a)). As shown in Fig. 4.1(b) this sign change is,

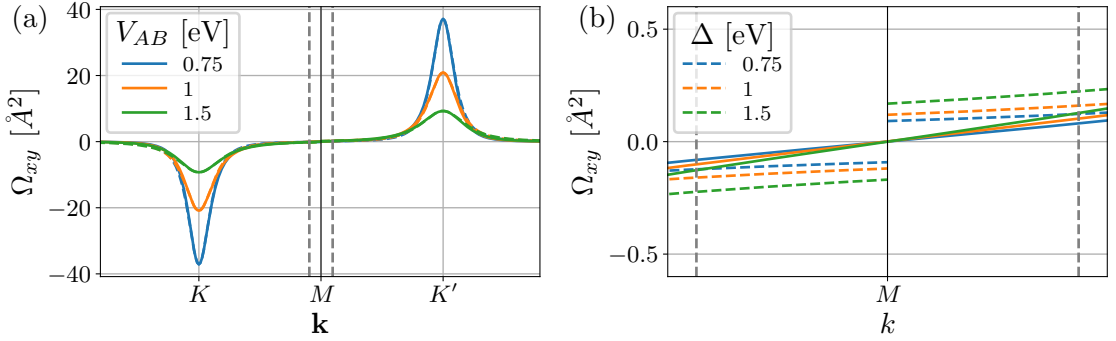


**Figure 4.1:** Comparison of Berry curvatures in the low energy and tight-binding models. (a) Berry curvature from the tight-binding calculation (full lines) compared with the analytical result in the low energy massive Dirac model (dashed lines). Results are shown for a several magnitudes of the staggered potential (induced mass). (b) Same quantities shown at the edge of the valley region [across the  $M \rightarrow \Gamma$  symmetry line of Fig. 3.1(a)] as indicated by the dashed lines in (a). The tight-binding Berry curvature changes sign across the boundary as required by time-reversal symmetry. The analytical expression shows the same behavior but becomes discontinuous across the valley region boundary due to the assumed decoupling into separate  $K, K'$  massive Dirac models. The magnitude of the discontinuity increasing with the size of the staggered potential (induced mass).

as should be the case, obeyed by the tight-binding result. The corresponding analytical result becomes discontinuous as the valley index is exchanged across the boundary, with the magnitude of the discontinuous jump increasing with the size of the mass term. We clearly see the limit of applicability of the low energy model - the Berry curvature only becomes fully localized in one valley region for small mass terms, and only in this limit does the above expression for the valley Hall conductivity holds. For larger induced mass terms the valleys are no longer fully decoupled, and the graphene system cannot be viewed as two copies of a topological insulators having opposite masses, an interpretation usually assumed in the modeling of experimental results [38–40]. We note that the assumption of decoupling of the valleys remains a good approximation if only small perturbations are considered as is often the case in such experiments, but exceptions do exist, e.g., within artificial honeycomb lattices as pointed out by Qian et al. [102] wherein the implications for the bulk-boundary principle are also discussed. As a consequence of the extension of the Berry curvature distribution across the valley boundary, integration of the analytical result in the numerical grid yields a conductivity smaller than the quantized value in the massive Dirac model of  $2e^2/h$ , a result consequently mirrored in the integrated tight-binding Berry curvature. We find that limiting value of  $2e^2/h$  is approached in the opposite limit when the staggered potential (induced mass) tends to zero.

## 4.2 Electronic structure of the superlattice

Our choice of superlattice geometry was inspired by the experimental work by Forsythe et al. [41], wherein a triangular superlattice of cylindrical indentations was constructed in the dielectric  $\text{SiO}_2$  beneath the graphene sheet and band engineering was demonstrated as discussed in Section 1.3. Based on initial studies of this superlattice system and our earlier symmetry arguments for the Berry curvature, we consider the effect of triangular indentations in the dielectric corresponding to the induced potential of Fig. 4.2(a). The full heterostructure is illustrated schematically in Fig. 4.2(c), showing the deformation of the nanostructured regions in the dielectric (circular  $\rightarrow$  triangular). According to our

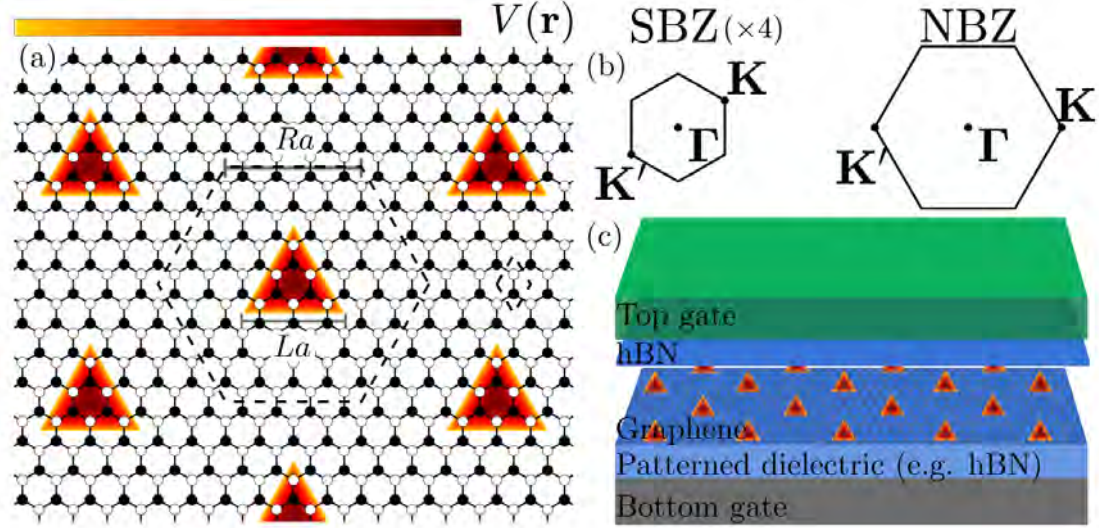


**Figure 4.2:** The gate-defined graphene superlattice. (a) The graphene superlattice considered in this chapter. The supercell, characterized by the side-length  $L$ , is outlined (dashed black line) alongside the triangular superlattice potential (white-to-red gradient) characterized by the length  $R$ . (b) The superlattice and normal Brillouin zones, with the former shown enlarged (times 4) for clarity. (c) Schematic of the dielectric setup for achieving the gate-tunable superlattice potential, showing graphene encapsulated between dielectrics with a nanostructured dielectric on beneath the graphene which enables definition of the superlattice potential by a bottom gate.

earlier definitions [see Eq. (3.16)], we can define the superlattice geometry by the matrix

$$\mathbf{M} = L \begin{pmatrix} 2 & 1 \\ 1 & 2 \end{pmatrix}, \quad (4.3)$$

with  $L$  the side-length of the supercell hexagon in units of lattice constant  $a$  as shown in Fig. 4.2(a). A comparison of the "normal" Brillouin zone (NBZ) of the graphene unit cell and the superlattice Brillouin zone (SBZ) of the supercell is shown in Fig. 4.2(b).

The superlattice potential is modeled as shifts in the onsite energies in the tight-binding model

$$H = \sum_{i,\sigma} V(\mathbf{r}_i) c_{i\sigma}^\dagger c_{i\sigma} - t \sum_{\langle ij \rangle, \sigma} c_{i\sigma}^\dagger c_{j\sigma} + H.c., \quad (4.4)$$

where  $\mathbf{r}_i$  labels positions of graphene orbitals, and  $V(\mathbf{r})$  is defined by the geometry of the nanostructured region. In Fig. 4.2(a) we characterize the extent of this potential by the triangle side-length  $R$ . The second term is the conventional nearest neighbor tight-binding model of graphene, with  $t = 3.033$  eV. We initially consider the induced potential to have perfectly flat edges and to be aligned to a zigzag edge in the graphene sheet, corresponding to, e.g., the triangular defects observed in hBN nucleated selectively on a single sublattice [103], an edge profile which minimizes the effects of intervalley scattering [104, 105]. We return later to realistic modeling of both irregularities in the nanostructuring and the decay of the potential towards the edges of the gated region as found in, e.g., COMSOL simulations [77]. The  $C_3$  symmetry of the induced potential is found to guarantee the universal formation of band gaps in the system as the superlattice potential magnitude is increased, as previously found from a general symmetry argument by Malterre et al. [100].

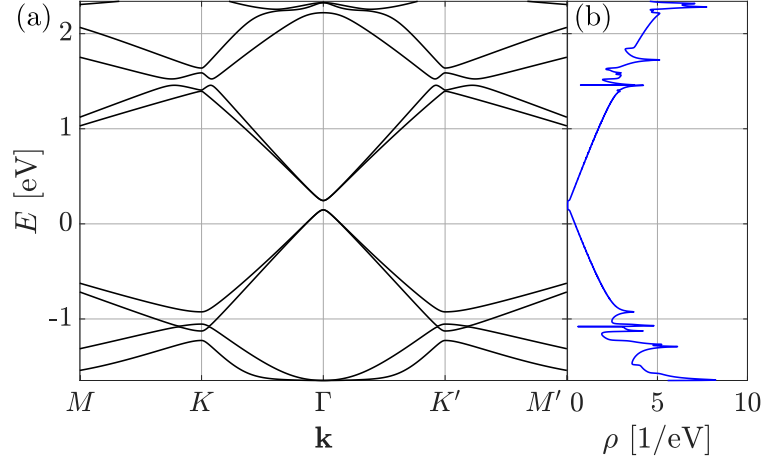


**Figure 4.3:** Typical electronic structure of the gate-defined superlattice. (a) Band structure of the superlattice shown in Fig. 4.2(a) [ $V = t/2$ ] demonstrating a band gap at the downfolding point of the NBZ Dirac cones, which is the SBZ  $\Gamma$  point in this specific geometry. (b) Corresponding density of states.

We note that the induced band gaps are diminished upon rotation of the potential with respect to the perfect zigzag alignment of Fig. 4.2(a), but remain robust up until large rotation angles, with gap closing only at the critical angle  $\phi = 60^\circ$  where the potential recovers A/B symmetry (as also found for a continuum model of similar systems by Jung et al. [77]).

We show a typical band structure of the nanostructured system in Fig. 4.3(a) for the specific geometry ( $L = 4, R = 3, V = 2 \text{ eV}$ ) of Fig. 4.2(a), where we have selected a large magnitude of the potential to clearly show the general features of the band structure engineering. The corresponding DOS is shown in Fig. 4.3(b). In the considered geometry, the graphene valleys downfold to the SBZ  $\Gamma$  point, forming the valence and conduction bands of the superlattice and inducing a band gap at finite potential magnitudes. These bands, which resemble the bands of the massive Dirac close to the gap, remain nondegenerate due to the different symmetry of the downfolded bands depending on whether they downfold from the  $K$  or  $K'$  valley, and the center of the band gap is shifted up in energy by the superlattice potential.

The band structure shown in Fig. 4.3(a) is typical in the sense that a band gap is universally formed in the described geometries as the magnitude of the superlattice potential is increased. However, the width of the gap depends on the detailed specifics of the geometry, a fact found generally in nanostructured graphene [48, 50, 52, 106], and the bands may split further as the potential magnitude is increased. This important feature is shown in Fig. 4.4(a) where we present the DOS for three different geometries with varying extents of the superlattice potential. We characterize these band structures and related DOS by the width of the gap  $\Delta$  and the shift in the center of the gap  $E_s$  (with  $E_s = 0$  in unperturbed graphene). The inset shows the variation with the magnitude of the superlattice potential of the gap width (full lines,  $x$ -markers) and gap shift (dashed lines, circle markers). The gap shift is shown to vary linearly with the magnitude of the superlattice potential in all cases, and we find the slope of these curves to be well-fitted by a simple linear model which considers the average potential in the supercell  $V_{avg} = V(N_V/N_{SC}) \propto V(R^2/L^2)$ , where  $N_V = R^2$  is the number of gated sites and  $N_{SC} = 6L^2$  is the total number of sites in the supercell.

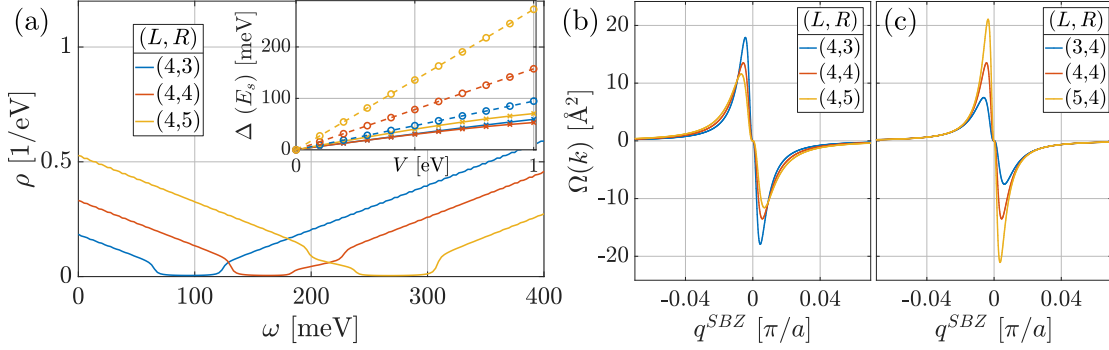


**Figure 4.4:** Band structure and Berry curvature engineering in gate-defined superlattices. (a) Progression of the DOS as the supercell size is increased ( $V = 1$  eV), demonstrating the enhancement of the band gap at larger potentials, and the step-wise variation as bands split. The inset shows the extracted band gap and shift increasing with the magnitude of  $V$ . (b-c) Linecut of the Berry curvature for different geometries. The width of the sign changing peak is determined by the ratio of  $L$  to  $R$ , and the superlattice potential magnitude  $V$ .

Naive applications of similar simple models for the expected width of the band gap fail to capture the sensitive dependence on the specific geometry and thus do not fit the tight-binding result, a fact that has been shown previously in similar studies of both periodically gated graphene [50] and for antidot lattices [48, 52]. In particular, such models fail to take into account the interplay between the magnitude of the induced asymmetry for the  $C_3$  potentials considered here and the effect on graphene of periodic potentials where even simple disk-shaped potentials can induce band gap formation. The latter of these mechanisms can yield extreme sensitivity to small variations in the supercell size  $L$  [106]. In our case we thus restrict ourselves to making the general prediction that the width of the induced band gap is directly proportional to the magnitude of the potential  $V$  and the extent of the gated region  $R$ , and inversely proportional to the supercell size  $L$ , i.e., the distance between the nanostructured indentations in the dielectric.

#### 4.2.1 Tuning and unfolding the Berry curvature

The band gap formation in the superlattice is accompanied by the development of Berry curvature "hot spots" near the band edge. In Fig. 4.4(b)-(c) we show the variation with the superlattice geometry of the occupied Berry curvature of the fully filled valence bands, i.e., with the Fermi level fixed in the gap. The Berry curvature in the SBZ forms a sign changing peak around the point to which the valleys fold ( $q = 0$ ), with the width of the peak proportional to the size of the induced band gap. This translates into a Berry curvature distribution which can be tuned by varying the extent of the induced potential ( $R$ ), as shown in Fig. 4.4(b), or the size of the supercell ( $L$ ), as shown in Fig. 4.4(c). We explore this connection between the engineering of the band structure and the resulting Berry curvature distribution further in Fig. 4.5, where we plot in Fig. 4.5(a) the spectral weight in the SBZ for two values of the superlattice potential for a fixed geometry ( $L = 4, R = 3$ ). The dashed lines in the first of these plots shows the  $V = 0$  result for comparison, i.e., the pristine graphene bands downfolded into the SBZ. As the superlattice potential is increased we see the widening and shift of the gap, and in Fig. 4.5(b) we demonstrate the corresponding effect on the Berry curvature, i.e., a widening of the peak.

With the superlattice results for the band structure and Berry curvature established, we now turn to our quantity of interest for the valley Hall effect - the unfolded Berry curvature

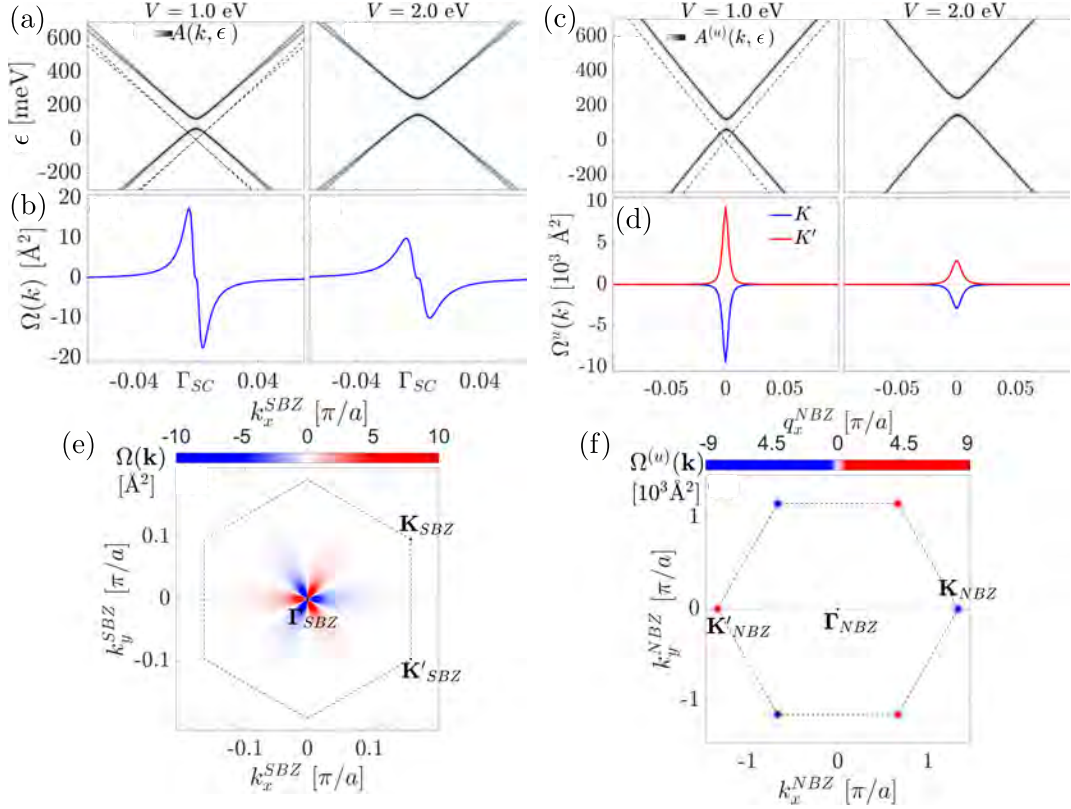


**Figure 4.5:** Unfolding of the spectral weight and Berry curvature. (a) Spectral weight linecut through the  $\Gamma_{SC}$  point in the SBZ for  $V = 1, 2$  eV. The pristine graphene band structure is indicated by the black dashed lines. (b) Occupied Berry curvature with the Fermi level in the middle of the band gap in the SBZ, showing the sign changing peak across the  $\Gamma$  point. (c) Unfolded spectral weight from (a) shown in the NBZ, here presented in the  $K$  valley. (d) Unfolded Berry curvature from (b). The Berry curvature unfolds to form peaks localized in the valley regions of opposite signs in the  $K, K'$  valleys, indicating the presence of the valley Hall effect. (e) Full BZ results of the Berry curvature for  $V = 2$  in the SBZ and (f) unfolded to the NBZ, respectively. The "flower-like" symmetry structure of the SBZ Berry curvature arises from the downfolding of the peaks near the  $K, K'$  points of the NBZ.

in the NBZ. In Fig. 4.5(c) we consider first the unfolded spectral weight from the earlier result of Fig. 4.5(a), shown in this case in the  $K$  valley. The bands unfold into massive Dirac model like bands albeit shifted up in energy as mentioned earlier. The corresponding result in the  $K'$  valley can be found by simply rotating the above linecut around the  $q = 0$  point. The unfolded Berry curvature is shown in Fig. 4.5(d) superimposed in both the  $K$  (blue curve) and  $K'$  (red curve) valleys. The Berry curvature unfolds to peaks of opposite signs in the two valley regions, indicating the presence of the valley Hall effect in the superlattice. The unfolded peaks, which resemble the massive Dirac model result, can be tuned by varying the magnitude of the superlattice potential or the geometry of the superlattice in a similar manner to the band structure nanostructuring. Comparing the Berry curvature distribution obtained directly in the full SBZ and unfolded to the NBZ, as shown in Fig. 4.5(e)-(f), sheds further light on the sign changing peak we saw in Fig. 4.5(b): The full rotational symmetry of the flower-like structure of the Berry curvature in the SBZ in Fig. 4.5(e) is seen to correspond to the downfolding of the unfolded Berry

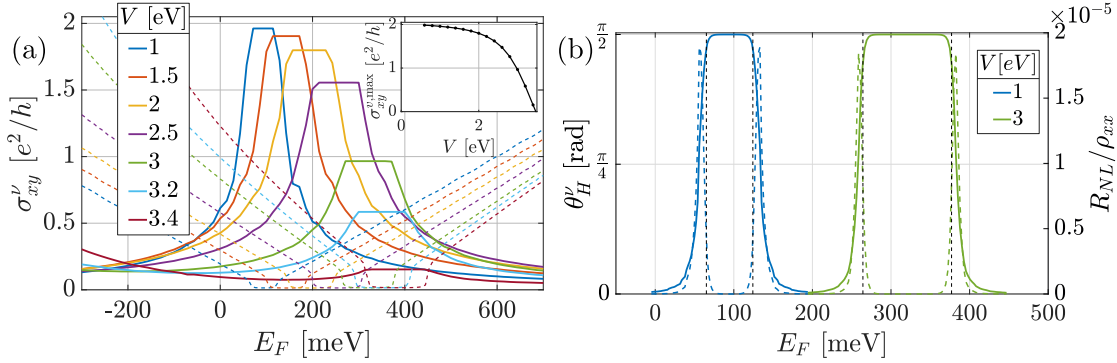


**Figure 4.6:** Tuning the valley Hall conductivity and associated nonlocal response. (a) Valley Hall conductivity as a function of the filling for different magnitudes of the superlattice potential (full lines), alongside the corresponding DOS (dashed lines). The inset shows the plateau value (max) of the VHC as a function of  $V$ , demonstrating the convergence towards the  $2e^2/h$  value of the massive Dirac model at small  $V$ , and the decay when the bands start to flatten at  $V \sim t$ . (b) Valley Hall angle (full lines) for two values of the superlattice potential, which closely mirrors the valley Hall conductivity. The expected nonlocal response is shown in dashed lines, indicating peaks at the band edges, the location of which are tuned by the superlattice potential.

curvature peaks of opposite sign in Fig. 4.5(f) with different symmetry depending on the valley index.

### 4.3 Tunable valley Hall conductivity

The valley Hall conductivity follows for all values of the Fermi level by integration of the unfolded Berry curvature as defined in Eq. (3.11). In Fig. 4.6(a) we show the result of this procedure for different values of the superlattice potential (full lines), alongside the corresponding DOS (dashed lines). Starting with the result for the smallest potential considered ( $V = 1$  eV, blue lines) we see the general structure of the variation with the Fermi level: As the gap edge is approached from below states in the Berry curvature "hot spot" are progressively filled, increasing the valley Hall conductivity to a value just below the low energy model result of  $2e^2/h$ . At the band edge the valley Hall conductivity saturates and remains constant in the gap until the next band edge is reached. Then, states with Berry curvature of the opposite sign are filled and the peak in the valley Hall conductivity decays. The peak structure resembles the massive Dirac model result [61], with some modifications: (i) the peak is progressively shifted in energy by the superlattice potential, (ii) the peak can occur in steps if, e.g., the nearly degenerate valence bands split further in energy, and (iii) the peak is asymmetrical around the gap center with a longer tail above the upper gap edge. The latter effect is due to the superlattice potential causing a flattening of the upper bands. The inset shows the variation of the value of the valley Hall conductivity in the gap as a function of the superlattice potential magnitude. For weak potentials the in-gap value approaches the expected value of  $2e^2/h$  found as a limiting value in the massive Dirac model, while flat-band formation in the opposite limit of strong potentials approaching the hopping energy ( $V \sim t$ ) causes a decay of the valley Hall conductivity peak. We note that while the former regime is the one most commonly probed in nonlocal resistance measurements, the latter limit can be probed in artificial honeycomb lattices with a clear signature in, e.g., the backscattering of interface states [102].

### 4.3.1 Valley Hall angle and expected nonlocal response in the pristine system

With the tunability of the valley Hall conductivity demonstrated, we now move on to our predictions of the expected experimental signature in nonlocal resistance measurements. In Fig. 4.6(b) we show the valley Hall angle alongside the expected nonlocal response close to the band edge based on the framework of Beconcini et al. [79], displayed here for two distinct values of the superlattice potential. The corresponding band gaps are indicated by the vertical dashed lines. As expected, the Hall angle quickly falls off as we move away from the band edge where  $\sigma_{xx} \gg \sigma_{xy}^v$  and reaches the limiting value of  $\pi/2$  in the gap. The small decay into the gap is due to the inclusion of a finite temperature of 1 K. The expected nonlocal response (dashed lines) is shown alongside the Hall angle for a sample of width  $W = 100$  nm, inter-terminal distance  $d = 10^3$  nm, and valley diffusion length  $l_v = 10^5$  nm. The relative nonlocal response  $R_{NL}/\rho_{xx}$  forms peaks close to the band edges where  $\theta = \pi/4$ , i.e., the crossover point where  $\sigma_{xx} = \sigma_{xy}^v$ . As mentioned previously we only show the nonlocal response away from the fully gapped region where the underlying interpretation as bulk valley currents remains valid (see the discussion in Section 2.5). We find that expected peaks in measurement can be tuned by the superlattice potential, which broadens and shift the response in terms of electronic filling of the superlattice potential. This mechanism enables a mapping in terms of both the backgate tuning the Fermi level and the applied superlattice potential (bottom gate in Fig. 4.2(c)), providing a clear way of distinguishing valleytronics induced by the dielectric nanostructuring of the superlattice system.

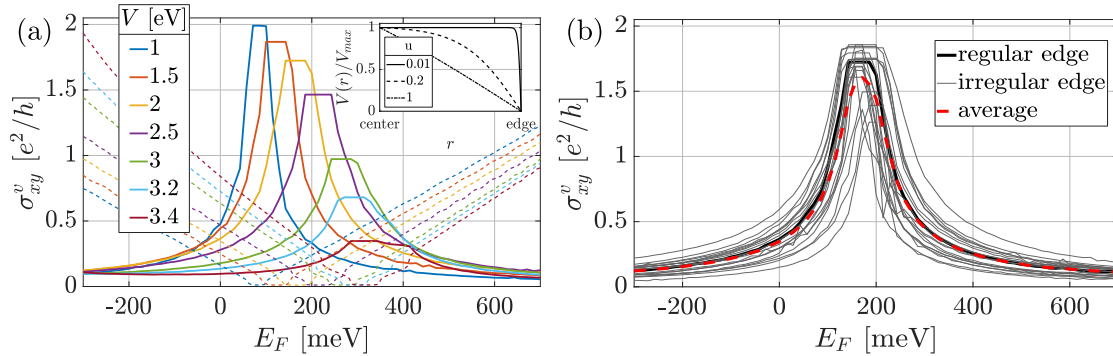


**Figure 4.7:** Robustness of the valley Hall effect. (a) Valley Hall conductivity for a realistic, i.e., smoothly decaying potential, the profile of which is shown in the inset for different values of the parametrization  $u$ . For small potentials we recover the VHC plateaus of Fig. 4.6(a) with a small decrease in the width, while more features appear at larger  $V$  where splitting of the conduction and valence bands lead to steps in the conductivity. (b) Robustness of the VHC with respect to irregularities in the superlattice potential. The VHC is shown for multiple random potentials added close to the edge (grey lines), alongside the regular edge result from earlier (black line). The average of the VHC result for the irregular configurations (red line) closely mirrors the regular result with a rounded peak resembling the finite temperature result.

#### 4.4 Robustness of results for realistic potentials and irregular gating

Having presented the electrostatic tuning of the Berry curvature and the associated valley Hall conductivity in the pristine and optimally aligned superlattice, we now need to also consider the effect of imperfections in the nanostructuring. In this section we include in our modeling the effects of realistic potential profiles as well irregularities in the induced potentials, leaving true disorder considerations to the following chapter. In Fig. 4.7(a) we consider first the effect of having the potential decay towards the edges, as can be expected for indentations in the dielectric of finite length [41, 50, 77]. The inset shows the potential variation from the center of the nanostructured region towards the edge for three values of the free parameter  $u$ , interpolating between the previous flat potential ( $u \ll 1$ , full line), decay toward the edge ( $u = 0.2$ , dashed line), and the extreme case of the linearly decreasing potential ( $u = 1$ , dashed-dotted line). More information about the spatial profile of the potential is included in Appendix B. In the figure itself we show the valley Hall conductivity for the representative value of  $u = 0.2$  for the same magnitudes of the potential as previously. The results are similar, with clear plateaus around the gapped regions of the corresponding DOS, with the gap widths slightly diminished. A difference is that the more complicated structure of the gated region yields split conduction bands, causing the valley Hall conductivity to decay in steps as each band edge is reached. This effect can be seen most clearly in the alignment between steps in the DOS (dashed lines) and steps in the valley Hall conductivity (full lines) and is more pronounced for the stronger potentials considered where the band splitting is enhanced.

In Fig. 4.7(b) we consider also the effect of irregularities in the superlattice potential corresponding to imperfections in the dielectric nanostructuring which could affect the valley Hall response. Most important is issues at the edges of the induced potential: Irregularities which deform the overall inversion asymmetric shape of the induced potential could lead to a vanishing of the valley Hall conductivity. We thus consider Anderson-like

disorder close to the edges of the potential, i.e., we add a random potential for each site which is a nearest neighbor to the edge

$$H_A = \sum_{i,\sigma} w_i c_{i\sigma}^\dagger c_{i\sigma}, \quad (4.5)$$

where the potentials  $w_i$  are drawn from a uniform distribution of width  $V/4$ . For the potential of  $V = 2$  eV (with  $u = 0.2$ ) chosen for the representative results in Fig. 4.7(b), this corresponds to  $w_i \in [-0.5, 0.5]$  eV. The previous result with no irregularities ( $w_i = 0$ ) is shown (full black line) alongside the results for several different random configurations (gray lines) and the average (red dashed line). Variation occurs around the previous result, but with a clear plateau or peak structure in the valley Hall conductivity in all cases. The average of these configurations tracks the regular result with a disorder-induced broadening which is similar to the effect of adding a finite temperature to the system, indicating that the valley Hall effect should be robust in the irregular superlattice.

We note that taking this average of perfectly repeated superlattice results in this manner only serves in this case as an initial indications of the stability of the valleytronic response in these systems with respect to real disorder in the nanostructuring, and we leave the full study for the following chapter (Chapter 5) where the important effect of disorder can be captured directly in the calculation in a consistent manner.

## 4.5 Summary and outlook

In this chapter we demonstrated a tunable valley Hall effect in graphene superlattices defined by periodic potentials with broken inversion symmetry. We quantified the emergence of tunable band gaps with associated Berry curvature hot spots near the band edges, and how the Berry curvature unfolds to peaks of opposite sign in each valley of the graphene Brillouin zone. When integrated, these peaks yield plateaus of finite valley Hall conductivity as a function of the electronic filling, plateaus which can be tuned by varying the superlattice potential which also shifts the expected experimental signature in nonlocal transport measurements.

We have considered the robustness of these effects with respect to realistic induced potential shapes, and found only minor modifications to the valley Hall response. Our initial considerations of irregularities in the nanostructuring and thus in the induced potential also indicated this robustness. These considerations were by computational necessity limited to simple repeated irregularities from the perfectly aligned system, and we thus require further techniques to study true disorder effects. In the following chapter (Chapter 5) we present the application of such methods to this problem when we use large-scale real-space calculations to study the valley Hall conductivity in the disordered system.



## Chapter 5

# Valley Hall effect in the disordered superlattice

*This chapter contains content which is in preparation for publication in collaboration with J. H. Garcia and S. Roche (Paper VI)*

We have in the preceding chapter presented a demonstration of the valley Hall effect in graphene superlattices with broken inversion symmetry. The superlattice potentials considered were in all cases perfectly periodic allowing for a calculation of the Berry curvature based on the diagonalization of the tight-binding Hamiltonian of a single supercell with period boundary conditions. The inclusion of disorder in the calculation modifies this simple picture. Previously, the dominant contribution to the valley Hall conductivity has been intrinsic - related to the formation of Berry curvature "hot spots" at the band edges near the induced band gap in the perfectly ordered superlattice.

In this chapter we move beyond this idealized system and consider also the extrinsic contribution to the valley Hall effect induced by disorder such as vacancies, add-atoms, and the like. For the indirectly nanostructured systems we considered in Chapter 4, the most interesting type of disorder to consider is the effect of imperfections in the regular nanostructuring of the dielectric environment. Within our modeling this corresponds to corrections to the induced superlattice potential. The motivation for these studies is twofold: In addition to investigating the robustness of our earlier result we are also interested in the regime where the extrinsic contribution becomes dominant. As previously discussed in Section 2.5.2 the usual interpretation of nonlocal transport measurements breaks down within the gapped system, and thus only a response at the band edge is expected in the pristine system. In the gapless disordered system, however, an extended peak in the valley Hall conductivity driven by the Fermi surface contribution is expected to induce a broad nonlocal response [107]. In addition, the extrinsic contributions also allow new applications for these types of systems not possible in the pristine case as proposed, e.g., within current rectification by Isobe et al. [97]. The work presented is still in preparation, and while we only include figures of fully converged calculations, we do provide some comments on other initial results and indications in these systems.

### 5.1 Intrinsic and extrinsic contributions to the valley Hall effect

When considering extrinsic contributions to the valley Hall effect in the disordered system, we are fortunate in being able to draw upon the extensive literature concerning the same

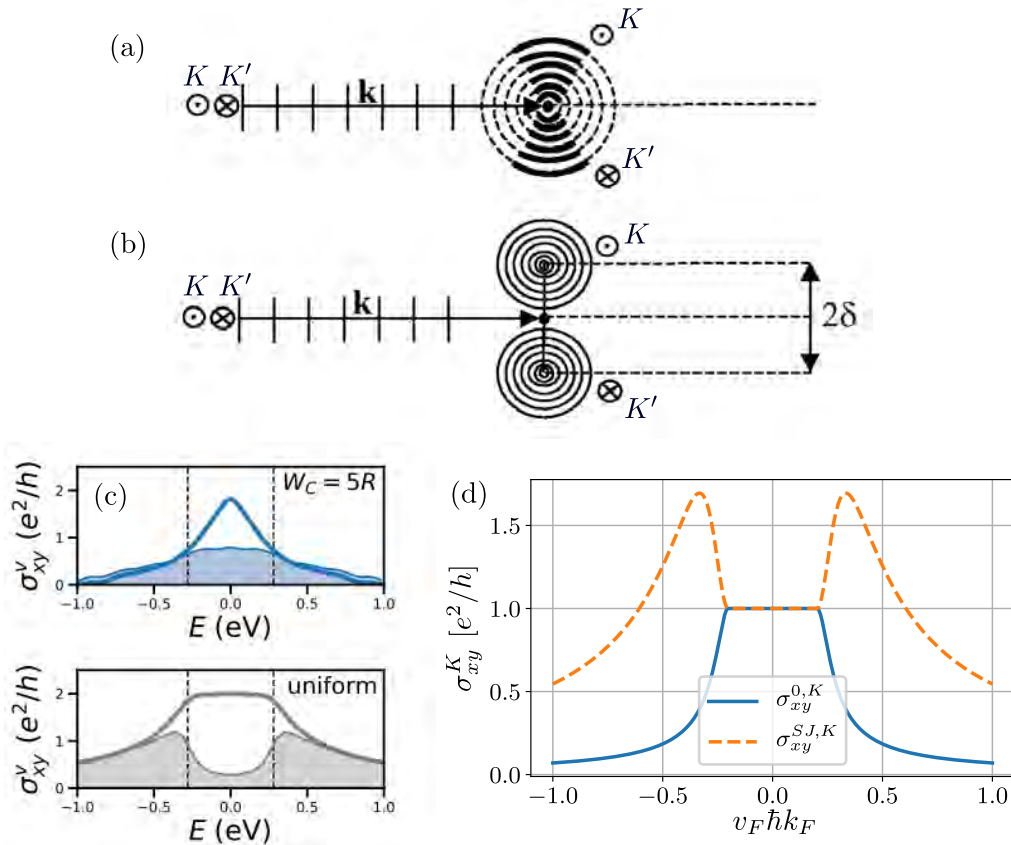


**Figure 5.1:** Disorder corrections to the valley Hall conductivity. (a-b) Illustration of the two conventional classifications of extrinsic contributions to the valley Hall conductivity: (a) Skew-scattering, and (b) side-jump. Adapted from Crépieux and Bruno [94]. (c) Transition from the topological (Fermi sea dominated) regime in graphene under a uniform staggered potential to the Fermi surface dominated (shaded part) regime in a "mass dots" superlattice on graphene where the staggered potential is applied in select disk-shaped regions. Reproduced from Aktor et al. [107]. (d) Intrinsic (blue curve) and side-jump (orange dashed curve) contributions to the valley Hall conductivity of the massive Dirac model. The side-jump contribution enhances the response near the band edge but disappears in the band gap.

problem within the anomalous Hall effect in ferromagnetic metals [66, 108]. Here, studies seeking to distinguish intrinsic and extrinsic contributions to the anomalous Hall conductivity are, broadly speaking, split between (i) extensions of semiclassical approaches based on the Boltzmann equation discussed in Section 3.3, and (ii) systematic Green's function approaches like the Kubo formalism we considered in Section 3.4.2 [109]. The former approach (i) has the advantage of being physically transparent but lacks a systematic derivation within a controlled expansion. In Fig. 5.1(a-b) we show the two different extrinsic contributions considered in this approach and their physical interpretation, adapted here for the valley Hall effect. Skew-scattering, as illustrated in (a), is a valley selective scattering of electrons upon the impurity potential related to asymmetries in higher order scattering processes, and is usually classified as the part of the disorder correction to the conductivity which depends explicitly upon the impurity concentration  $n_{dis}$  as the skew-scattering contribution  $\sigma_{xy}^{SK}$ .

When a wavepacket interacts with a local impurity potential, the interaction is not fully

described as a simple instantaneous change of direction [108]. Integrating over the anomalous velocity during the time interval during which the wavepacket interacts with the impurity potential, another extrinsic contribution is found which corresponds to a coordinate shift or "side-jump" of the wavepacket center as illustrated schematically in (b) with different shifts depending on the valley index. The resulting anomalous correction to the distribution function and the direct accumulation of coordinate shifts of the wavepacket are classified collectively as the side-jump contribution  $\sigma_{xy}^{SJ}$  [110]. These contributions are usually classified as the part of the extrinsic contribution which does not depend explicitly on the disorder density  $n_{dis}$ .

In contrast to the above picture, the systematic Kubo approach (ii) can be technically difficult to implement in full and lacks the same physical transparency. A comparison between these two approaches has been undertaken by Sinitsyn et al. [109] for exactly the massive Dirac model we considered as a simple model of the valley Hall effect in Section 2.4. Here, the semiclassical side-jump and skew-scattering contributions were identified as distinct sums of Feynman diagrams within the Kubo approach. Their results rely upon the decomposition of the Kubo-Bastin formula of Eq. (3.44) into distinct Fermi sea and Fermi surface contributions, with the latter contribution capturing all extrinsic corrections in the weak disorder limit. Prior to presenting the analytical results for extrinsic contributions within the massive Dirac model, we thus consider this decomposition of the Kubo-Bastin formula and its implementation within the kernel polynomial method.

### 5.1.1 Fermi sea and Fermi surface contributions to the Hall conductivity

The Kubo-Bastin equation presented in Eq. (3.44) depends on the full spectrum of the Hamiltonian through the integral over energy, in contradiction to our intuitive understanding that the longitudinal conductivity should depend only on states close to the Fermi level. We saw such a result when considering the Boltzmann result for the conductivity in Section 3.3. The result by Streda [111], as later generalized by Crépieux and Bruno [94], resolves this issue by demonstrating that the Kubo-Bastin equation can be split into two components, often called the Fermi surface (FS) and Fermi sea (or topological, T) contributions [80]

$$\sigma_{\alpha\beta} = \sigma_{\alpha\beta}^{FS} + \sigma_{\alpha\beta}^T. \quad (5.1)$$

Here, the Fermi surface contribution

$$\sigma_{\alpha\beta}^{FS} = \hbar\mathcal{V} \int d\epsilon \frac{df(\epsilon)}{d\epsilon} \text{Im} \left( \text{Tr} \left[ \delta(H - \epsilon) \hat{J}_\alpha G^R(\epsilon, H) \hat{J}_\beta \right] \right), \quad (5.2)$$

only involves states near the Fermi level, and the Fermi sea contribution

$$\sigma_{\alpha\beta}^T = \frac{\hbar\mathcal{V}}{2\pi} \text{Re} \left( \int d\epsilon f(\epsilon) \text{Tr} \left[ \left( G^R(\epsilon) \hat{J}_\alpha \frac{dG^R(\epsilon)}{d\epsilon} - \frac{dG^R(\epsilon)}{d\epsilon} \hat{J}_\alpha G^R(\epsilon) \right) \hat{J}_\beta \right] \right), \quad (5.3)$$

turns out to be responsible for, e.g., the quantized conductivity in the conventional quantum Hall effect [80]. A benefit of the Kubo-Bastin approach to the conductivity is that both of these components can be calculated independently, enabling us to study in detail the effect of disorder scattering through the Fermi surface term.

It turns out that even when a high degree of disorder in the system closes the gap, suppressing the intrinsic contribution to the valley Hall effect, a transition to a disordered regime can occur where the Fermi surface contributions dominates. Aktor et al. [107] recently considered the difference between a uniform staggered potential on graphene as studied in Section 2.4 and small disk-shaped "mass dots" where this staggered potential is

present. In the latter case a global band gap is not formed, but the valley Hall conductivity may remain nonzero stemming from the scattering effects on these local mass dots. The result, as shown in Fig. 5.1(c), is a transition from the usual uniform regime with a peak in the gap stemming from Fermi sea contribution to a different regime where the Fermi surface contribution (shaded region) dominates. As discussed previously in Section 2.5.2 this formation of a broad peak in the valley Hall conductivity in the absence of a transport gap should enable a unambiguous detection within nonlocal resistance measurements with the response mediated by valley currents flowing in bulk of the sample.

We proceed within the kernel polynomial method by expanding the Fermi surface contribution (for the full derivation see Appendix C) [80]

$$\sigma_{\alpha\beta}^{FS}(E_F) = \frac{\hbar e^2}{\mathcal{V}} \int d\epsilon \frac{df(\epsilon)}{d\epsilon} \text{Im Tr} [\hat{v}_\alpha \delta(H - \epsilon) \hat{v}_\beta G^R(\epsilon, H)] \quad (5.4)$$

$$= \frac{\hbar e^2}{\mathcal{V}} \int_{-1}^1 d\tilde{\epsilon} a \frac{df(\epsilon)}{d\epsilon} \text{Im Tr} \left[ \hat{v}_\alpha \frac{-1}{a} \delta(\tilde{\epsilon} - \tilde{H}) \hat{v}_\beta \frac{1}{a} G^R(\tilde{\epsilon}, \tilde{H}) \right] \quad (5.5)$$

$$\approx \frac{4\hbar e^2}{\pi\mathcal{V}} \int_{-1}^1 d\tilde{\epsilon} [-2k_B T (\cosh[(a\tilde{\epsilon} - E_F)/kT] + 1)]^{-1} \text{Re} \left( \sum_{m,n}^M \Gamma_{mn}^{FS}(\tilde{\epsilon}) \mu_{mn}^{\alpha\beta} \right), \quad (5.6)$$

where we have utilized the previously defined moments  $\mu_{mn}^{\alpha\beta}$  of Eq. (3.51), and defined

$$\Gamma_{mn}^{FS}(\tilde{\epsilon}) = \frac{1}{a(1 - \tilde{\epsilon}^2)(\delta_{m0} + 1)(\delta_{n0} + 1)} e^{in \arccos(\tilde{\epsilon})} T_m(\tilde{\epsilon}). \quad (5.7)$$

The missing Fermi sea component can either be computed independently or obtained the earlier definition in Eq. (5.1) as  $\sigma_{\alpha\beta}^T = \sigma_{\alpha\beta} - \sigma_{\alpha\beta}^{FS}$ .

### 5.1.2 Analytical results in the massive Dirac model

Assuming a disorder modeled by random potentials following Gaussian correlations  $\langle V(\mathbf{r}_1)V(\mathbf{r}_2) \rangle = n_{dis} V_0^2 \delta(\mathbf{r}_1 - \mathbf{r}_2)$ , Sinitzyn et al. [98] calculated the Hall conductivity within the massive Dirac model using the Kubo-Bastian approach outlined in Section 5.1.1 above. We present here the result adapted for the valley Hall conductivity [86]

$$\sigma_{xy}^K = \sigma_{xy}^{0,K} + \sigma_{xy}^{SJ,K} \quad (5.8)$$

$$= \frac{e^2 \Delta}{2h \sqrt{(v_F \hbar k_F)^2 + \Delta^2}} \times \left[ 1 + \frac{4(v_F \hbar k_F)^2}{4\Delta^2 + (v_F \hbar k_F)^2} + \frac{3(v_F \hbar k_F)^4}{(4\Delta^2 + (v_F \hbar k_F)^2)^2} \right], \quad (5.9)$$

where we recognize the first term as the intrinsic contribution studied previously in Section 2.4 [Eq. (2.25)], and the two additional terms are classified as side-jump since they do not depend explicitly on the impurity concentration  $n_{dis}$  [98]. The intrinsic and side-jump contributions are shown in Fig. 5.1(d), demonstrating that the side-jump contributions stem from the Fermi surface term [Eq. (5.2)] in the Streda decomposition of the Kubo-Bastian formula, enhancing the valley Hall conductivity near the band edges but disappearing in the band gap. The skew-scattering contribution is absent for the specific choice of disorder correlations. We note that although this contribution will in general be proportional to the often small third moment of the disorder distribution, but may diverge even in the dilute disorder limit [98].

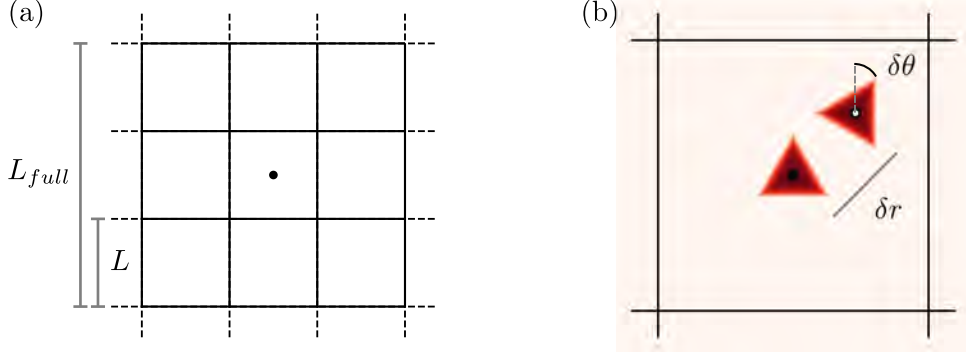


**Figure 5.2:** Schematics of the superlattice geometry. (a) Supercell of the full calculation within the large-scale method of length  $L_{full}$ . Dashed lines indicate periodic boundary conditions. The inner cells of length  $L$  are defined by period of the superlattice potential. (b) Zoom of the central potential-defined supercell in (a), showing the superlattice potential in the pristine and disordered cases. Imperfections in the superlattice potential are defined by the center shift  $\delta r$  and the rotation  $\delta\theta$ .

## 5.2 Electronic structure of the disordered superlattice

Perfectly regular superlattices, as often assumed in initial theoretical modeling, is not available in the laboratory, and such idealized modeling can fail to account for the dramatic effect of disorder on band structure engineering [112]. Hence, we include here a study of the band gap formation in the disordered superlattice. We study similar superlattice systems as the ones investigated in Chapter 4, yet with a slightly different superlattice structure where the basis vectors of graphene are directly extended to define the supercell. This choice for the superlattice geometry makes possible a simple application of the valley projection method outlined in Section 3.4.3, avoiding the complicating need to involve further unfolding techniques. In terms of our earlier geometrical definitions of Eq. (3.16), we define the superlattice geometry of the induced potential by  $\mathbf{M} = L \times \mathbf{I}_{2 \times 2}$ , width  $\mathbf{I}_{2 \times 2}$  the identity matrix. Within the Chebyshev expansion method, the full supercell encompasses multiple such cells tiled along each axis, thus allowing the inclusion of disorder in the superlattice by including different perturbations in each cell. The size of this full supercell, denoted by  $L_{full}$  in the following, is chosen commensurate with the potential periodicity so as to allow for period boundary conditions by setting  $L_{full} = s \times L$ , where  $s$  is an integer counting the number of repeated potentials tiled along one axis. The geometrical setup of the system considered in these calculations is illustrated schematically in Fig. 5.2(a), showing a full supercell enclosing  $s \times s = 3 \times 3$  periods of the superlattice potential. A zoom of the central supercell (indicated by the dot in Fig. 5.2(a)) is shown Fig. 5.2(b), including an illustration of the superlattice potential.

A further requirement for our choice of superlattice geometry is  $\text{mod}(L_{full}, 3) = 0$  which guarantees that we sample the exact  $K, K'$  points in the calculation. This requirement becomes obsolete as the density of the numerical grid increases but is enforced to avoid any obfuscating features caused by asymmetric sampling of the valley regions. We thus write the supercell size as  $L_{full} = 3mL$  where  $m$  is an integer, and the number of gate potentials included is  $L_{full}/L = 3m$ . A typical system size when calculating the density of states in the following is  $L_{full} = 696$ , which includes  $\sim 1 \times 10^6$  orbitals in the calculation.

In Fig. 5.3(a) we show a subset of the full supercell of the calculation enclosing multiple periods of the superlattice potential (red gradient). We have here chosen a representative

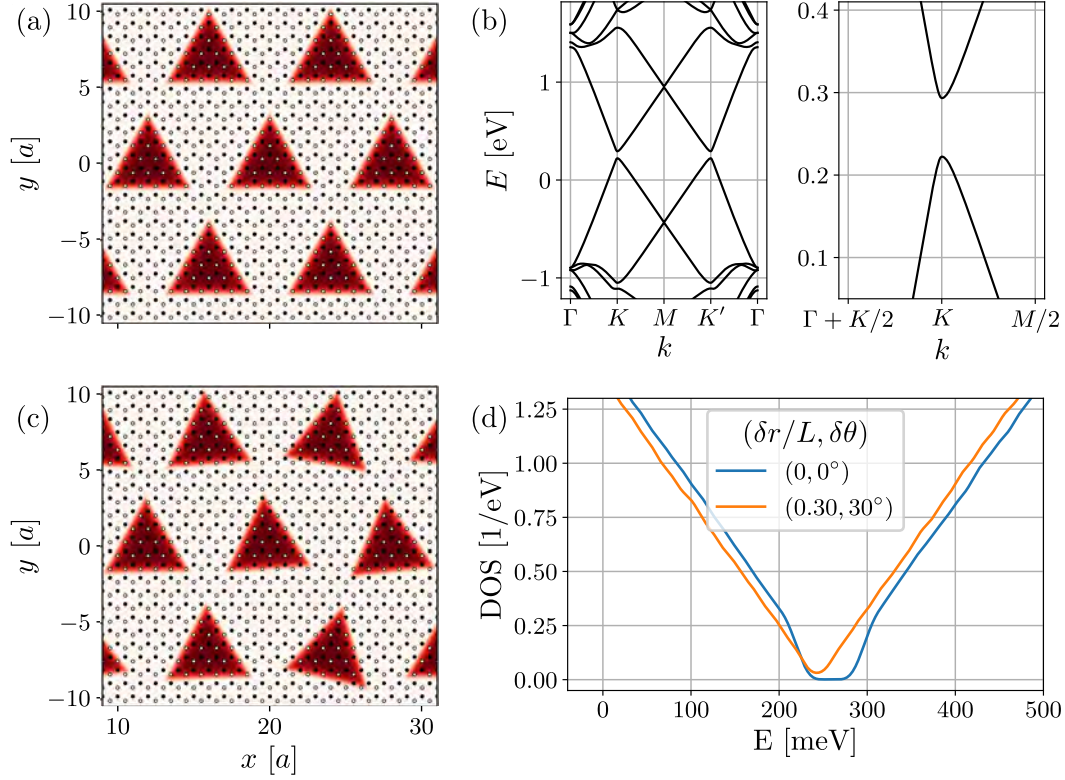


**Figure 5.3:** Electronic structure of clean and disordered superlattices. (a) The pristine superlattice ( $L = 8, R = 6$ ) [see Fig. 4.2(a)], with the superlattice potential magnitude shown by the red shading (here:  $u = 0.1$ ). (b) Band structure of the pristine superlattice with  $V = 0.91$  eV [ $\sim 0.3t$ ] showing the band gap formation at the Dirac points. (c) The strongly disordered superlattice with  $\delta\theta = 60^\circ$  and  $\delta r/L = 0.3$ . (d) Density of states of the pristine (blue curve) and disordered (orange curve) superlattices.

geometry [ $(L = 8, R = 8, V = 0.91$  eV) in our earlier notation of Fig. 4.2(a)] with gated regions large enough so as to allow inclusion of imperfections, while still small enough to facilitate the required number of uniquely perturbed supercells to accommodate a stable average over disorder configurations within a single calculation. The band structure of the pristine superlattice is shown in Fig. 5.3(b), displaying a gap formation at the SBZ  $K, K'$  points with a similar magnitude to our earlier calculations. We again find a gap to be universally formed in these geometries as the superlattice potential  $V$  is increased.

We model disorder corresponding to imperfections in the dielectric etching as random shifts in the position  $\delta r$  and orientation  $\delta\theta$  of the triangular potentials as indicated in Fig. 5.2(b). These corrections are drawn from normal distributions with zero mean

$$\delta\theta \sim \mathcal{N}(0, \sigma_{\delta\theta}^2), \quad (5.10a)$$

$$\delta r \sim \mathcal{N}(0, \sigma_{\delta r}^2), \quad (5.10b)$$

where the degree of disorder is parametrized by the standard deviations  $\sigma_{\delta\theta/\delta r}$ . We will usually denote the shift in the position of the potential  $\delta r$  relative to the potential supercell size, i.e., as the fraction  $\delta r/L$ . An example of a disordered superlattice is shown in Fig. 5.3(c) with ( $\delta r/L = 0.3, \delta\theta = 30^\circ$ ), alongside a comparison in Fig. 5.3(d) of the DOS in the pristine and disordered superlattices demonstrating the lifting of the band gap by sufficiently strong disorder.

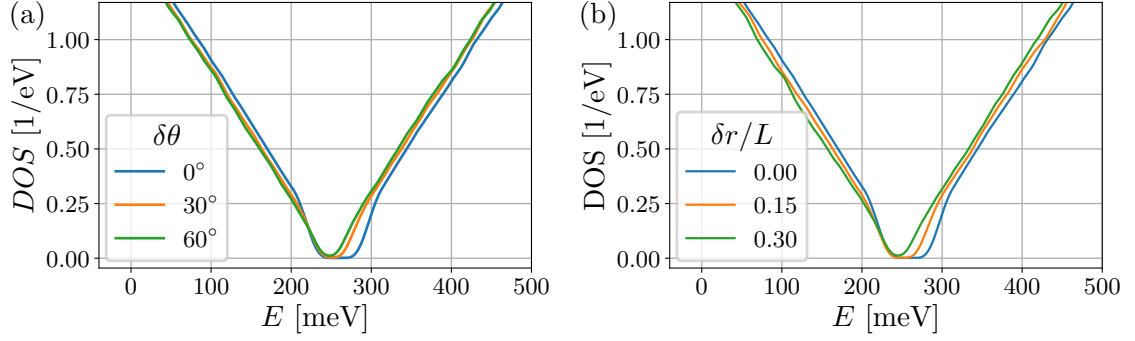


**Figure 5.4:** Robustness of the band gap in the disordered superlattice. (a) DOS for systems with increasing random rotations in the orientation of the gated regions. The gap closes at  $d\theta \sim 60^\circ$ . (b) DOS for systems with increasing random shifts in the location of the gated regions. The gap is robust at small shifts but closes at  $dr/L \sim 0.3$ .

In Fig. 5.4 we investigate the stability of the band gap with respect to these two different sources of disorder by calculating the DOS in the disordered superlattice. As the random rotation in the orientation of the gated region increases, we see in (a) that the width band gap in the DOS first decreases continuously until a critical degree of disorder lifts the gap at  $d\theta \sim 60^\circ$  degrees. A similar result applies to random shifts in the location of gated regions as shown in (b), where the magnitude of the band gap is again decreasing until it fully closes at a critical value of  $dr/L \sim 0.3$ .

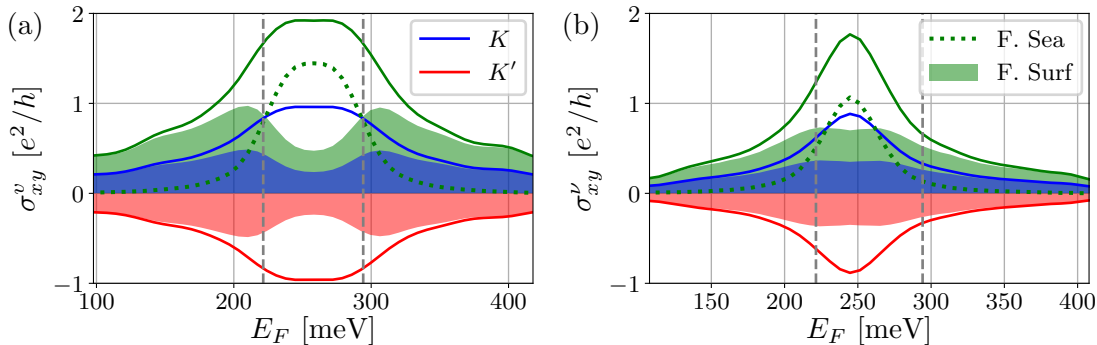


**Figure 5.5:** Valley Hall conductivity in the pristine and disordered superlattices. (a) Valley Hall conductivity in the pristine system (green curve), also resolved in the individual valleys  $K$  (blue curve) and  $K'$  (red curve). The Fermi sea contribution (dotted line) becomes nonzero inside the band gap, while the Fermi surface contribution (shaded part) peaks at the band edges. (b) Valley Hall conductivity in the disordered superlattice, demonstrating that the valley Hall effect survives the closing of the band gap with a dominant Fermi surface contribution. Both calculations performed at a temperature of  $T = 10$  K to fully resolve the Fermi surface contribution.

### 5.3 Valley Hall conductivity in the disordered superlattice

With the effects of disorder in the nanostructuring on the stability of the band gap in the electronic structure established, we can now move on to consider the valley Hall conductivity in the disordered superlattice. As a comparison point, we consider first the pristine case with  $V = 0.91$  eV [ $\sim 0.3t$ ], calculated here in a system size of  $L_{full} = 600$  including  $N_{rv} = 1300$  random vectors. We note that this is very similar to the system we investigated earlier in Chapter 4 through our studies of the electronic Berry curvature. The result obtained using now the large scale Chebyshev expansion method for the valley Hall conductivity is shown in Fig. 5.5(a), where we present both valley resolved conductivities (blue, red full lines), and the valley Hall conductivity itself (green full line). The band gap obtained by direct diagonalization above is shown by vertical dashed lines. As expected, the result within this new theoretical framework mirrors the earlier result of Section 4.3 [Fig. 4.6]. Using the decomposition of the Kubo-Bastin formula, we can now see the formation of the characteristic peak in the valley Hall conductivity. We indicate this decomposition in Fig. 5.5(a) by a dotted line for the Fermi sea contribution, and shading indicating the Fermi surface contribution. Dual peaks are seen in the Fermi surface contribution as the Fermi level nears the band edges around the band gap. Inside the band gap this contribution vanishes, and the valley Hall conductivity is instead driven by the Fermi sea contribution from the filled bands.

For the study of disordered superlattices we choose here a representative geometry with random shifts in alignment of the superlattice potential in each supercell of  $\delta r/L = 0.300$  but remark that similar results apply for imperfections in the potential alignment ( $\delta\theta$ ) as we also found in our study of the DOS. The valley Hall conductivity in this disordered superlattice is shown in Fig. 5.5(b), where we see a transition to a regime where the response is dominated by the Fermi surface contribution (shaded part), with the Fermi sea contribution only present as a narrow peak in the center of the former band gap. The result indicates that the valley Hall effect can survive in the gapless strongly disordered regime, providing valley currents flowing in the bulk of the sample and a well-defined nonlocal response as discussed in Section 2.5.2. We have here presented the extreme cases

of the purely pristine and the strongly gapless superlattices. In the intermediate regime where disorder is present but the band gap survives we find a crossover between these two domains, with the Fermi surface driven peaks at the band edges expanding and moving towards the center of the band gap as the level of disorder is increased.

## 5.4 Summary and outlook

In this chapter we have considered the effects of disorder on our previous results for the valley Hall effect in nanostructured graphene superlattices. We have found the predicted band gaps in the electronic structure are stable up to a high degree of imperfections in the regular pattern of the superlattice potential, including both shifts and rotations in the location of nanostructured region. We have considered the valley Hall conductivity within the expansion of the Kubo-Bastin formula, and found that our earlier results of Chapter 4 based on the integration of the electronic Berry curvature are reproduced. The decomposition of the Kubo-Bastin result for the conductivity into Fermi surface and Fermi sea component has enabled us to understand formation of the band gap-centered peak in the intrinsic valley Hall conductivity. In addition, we have presented our results for the valley Hall conductivity in the disordered superlattice and found a transition into a regime where the conductivity is dominated by the Fermi surface contribution. This finding indicates that such superlattice systems can be used to induce a broad response in the form of valley currents flowing within the bulk of the sample as required for unambiguous detection within nonlocal resistance measurements.

Our initial results do not yet include a study of the longitudinal conductivity, which in the Kubo-Bastin framework can be obtained in the same calculation step as the Hall conductivity, enabling a solid foundation for studies of the valley Hall angle in such systems. Comparison with similar results within the field of spintronics, where the spin Hall angle is often considered as a figure of merit of devices, would be interesting in terms of the practical implementation of valleytronics devices. In addition, defects in the graphene sheet itself could be included, and their effects on the intervalley scattering rate investigated.



## Chapter 6

# Impurity bound states and local magnetic order in the iron-based superconductor FeSe

*The contents of this chapter have been published in Physical Review B **99** (1), 014509 (2018) or are currently under review in Paper V (preprint: arXiv:1909.13515).*

In this chapter we move beyond our studies of 2D materials by investigating bulk and surface properties the iron-based superconductor FeSe, yet still retain our overarching theme of studying the effects of disorder. In particular, the first two studies covered herein provide a clear outline for using disorder to probe the bulk system by combining theoretical predictions with measurement: An initial theoretical study of impurity physics and bound states in the iron-based superconductor FeSe predicts signatures of local magnetic order nucleated near point-like Fe-centered impurities [113] - signatures later examined in scanning tunneling microscopy (STM) measurements [114]. In the later study we extend our theoretical modeling to include also magnetism on the edges of FeSe islands and impurities centered on Se sites defining extended "plaquette" impurity potentials in the model. We begin this chapter by providing a brief introduction to FeSe, with special attention paid to the possible proximity of this material to a magnetic quantum critical point. We then go on to cover the details of our tight-binding model, where interactions are included on the mean field level, and present a self-consistent procedure for capturing the appearance of impurity-nucleated magnetism. For this work we apply, with some minor modifications, the Chebyshev expansion procedure of Section 3.4, which we now use for obtaining the mean fields in a self-consistent calculation of real space densities and magnetizations.

### 6.1 A brief introduction to FeSe

The unconventional properties of the family of iron-based superconductors continues to be a field of intensive research into the complex interplay between structural, magnetic, and superconducting phase transitions [121]. A specific member of the family of these compounds, FeSe, is particularly interesting due to the phase transition to an extended phase of structural distortion called the nematic phase, and the interplay thereof with both magnetic and superconducting phases. The superconducting phase is characterized by a highly anisotropic gap structure, and is particularly interesting due to the high degree of tunability of the associated critical temperature  $T_c$ , which varies from the bulk value of 8 K to values approaching 40 K upon intercalation, pressure, or doping [118, 119, 121–126]. In

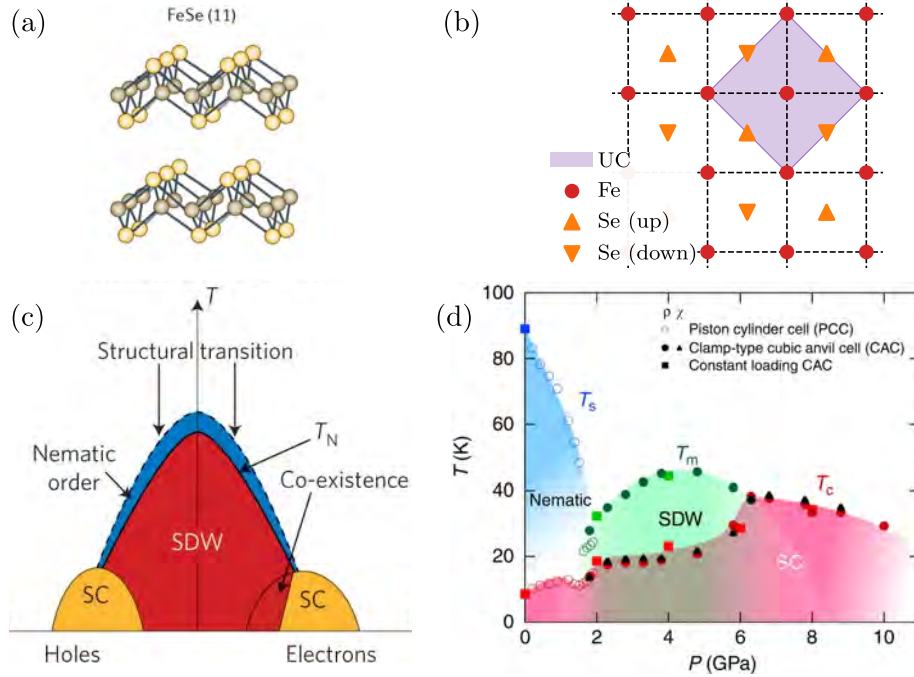


**Figure 6.1:** An introduction to FeSe. (a) The layered crystal structure of bulk FeSe, each layer consisting of the central Fe lattice with surrounding upper and lower Se sublattices. Reproduced from Si et al. [115]. (b) Top view of the crystal structure in (a) with the shaded region indicating the unit cell composed of two Fe atoms due to the staggered Se positions. Reconstructed from Martiny [116]. (c) Schematic phase diagram of the iron-based superconductors showing the complicated interplay between magnetic, structural, and superconducting transitions. In FeSe the spin density wave phase shown here is absent at ambient pressure. Reproduced from Basov and Chubukov [117]. (d) Phase diagram of FeSe as a function of pressure. The nematic phase extends all the way to the tail of the superconducting dome at zero doping ( $T_c \approx 9$  K). The missing SDW phase can be induced by pressure [118–120]. Reproduced from Sun et al. [119].

addition,  $T_c$  increases in the thin film limit, with monolayers of FeSe on  $\text{SrTiO}_3$  reaching values upwards of 65 K [127].

In Fig. 6.1(a) we show the layered structure of bulk FeSe, displaying the central Fe lattice (red disks) surrounded by lower and upper Se sublattices (yellow triangles). A top-down view is provided in Fig. 6.1(b), including the definition of the unit cell which contains two Fe atoms due to the different local environments provided by the staggered pattern of the Se locations. The  $3d$  orbitals of these two inequivalent Fe sites serve as the basis of our tight-binding modeling below. A schematic phase diagram of the family of iron-based superconductors is shown in Fig. 6.1(c). In the undoped compound a weak structural distortion sets in as the temperature is lowered, reducing the crystal symmetry from tetragonal to orthorhombic and defining the nematic (thread-like) phase. Just below this transition an antiferromagnetic (spin density wave [SDW]) phase dominates the phase diagram down to  $T = 0$ . Superconductivity emerges upon either hole or electron doping, forming characteristic domes in the phase diagram.

The phase diagram of FeSe itself, as shown in Fig. 6.1(d), is notably differentiated from those of most iron-based superconductors by the absence of such magnetic ordering in the bulk at ambient pressure. Instead, the nematic phase extends all the way to zero

temperature. However, experimental evidence exists which indicates that FeSe is close to a magnetic quantum critical point [128], including the observation of a transition to an SDW phase at modest pressures indicated in Fig. 6.1(d) [119]. The influence of this proximity to a magnetic instability has also been seen in recent inelastic neutron scattering experiments [129–131], where, as a function of temperature, spectral weight is shifted from  $(\pi, \pi)$  Neel-like fluctuations at high temperatures to stripe-like  $(\pi, 0)$  fluctuations which dominate at low temperatures.

As we explore in this chapter, this proximity to a magnetic quantum critical point suggests that the emergence of impurity-induced magnetism could appear from imperfections such as twin boundaries, atomic vacancies, interstitials, and add-atoms [132]. The very high quality of available FeSe samples [133] make such identifications difficult due to the rarity of crystal imperfections, but some recent evidence does suggest the appearance of local magnetic ordering in bulk probes such as magnetoconstriction [134] and  $\mu$ SR measurements [135, 136]. In addition, a recent STM study of multilayer FeSe found evidence of impurity induced local order in the form of charge stripes nucleated around Fe vacancy sites [137]. This local charge order was suggested to arise from magnetic fluctuations pinned by the vacancy sites, an interpretation mirrored in a study of FeSe films on SrTiO<sub>3</sub> [138].

We are motivated by these observations to study impurity physics in FeSe and in particular the formation of strongly localized local magnetic order nucleated on defect sites. In the following sections we present first a tight-binding model applicable to the study of impurity physics in FeSe, and then move on to study the formation of local magnetic order nucleated around Fe-centered impurities.

## 6.2 Theoretical model of FeSe

The low-energy magnetic fluctuations in bulk FeSe described above have been included by theoretical modeling within an itinerant approach which captures both the temperature and momentum dependence of spin excitations [139–141]. This is only the case, however, when the initial "bare" model is adapted to include the effects of so-called orbitally selective effects: in the multi-orbital correlated system distinct orbitals experience different renormalization of the self energy, leading to orbital-dependent mass effective masses and quasiparticle weights [142–152]. Such renormalizations have been suggested to be characteristic of Hund's metals, and the inclusion of such effects explain recent STM quasiparticle interference measurements in both the normal and superconducting states of iron-based superconductors [153–155]. We note that a multitude of works within the field of unconventional superconductivity have suggested similar effects of bare impurity potentials being dressed by the effects of electronic interactions [156–164].

In this section we introduce the bare version of our model and return at a later point to the inclusion of orbitally selective effects in a "dressed" version of this model. The starting point of our analysis is a tight binding model of FeSe based on initial density functional theory (DFT) calculations later fitted to angle-resolved photoemission spectroscopy and quantum oscillation experiments in the nematic phase of FeSe [153]

$$H_0 = \sum_{ij, \mu\nu, \sigma} (t_{ij}^{\mu\nu} - \delta_{ij} \delta_{\mu\nu} \mu_0) c_{i\mu\sigma}^\dagger c_{j\nu\sigma}. \quad (6.1)$$

Here,  $i, j$  are unit cell indexes and  $\mu, \nu$  span the 3d-orbitals of the two inequivalent iron atoms in the unit cell of Fig. 6.1(b) [10 orbitals in total]. Note the explicit inclusion of the chemical potential  $\mu_0$  in the Hamiltonian, the value of which is set to fix the same density

in each considered system size. Further details of this model including the band structure and Fermi surface can be found in Kreisel et al. [153], Sprau et al. [154], and Kostin et al. [155]. A single point-like impurity on site  $i'$  is included as the term

$$H_{imp} = V_0 \sum'_{\mu,\sigma} c_{i'\mu\sigma}^\dagger c_{i\mu\sigma}, \quad (6.2)$$

where the prime on the sum  $\sum'$  indicates that only the orbitals of a single iron site are included. Interactions are included in the multi-orbital Hubbard-Hund model

$$\begin{aligned} H_{int} = & U \sum_{i,\mu} n_{i\mu\uparrow} n_{i\mu\downarrow} + U' \sum'_{i,\mu<\nu,\sigma} n_{i\mu\sigma} n_{i\nu\bar{\sigma}} + (U' - J) \sum'_{i,\mu<\nu,\sigma} n_{i\mu\sigma} n_{i\nu\sigma} \\ & + J \sum'_{i,\mu<\nu,\sigma} c_{i\mu\sigma}^\dagger c_{i\nu\bar{\sigma}}^\dagger c_{i\mu\bar{\sigma}} c_{i\nu\sigma} + J' \sum'_{i,\mu\neq\nu} c_{i\mu\uparrow}^\dagger c_{i\mu\downarrow}^\dagger c_{i\nu\downarrow} c_{i\nu\uparrow}, \end{aligned} \quad (6.3)$$

where we set  $J = J' = U/4$  and use spin-rotational invariant interactions,  $U' = U - 2J$ , and the primed sums  $\sum'$  only include contributions where the indices  $\mu$  and  $\nu$  label an orbital on the same iron atom. We include this interaction term on the mean field level where decoupling yields

$$H_{int}^{MF} = \sum_{i,\nu,\sigma} \left[ U \langle n_{i\nu\bar{\sigma}} \rangle + \sum'_{\mu\neq\nu} \{ U' \langle n_{i\mu\bar{\sigma}} \rangle + (U' - J) \langle n_{i\mu\sigma} \rangle \} \right] c_{i\nu\sigma}^\dagger c_{i\nu\sigma} \quad (6.4)$$

$$\begin{aligned} & - \sum'_{i,\mu\neq\nu,\sigma} \left[ (U' - J) \langle c_{i\nu\sigma}^\dagger c_{i\mu\sigma} \rangle - J' \langle c_{i\mu\bar{\sigma}}^\dagger c_{i\nu\bar{\sigma}} \rangle - J \langle c_{i\nu\bar{\sigma}}^\dagger c_{i\mu\bar{\sigma}} \rangle \right] c_{i\mu\sigma}^\dagger c_{i\nu\sigma} \\ & - \sum_{i,\nu,\sigma} \left[ U \langle c_{i\nu\sigma}^\dagger c_{i\nu\bar{\sigma}} \rangle + J \sum'_{\mu\neq\nu} \langle c_{i\mu\sigma}^\dagger c_{i\mu\bar{\sigma}} \rangle \right] c_{i\nu\bar{\sigma}}^\dagger c_{i\nu\sigma} \\ & - \sum'_{i,\mu\neq\nu,\sigma} \left[ U' \langle c_{i\nu\sigma}^\dagger c_{i\mu\bar{\sigma}} \rangle + J' \langle c_{i\mu\sigma}^\dagger c_{i\nu\bar{\sigma}} \rangle \right] c_{i\mu\bar{\sigma}}^\dagger c_{i\nu\sigma}. \end{aligned} \quad (6.5)$$

We perform self-consistent calculations of mean fields within this model by expanding the Green's function in a series of Chebyshev polynomials. For this purpose we use a slightly modified version of the method introduced earlier in Section 3.4, obtaining the following expression for the expanded Green's function [91]

$$\begin{aligned} G_{\mu\nu}^{\sigma\sigma'}(i, j, \tilde{\epsilon}) &= \lim_{\eta \rightarrow 0} \left\langle c_{i\mu\sigma} \left| \frac{1}{\tilde{\epsilon} + i\eta - \tilde{H}} \right| c_{j\nu\sigma'}^\dagger \right\rangle \\ &= \frac{-2i}{\sqrt{1 - \tilde{\epsilon}^2}} \sum_{n=0}^{N-1} a_{\mu\nu,n}^{\sigma\sigma'}(i, j) \exp(-in \arccos(\tilde{\epsilon})), \end{aligned} \quad (6.6)$$

where  $N$  is the expansion order,  $|c_{j\nu\sigma'}^\dagger\rangle = c_{j\nu\sigma'}^\dagger |0\rangle$  denotes a single occupied state in the Fermi sea, and we defined the expansion moments

$$a_{\mu\nu,n}^{\sigma\sigma'}(i, j) = \frac{1}{1 + \delta_{0,n}} \left\langle c_{i\mu\sigma} \left| T_n(\tilde{H}) \right| c_{j\nu\sigma'}^\dagger \right\rangle. \quad (6.7)$$

Here, as before,  $T_n$  is the  $n$ th Chebyshev polynomial of the first kind. Note the slight change of notation from our earlier definitions, the expansion moments are now denoted  $a_n$  instead of  $\mu_n$  to avoid confusion with the orbital index. Calculation of the Green's function expansion moments follow as outlined in Section 3.4 [Eq. (3.57)], and we apply again the Lorentz kernel of Eq. (3.33) ( $a_n \rightarrow g_n^L a_n$ ) to damp Gibbs oscillations in the expanded

function (see Section 3.4.1). At the expansion order chosen, this kernel convolution yields a numerical broadening in the region of interest of  $\eta \approx 3$  meV.

The mean fields, which enter into the Hamiltonian through the decoupled interaction Hamiltonian of Eq. (6.6) and in the calculation of the self-consistently updated chemical potential  $\mu_0$ , can be constructed directly from the expanded Green's function

$$\langle c_{i\mu\sigma}^\dagger c_{i\nu\sigma'} \rangle = \int_{-1}^1 d\tilde{\epsilon} \text{Im} G_{\mu\nu}^{\sigma\sigma'}(i, i, \tilde{\epsilon}) f(\tilde{\epsilon}), \quad (6.8)$$

with the Fermi function evaluated at a temperature of  $T = 1$  K in all following calculation. Since the integration over energy occurs at every step in the self-consistent iteration, we require a faster method, different from the trapezoidal integration used previously in Eq. (3.49), for performing these integrals efficiently. The solution is to calculate these integrals by Chebyshev-Gauss quadrature where an efficient FFT-based method can be applied [91], a method which we find to yield excellent convergence properties by selection of a fine energy grid (here:  $N_\epsilon = 2N$ ). In addition to the mean fields, we study also the local density of states (LDOS)

$$\rho_\mu^\sigma(i, \epsilon) = -\frac{1}{\pi} \text{Im} G_{\mu\mu}^{\sigma\sigma}(i, i, \epsilon), \quad (6.9)$$

which in this case is constructed directly from the imaginary part of the Green's function. The obtained mean fields of Eq. (6.8) are found to be fully converged within the numerical broadening at  $N = 1000$ , and we fix this value in all following calculations except when we need to consider the LDOS at a high energy resolution. In that case we set  $N = 20000$ .

The self-consistent procedure proceeds by (i) making an initial guess for the densities  $n(\mathbf{r}_i)$  and magnetizations  $m_z(\mathbf{r}_i) = n_\uparrow(\mathbf{r}_i) - n_\downarrow(\mathbf{r}_i)$ , (ii) calculating the mean fields (e.g.  $n^{calc}, m_z^{calc}$ ) through Eq. (6.8), and (iii) feeding the result back into the mean field Hamiltonian. This procedure is then iterated until convergence is reached. The convergence criterion for this self-consistent iteration is chosen as a maximal variation of the mean fields  $\max(n_{m-1} - n_m) < 10^{-7}$ ,  $n_m$  being the mean field at iteration step  $m$ , with the criterion being satisfied for at least 100 iteration steps before the calculation is deemed converged. For ease of notation this criterion is defined here in terms of the density, but we stress that we apply the criterion to the full set of mean fields obtained from Eq. (6.8). Convergence is usually accomplished within 1500 iterations steps, the exception being calculations with parameters extremely close to phase boundaries where additional iterations must be included. In part (iii) of the self-consistent procedure we ensure numerical stability by using a "mixing" procedure whereby the new mean field at some iteration step  $n_m$  is defined as a linear combination of the previous mean field  $n_{m-1}$  and the result of the direct calculation  $n_m^{calc}$

$$n_m = \gamma n_{m-1} + (1 - \gamma) n_m^{calc}, \quad (6.10)$$

where the choice of  $\gamma \in [0, 1]$  is a trade-off between stability and speed of the calculation. We set  $\gamma = 0.7$  in the following.

This implementation of the Chebyshev expansion method for self-consistent calculations in mean field models is commonly referred to as the Chebyshev-Bogoliubov-de-Gennes (CBdG) method in analogy with the well-known Bogoliubov-de-Gennes (BdG) method for direct calculations of (commonly the superconducting order parameter) mean fields from the eigenvalues and eigenstates of the diagonalized Hamiltonian [91, 165, 166]. Applying the Chebyshev expansion procedure for this problem is extremely efficient (and of

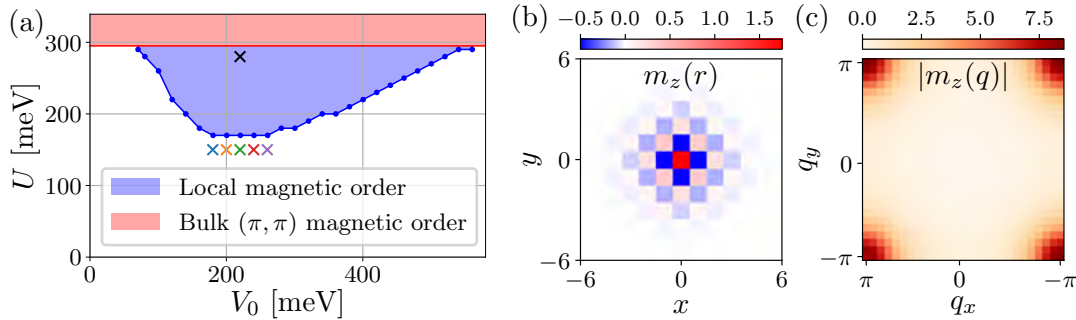


**Figure 6.2:** Nucleation of local magnetic order on impurity sites in the "bare" model. (a) Phase diagram of local magnetic order nucleated on a point-like impurity in FeSe, shown as a function of the Hubbard  $U$  and impurity potential  $V_0$ . A pocket of local magnetic order (blue shading) appears underneath the bulk  $(\pi, \pi)$  phase above  $U_c = 295$  meV (red shading). The system is most susceptible to the formation of local magnetic order at  $V_0 = 220$  meV where the pocket extends the furthest. The black  $x$ -marker deep in this pocket indicates the set of parameters for which we show the real space structure of the local magnetic order in (b), [ $U = 280$  meV,  $V_0 = 220$  meV]. As evident in the Fourier transform of this magnetization in (c), the local order inherits the  $C_4$  structure of the  $(\pi, \pi)$  long range magnetic order above  $U_c$ .

often necessary) for systems where large-scale Hamiltonian need to be considered, such as the multi-orbital model considered in this chapter. The method allows for calculations in systems where diagonalization of the Hamiltonian becomes computationally unfeasible, and yields results consistent with conventional BdG calculations within a well-behaved approximation controlled by the linearly scaling inclusion of additional expansion moments (increasing the expansion order  $N$ ). We do note, however, that a crossover in efficiency between conventional BdG and CBdG calculations occurs at small system sizes if very small mean fields are considered. Here, the exact nature of constructing mean fields directly from the eigenspectrum of the Hamiltonian in the conventional BdG procedure may be more efficient than expanding the Green's function to a very high order within the CBdG framework. For large Hamiltonians, however, direct diagonalization becomes computationally unfeasible and the extremely sparse nature of the tight-binding Hamiltonian allows for easy application of Chebyshev expansion.

### 6.3 Local magnetic order nucleated on resonant states

We begin our study of impurity physics in FeSe by mapping out the phase diagram of bulk and local magnetic order as a function of the Hubbard  $U$  and impurity potential  $V_0$ . We choose a system large enough to ensure converged results for the transition to the bulk magnetically ordered phase and which can accommodate extended local magnetic order around a central impurity site. We thus choose a system size of  $12 \times 12$  unit cells of the 10-band model, containing  $2 \times 12^2 = 288$  iron sites, and enforce periodic boundary conditions. The obtained location of phase boundaries in the parameter space is tested in a much larger  $24 \times 24$  supercell to check for finite size effects.

In the clean system a transition to a bulk  $(\pi, \pi)$  antiferromagnetic phase is found at critical interaction strength  $U_c = 295$  meV, as shown by red shading in Fig. 6.2(a). This transition is expected from earlier susceptibility calculations [153]. Including a single central impurity in the calculations, we find underneath the bulk phase also a region where local magnetic order is nucleated on the impurity (blue shading) for a range of impulsive

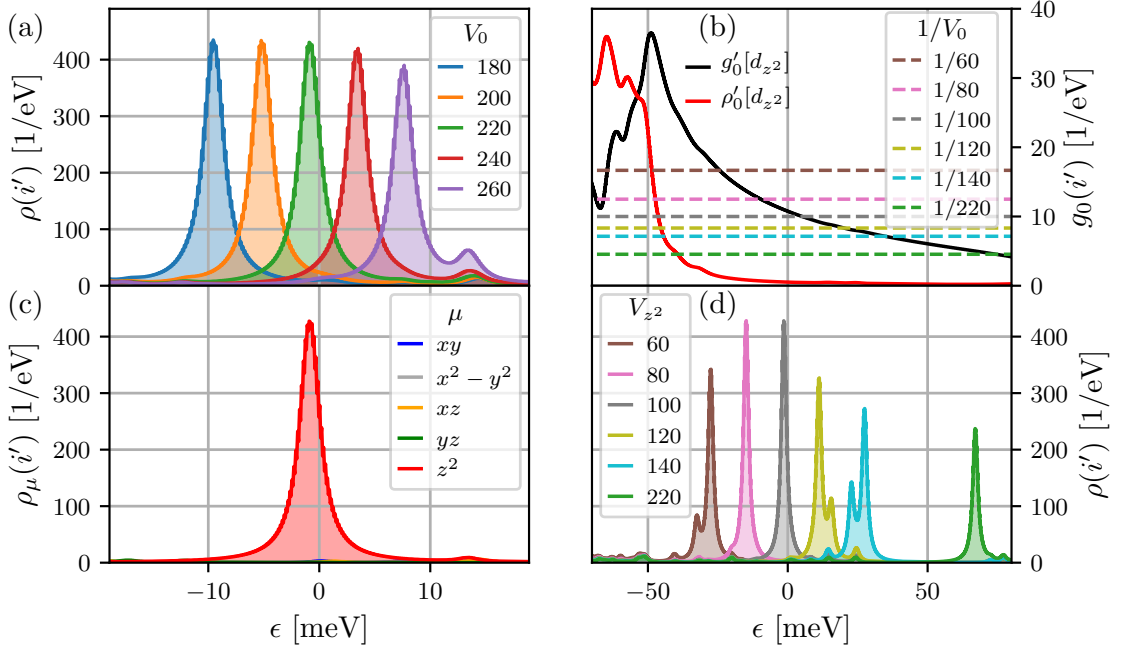


**Figure 6.3:** Impurity-induced resonant states near the Fermi level ( $\epsilon = 0$ ). (a) LDOS at the impurity site  $i'$  with the Hubbard  $U$  chosen just below the local magnetic transition ( $U = 150$  meV), showing a progression of bound states for different values of  $V_0$ . The parameters for these resonant states are indicated by the colored crosses in the phase diagram of Fig. 6.2(a), demonstrating that the local magnetic transition occurs as a local Stoner transition when these resonant states approach the Fermi level. (b) Real (black line) and imaginary part (red line, proportional to the LDOS) of the  $d_{z^2}$  orbital component of the clean system Green's function. Bound (resonant) states are predicted by the T-matrix argument at energies where the inverse impurity potential  $1/V_0$  (dashed lines) crosses the real part of the Green's function and the LDOS is gapped (approximately gapped). (c) Orbital components of the LDOS of the central resonant state in (a) [ $V_0 = 220$  meV], showing that the resonant state is of almost pure  $d_{z^2}$  character. (d) Resonant states close to the Fermi level when self-consistency is removed from the impurity calculation and a purely  $d_{z^2}$  impurity is included, yielding resonant states at the positions predicted from the T-matrix argument.

impurity potentials  $70 \text{ meV} \leq V_0 \leq 560 \text{ meV}$ . The system is seen to be most susceptible to the formation of local magnetic order at around  $V_0 = 220$  meV where the pocket extends the furthest. Selecting a set of parameters deep in this pocket, as indicated by the black  $x$ -marker in the phase diagram, we investigate in Fig. 6.2(b) the real phase structure of the induced magnetization  $m_z(r)$ . The local magnetic order is seen to inherit the bulk phase  $(\pi, \pi)$  ordering, a fact which becomes clear when the Fourier transform  $m_z(q)$  of the local order is considered in Fig. 6.2(c). The local order is of almost perfect  $C_4$  symmetry, with an imperceptible degree of anisotropy arising from the orbital order terms included in the tight-binding model of Eq. (6.1) to capture the nematic order in FeSe at low temperatures.

We now turn to our study of how the local magnetic order is formed and how the local magnetic transition can be predicted directly from the properties of the clean system. In this investigation we follow previous studies which have found a connection between the appearance of local magnetic order and the formation of impurity resonant states at the Fermi level immediately below the local magnetic transition [167, 168], suggesting that the

locally enhanced LDOS of the resonant state causes a local Stoner transition to a magnetic state. We investigate this interpretation in Fig. 6.3. Fixing the Hubbard  $U = 150$  meV immediately below the local magnetic transition, we show in Fig. 6.3(a) the LDOS on the impurity site for a range of impurity potentials as indicated by colored  $x$ -markers in Fig. 6.2(a). We find a progression of resonant states shifting position from below the Fermi level to above the Fermi level as the impurity potential is increased. The point in the phase diagram where the system is most susceptible to the formation of local order, i.e., the maximal extension downwards in  $U$  of the critical coupling line  $U_c^{local}(V_0)$  defining the local transition, is exactly the point where the resonant state crosses the Fermi level ( $V_0 \approx 220$  meV). This fact supports our interpretation of the local order formation as a local Stoner transition.

With the above indications of the local Stoner scenario for the induction of local magnetic order on impurity sites, we can now go one step further and in turn predict how the resonant states are formed directly from the properties of the clean system Green's function. In the presence of a point-like impurity at a single site (here,  $r_{i'} = 0$ ) the Green's function can be written [95, 169]

$$\mathbf{G}(r, \epsilon) = \mathbf{G}_0(r, \epsilon) + \mathbf{G}_0(r - 0, \epsilon)\mathbf{T}(\epsilon)\mathbf{G}_0(0 - r, \epsilon), \quad (6.11)$$

with all quantities representing matrices in the spin and orbital subspaces as defined in Eq. (6.7) ( $\mathbf{V}_0 = V_0\mathbb{I}$  being diagonal in this basis), and where we have defined the impurity T-matrix

$$\mathbf{T}(\epsilon) = \frac{\mathbf{V}_0}{\mathbb{I} - \mathbf{V}_0 \sum_k \mathbf{G}_0(k, \epsilon)} = \frac{\mathbb{I}}{(\mathbf{V}_0)^{-1} - \mathbf{g}_0(\epsilon)}, \quad (6.12)$$

which describes successive scattering on the same impurity. Here, we introduced notation for the local (clean) Green's function  $\mathbf{g}_0(\epsilon) = \mathbf{G}_0(0, \epsilon) = \sum_k \mathbf{G}_0(k, \epsilon)$ . Following Eq. (6.11), we see that the Green's function, and hence also the associated LDOS, can be written as the sum of the clean system LDOS and an impurity induced component

$$\begin{aligned} \delta\rho(r, \epsilon) &= \rho(r, \epsilon) - \rho_0(r, \epsilon) \\ &= -\frac{1}{\pi} \text{Im} [\mathbf{G}_0(r - 0, \epsilon)\mathbf{T}(\epsilon)\mathbf{G}_0(0 - r, \epsilon)]. \end{aligned} \quad (6.13)$$

From the structure of this component, we see that impurity induced bound states correspond to poles of the T-matrix defined in Eq. (6.12). If we consider the local Green's function to be diagonal in the orbital basis, we find five independent criteria for the formation of bound states by solving for these poles

$$\det[(\mathbf{V}_0)^{-1} - \mathbf{g}_0(\epsilon)] \approx \prod_{\mu} \left( \frac{1}{V_0} - g_0^{\mu}(\epsilon) \right) = 0, \quad (6.14)$$

which indicates that a bound state appears at some energy  $\xi$  when the two following conditions are fulfilled for any single orbital  $\mu$ :

$$0 = \rho_0^{\mu}(0, \xi), \quad (6.15a)$$

$$\frac{1}{V_0} = \text{Re } g_0^{\mu\mu}(\xi). \quad (6.15b)$$

Exact solutions of these equations appear in the region where the LDOS is fully gapped, and yield true bound states with a delta function profile of the impurity site LDOS  $\delta\rho(0, \epsilon) = \delta(\epsilon - \xi)$ . When the LDOS is only partially gapped in the given orbital, as

is the case in our model of FeSe, these true bound states broaden into resonant states with a Lorentzian lineshape [170], corresponding to complex solutions  $\xi = \xi' + i\xi''$  of the above equations. As such, resonant states of  $\mu$ -orbital character are predicted to appear in regions where the orbitally resolved LDOS  $\rho_0^\mu(0, \epsilon)$  is partially gapped, with resonant energy  $\xi$  determined by the impurity strength  $V_0$ .

In Fig. 6.3(b) we show the graphical solution to these equations, with the clean system Green's function (solid lines) extracted by converging the supercell densities with  $U = 150$  meV and  $V_0 = 0$ , and the inverse potentials shown as dashed lines. The LDOS components of the three  $t_{2g}$  orbitals all have finite weight in the region of interest around the Fermi level, leaving the two  $e_g$  orbitals  $d_{z^2}, d_{x^2-y^2}$  as candidates for the formation of resonant states. The  $d_{x^2-y^2}$  orbital can be discarded as a candidate since only unrealistically large impurity potentials would fulfill the second condition on the real part of the Green's function, leaving only the  $d_{z^2}$  orbital remaining. In Fig. 6.3(c) we show the orbital components of the LDOS of the central resonant state [the  $V_0 = 220$  meV state in Fig. 6.3(a)] demonstrating that the LDOS is of nearly full  $d_{z^2}$  character as predicted from the T-matrix argument. This argument also explains the progression of resonant states found for increasing impurity potential, since the slope of the real part of the Green's function (black line) is seen to shift the crossing point with the inverse potentials (dashed lines) within the quasigapped region for the  $d_{z^2}$  orbital LDOS (red line).

We have so far seen that the study of the impurity T-matrix correctly predicts both the orbital character of the resonant state and the variation of the resonance energy with the impurity potential. A major caveat to the above argument, however, is that the locations of the predicted resonant state energies of Fig. 6.3(b), i.e., the crossing point of dashed and full lines, does not exactly match the observed center of the Lorentzian profiles in Fig. 6.3(a), being shifted in energy by upwards of 80 meV, a discrepancy between the T-matrix prediction and our self-consistent numerical result. Upon further examination, this shift between model and numerical result is seen arise from the assumptions of the T-matrix solution which (i) does not capture the effects of self-consistent calculation of the densities around the impurity site, and (ii) assumes implicitly a fully  $d_{z^2}$  polarized impurity potential of  $V_0^\mu = \delta_{\mu, z^2} V_0$ . In contrast, the CBdG calculation includes the effects of self-consistency, and a realistic impurity potential chosen equal in all orbitals ( $V_0^\mu = V_0 \forall \mu$ ). Repeating the CBdG calculation with these restrictions, i.e., neglecting self-consistency and including a purely  $d_{z^2}$  impurity of equal strength, creates resonant states which now, within the numerical broadening, match the expected position from the T-matrix solution. These resonant states are shown in Fig. 6.3(d), with a color scheme matching that of the dashed lines in Fig. 6.3(b). Relaxing each of these restrictions individually reveals that the effects of self-consistency (i) are minor, with the main shift in resonant state energy arising from the different form of the impurity potential (ii). Combined with the local Stoner argument presented above, the prediction of resonant states directly from the clean system properties suggests an efficient way of predicting regions of local magnetic order in the phase diagram. Instead of searching for this pocket by brute-force evaluation of the phase diagram on a grid in the  $(U, V)$  parameter space, an guideline for the calculation can be obtained directly from a single calculation of the Green's function in the clean system.

### 6.3.1 Orbital selectivity

Correlated multi-orbital models, such as the ones applicable to the FeSCs and FeSe in particular, have been proposed to include effects of so-called orbital selectivity. Dynamical mean field theory [142, 143] and slave-spin methods [144–147] have been used to investigate self-energy effects on, e.g., the band structure of these materials, finding a strong orbital dependence of the mass renormalization and splitting of quasiparticle weights  $Z_\mu$ . Recent

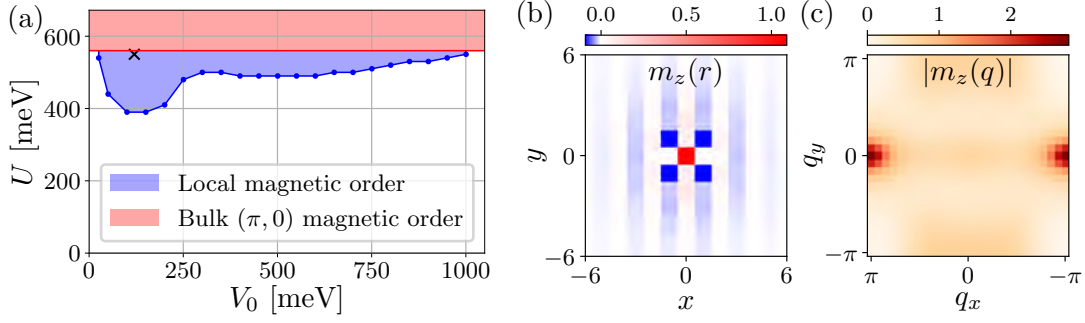


**Figure 6.4:** Nucleation of local magnetic order on impurity sites in the dressed model. (a) Phase diagram of local magnetic order nucleated on the point-like impurity when orbital selectivity is added to the model. The bulk magnetism is now  $(\pi, 0)$  [stripe] ordered above the new  $U_c = 560$  meV (red shading). A pocket of local magnetic order (blue shading) is again evident, with the local magnetic order, with parameters indicated by the black  $x$ -marker, inheriting the new bulk  $(\pi, 0)$  ordering as shown in (b). This is more clearly demonstrated in (c), where the Fourier transform of the local magnetic order is shown to display peaks at  $(\pm\pi, 0)$ .

experiments have found evidence of such effects in FeSe [153, 154], and we thus consider also a "dressed" version of our mean field model. The effect of different renormalizations of the quasiparticle weight factors are done within second quantization by including the orbitally selective ansatz

$$c_{i\mu}^\dagger \rightarrow \sqrt{Z_\mu} c_{i\mu}^\dagger. \quad (6.16)$$

This inclusion of nondegenerate quasiparticle weights  $Z_\mu$  for the five  $3d$ -orbitals of iron leads directly to a modified version of the interaction Hamiltonian Eq. (6.4) with all effects of orbital selectivity contained in dressed interaction parameters

$$U_\mu \rightarrow Z_\mu^2 U_\mu, \quad (6.17)$$

$$U'_{\mu\nu} \rightarrow Z_\mu Z_\nu U'_{\mu\nu}, \quad (6.18)$$

with similar expressions to the latter for  $J$  and  $J'$ . Based on previous experimental studies where such parameters have been extracted for FeSe [153], we fix the following values of the quasiparticle weights:  $\{Z_\mu\} = \{0.2715, 0.9717, 0.4048, 0.9236, 0.5916\}$  for the five Fe  $3d$  orbitals  $\{d_{xy}, d_{x^2-y^2}, d_{xz}, d_{yz}, d_{z^2}\}$ . We note that the tight-binding model itself is not modified, since, being fitted directly to experiment, the hopping parameters already contains the effects of these correlations in the multi-orbital system.

The result of recomputing the phase diagram using this dressed version of our earlier model is shown in Fig. 6.4(a), showing again a transition to bulk magnetic order. Calculation of the susceptibility of this dressed model in Kreisel et al. [153] found the dominant splitting of the  $Z_{xz}$  and  $Z_{yz}$  quasiparticle weights to lead to a shift in the leading magnetic transition to  $(\pi, 0)$  [stripe] order, a result we also find in the self-consistent mean field CBdG calculation of the bulk phase above the new critical coupling  $U_c = 560$  meV (red shaded region). Underneath the bulk phase transition, we recover a region of impurity-induced local magnetic order (blue shading). We show in Fig. 6.4(b) the real space structure of the magnetization  $m_z(r)$  for a point deep in this pocket of local ordering ( $\{U = 550$  meV,  $V_0 = 120$  meV}, as indicated by the black  $x$ -marker). Close to the critical coupling  $U_c$ , the local ordering is again found to inherit the structure of the bulk magnetic phase. This reduction

in symmetry from the previous  $(\pi, \pi)$  ordering can be seen in the Fourier transform of Fig. 6.4(c) where a clear reduction to  $C_2$  symmetry is observed in the formation of peaks at  $(\pm\pi, 0)$ . However, in contrast to the bare model where the local order did not vary with the Hubbard  $U$ , we now find the structure of the local order to vary as the Hubbard  $U$  is decreased, starting out strongly  $C_2$  symmetric but then transitioning to a nearly  $C_4$  symmetric  $(\pi, 0) + (0, \pi)$  structure when approaching the phase boundary at the lower end of the pocket. Finally, we note that nucleation of local magnetic order can again be understood as a local Stoner transition (by repetition of the analysis of Fig. 6.3), with resonant states, as can be predicted from T-matrix modeling, crossing the Fermi level for parameters just below the local magnetic transition.

### 6.3.2 Experimental signature of the local magnetic order

We now turn to our prediction of experimental signatures of the local magnetic order. As introduced previously, such local pockets of finite magnetization has been suggested previously using bulk probes of FeSe crystals [134–136]. Here, we are motivated by the high quality of available crystals [133], making imaging of a single isolated impurity possible, to suggest a local signature in STM experiments without adding the complication of spin resolved imaging with a spin polarized tip. We note that our suggestion here is purely based on a general symmetry argument for the measured STM profile, and we leave detailed simulation of topographies and differential conductance maps for further work. In summary, we suggest a simple way of distinguishing between the  $C_2$  and  $C_4$  local orders introduced here for the bare and dressed models, respectively, using only information about the LDOS at the surface of a sample as measured in conventional (non spin polarized) STM experiments.

The STM experiment probes the tunneling current between tip and sample, which is directly proportional to the LDOS at the position of the STM tip fixed at some height above the sample [95, 171]. The model considered here is constructed directly on the lattice, and thus the LDOS above the sample involves a basis transform containing the Wannier functions of the electronic states as matrix elements [172–176]. Fig. 6.5(a) shows the positions of the atoms on a cleaved surface of FeSe, including the Fe atoms (red disks) which define the lattice of our tight-binding model, and the upper Se sublattice observed in STM [137, 154, 155]. A Fe centered impurity is known to lead to a dumbbell like formation of  $C_2$  symmetry in the STM image, resulting from the tails of Wannier functions with weights close to the two nearest (upper) Se atoms [172]. These Wannier functions above the surface of FeSe are shown in Fig. 6.5(f), alongside a mirror plane  $m$ . The lower panels show the symmetry properties of these functions under this operation, demonstrating that the  $d_{xz}$  and  $d_{yz}$  Wannier functions have opposite chiral structures. In the bare model local magnetic  $(\pi, \pi)$  order is of nearly perfect  $C_4$  symmetry, indicating that the convolution of real space ordering and Wannier functions which enters into the LDOS above the surface will simply have the symmetry of the Wannier functions themselves - leading to the aforementioned dumbbell formation shown in Fig. 6.5(c) along the dotted line. Importantly, the aforementioned chiral components will enter with the same weight leading to an absence of chiral character in the predicted STM image. In contrast, the strongly  $C_2$  symmetric  $(\pi, 0)$  magnetic order found for the dressed model is not symmetric under the mirror plane as illustrated in Fig. 6.5(d) (top and bottom panels). The convolution of Wannier functions with the asymmetric lattice LDOS of the magnetic pattern will thus induce a chiral pattern in the predicted STM image, as indicated schematically in Fig. 6.5(e) where the maxima of the above-surface LDOS are shifted away from the dotted symmetry line of the Se lattice. This suggest that the symmetry of the local magnetic order nucleated around an Fe centered impurity can be distinguished by identifying a

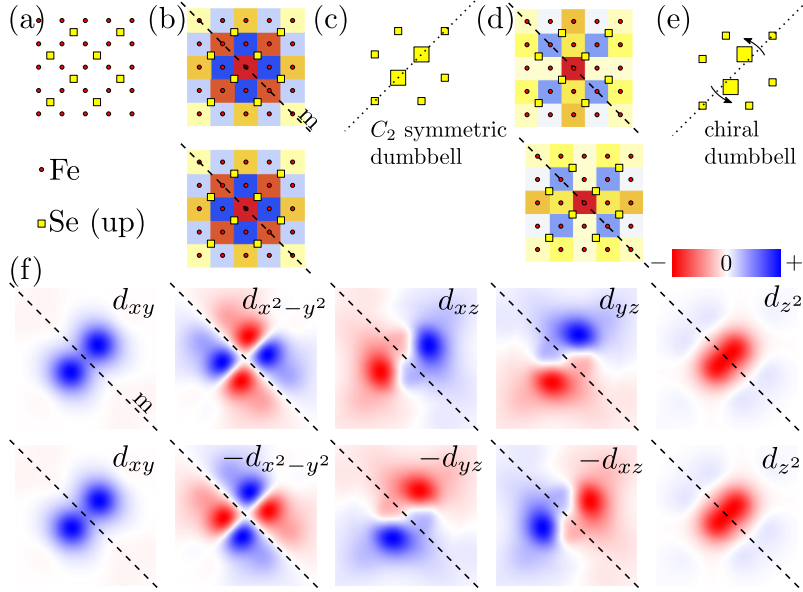


**Figure 6.5:** Distinguishing between symmetries of the local magnetic order on the surface of FeSe. (a) Schematic of the Fe atoms (red circles) and upper sublattice of Se atoms (yellow squares). (b) The magnetic order parameter around a Fe-centered impurity found previously in the non-orbitally-selective case (displayed here in a slightly different colorscale), with the atomic positions superimposed alongside a mirror plane  $m$  (dashed line). The local magnetic order (upper panel) is (approximately) symmetric under reflection in the mirror plane (lower panel). (c) Expected pattern in the LDOS as measured by STM for this case, showing a  $C_2$  symmetric dumbbell formation along the symmetry axis connecting the neighboring (upper) Se sites (dotted line). (d) Magnetic order parameter in the orbitally-selective case which is now asymmetric under reflection in the mirror plane, which is expected to shift the maxima of the LDOS away from the symmetry axis forming a chiral dumbbell formation (e). (f) Symmetry of the five Wannier functions for FeSe at the Fe site and their mirror image with respect to the mirror plane  $m$ . The  $d_{xz}$  and  $d_{yz}$  Wannier functions exhibit a chiral structure of opposite direction.

deviation of the dumbbell maxima from the symmetry (dotted) line indicating the upper Se sublattice. We note that similar features have been suggested in both bulk [155] and thin films of FeSe [137].

## 6.4 Recent evidence for impurity-nucleated local magnetic order in FeSe

The experimental evidence presented previously was based on bulk probes where the formation of local magnetic order has been suggested as a possible interpretation. In this section we introduce a recent STM study where the system is instead probed locally, providing evidence for the strongly localized magnetic order suggested in our theoretical modeling. Probing magnetic order locally without the inclusion of a spin polarized STM tip is accomplished using a novel method based on bound states within a proximity induced superconducting gap of known symmetry. Our contributions to this work were on the theoretical modeling side, and we provide here only a brief introduction to the experimental details (for further information see Song et al. [114]).

### 6.4.1 Using in-gap states in superconductors as signatures of local magnetic order

The T-matrix formalism presented in Eqs. (6.12) to (6.15) provided a method for predicting the formation of impurity induced states within fully gapped or quasi-gapped regions in the non-superconducting (normal) state, yielding true bound states and resonant states, respectively. The inclusion of conventional s-wave superconductivity in the model modifies this result, however, predicting that no such states can be induced within the superconducting gap by non-magnetic disorder [177–180]. Instead, in-gap states appear only in the presence of magnetic impurities. Extending the above T-matrix formalism to include also anomalous components of the Greens function, i.e., the considering the Gorkov Green's function, yields a similar result for the energy of the bound state as found previously, but now with the bound state energy determined by size of the local magnetic moment [180, 181]. Such selective formation of in-gap states makes the appearance of a tunneling current within the STM experiment serve as a signature of magnetic ordering at the local point of the STM tip.

We note that this result applies only for specific symmetries of the superconducting gap structure, the simplest case being conventional s-wave symmetry investigated here. The gap symmetry of FeSe itself is still in dispute [182, 183], with the complicated structure of the Fermi surface in this compound opening several possibilities of the gap structure. As such, an analysis in the superconducting state of FeSe itself would be inconclusive as to the formation of local magnetic moments. In Song et al. [114] this issue is circumvented by growing a FeSe island on top of Pb, itself a well-known s-wave superconductor with a critical temperature of  $T_c = 7.2$  K. A topography image of the system is displayed in Fig. 6.6(a), showing the FeSe island surrounded by regions of both (single-layer) PbSe and bare regions of the underlying Pb. Fourier transform analysis of the image reveals that the image captures the upper Se sublattice of a thin film of FeSe of estimated thickness corresponding to a trilayer. Comparing differential conductance spectra, probing the system LDOS, on and off the FeSe island at a temperature of  $T = 4.3$  K establishes that superconductivity is proximity induced from the Pb with an induced gap of  $2\Delta_{pb} = 2.3$  meV. Due to the inclusion of a superconducting Pb tip in the experiment, used here to enhance the resolution at the finite temperature, the gaps measured are twice this value ( $2\Delta_{meas} = 4.6$  meV) [184].

Before we move on to compare our theoretical modeling and the experimental STM results, some important limitations of this comparison are worth noting: (i) The FeSe is in the thin film limit and (ii) due to this thin film formation a Moire pattern is formed at the Pb substrate/FeSe island interface, as evident by the stripes seen in on the FeSe island in Fig. 6.6(a). However, the effects of the Moire pattern (ii) can be investigated by

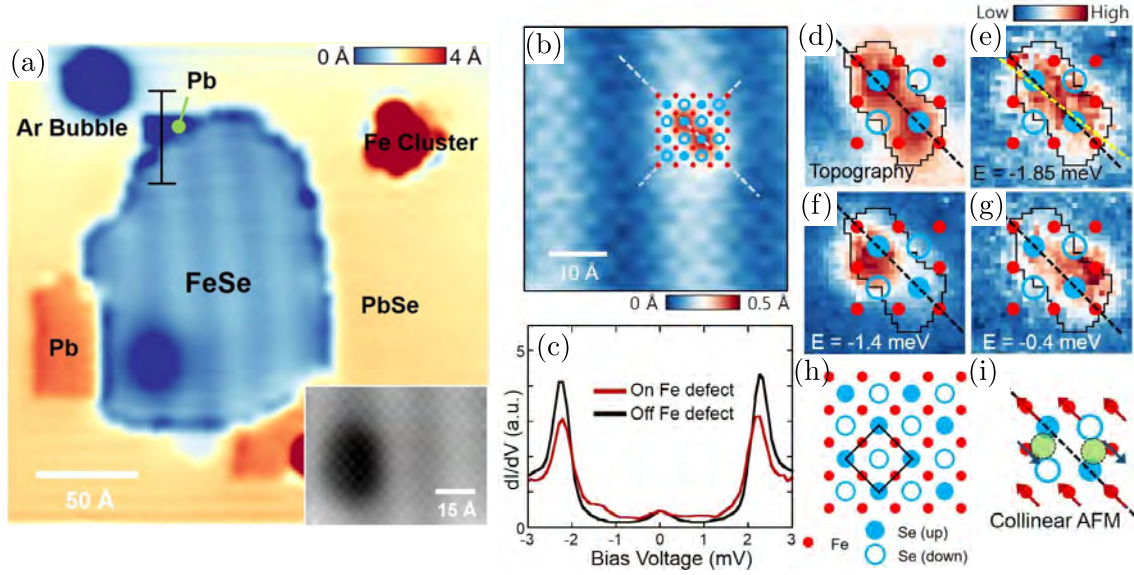


**Figure 6.6:** STM measurements of FeSe on a superconducting substrate. (a) Topography of a FeSe island grown on Pb, with an inset showing the atomically resolved (zoomed) image. (b) Topography around a single isolated defect. (c)  $dI/dV$  spectra on (red curve) and off (black curve) a Fe-centered impurity site, showing the emergence of in-gap (YSR) states on the defect. (d) Topography around the defect (and zoom thereof) showing the aforementioned mirror symmetry plane of the topography oriented along the dumbbell formation (black dashed line in zoom). The FeSe surface schematic is shown on top (legend in (h)). (e-g)  $dI/dV$  spectra at the energies of in-gap states. The yellow dot-dashed line in (e) indicates the axis of the magnetic pattern, which is rotated with respect to the mirror plane (black dashed line). The measured gap (distance between the coherence peaks) is twice that of Pb due to the use of a superconducting Pb tip. (i) The predicted symmetry breaking induced by a local  $(\pi, 0)$  magnetic order and the resulting chiral pattern in the maxima of the STM image. Adapted from Song et al. [114] (paper V).

considering samples or regions with different alignments of the Moire pattern with respect to the FeSe island (see the supplement of Song et al. [114]), and the results discussed here, i.e., the alignment of the symmetry axis of various impurity induced features, turn out to be independent of this effect, showing instead universal alignment of measured features directly to the FeSe lattice.

#### 6.4.2 Fe-centered impurities

The first feature we investigate is the Fe-centered impurity which was the subject of our previous theoretical study in Section 6.3. The high-quality sample of FeSe grown has a low density of Fe-centered impurities, which are most commonly identified as Fe vacancies [185]. As discussed previously in Section 6.3.2, these Fe-centered impurities are distinguished by their signature in STM topography: a dumbbell formation with maxima along the line connecting the nearest two upper Se atoms, as illustrated schematically in Fig. 6.5(c). Such a defect is imaged in the topography of Fig. 6.6(b), showing the characteristic dumbbell formation which appears to be centered on the crossing of the two orthogonal Se-Se directions (dashed white lines) as fitting for an Fe-centered impurity. A schematic of the FeSe surface is shown superimposed, including the the upper Se and the Fe lattice [see Fig. 6.6(h)]. The differential conductance on and off the defect site is shown in Fig. 6.6(c), showing the emergence of states inside the proximity induced superconducting gap, indicating the presence of local magnetic moments strongly localized around the

defect site. Zoomed real space maps of the topography and differential conductance at the in-gap state energies, as provided in Fig. 6.6(d-g), allows us to investigate the symmetry of the induced dumbbell formation in more detail. In the topography the dumbbell formation is seen to have a clear mirror symmetry plane along the Se-Se direction (dashed line). In the differential conductance maps, however, the mirror symmetry is broken at all in-gap energies and the maxima of the dumbbell formation are rotated off the mirror symmetry line of the topography. This is exactly the chiral scenario outlined above for the orbitally selective model in Fig. 6.5(e), indicating that the locally nucleated magnetization is of  $(\pi, 0)$  ordering. This interpretation is reiterated schematically in Fig. 6.6(i) in terms of the experimental notation, with green circles indicating the rotated pattern of the dI/dV maps at the in-gap state energies.

### 6.4.3 Se-centered "plaquette" impurities

To widen the scope of their study of local magnetic order in FeSe beyond the rare and isolated Fe-centered impurities studied above, Song et al. [114] induce further defect formation by depositing Ag atoms onto the sample. A topography of a FeSe island after deposition is shown in Fig. 6.7(a), and in Fig. 6.7(b) we include the height profile of the Ag atom (through the dashed line in Fig. 6.7(a)). Fourier transform analysis demonstrates that the Ag atoms are centered on top of the upper Se sublattice as indicated schematically in Fig. 6.7(c). Differential conductance spectra on these new impurity sites, as shown in Fig. 6.7(d), demonstrate that in-gap states are induced selectively on the FeSe island, being absent in the neighboring Pb region. In Fig. 6.7(e) we show a real-space zoom of both the topography and the dI/dV spectra at energies corresponding to in-gap states. The real-space region where in-gap states appear is again confined to the immediate surroundings of the impurity, indicating that the local magnetic order is strongly localized around the defect site. Being centered on the Se site and thus surrounded by a symmetrical pattern of four Fe atoms, we would naively expect the signature in STS spectra to be of almost perfect  $C_4$  symmetry. However, this is only true for the topography, and the all in-gap dI/dV spectra obtained show a lowering of the local symmetry. In Fig. 6.7(f) a simple interpretation of this fact is found by comparing local collinear  $(\pi, 0)$  magnetic order [shown in the the transposed coordinate system compared to our earlier definitions], with Neel  $(\pi, \pi)$  local magnetic order. Only the  $(\pi, 0)$  order fits the local symmetry of the differential conductance maps around the impurity, and the  $(\pi, \pi)$  order possesses a mirror symmetry plane (dashed line) which is in contradiction with the obtained patterns. We note that, as mentioned earlier, the asymmetry of Ag centered impurity in-gap STS maps is aligned with Fe lattice independently of the direction of the Moire pattern, ruling factor out as an alternative explanation.

In order to study this new type of impurity in more detail, we expand our previous theoretical modeling to include also Se-centered impurities. Based on the previous evidence for chiral patterns around Fe-centered impurities, we use the dressed version of our model which includes the effects of orbital selectivity. We again fix  $U = 550$  meV just below the bulk magnetic transition, but stress that our result apply for an interval of interactions strengths the extent of which depends on the type of impurity or disorder potential. A Se-centered impurity, such as Ag, is included in the 10-band model as an onsite potential on the four nearest Fe sites

$$H_{Se-imp} = V_{Se} \sum_{j,\mu,\sigma} c_{j\mu\sigma}^\dagger c_{j\mu\sigma}, \quad (6.19)$$

where the set of indices  $j, \mu$  label the corresponding unit cell and associated orbitals on the surrounding sites as shown in the plaquette formation of Fig. 6.7(c). The result of

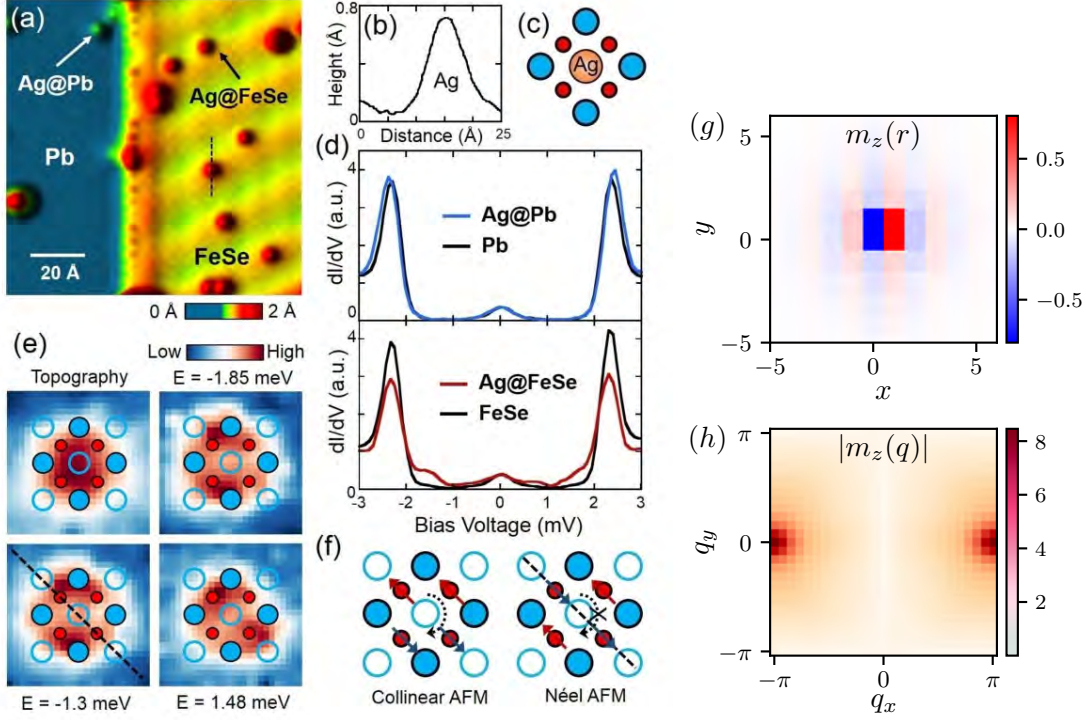


**Figure 6.7:** Investigations of Ag (nonmagnetic, Se-centered) impurities on the FeSe island. (a) Topography of Ag atoms on the FeSe island and the surrounding Pb surface. (b) Height profile of a single Ag impurity of FeSe along the dashed line in (a). (c) Schematic of the Ag position above a site of the upper Se sublattice. In the theoretical model an equal potential is included on the four nearest Fe sites (red disks), forming a "plaquette" impurity. (d)  $dI/dV$  comparison spectra of Ag on Pb and FeSe, respectively. In-gap states are found only on the FeSe island. (e) Local topography and  $dI/dV$  real-space maps around a single Ag impurity (zoomed to  $9.5 \text{ \AA} \times 9.5 \text{ \AA}$ ). The  $dI/dV$  spectra lower the local symmetry from  $C_4$  to  $C_2$  at the energies of the bound states. (f) Comparison of collinear  $(\pi, 0)$  (rotated) and Neel  $(\pi, \pi)$  magnetic orders. Only the  $(\pi, 0)$  magnetic order is expected to lower the symmetry as observed. (g) Local magnetic order nucleated on a plaquette (Se-centered) impurity in the orbitally-selective version of the theoretical model. (h) Fourier transform of the local magnetic order parameter displaying peaks at  $(\pm\pi, 0)$ . Panels (a-f) adapted from Song et al. [114] (paper V).

including such a plaquette impurity ( $V_{Se} = 50 \text{ meV}$ ) in the previous supercell is shown in Fig. 6.7(g) as a zoom of the real space magnetization. In agreement with the measurement of Fig. 6.7(e), a local magnetic order is present and is found to be strongly localized around the impurity site. The structure of the order is again inherited from the bulk phase as seen in the Fourier transform Fig. 6.7(h). The  $(\pi, 0)$  local magnetic order, in contrast to the  $C_4$   $(\pi, \pi)$  order, reduces the symmetry of the induced magnetization and thus serves as a possible explanation for the symmetry breaking in the  $dI/dV$  spectra of the in-gap states as shown in Fig. 6.7(e-g). We reiterate that while the result is shown here for a single impurity potential, we find similar results for a range of impurity strengths down to at least  $V_{Se} \approx 25 \text{ meV}$  (although with corresponding reduced magnitude of the induced magnetic order).

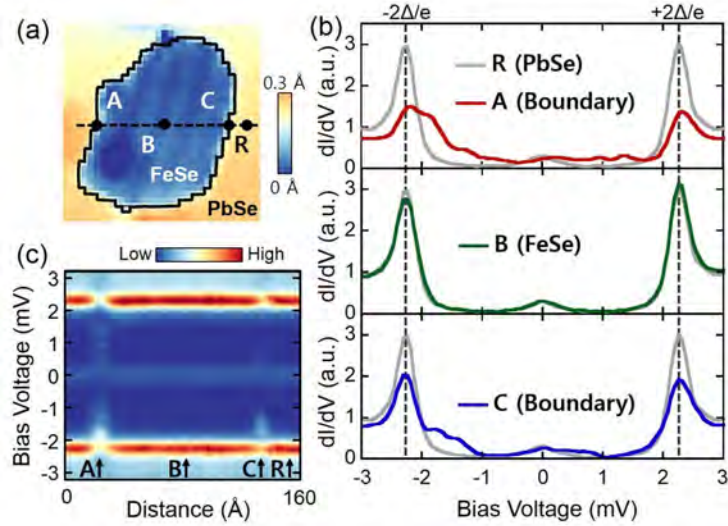


**Figure 6.8:** Indication of edge magnetism on a FeSe island (before Ag deposition). (a) Topography of the FeSe island. (b)  $dI/dV$  spectra at the different tip locations marked in (a). In-gap states are present at the edges (points A, C) when compared with the reference point (R), and no such states are observed deep in the clean sample (point B). (c) Linecut of the differential conductance  $dI/dV$  along the dashed line in (a) further demonstrating that in-gap states only develop at the sample edges (unless impurities are included in the bulk). Adapted from Song et al. [114] (paper V).

#### 6.4.4 Edge magnetism

In addition to the the previous evidence for impurity-nucleated local magnetic order found in the STM experiment, in-gap states are also observed on the edges of the sample prior to the inclusion of Ag impurities. In Fig. 6.8(a) we show a zoomed version of the STM topography of the FeSe island with indication of two points on different boundaries (A, C), a point deep in the sample (B), and a reference point (R) in the surrounding PbSe. The  $dI/dV$  spectra taken with the STM tip at these locations are shown in Fig. 6.8(b), demonstrating that in-gap states indicating the formation of local magnetic order occur at both boundary points, while the spectra taken at the point deep in the bulk resembles the reference, indicating the absence of bulk magnetic ordering. The point in the PbSe is chosen as the reference since, PbSe not being an intrinsic superconductor, there can be no doubt about the proximity-induced nature of the observed band gap in the spectrum. A linecut of the differential conductance as shown in Fig. 6.8(c), measured along the path of the dashed line in Fig. 6.8(a), further demonstrates that in-gap are absent in the bulk of the clean sample and only form at the boundary.

We study the appearance of edge magnetism within our theoretical model by substituting the periodic boundary conditions to open (hard) boundaries at the edges of the supercell. A suitable choice of supercell dimensions then creates FeSe islands with a given dominant edge type, of which we study both (110), as well as (010) and (100) types. In Fig. 6.9 we show the results of the self-consistent calculation for such a FeSe island. Our general finding is that, as the Hubbard  $U$  is increased from below, local magnetic order forms first on the corners of the island but extend to fully cover the edges of the sample as the bulk phase boundary is approached. We demonstrate this phenomenon in Fig. 6.9(a-b) for geometries with dominant (100)-type edges ( $U = 550$  meV) and (110)-type edges, respectively. Fig. 6.9(c) shows a linecut of the magnetization in Fig. 6.9(a) as indicated

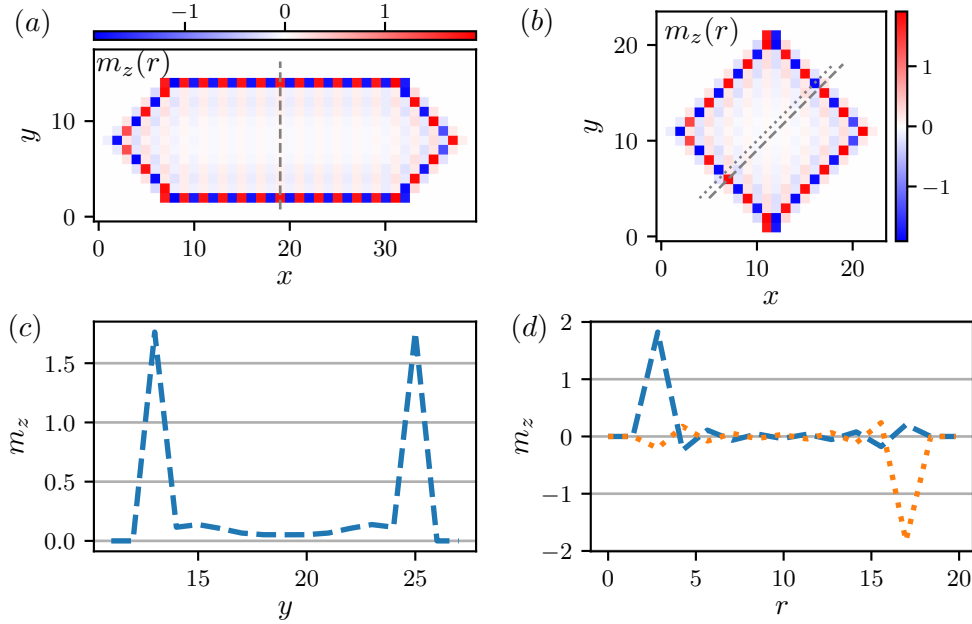


**Figure 6.9:** Theoretical modeling of edge magnetism. (a) Edge-nucleated magnetism on a FeSe island with long (100)-type edges with the Hubbard  $U$  fixed just beneath the bulk transition ( $U = 550 \text{ meV} \lesssim U_c$ ). (b) Edge magnetism on a FeSe island consisting of (110)-type edges. The magnetic order parameter peaks at every other site along the staggered edge, with the ordering still being inherited from the bulk magnetic phase. (c) Line-cut through the magnetic order parameter in (c) as indicated by the dashed line. The magnetization peaks close to the edge and decays into the bulk. (d) Line-cuts through the magnetic order parameter in (d) as indicated by the dashed and dotted lines, showing the sign change in the magnetization along the edge as well as the decay of the edge-magnetization into the bulk.

by the dashed line transverse to the (100) edge. The magnetization peaks directly on the edge site, with a tail decaying into the bulk of the island. In Fig. 6.9(d) we repeat this analysis for the island with (110)-type edges of Fig. 6.9(c), now including the two different linecuts indicating by the dashed and dotted lines, respectively. Both linecuts are thus taken transverse to the edge. For this type of staggered "staircase" edge the magnetization peaks at every other site with an oscillating tail extending into the bulk, causing the two linecuts to become mirror images of each other when reflected in the center of the island.

## 6.5 Summary

We have in this chapter explored the formation of local magnetic order on nonmagnetic impurities in a model of the iron-based superconductor FeSe. Varying the impurity potential and the strength of electron-electron interactions by tuning the Hubbard  $U$ , we found regions in the resulting phase diagram where such local order manifests. We found the appearance of such local magnetic order to be preceded by impurity resonant states forming close to the Fermi level, indicating a mechanism of formation similar to a local Stoner transition. We considered the effects of orbital selectivity and found that the inclusion of these effects dramatically shifts the structure of both the bulk and local magnetic ordering. Furthermore, we predicted the signature of such local magnetic order in STM experiments using robust symmetry arguments to differentiate between distinct structures of the impurity-nucleated local magnetic order.

In addition, we have discussed the results of a recent STM measurement in FeSe where indications of these predicted effects have been observed. We have expanded our theoretical model to also capture other effects investigated in this experiment and found the formation of locally nucleated magnetism on both Se-centered impurities and the edges of FeSe islands.

The arguments for the predicted signatures of local magnetic order presented here have entirely based on the different symmetries of predicted STS spectra arising selectively from either local  $(\pi, \pi)$  or  $(\pi, 0)$  magnetic order. More detailed modeling could be performed within a natural extension of the theoretical framework. In particular, the mean field analysis could be extended to include the proximity induced s-wave order parameter directly in the calculation, and the LDOS at the tip position could be calculated in full detail in order to enable direct comparison with the experimental  $dI/dV$  spectra [173].



# Chapter 7

## Summary and outlook

The unique properties of graphene have motivated research into a multitude of applications. The various nanostructuring techniques possible in the world of 2D materials expands the domain of such research, providing possibilities for combining the intrinsic properties of graphene with controllable features induced by the nanostructuring. In the first part of this thesis we have investigated such a phenomenon by suggesting a method of indirectly engineering graphene for application in valleytronics. Inspired by recent demonstrations of indirect band structure engineering, we defined a superlattice by a regular external potential with broken inversion symmetry - a prerequisite for realizing a valley Hall effect in the time-reversal invariant system.

For the study of this phenomenon we introduced in Chapter 3 two different techniques for the calculation of the valley Hall conductivity in the graphene superlattice system, the semiclassical approach based on integration of the electronic Berry curvature to capture the anomalous velocity of wavepackets, and the direct expansion of the linear response Kubo-Bastin formula. Chapter 4 detailed our investigations of the superlattice system using the first of these techniques. We demonstrated a tunable band structure engineering and explored the variation of the induced band gap with both the geometry of the superlattice and the local structure of the external potential. Turning to the study of the valley Hall effect in these systems, we calculated the electronic Berry curvature and projected this quantity to the graphene Brillouin zone, thereby demonstrating the emergence of valley-selective anomalous velocities in the superlattice. The distribution of the Berry curvature was found to be tunable by the magnitude of the superlattice potential, and we found characteristic plateaus of the valley Hall conductivity centered on the band gap with tails of the peaks extending into the band edges. Providing a simple prediction for the associated signature in nonlocal transport measurements, we found that the indirect engineering of the superlattice potential provides an external degree of control over the valley Hall effect in these systems. Finally, we provided initial evidence that these effects remain robust when the effects of irregularities and realistic shapes of the potentials expected from dielectric nanostructuring are included.

The inclusion of disorder in the study of the valley Hall effect necessitated that a large-scale method be employed. In Chapter 5 we used an expansion procedure for the Kubo-Bastin formula to study large-scale superlattices with random shifts and rotations in the superlattice potential. Using this method removes the intuitive understanding of the result in terms of the electronic Berry curvature and the associated anomalous velocity but makes efficient calculation of the conductivity possible. In addition, the large-scale procedure enables us to study the DOS in detail in the disordered system, where we

found the potential-induced band gap to be stable up a large degree of disorder in the nanostructuring of the system. In our study of the valley Hall conductivity, we reproduced our earlier result in the pristine superlattice, and were able to differentiate the different contributions stemming from, respectively, the Fermi sea and the Fermi surface. In the disordered system we found that the valley Hall effect could survive even when the band gap fully closes, with a wide region of finite valley Hall conductivity arising from Fermi surface contributions. This Fermi surface driven regime of the valley Hall effect makes a simple interpretation of nonlocal resistance measurements possible, where valley currents are induced in the bulk of the sample and do not rely on the details of the edge geometry.

The study of disorder contributions to the valley Hall effect, and to the anomalous Hall effect in general, is a topic of much research interest. Nanostructured systems provide a degree of control over such disorder, which could be used to perform detailed investigations of both side-jump and skew-scattering contributions by tuning the profile of the induced disorder. In addition, the indirectly induced nature of the valley Hall effect in the superlattice makes it a promising platform for studying also the protection of interface states between different domains constructed using, e.g., a split-gate setup.

In the final part of the thesis (Chapter 6) we moved beyond the field of 2D materials, and explored the formation of impurity-induced local magnetic order on the surface of the bulk high-temperature superconductor FeSe. Using a multi-orbital tight-binding model fitted to experiments, and adding interactions through the Hubbard-Hund model, we mapped out pockets of the phase diagram where a Fe-centered impurity locally induced the formation of magnetic order centered on the defect site. We found the local magnetic order to be preceded in the phase diagram by the formation of impurity resonant states at the Fermi level, indicating that the local magnetism could be understood as a local form of the conventional Stoner transition into the bulk magnetic phase. We also considered the inclusion of so-called orbitally selective effects, which were found to change the ordering of the local magnetism. Furthermore, we provided predictions of the signature of the symmetry of the induced local magnetic order in STM experiments. We were able to compare these predictions with a recent STM experiment where a novel approach enabled a local probe of magnetic order. For this comparison we extended our theoretical study to include also the prediction of local magnetic order on Se-centered impurities and on the edges of finite FeSe islands.

Our enclosed predictions of the signature of local magnetic order in the local spectra of STM measurements have been made purely from general symmetry arguments. For a true quantitative comparison with experiment the LDOS at the tip locations should be calculated in full detail, and the effects of the experimental substrate included directly in the theoretical model. For our studies we considered only isolated impurities, the selective addition of multiple Ag impurities in the sample would also allow for studies of multi-impurity effects, such as the possible impurity-induced transition to a bulk magnetic phase.

# Bibliography

- [1] R. P. Feynman, “There’s Plenty of Room at the Bottom”, *Engineering and Science*, **22** (1960).
- [2] R. Jones, “Feynman’s unfinished business”, *Nature Nanotechnology* **4**, 785 (2009).
- [3] A. K. Geim and I. V. Grigorieva, “Van der Waals heterostructures”, *Nature* **499**, 419 (2013).
- [4] P. Ajayan, P. Kim, and K. Banerjee, “Two-dimensional van der Waals materials”, *Physics Today* **69**, 38 (2016).
- [5] K. S. Novoselov, A. K. Geim, S. V. Morozov, D. Jiang, Y. Zhang, S. V. Dubonos, I. V. Grigorieva, and A. A. Firsov, “Electric field in atomically thin carbon films”, *Science* **306**, 666 (2004).
- [6] S. Z. Butler, S. M. Hollen, L. Cao, Y. Cui, J. A. Gupta, H. R. Gutiérrez, T. F. Heinz, S. S. Hong, J. Huang, A. F. Ismach, E. Johnston-Halperin, M. Kuno, V. V. Plashnitsa, R. D. Robinson, R. S. Ruoff, S. Salahuddin, J. Shan, L. Shi, M. G. Spencer, M. Terrones, W. Windl, and J. E. Goldberger, “Progress, challenges, and opportunities in two-dimensional materials beyond graphene”, *ACS Nano* **7**, 2898 (2013).
- [7] M. Xu, T. Liang, M. Shi, and H. Chen, “Graphene-like two-dimensional materials”, *Chemical Reviews* **113**, 3766 (2013).
- [8] F. Schwierz, “Graphene transistors”, *Nature Nanotechnology* **5**, 487 (2010).
- [9] Y. Wu, D. B. Farmer, F. Xia, and P. Avouris, “Graphene electronics: Materials, devices, and circuits”, *Proceedings of the IEEE* **101**, 1620 (2013).
- [10] S. Kabiri Ameri, R. Ho, H. Jang, L. Tao, Y. Wang, L. Wang, D. M. Schnyer, D. Akinwande, and N. Lu, “Graphene Electronic Tattoo Sensors”, *ACS Nano* **11**, 7634 (2017).
- [11] Z. Huang, Y. Hao, Y. Li, H. Hu, C. Wang, A. Nomoto, T. Pan, Y. Gu, Y. Chen, T. Zhang, W. Li, Y. Lei, N. H. Kim, C. Wang, L. Zhang, J. W. Ward, A. Maralani, X. Li, M. F. Durstock, A. Pisano, Y. Lin, and S. Xu, “Three-dimensional integrated stretchable electronics”, *Nature Electronics* **1**, 473 (2018).
- [12] D. Akinwande and D. Kireev, “Wearable graphene sensors use ambient light to monitor health”, *Nature* **576**, 220 (2019).
- [13] H. Park, J. A. Rowehl, K. K. Kim, V. Bulovic, and J. Kong, “Doped graphene electrodes for organic solar cells”, *Nanotechnology* **21**, 505204 (2010).
- [14] Y. Song, S. Chang, S. Gradecak, and J. Kong, “Visibly-Transparent Organic Solar Cells on Flexible Substrates with All-Graphene Electrodes”, *Advanced Energy Materials* **6**, 1600847 (2016).
- [15] S. Jung, J. Lee, Y. Choi, S. M. Lee, C. Yang, and H. Park, “Improved interface control for high-performance graphene-based organic solar cells”, *2D Materials* **4**, 045004 (2017).

- [16] A. C. Neto, F. Guinea, and N. M. Peres, “Drawing conclusions from graphene”, *Physics World* **19**, 33 (2006).
- [17] C. R. Dean, A. F. Young, I. Meric, C. Lee, L. Wang, S. Sorgenfrei, K. Watanabe, T. Taniguchi, P. Kim, K. L. Shepard, and J. Hone, “Boron nitride substrates for high-quality graphene electronics”, *Nature Nanotechnology* **5**, 722 (2010).
- [18] F. Forster, A. Molina-Sanchez, S. Engels, A. Epping, K. Watanabe, T. Taniguchi, L. Wirtz, and C. Stampfer, “Dielectric screening of the Kohn anomaly of graphene on hexagonal boron nitride”, *Physical Review B* **88**, 085419 (2013).
- [19] N. J. Couto, D. Costanzo, S. Engels, D. K. Ki, K. Watanabe, T. Taniguchi, C. Stampfer, F. Guinea, and A. F. Morpurgo, “Random strain fluctuations as dominant disorder source for high-quality on-substrate graphene devices”, *Physical Review X* **4**, 041019 (2014).
- [20] C. Berger, Z. Song, T. Li, X. Li, A. Y. Ogbazghi, R. Feng, Z. Dai, N. Alexei, M. E. H. Conrad, P. N. First, and W. A. De Heer, “Ultrathin epitaxial graphite: 2D electron gas properties and a route toward graphene-based nanoelectronics”, *Journal of Physical Chemistry B* **108**, 19912 (2004).
- [21] L. Banszerus, M. Schmitz, S. Engels, J. Dauber, M. Oellers, F. Haupt, K. Watanabe, T. Taniguchi, B. Beschoten, and C. Stampfer, “Ultrahigh-mobility graphene devices from chemical vapor deposition on reusable copper”, *Science Advances* **1**, 1500222 (2015).
- [22] P. R. Kidambi, D. D. Mariappan, N. T. Dee, A. Vyatskikh, S. Zhang, R. Karnik, and A. J. Hart, “A Scalable Route to Nanoporous Large-Area Atomically Thin Graphene Membranes by Roll-to-Roll Chemical Vapor Deposition and Polymer Support Casting”, *ACS Applied Materials and Interfaces* **10**, 10369 (2018).
- [23] A. S. Mayorov, R. V. Gorbachev, S. V. Morozov, L. Britnell, R. Jalil, L. A. Ponomarenko, P. Blake, K. S. Novoselov, K. Watanabe, T. Taniguchi, and A. K. Geim, “Micrometer-scale ballistic transport in encapsulated graphene at room temperature”, *Nano Letters* **11**, 2396 (2011).
- [24] I. Meric, N. Baklitskaya, P. Kim, and K. L. Shepard, “RF performance of top-gated, zero-bandgap graphene field-effect transistors”, in *Technical Digest - International Electron Devices Meeting, IEDM* (2008).
- [25] Y. Q. Wu, D. B. Farmer, A. Valdes-Garcia, W. J. Zhu, K. A. Jenkins, C. Dimitrakopoulos, P. Avouris, and Y. M. Lin, “Record high RF performance for epitaxial graphene transistors”, in *Technical Digest - International Electron Devices Meeting, IEDM* (2011).
- [26] Y. M. Lin, C. Dimitrakopoulos, K. A. Jenkins, D. B. Farmer, H. Y. Chiu, A. Grill, and P. Avouris, “100-GHz transistors from wafer-scale epitaxial graphene”, *Science* **327**, 662 (2010).
- [27] L. Huang, H. Xu, Z. Zhang, C. Chen, J. Jiang, X. Ma, B. Chen, Z. Li, H. Zhong, and L. M. Peng, “Graphene/Si CMOS Hybrid hall integrated circuits”, *Scientific Reports* **4**, 5548 (2014).
- [28] B. S. Jessen, L. Gammelgaard, M. R. Thomsen, D. M. Mackenzie, J. D. Thomsen, J. M. Caridad, E. Duegaard, K. Watanabe, T. Taniguchi, T. J. Booth, T. G. Pedersen, A.-P. Jauho, and P. Bøggild, “Lithographic band structure engineering of graphene”, *Nature Nanotechnology* **14**, 340 (2019).
- [29] M. Yamamoto, Y. Shimazaki, I. V. Borzenets, and S. Tarucha, “Valley hall effect in two-dimensional hexagonal lattices”, *Journal of the Physical Society of Japan* **84**, 121006 (2015).
- [30] E. Pop, “Energy dissipation and transport in nanoscale devices”, *Nano Research* **3**, 147 (2010).

- [31] F. Pulizzi, “Spintronics”, *Nature Materials* **11**, 367 (2012).
- [32] M. I. D’yakonov and V. I. Perel, “Possibility of orienting electron spins with current”, *Sov. Phys. JETP Lett* **13**, 657660 (1971).
- [33] I. Žutić, J. Fabian, and S. D. Sarma, “Spintronics: Fundamentals and applications”, *Reviews of Modern Physics* **76**, 323 (2004).
- [34] A. Cresti, B. K. Nikolić, J. H. García, and S. Roche, “Charge, spin and valley Hall effects in disordered grapheme”, *Rivista del Nuovo Cimento* **39**, 587 (2016).
- [35] D. Xiao, M. C. Chang, and Q. Niu, “Berry phase effects on electronic properties”, *Reviews of Modern Physics* **82**, 1959 (2010).
- [36] N. Rohling and G. Burkard, “Universal quantum computing with spin and valley states”, *New Journal of Physics* **14**, 083008 (2012).
- [37] D. Culcer, A. L. Saraiva, B. Koiller, X. Hu, and S. Das Sarma, “Valley-based noise-resistant quantum computation using Si quantum dots”, *Physical Review Letters* **108**, 126804 (2012).
- [38] Y. Shimazaki, M. Yamamoto, I. V. Borzenets, K. Watanabe, T. Taniguchi, and S. Tarucha, “Generation and detection of pure valley current by electrically induced Berry curvature in bilayer graphene”, *Nature Physics* **11**, 1032 (2015).
- [39] R. V. Gorbachev, J. C. Song, G. L. Yu, A. V. Kretinin, F. Withers, Y. Cao, A. Mishchenko, I. V. Grigorieva, K. S. Novoselov, L. S. Levitov, and A. K. Geim, “Detecting topological currents in graphene superlattices”, *Science* **346**, 448 (2014).
- [40] K. Komatsu, Y. Morita, E. Watanabe, D. Tsuya, K. Watanabe, T. Taniguchi, and S. Moriyama, “Observation of the quantum valley Hall state in ballistic graphene superlattices”, *Science Advances* **4**, eaaq0194 (2018).
- [41] C. Forsythe, X. Zhou, K. Watanabe, T. Taniguchi, A. Pasupathy, P. Moon, M. Koshino, P. Kim, and C. R. Dean, “Band structure engineering of 2D materials using patterned dielectric superlattices”, *Nature Nanotechnology* **13**, 566 (2018).
- [42] C. Si, Z. Sun, and F. Liu, “Strain engineering of graphene: A review”, *Nanoscale* **8**, 3207 (2016).
- [43] X. P. Zhang, C. Huang, and M. A. Cazalilla, “Valley Hall effect and nonlocal transport in strained graphene”, *2D Materials* **4**, 024007 (2017).
- [44] M. Settnes, S. R. Power, M. Brandbyge, and A. P. Jauho, “Graphene Nanobubbles as Valley Filters and Beam Splitters”, *Physical Review Letters* **117**, 276801 (2016).
- [45] J. C. Song, P. Samutpraphoot, and L. S. Levitov, “Topological Bloch bands in graphene superlattices”, *Proceedings of the National Academy of Sciences of the United States of America* **112**, 10879 (2015).
- [46] T. M. Wolf, O. Zilberberg, I. Levkivskiy, and G. Blatter, “Substrate-induced topological minibands in graphene”, *Physical Review B* **98**, 125408 (2018).
- [47] C. Hu, V. Michaud-Rioux, W. Yao, and H. Guo, “Moiré Valleytronics: Realizing Dense Arrays of Topological Helical Channels”, *Physical Review Letters* **121**, 186403 (2018).
- [48] T. G. Pedersen, C. Flindt, J. Pedersen, N. A. Mortensen, A. P. Jauho, and K. Pedersen, “Graphene antidot lattices: Designed defects and spin qubits”, *Physical Review Letters* **100**, 136804 (2008).
- [49] A. Sandner, T. Preis, C. Schell, P. Giudici, K. Watanabe, T. Taniguchi, D. Weiss, and J. Eroms, “Ballistic Transport in Graphene Antidot Lattices”, *Nano Letters* **15**, 8402 (2015).
- [50] J. G. Pedersen and T. G. Pedersen, “Band gaps in graphene via periodic electrostatic gating”, *Physical Review B* **85**, 235432 (2012).
- [51] J. M. Caridad, S. Connaughton, C. Ott, H. B. Weber, and V. Krstić, “An electrical analogy to Mie scattering”, *Nature Communications* **7**, 12894 (2016).

- [52] R. Petersen and T. G. Pedersen, “Quasiparticle properties of graphene antidot lattices”, *Physical Review B - Condensed Matter and Materials Physics* **80**, 14 (2009).
- [53] C. L. Kane, “Topological band theory and the  $Z_2$  invariant”, *Contemporary Concepts of Condensed Matter Science* **6**, 3 (2013).
- [54] K. V. Klitzing, G. Dorda, and M. Pepper, “New method for high-accuracy determination of the fine-structure constant based on quantized hall resistance”, *Physical Review Letters* **45**, 494 (1980).
- [55] A. Altland, D. Bagrets, and A. Kamenev, “Topology versus Anderson localization: Nonperturbative solutions in one dimension”, *Physical Review B - Condensed Matter and Materials Physics* **91**, 85429 (2015).
- [56] D. J. Rizzo, G. Veber, T. Cao, C. Bronner, T. Chen, F. Zhao, H. Rodriguez, S. G. Louie, M. F. Crommie, and F. R. Fischer, “Topological band engineering of graphene nanoribbons”, *Nature* **560**, 204 (2018).
- [57] E. Mania, A. R. Cadore, T. Taniguchi, K. Watanabe, and L. C. Campos, “Topological valley transport at the curved boundary of a folded bilayer graphene”, *Communications Physics* **2**, 6 (2019).
- [58] M. Gradhand, V. Fedorov, F. Pientka, P. Zahn, I. Mertig, L. Györffy, M. Gradhand, D. V. Fedorov, F. Pientka, P. Zahn, I. Mertig, and B. L. Györffy, “First-principle calculations of the Berry curvature of Bloch states for charge and spin transport of electrons”, *Journal of Physics Condensed Matter* **24**, 213202 (2012).
- [59] D. C. Ralph, “Berry Curvature, Semiclassical Electron Dynamics, and Topological Materials: Lecture Notes for Introduction to Solid State Physics”, arXiv:2001.04797 (2020).
- [60] K. S. Novoselov, A. K. Geim, S. V. Morozov, D. Jiang, M. I. Katsnelson, I. V. Grigorieva, S. V. Dubonos, and A. A. Firsov, “Two-dimensional gas of massless Dirac fermions in graphene”, *Nature* **438**, 197 (2005).
- [61] D. Xiao, W. Yao, and Q. Niu, “Valley-contrasting physics in graphene: Magnetic moment and topological transport”, *Physical Review Letters* **99**, 236809 (2007).
- [62] D. Culcer, Y. Yao, and Q. Niu, “Coherent wave-packet evolution in coupled bands”, *Physical Review B - Condensed Matter and Materials Physics* **72**, 085110 (2005).
- [63] C. Z. Chang and M. Li, “Quantum anomalous Hall effect in time-reversal-symmetry breaking topological insulators”, *Journal of Physics Condensed Matter* **28**, 123002 (2016).
- [64] D. J. Thouless, M. Kohmoto, M. P. Nightingale, and M. Den Nijs, “Quantized hall conductance in a two-dimensional periodic potential”, *Physical Review Letters* **49**, 405 (1982).
- [65] F. D. Haldane, “Model for a quantum hall effect without landau levels: Condensed-matter realization of the ”parity anomaly””, *Physical Review Letters* **61**, 2015 (1988).
- [66] N. Nagaosa, J. Sinova, S. Onoda, A. H. MacDonald, and N. P. Ong, “Anomalous Hall effect”, *Reviews of Modern Physics* **82**, 1539 (2010).
- [67] E. McCann, in *Raza h. (eds) graphene nanoelectronics. nanoscience and technology* (Springer, Berlin, Heidelberg, 2011), pp. 237–275.
- [68] F. Guinea and T. Low, “Band structure and gaps of triangular graphene superlattices”, *Philosophical Transactions of the Royal Society A: Mathematical, Physical and Engineering Sciences* **368**, 5391 (2010).
- [69] A. Zabet-Khosousi, L. Zhao, L. Pálová, M. S. Hybertsen, D. R. Reichman, A. N. Pasupathy, and G. W. Flynn, “Segregation of sublattice domains in nitrogen-doped graphene”, *Journal of the American Chemical Society* **136**, 1391 (2014).

- [70] L. Zhao, R. He, K. T. Rim, T. Schiros, K. S. Kim, H. Zhou, C. Gutiérrez, S. P. Chockalingam, C. J. Arguello, L. Pálková, D. Nordlund, M. S. Hybertsen, D. R. Reichman, T. F. Heinz, P. Kim, A. Pinczuk, G. W. Flynn, and A. N. Pasupathy, “Visualizing individual nitrogen dopants in monolayer graphene”, *Science* **333**, 999 (2011).
- [71] D. Xiao, G. B. Liu, W. Feng, X. Xu, and W. Yao, “Coupled spin and valley physics in monolayers of MoS<sub>2</sub> and other group-VI dichalcogenides”, *Physical Review Letters* **108**, 196802 (2012).
- [72] X. Xu, W. Yao, D. Xiao, and T. F. Heinz, “Spin and pseudospins in layered transition metal dichalcogenides”, *Nature Physics* **10**, 343 (2014).
- [73] A. H. Castro Neto, F. Guinea, N. M. Peres, K. S. Novoselov, and A. K. Geim, “The electronic properties of graphene”, *Reviews of Modern Physics* **81**, 109 (2009).
- [74] A. Rycerz, J. Tworzydło, and C. W. Beenakker, “Valley filter and valley valve in graphene”, *Nature Physics* **3**, 172 (2007).
- [75] K. F. Mak, K. L. McGill, J. Park, and P. L. McEuen, “The valley hall effect in MoS<sub>2</sub> transistors”, *Science* **344**, 1489 (2014).
- [76] W. Yao, D. Xiao, and Q. Niu, “Valley-dependent optoelectronics from inversion symmetry breaking”, *Physical Review B* **77**, 235406 (2008).
- [77] M. Jung, Z. Fan, and G. Shvets, “Midinfrared Plasmonic Valleytronics in Metagated Graphene”, *Physical Review Letters* **121**, 086807 (2018).
- [78] M. Sui, G. Chen, L. Ma, W. Y. Shan, D. Tian, K. Watanabe, T. Taniguchi, X. Jin, W. Yao, D. Xiao, and Y. Zhang, “Gate-tunable topological valley transport in bilayer graphene”, *Nature Physics* **11**, 1027 (2015).
- [79] M. Beconcini, F. Taddei, and M. Polini, “Nonlocal topological valley transport at large valley Hall angles”, *Physical Review B* **94**, 121408 (2016).
- [80] Z. Fan, J. H. Garcia, A. W. Cummings, J. E. Barrios-Vargas, M. Panhans, A. Harju, F. Ortmann, and S. Roche, “Linear Scaling Quantum Transport Methodologies”, arXiv:1811.07387 (2018).
- [81] Y. D. Lensky, J. C. Song, P. Samutpraphoot, and L. S. Levitov, “Topological Valley Currents in Gapped Dirac Materials”, *Physical Review Letters* **114**, 256601 (2015).
- [82] G. Kirczenow, “Valley currents and nonlocal resistances of graphene nanostructures with broken inversion symmetry from the perspective of scattering theory”, *Physical Review B - Condensed Matter and Materials Physics* **92**, 125425 (2015).
- [83] J. M. Marmolejo-Tejada, J. H. García, M. D. Petrović, P.-H. Chang, X.-L. Sheng, A. Cresti, P. Plecháč, S. Roche, and B. K. Nikolić, “Deciphering the origin of nonlocal resistance in multiterminal graphene on hexagonal-boron-nitride with ab initio quantum transport: Fermi surface edge currents rather than Fermi sea topological valley currents”, *Journal of Physics: Materials* **1**, 015006 (2018).
- [84] W. Y. Shan and D. Xiao, “Strain-fluctuation-induced near quantization of valley Hall conductivity in graphene systems”, *Physical Review B* **99**, 205416 (2019).
- [85] F. D. Haldane, “Berry curvature on the fermi surface: Anomalous hall effect as a topological fermi-liquid property”, *Physical Review Letters* **93**, 206602 (2004).
- [86] T. Olsen and I. Souza, “Valley Hall effect in disordered monolayer MoS<sub>2</sub> from first principles”, *Physical Review B* **92**, 125146 (2015).
- [87] F. Pientka, *Geometrical Concepts in the Band Theory of Solids*, Diploma Thesis, University Halle-Wittenberg, 2010.
- [88] V. Popescu and A. Zunger, “Extracting  $e$  versus  $k$  - Effective band structure from supercell calculations on alloys and impurities”, *Physical Review B - Condensed Matter and Materials Physics* **85**, 85201 (2012).

- [89] R. Bianco, R. Resta, and I. Souza, “How disorder affects the Berry-phase anomalous Hall conductivity: A reciprocal-space analysis”, *Physical Review B* **90**, 125153 (2014).
- [90] H. Smith and H. H. Jensen, *Transport phenomena* (Oxford University Press, Oxford, 1989), p. 912.
- [91] A. Weiße, G. Wellein, A. Alvermann, and H. Fehske, “The kernel polynomial method”, *Reviews of Modern Physics* **78**, 275 (2006).
- [92] J. H. García, L. Covaci, and T. G. Rappoport, “Real-space calculation of the conductivity tensor for disordered topological matter”, *Physical Review Letters* **114**, 116602 (2015).
- [93] A. Bastin, C. Lewiner, O. Betbeder-matibet, and P. Nozieres, “Quantum oscillations of the hall effect of a fermion gas with random impurity scattering”, *Journal of Physics and Chemistry of Solids* **32**, 1811 (1971).
- [94] A. Crépieux and P. Bruno, “Theory of the anomalous Hall effect from the Kubo formula and the Dirac equation”, *Physical Review B - Condensed Matter and Materials Physics* **64**, 014416 (2001).
- [95] Karsten Flensberg and Henric Bruus, *Introduction To Quantum Field Theory In Condensed Matter Physics*, August (Oxford University Press, Oxford, 2001).
- [96] E. J. König, M. Dzero, A. Levchenko, and D. A. Pesin, “Gyrotropic Hall effect in Berry-curved materials”, *Physical Review B* **99**, 155404 (2019).
- [97] H. Isobe, S.-Y. Xu, and L. Fu, “High-frequency rectification via chiral Bloch electrons”, arXiv:1812.08162 (2018).
- [98] N. A. Sinitsyn, J. E. Hill, H. Min, J. Sinova, and A. H. MacDonald, “Charge and spin hall conductivity in metallic graphene”, *Physical Review Letters* **97**, 106804 (2006).
- [99] J. Li, K. Wang, K. J. McFaul, Z. Zern, Y. Ren, K. Watanabe, T. Taniguchi, Z. Qiao, and J. Zhu, “Gate-controlled topological conducting channels in bilayer graphene”, *Nature Nanotechnology* **11**, 1060 (2016).
- [100] D. Malterre, B. Kierren, Y. Fagot-Revurat, C. Didiot, F. J. García De Abajo, F. Schiller, J. Cordón, and J. E. Ortega, “Symmetry breaking and gap opening in two-dimensional hexagonal lattices”, *New Journal of Physics* **13**, 013026 (2011).
- [101] S. S. Gregersen, J. H. Garcia, A.-P. Jauho, S. Roche, and S. R. Power, “Charge and spin transport anisotropy in nanopatterned graphene”, *Journal of Physics: Materials* **1**, 015005 (2018).
- [102] K. Qian, D. J. Apigo, C. Prodan, Y. Barlas, and E. Prodan, “Topology of the valley-Chern effect”, *Physical Review B* **98**, 155138 (2018).
- [103] G. H. Ryu, H. J. Park, J. Ryou, J. Park, J. Lee, G. Kim, H. S. Shin, C. W. Bielawski, R. S. Ruoff, S. Hong, and Z. Lee, “Atomic-scale dynamics of triangular hole growth in monolayer hexagonal boron nitride under electron irradiation”, *Nanoscale* **7**, 10600 (2015).
- [104] L. Brey and H. A. Fertig, “Edge states and the quantized Hall effect in graphene”, *Physical Review B - Condensed Matter and Materials Physics* **73**, 195408 (2006).
- [105] A. Orlof, J. Ruseckas, and I. V. Zozoulenko, “Effect of zigzag and armchair edges on the electronic transport in single-layer and bilayer graphene nanoribbons with defects”, *Physical Review B - Condensed Matter and Materials Physics* **88**, 125409 (2013).
- [106] R. Petersen, T. G. Pedersen, and A. P. Jauho, “Clar sextet analysis of triangular, rectangular, and honeycomb graphene antidot lattices”, *ACS Nano* **5**, 523 (2011).
- [107] T. Aktor, J. H. Garcia, S. Roche, A.-P. Jauho, and S. R. Power, “Topological Valley Currents in Graphene with Local Sublattice Asymmetry”, arXiv:1910.00489 (2019).

- [108] N. A. Sinitsyn, “Semiclassical theories of the anomalous Hall effect”, *Journal of Physics Condensed Matter* **20**, 023201 (2008).
- [109] N. A. Sinitsyn, A. H. MacDonald, T. Jungwirth, V. K. Dugaev, and J. Sinova, “Anomalous Hall effect in a two-dimensional Dirac band: The link between the Kubo-Streda formula and the semiclassical Boltzmann equation approach”, *Physical Review B - Condensed Matter and Materials Physics* **75**, 045315 (2007).
- [110] N. A. Sinitsyn, Q. Niu, and A. H. MacDonald, “Coordinate shift in the semiclassical Boltzmann equation and the anomalous Hall effect”, *Physical Review B - Condensed Matter and Materials Physics* **73**, 075318 (2006).
- [111] P. Streda, “Theory of quantised Hall conductivity in two dimensions”, *Journal of Physics C: Solid State Physics* **15**, 717 (1982).
- [112] S. Yuan, R. Roldán, A. P. Jauho, and M. I. Katsnelson, “Electronic properties of disordered graphene antidot lattices”, *Physical Review B* **87**, 085430 (2013).
- [113] J. H. J. Martiny, A. Kreisel, and B. M. Andersen, “Theoretical study of impurity-induced magnetism in FeSe”, *Physical Review B* **99**, 14509 (2019).
- [114] S. Y. Song, J. H. J. Martiny, A. Kreisel, B. M. Andersen, and J. Seo, “Visualization of local magnetic moments emerging from impurities in the Hund’s metal states of FeSe”, (2019).
- [115] Q. Si, R. Yu, and E. Abrahams, “High-temperature superconductivity in iron pnictides and chalcogenides”, *Nature Reviews Materials* **1**, 16017 (2016).
- [116] J. H. J. Martiny, *A Chebyshev-Bogoliubov-de Gennes Approach to Quasiparticle Interference in the Nematic Phase of FeSe*, Master Thesis, Niels Bohr Institute, University of Copenhagen, 2016.
- [117] D. N. Basov and A. V. Chubukov, “Manifesto for a higher  $T_c$ ”, *Nature Physics* **7**, 272 (2011).
- [118] M. Bendele, A. Ichsanow, Y. Pashkevich, L. Keller, T. Strässle, A. Gusev, E. Pomjakushina, K. Conder, R. Khasanov, and H. Keller, “Coexistence of superconductivity and magnetism in  $\text{FeSe}_{1-x}$  under pressure”, *Physical Review B - Condensed Matter and Materials Physics* **85**, 64517 (2012).
- [119] J. P. Sun, K. Matsuura, G. Z. Ye, Y. Mizukami, M. Shimosawa, K. Matsubayashi, M. Yamashita, T. Watashige, S. Kasahara, Y. Matsuda, J. Q. Yan, B. C. Sales, Y. Uwatoko, J. G. Cheng, and T. Shibauchi, “Dome-shaped magnetic order competing with high-temperature superconductivity at high pressures in FeSe”, *Nature Communications* **7**, 12146 (2016).
- [120] T. Terashima, N. Kikugawa, S. Kasahara, T. Watashige, T. Shibauchi, Y. Matsuda, T. Wolf, A. E. Böhmer, F. Hardy, C. Meingast, H. V. Löhneysen, and S. Uji, “Pressure-induced antiferromagnetic transition and phase diagram in FeSe”, *Journal of the Physical Society of Japan* **84**, 063701 (2015).
- [121] A. E. Böhmer and A. Kreisel, “Nematicity, magnetism and superconductivity in FeSe”, *Journal of Physics Condensed Matter* **30**, aa9caa (2018).
- [122] S. Medvedev, T. M. McQueen, I. A. Troyan, T. Palasyuk, M. I. Eremets, R. J. Cava, S. Naghavi, F. Casper, V. Ksenofontov, G. Wortmann, and C. Felser, “Electronic and magnetic phase diagram of  $\beta\text{-Fe}_{1.01}\text{Se}$  with superconductivity at 36.7 K under pressure”, *Nature Materials* **8**, 630 (2009).
- [123] K. Kothapalli, A. E. Böhmer, W. T. Jayasekara, B. G. Ueland, P. Das, A. Sapkota, V. Taufour, Y. Xiao, E. Alp, S. L. Bud’ko, P. C. Canfield, A. Kreyssig, and A. I. Goldman, “Strong cooperative coupling of pressure-induced magnetic order and nematicity in FeSe”, *Nature Communications* **7**, 12728 (2016).
- [124] M. Burrard-Lucas, D. G. Free, S. J. Sedlmaier, J. D. Wright, S. J. Cassidy, Y. Hara, A. J. Corkett, T. Lancaster, P. J. Baker, S. J. Blundell, and S. J. Clarke, “Enhance-

- ment of the superconducting transition temperature of FeSe by intercalation of a molecular spacer layer”, *Nature Materials* **12**, 15 (2013).
- [125] T. P. Ying, X. L. Chen, G. Wang, S. F. Jin, T. T. Zhou, X. F. Lai, H. Zhang, and W. Y. Wang, “Observation of superconductivity at  $30 \sim 46K$  in  $A_x\text{Fe}_2\text{Se}_2$  ( $A = \text{Li}, \text{Na}, \text{Ba}, \text{Sr}, \text{Ca}, \text{Yb}, \text{and Eu}$ )”, *Scientific Reports* **2**, 426 (2012).
- [126] A. Krzton-Maziopa, V. Svitlyk, E. Pomjakushina, R. Puzniak, and K. Conder, “Superconductivity in alkali metal intercalated iron selenides”, *Journal of Physics Condensed Matter* **28**, 293002 (2016).
- [127] Q. Y. Wang, Z. Li, W. H. Zhang, Z. C. Zhang, J. S. Zhang, W. Li, H. Ding, Y. B. Ou, P. Deng, K. Chang, J. Wen, C. L. Song, K. He, J. F. Jia, S. H. Ji, Y. Y. Wang, L. L. Wang, X. Chen, X. C. Ma, and Q. K. Xue, “Interface-induced high-temperature superconductivity in single unit-cell FeSe films on  $\text{SrTiO}_3$ ”, *Chinese Physics Letters* **29**, 037402 (2012).
- [128] T. Imai, K. Ahilan, F. L. Ning, T. M. McQueen, and R. J. Cava, “Why does undoped FeSe become a high- $T_c$  superconductor under pressure?”, *Physical Review Letters* **102**, 177005 (2009).
- [129] M. C. Rahn, R. A. Ewings, S. J. Sedlmaier, S. J. Clarke, and A. T. Boothroyd, “Strong  $(\pi, 0)$  spin fluctuations in  $\beta$ -FeSe observed by neutron spectroscopy”, *Physical Review B* **91**, 180501 (2015).
- [130] Q. Wang, Y. Shen, B. Pan, X. Zhang, K. Ikeuchi, K. Iida, A. D. Christianson, H. C. Walker, D. T. Adroja, M. Abdel-Hafiez, X. Chen, D. A. Chareev, A. N. Vasiliev, and J. Zhao, “Magnetic ground state of FeSe”, *Nature Communications* **7**, 12182 (2016).
- [131] M. Ma, P. Bourges, Y. Sidis, Y. Xu, S. Li, B. Hu, J. Li, F. Wang, and Y. Li, “Prominent role of spin-orbit coupling in FeSe revealed by inelastic neutron scattering”, *Physical Review X* **7**, 021025 (2017).
- [132] B. M. Andersen, S. Graser, and P. J. Hirschfeld, “Disorder-induced freezing of dynamical spin fluctuations in underdoped cuprate superconductors”, *Physical Review Letters* **105**, 147002 (2010).
- [133] A. E. Böhrer, F. Hardy, F. Eilers, D. Ernst, P. Adelman, P. Schweiss, T. Wolf, and C. Meingast, “Lack of coupling between superconductivity and orthorhombic distortion in stoichiometric single-crystalline FeSe”, *Physical Review B - Condensed Matter and Materials Physics* **87**, 180505 (2013).
- [134] M. He, L. Wang, F. Hardy, L. Xu, T. Wolf, P. Adelman, and C. Meingast, “Evidence for short-range magnetic order in the nematic phase of FeSe from anisotropic in-plane magnetostriction and susceptibility measurements”, *Physical Review B* **97**, 104107 (2018).
- [135] V. Grinenko, R. Sarkar, P. Materne, S. Kamusella, A. Yamamshita, Y. Takano, Y. Sun, T. Tamegai, D. V. Efremov, S. L. Drechsler, J. C. Orain, T. Goko, R. Scheuermann, H. Luetkens, and H. H. Klauss, “Low-temperature breakdown of antiferromagnetic quantum critical behavior in FeSe”, *Physical Review B* **97**, 201102 (2018).
- [136] R. Khasanov, K. Conder, E. Pomjakushina, A. Amato, C. Baines, Z. Bukowski, J. Karpinski, S. Katrych, H. H. Klauss, H. Luetkens, A. Shengelaya, and N. D. Zhigadlo, “Evidence of nodeless superconductivity in  $\text{FeSe}_{0.85}$  from a muon-spin-rotation study of the in-plane magnetic penetration depth”, *Physical Review B - Condensed Matter and Materials Physics* **78**, 220510 (2008).
- [137] W. Li, Y. Zhang, P. Deng, Z. Xu, S. K. Mo, M. Yi, H. Ding, M. Hashimoto, R. G. Moore, D. H. Lu, X. Chen, Z. X. Shen, and Q. K. Xue, “Stripes developed at the strong limit of nematicity in FeSe film”, *Nature Physics* **13**, 957 (2017).

- [138] Y. Zhou, L. Miao, P. Wang, F. F. Zhu, W. X. Jiang, S. W. Jiang, Y. Zhang, B. Lei, X. H. Chen, H. F. Ding, H. Zheng, W. T. Zhang, J. F. Jia, D. Qian, and D. Wu, “Antiferromagnetic Order in Epitaxial FeSe Films on SrTiO<sub>3</sub>”, *Physical Review Letters* **120**, 097001 (2018).
- [139] S. Mukherjee, A. Kreisel, P. J. Hirschfeld, and B. M. Andersen, “Model of Electronic Structure and Superconductivity in Orbitally Ordered FeSe”, *Physical Review Letters* **115**, 026402 (2015).
- [140] A. Kreisel, S. Mukherjee, P. J. Hirschfeld, and B. M. Andersen, “Spin excitations in a model of FeSe with orbital ordering”, *Physical Review B - Condensed Matter and Materials Physics* **92**, 224515 (2015).
- [141] A. Kreisel, B. M. Andersen, and P. J. Hirschfeld, “Itinerant approach to magnetic neutron scattering of FeSe: Effect of orbital selectivity”, *Physical Review B* **98**, 214518 (2018).
- [142] K. Haule and G. Kotliar, “Coherence-incoherence crossover in the normal state of iron oxypnictides and importance of Hund’s rule coupling”, *New Journal of Physics* **11**, 025021 (2009).
- [143] Z. P. Yin, K. Haule, and G. Kotliar, “Kinetic frustration and the nature of the magnetic and paramagnetic states in iron pnictides and iron chalcogenides”, *Nature Materials* **10**, 932 (2011).
- [144] L. De’Medici, J. Mravlje, and A. Georges, “Janus-Faced Influence of Hund’s Rule Coupling in Strongly Correlated Materials”, *Physical Review Letters* **107**, 256401 (2011).
- [145] N. Lanatà, H. U. Strand, G. Giovannetti, B. Hellsing, L. De’Medici, and M. Capone, “Orbital selectivity in Hund’s metals: The iron chalcogenides”, *Physical Review B - Condensed Matter and Materials Physics* **87**, 045122 (2013).
- [146] A. Georges, L. de’Medici, and J. Mravlje, “Strong Correlations from Hund’s Coupling”, *Annual Review of Condensed Matter Physics* **4**, 137 (2013).
- [147] L. De Medici, G. Giovannetti, and M. Capone, “Selective Mott physics as a key to iron superconductors”, *Physical Review Letters* **112**, 177001 (2014).
- [148] L. Fanfarillo and E. Bascones, “Electronic correlations in Hund metals”, *Physical Review B - Condensed Matter and Materials Physics* **92**, 075136 (2015).
- [149] L. de’Medici and M. Capone, in *The iron pnictide superconductors: an introduction and overview*, edited by F. Mancini and R. Citro (Springer International Publishing, Cham, 2017), pp. 115–185.
- [150] A. van Roekeghem, P. Richard, H. Ding, and S. Biermann, “Spectral properties of transition metal pnictides and chalcogenides: Angle-resolved photoemission spectroscopy and dynamical mean-field theory”, *Comptes Rendus Physique* **17**, 140 (2016).
- [151] D. Guterding, S. Backes, M. Tomić, H. O. Jeschke, and R. Valentí, “Ab initio perspective on structural and electronic properties of iron-based superconductors”, *Physica Status Solidi (B) Basic Research* **254**, 164 (2017).
- [152] L. de Medici, *Iron-Based Superconductivity, Weak and Strong Correlations in Fe Superconductors*, edited by Peter D. Johnson, Guangyong Xu and W.-G. Yin, Springer Series in Materials Science (Springer, 2015).
- [153] A. Kreisel, B. M. Andersen, P. O. Sprau, A. Kostin, J. C. Davis, and P. J. Hirschfeld, “Orbital selective pairing and gap structures of iron-based superconductors”, *Physical Review B* **95**, 174504 (2017).
- [154] P. O. Sprau, A. Kostin, A. Kreisel, A. E. Böhmer, V. Taufour, P. C. Canfield, S. Mukherjee, P. J. Hirschfeld, B. M. Andersen, and J. C. Davis, “Discovery of orbital-selective Cooper pairing in FeSe”, *Science* **357**, 75 (2017).

- [155] A. Kostin, P. O. Sprau, A. Kreisel, Y. X. Chong, A. E. Böhmer, P. C. Canfield, P. J. Hirschfeld, B. M. Andersen, and J. C. Davis, “Imaging orbital-selective quasi-particles in the Hund’s metal state of FeSe”, *Nature Materials* **17**, 869 (2018).
- [156] H. Alloul, J. Bobroff, M. Gabay, and P. J. Hirschfeld, “Defects in correlated metals and superconductors”, *Reviews of Modern Physics* **81**, 45 (2009).
- [157] H. Tsuchiura, Y. Tanaka, M. Ogata, and S. Kashiwaya, “Local magnetic moments around a nonmagnetic impurity in the two-dimensional  $t - J$  model”, *Physical Review B - Condensed Matter and Materials Physics* **64**, 140501 (2001).
- [158] Z. Wang and P. A. Lee, “Local Moment Formation in the Superconducting State of a Doped Mott Insulator”, *Physical Review Letters* **89**, 217002 (2002).
- [159] J. X. Zhu, I. Martin, and A. R. Bishop, “Spin and Charge Order around Vortices and Impurities in High- $T_c$  Superconductors”, *Physical Review Letters* **89**, 067003 (2002).
- [160] Y. Chen and C. S. Ting, “States of Local Moment Induced by Nonmagnetic Impurities in Cuprate Superconductors”, *Physical Review Letters* **92**, 077203 (2004).
- [161] J. W. Harter, B. M. Andersen, J. Bobroff, M. Gabay, and P. J. Hirschfeld, “Antiferromagnetic correlations and impurity broadening of NMR linewidths in cuprate superconductors”, *Physical Review B - Condensed Matter and Materials Physics* **75**, 054520 (2007).
- [162] H. Kontani and M. Ohno, “Effect of a nonmagnetic impurity in a nearly antiferromagnetic Fermi liquid: Magnetic correlations and transport phenomena”, *Physical Review B - Condensed Matter and Materials Physics* **74**, 014406 (2006).
- [163] M. N. Gastiasoro, P. J. Hirschfeld, and B. M. Andersen, “Impurity states and cooperative magnetic order in Fe-based superconductors”, *Physical Review B - Condensed Matter and Materials Physics* **88**, 220509 (2013).
- [164] M. N. Gastiasoro, F. Bernardini, and B. M. Andersen, “Unconventional Disorder Effects in Correlated Superconductors”, *Physical Review Letters* **117**, 257002 (2016).
- [165] L. Covaci, F. M. Peeters, and M. Berciu, “Efficient numerical approach to inhomogeneous superconductivity: The chebyshev-bogoliubov-de gennes method”, *Physical Review Letters* **105**, 167006 (2010).
- [166] D. Möckli and E. V. de Mello, “The  $\text{Ba}_{0.6}\text{K}_{0.4}\text{Fe}_2\text{As}_2$  superconducting four-gap temperature evolution: A multi-band Chebyshev–BdG approach”, *Physics Letters, Section A: General, Atomic and Solid State Physics* **380**, 2565 (2016).
- [167] M. N. Gastiasoro and B. M. Andersen, “Local Magnetization Nucleated by Nonmagnetic Impurities in Fe-based Superconductors”, *Journal of Superconductivity and Novel Magnetism* **28**, 1321 (2015).
- [168] M. N. Gastiasoro and B. M. Andersen, “Enhancing superconductivity by disorder”, *Physical Review B* **98**, 184510 (2018).
- [169] P. J. Hirschfeld, D. Altenfeld, I. Eremin, and I. I. Mazin, “Robust determination of the superconducting gap sign structure via quasiparticle interference”, *Physical Review B - Condensed Matter and Materials Physics* **92**, 184513 (2015).
- [170] M. N. Gastiasoro, *Emergent disorder phenomena in correlated Fe-based superconductors*, Ph.D. Thesis, Niels Bohr Institute, University of Copenhagen, 2016.
- [171] J. Tersoff and D. R. Hamann, “Theory of the scanning tunneling microscope”, *Physical Review B* **31**, 805 (1985).
- [172] P. Choubey, T. Berlijn, A. Kreisel, C. Cao, and P. J. Hirschfeld, “Visualization of atomic-scale phenomena in superconductors: Application to FeSe”, *Physical Review B - Condensed Matter and Materials Physics* **90**, 134520 (2014).

- [173] A. Kreisel, R. Nelson, T. Berlijn, W. Ku, R. Aluru, S. Chi, H. Zhou, U. R. Singh, P. Wahl, R. Liang, W. N. Hardy, D. A. Bonn, P. J. Hirschfeld, and B. M. Andersen, “Towards a quantitative description of tunneling conductance of superconductors: Application to LiFeAs”, *Physical Review B* **94**, 224518 (2016).
- [174] A. Kreisel, P. Choubey, T. Berlijn, W. Ku, B. M. Andersen, and P. J. Hirschfeld, “Interpretation of scanning tunneling quasiparticle interference and impurity states in cuprates”, *Physical Review Letters* **114**, 217002 (2015).
- [175] S. Chi, R. Aluru, U. R. Singh, R. Liang, W. N. Hardy, D. A. Bonn, A. Kreisel, B. M. Andersen, R. Nelson, T. Berlijn, W. Ku, P. J. Hirschfeld, and P. Wahl, “Impact of iron-site defects on superconductivity in LiFeAs”, *Physical Review B* **94**, 134515 (2016).
- [176] D. Huang and J. E. Hoffman, “Monolayer FeSe on SrTiO<sub>3</sub>”, *Annual Review of Condensed Matter Physics* **8**, 311 (2017).
- [177] L. Yu, “Bound State in Superconductors with Paramagnetic Impurities”, *Acta Physica Sinica* **21**, 75 (1965).
- [178] H. Shiba, “Classical Spins in Superconductors”, *Progress of Theoretical Physics* **40**, 435 (1968).
- [179] A. I. Rusinov, “Superconductivity near a paramagnetic impurity”, *ZhETF Pis. Red.* **9**, 146 (1968).
- [180] A. V. Balatsky, I. Vekhter, and J. X. Zhu, “Impurity-induced states in conventional and unconventional superconductors”, *Reviews of Modern Physics* **78**, 373 (2006).
- [181] B. M. Andersen, *Coexistence of Magnetic and Superconducting Order in the High-T<sub>c</sub> Materials*, Ph.D. Thesis in Physics, Niels Bohr Institute, Copenhagen University, 2004.
- [182] A. Chubukov, “Pairing Mechanism in Fe-Based Superconductors”, *Annual Review of Condensed Matter Physics* **3**, 57 (2012).
- [183] P. J. Hirschfeld, “Using gap symmetry and structure to reveal the pairing mechanism in Fe-based superconductors”, *Comptes Rendus Physique* **17**, 197 (2016).
- [184] S. H. Pan, E. W. Hudson, and J. C. Davis, “Vacuum tunneling of superconducting quasiparticles from atomically sharp scanning tunneling microscope tips”, *Applied Physics Letters* **73**, 2992 (1998).
- [185] D. Huang, T. A. Webb, C. L. Song, C. Z. Chang, J. S. Moodera, E. Kaxiras, and J. E. Hoffman, “Dumbbell Defects in FeSe Films: A Scanning Tunneling Microscopy and First-Principles Investigation”, *Nano Letters* **16**, 4224 (2016).
- [186] J. H. J. Martiny, K. Kaasbjerg, and A. P. Jauho, “Tunable valley Hall effect in gate-defined graphene superlattices”, *Physical Review B* **100**, 155414 (2019).



# Appendix A

## Unfolding procedure

In this section we expand upon the unfolding procedure used to calculate the valley Hall conductivity in the superlattice system. Throughout this section we denote quantities defined in the normal (graphene) unit cell (NC) by uncapitalized letters and quantities defined in the supercell (SC) by capital letters. We denote the corresponding Brillouin zones as the normal (SBZ) and supercell (SBZ) Brillouin zones. The supercell is here an extension of the normal cell, and the area of the SBZ is thus smaller than (or, trivially, equal to) the NBZ. In the following discussion we assume that the definition of the supercell is nontrivial for ease of notation, i.e., we assume that the area of the supercell is strictly larger than that of the normal cell. We follow the similar presentation in Martiny et al. [186] closely.

Following the definition of a supercell using the notation of Eq. (3.16), a wavevector  $\mathbf{k}$  in the normal Brillouin NBZ is folded into a unique  $\mathbf{K} \in \text{SBZ}$  by a reciprocal lattice vector [88]

$$\mathbf{K} = \mathbf{k} - \mathbf{G}_0, \quad (\text{A.1})$$

with  $\mathbf{G}_0 = \sum_i q_i \mathbf{B}_i$ , where the  $q_i$  are integers, and we define  $\mathbf{K}'(\mathbf{k})$  as the unique SBZ wavevector  $\mathbf{K}$  to which a given NBZ wavevector  $\mathbf{k}$  folds. Conversely, a wavevector in the

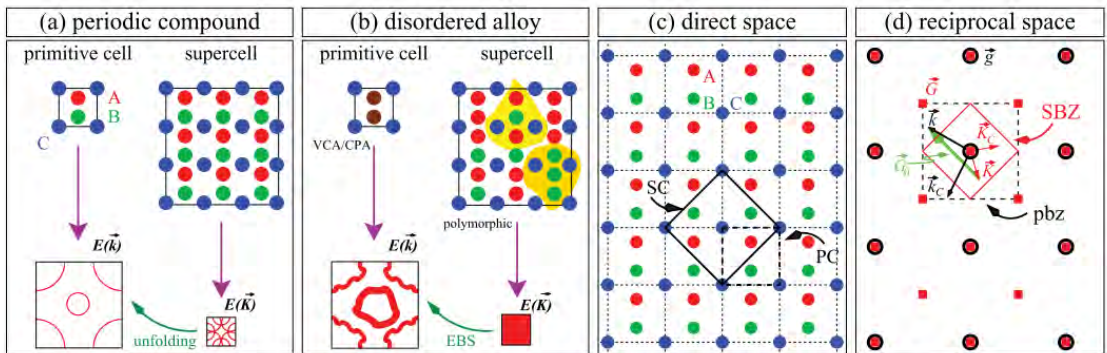


**Figure A.1:** A schematic interpretation of the unfolding procedure. (a) The normal cell with a trivial unfolding shown. (b) A disordered system where the breaking of symmetries leads to a dense grid of downfolded bands in the SBZ. (c) Geometrical definitions in real space. (d) Lattice vectors in reciprocal space. Reproduced from Popescu and Zunger [88].

SBZ can be unfolded into multiple values

$$\mathbf{k}_i = \mathbf{K} + \mathbf{G}_i, \quad (\text{A.2})$$

where the number of elements  $N_k$  in the set of such reciprocal lattice vectors  $\{\mathbf{G}_i\}$  given by  $N_k = \det \mathbf{M}$  [88].

Our tight-binding calculation is defined using a set of localized orbitals  $|\phi_{ir}\rangle$ , from which we construct the Bloch states as denoted in the main text Eq. (3.3), but now both for normal and supercells

$$|n\mathbf{k}\rangle = \sum_i C_{ink} |i\mathbf{k}\rangle \quad (\text{A.3a})$$

$$= \sum_{ir} C_{ink} e^{i\mathbf{k}\cdot(\mathbf{r}+\boldsymbol{\tau}_i)} |\phi_{ir}\rangle, \quad (\text{A.3b})$$

$$|N\mathbf{K}\rangle = \sum_{IR} C_{IN\mathbf{K}} e^{i\mathbf{K}\cdot(\mathbf{R}+\boldsymbol{\tau}_I)} |\phi_{IR}\rangle. \quad (\text{A.3c})$$

Here,  $\mathbf{r}, \mathbf{R}$  are lattice vectors in the normal and supercells, respectively. The vectors  $\boldsymbol{\tau}_{i/I}$  are the corresponding internal orbital positions in these cells.

With the initial definitions in place, we are now ready to consider the unfolding of some quantity in the supercell  $\mathcal{O}_{N\mathbf{K}}$ , which could be, e.g., the LDOS defined in Eq. (6.9). We define the corresponding unfolded quantity

$$\mathcal{O}_{i\mathbf{k}}^{(u)} = \sum_{N\mathbf{K}} |\langle i\mathbf{k}|N\mathbf{K}\rangle|^2 \mathcal{O}_{N\mathbf{K}} \quad (\text{A.4})$$

$$\equiv \sum_N \lambda_{iN\mathbf{k}} \mathcal{O}_{N\mathbf{K}'(\mathbf{k})}. \quad (\text{A.5})$$

We see that the unfolding procedure involves the Bloch state overlap  $\lambda_{iN\mathbf{k}}$ , which we now derive within the tight-binding formalism. Note that we initially consider unfolding of simple quantities which do not involve any derivatives with respect to the wavevector in their definitions and return below to the applicable procedure for, e.g., the Berry curvature.

Given the set of orbitals  $i$  in the normal cell and the corresponding set  $I$  in the supercell, we define a unique map  $\text{map } I \rightarrow \mathbf{R} + \mathbf{r}'(I), i'(I)$  relating positions and indexes in the normal and supercells. The overlap between localized orbitals is then written

$$\langle \phi_{ir} | \phi_{IR} \rangle = \langle \phi_{ir} | \phi_{i'(I)\mathbf{R}+\mathbf{r}'(I)} \rangle \quad (\text{A.6})$$

$$= \delta_{i'i'(I)} \delta_{\mathbf{r}, \mathbf{R}+\mathbf{r}'(I)}. \quad (\text{A.7})$$

Here, the final overlap follows from the choice of an orthogonal basis of normal cell orbitals. The Bloch state overlap of Eq. (A.5) then follows as

$$\lambda_{iN\mathbf{k}} = \langle i\mathbf{k} | N\mathbf{K} \rangle \quad (\text{A.8})$$

$$= \sum_{I, \mathbf{r}\mathbf{R}} C_{IN\mathbf{K}} e^{-i\mathbf{k}\cdot(\mathbf{r}+\boldsymbol{\tau}_i)} e^{i\mathbf{K}\cdot(\mathbf{R}+\boldsymbol{\tau}_I)} \langle \phi_{ir} | \phi_{IR} \rangle \quad (\text{A.9})$$

$$= \sum_{I, \mathbf{R}} C_{IN\mathbf{K}} e^{-i\mathbf{k}\cdot(\mathbf{R}+\mathbf{r}'(I)+\boldsymbol{\tau}_i)} e^{i\mathbf{K}\cdot(\mathbf{R}+\boldsymbol{\tau}_I)} \delta_{i'i'(I)} \quad (\text{A.10})$$

$$= \sum_I C_{IN\mathbf{K}} e^{-i\mathbf{k}\cdot(\mathbf{r}'(I)+\boldsymbol{\tau}_i)} e^{i\mathbf{K}\cdot\boldsymbol{\tau}_I} \delta_{i'i'(I)} \delta_{\mathbf{K}\{\mathbf{k}\}}. \quad (\text{A.11})$$

The delta function defined in the final equality [Eq. (A.11)] involves the set of NBZ wavevectors  $\{\mathbf{k}\}$  which downfold to the specific SBZ wavevector  $\mathbf{K}$ . As we saw previously, the number of elements in this set is  $N_k = \det \mathbf{M}$ . In the unfolding calculation we can collapse any sum over  $\mathbf{K}$  as the value  $\mathbf{K}'(\mathbf{k})$  is unique. Given the overlap calculated in this manner, quantities can then be unfolded by application of Eq. (A.5).

A similar procedure to the above for the Berry curvature becomes gauge-dependent, and an extended formalism must thus be applied. A gauge invariant expression for the unfolded Berry curvature was derived in Bianco et al. [89], calculating the occupied Berry curvature as a trace over the unfolded non-Abelian Berry curvature matrix (see Bianco et al. [89] Eqs. (20-31)). For the specific application in the tight-binding model we refer to the relevant appendix of Olsen and Souza [86].

## Appendix B

# Profile of the superlattice potential

In this appendix we include further information about the profile of the superlattice potential, specifically the variation of this potential towards the edges of the nanostructured region. The spatial variation is enforced using a modified Fermi distribution maximal at the center and vanishing at the edge of the potential

$$V(r)/V_{max} = \frac{1}{\exp\{(r - r_{max})/u\} + 1}, \quad (\text{B.1})$$

with  $r_{max} = |r_{edge} - r_{center}|$  the distance from the center to the edge of the potential-defined region. The potential is plotted in Fig. B.1(a) for  $u = 0.2$ , alongside a contour plot in (b). A linecut is included in (c) along the equivalent symmetry directions denoted by dashed lines in (b). The continuous parameter  $u \in [0, 1]$  sets the scale of the variation, with  $u = 0$  being the perfectly flat potential initially considered and  $u = 1$  being the extreme case of a linearly decreasing potential.

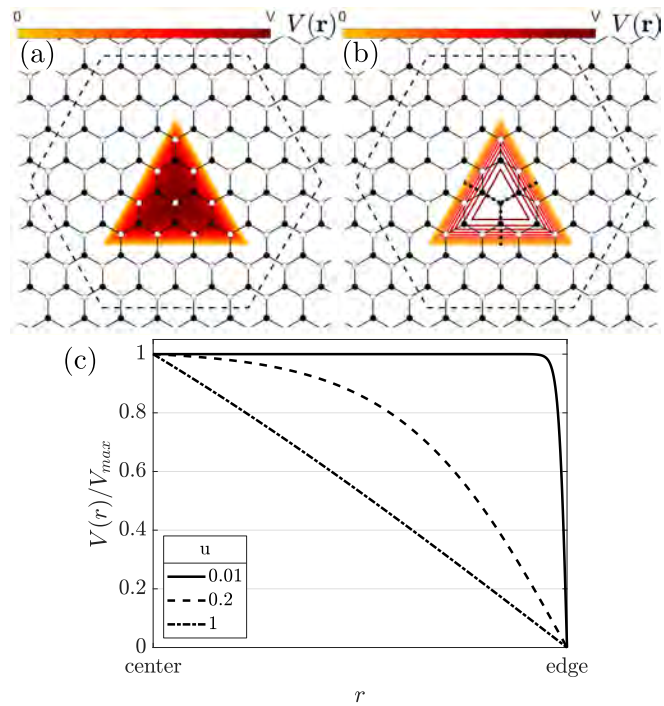


**Figure B.1:** (a) The superlattice potential shown in a single supercell for  $u = 0.2$ . (b) Contour plot of the potential showing the variation from edge to center. (c) Line cut of the potential along the dashed lines in (b), shown here for three different values of the free parameter  $u$ .

## Appendix C

# Chebyshev expansion details and derivations

### Expansion of the Fermi surface contribution

In this subsection we provide the full expansion of the Fermi surface contribution

$$\sigma_{\alpha\beta}^{FS}(\mu) = \frac{\hbar e^2}{\mathcal{V}} \int d\epsilon \frac{df(\epsilon)}{d\epsilon} \text{Im Tr} [\hat{v}_\alpha \delta(H - \epsilon) \hat{v}_\beta G^R(\epsilon)] \quad (\text{C.1})$$

$$= \frac{\hbar e^2}{\mathcal{V}} \int_{-1}^1 d\tilde{\epsilon} a \frac{df(\epsilon)}{d\epsilon} \text{Im Tr} \left[ \hat{v}_\alpha \frac{-1}{a} \delta(\tilde{\epsilon} - \tilde{H}) \hat{v}_\beta \frac{1}{a} G^R(\tilde{\epsilon}) \right] \quad (\text{C.2})$$

$$\approx \frac{\hbar e^2}{\mathcal{V}} \int_{-1}^1 d\tilde{\epsilon} \frac{df(\epsilon)}{d\epsilon} \times \text{Im Tr} \left[ \frac{4i}{a\pi(1 - \tilde{\epsilon}^2)} \hat{v}_\alpha \sum_m^M g_m \frac{T_m(\tilde{\epsilon})}{(\delta_{m0} + 1)} T_m(\tilde{H}) \sum_n^M \frac{e^{in \arccos(\tilde{\epsilon})}}{\delta_{n0} + 1} g_n \hat{v}_\beta T_n(\tilde{H}) \right] \quad (\text{C.3})$$

$$= \frac{4\hbar e^2}{\pi\mathcal{V}} \int_{-1}^1 d\tilde{\epsilon} \frac{df(\epsilon)}{d\epsilon} \times \text{Im} \left( \frac{i}{a(1 - \tilde{\epsilon}^2)} \sum_{m,n}^M \frac{g_m g_n}{(\delta_{m0} + 1)(\delta_{n0} + 1)} T_m(\tilde{\epsilon}) e^{in \arccos(\tilde{\epsilon})} \text{Tr} [\hat{v}_\alpha T_m(\tilde{H}) \hat{v}_\beta T_n(\tilde{H})] \right) \quad (\text{C.4})$$

$$= \frac{4\hbar e^2}{\pi\mathcal{V}} \int_{-1}^1 d\tilde{\epsilon} [-2k_B T (\cosh[(a\tilde{\epsilon} - \mu)/kT] + 1)]^{-1} \text{Re} \left( \sum_{m,n}^M \Gamma_{mn}^{FS}(\tilde{\epsilon}) \mu_{mn}^{\alpha\beta} \right). \quad (\text{C.5})$$

The expansions of the Fermi sea and the full Kubo-Bastin formula for the conductivity follow in similar fashion, using the same calculational steps for the expressions in Eq. (5.3) and Eq. (3.44), respectively

### Comments on the random vector approximation

The stochastic evaluation of the trace we introduced in Section 3.4.4 provides a dramatic improvement in the computational efficiency of the expansion procedure. We saw in Section 3.4.6 how this procedure yields a well-converged DOS by including only a few random vectors in the approximation ( $N_{rv} \sim 10$ ). We find this to be true for both the DOS and for our initial results for the longitudinal conductivity, but note here that care must be taken when using this approximation for the valley Hall conductivity. Here, we find a slower convergence of the conductivity, and thus include many more random vectors

when presenting these results ( $N_{rv} \sim 1300$ ). We note here that the valley projection creates a useful check for the convergence of results: Splitting the DOS into valley components should yield two exactly equal components which sum to the full result, i.e.,  $DOS^K = DOS^{K'} = DOS/2$ . For the valley Hall conductivity the symmetry requirement  $\sigma_{xy}^K = -\sigma_{xy}^{K'}$  can be used in similar fashion.



## Paper I

### **Symmetry-forbidden intervalley scattering by atomic defects in monolayer transition-metal dichalcogenides**

Kristen Kaasbjerg, Johannes H. J. Martiny, Tony Low, and Antti-Pekka Jauho

*Physical Review B* **96** (24), 241411(R) (2017)

# Symmetry-forbidden intervalley scattering by atomic defects in monolayer transition-metal dichalcogenides

Kristen Kaasbjerg,<sup>1,\*</sup> Johannes H. J. Martiny,<sup>1</sup> Tony Low,<sup>2</sup> and Antti-Pekka Jauho<sup>1</sup>

<sup>1</sup>*Center for Nanostructured Graphene (CNG), Department of Micro- and Nanotechnology, Technical University of Denmark, DK-2800 Kongens Lyngby, Denmark*

<sup>2</sup>*Department of Electrical and Computer Engineering, University of Minnesota, Minneapolis, Minnesota 55455, USA*

Intervalley scattering by atomic defects in monolayer transition metal dichalcogenides (TMDs;  $MX_2$ ) presents a serious obstacle for applications exploiting their unique valley-contrasting properties. Here, we show that the symmetry of the atomic defects can give rise to an unconventional protection mechanism against intervalley scattering in monolayer TMDs. The predicted defect-dependent selection rules for intervalley scattering can be verified via Fourier transform scanning tunneling spectroscopy (FT-STs), and provide a unique identification of, e.g., atomic vacancy defects ( $M$  vs  $X$ ). Our findings put the absence of the intervalley FT-STs peak in recent experiments in a different perspective.

**Introduction.**—Two-dimensional (2D) monolayers of transition metal dichalcogenides (TMDs;  $MX_2$ ) are promising candidates for spin- and valleytronics applications [1]. Their hallmarks include unique valley-contrasting properties and strong spin-valley coupling [1, 2] exemplified by, e.g., valley-selective optical pumping [3–5], a valley-dependent Zeeman effect [6–9], and the valley Hall effect [10]. Such means to control the valley degree of freedom are instrumental for valleytronics applications.

Another prerequisite for a successful realization of valleytronics is a sufficiently long valley lifetime [11, 12]; atomic defects are a common limiting factor which can provide the required momentum for intervalley scattering due to their short-range nature. However, as illustrated in Fig. 1(a), the spin-orbit (SO) induced spin-valley coupling in the  $K, K'$  valleys of 2D TMDs partially protects the valley degree of freedom against relaxation via intervalley scattering by nonmagnetic defects [2]. Due to the small spin-orbit splitting in the conduction band valleys [13, 14], only the valence-band valleys fully benefit from this protection. Identification of additional protection mechanisms in the conduction band would hence be advantageous for valleytronics in 2D TMDs.

In this work, we demonstrate that besides the spin-valley coupling, the symmetry and position of atomic defects give rise to unconventional selection rules for intervalley quasiparticle scattering in 2D TMDs. As illustrated in Fig. 1(b), we find that for defects with threefold rotational symmetry ( $C_3$ ), e.g., atomic vacancies, intervalley  $K \leftrightarrow K'$  scattering in the conduction band is forbidden for defects centered on the  $X$  site while it is allowed for  $M$  centered defects. In the valence band, intervalley scattering is forbidden in both cases. Analogous selection rules for the intervalley coupling due to confinement potentials in 2D TMD based quantum dots have previously been noted [15].

Our findings can be readily verified with scanning tunneling spectroscopy (STS) which has provided valuable

insight to the electronic properties of 2D TMDs [16–20]. In particular, Fourier transform STS (FT-STs) is a powerful method for investigating atomic defects and their scattering properties in 2D materials [21, 22]. The measured STS map is a probe of the local density of states (LDOS) whose real-space modulation, resembling Friedel oscillations, originates from quasiparticle interference (QPI) between electronic waves scattered by defects. Hence, the Fourier transform of the STS map provides direct access to the available scattering channels in  $\mathbf{q}$  space, and has shed important light on defect scattering in, e.g., graphene [23–30], monolayer TMDs [18, 19], and black phosphorus [31].

In the above-mentioned STS experiments on TMDs, the strong spin-valley coupling in the valence band of

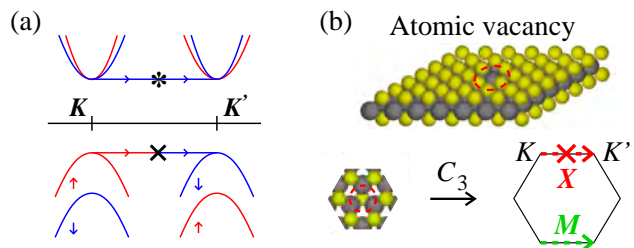


FIG. 1. Symmetry-dependent defect scattering in monolayer TMDs. (a) Sketch of the band structure near the  $K, K'$  points. The strong spin-valley coupling in the valence band suppresses intervalley scattering ( $\times$ ). In the conduction band, the small spin-orbit splitting, in principle, allows for intervalley scattering ( $*$ ). However, for defects with threefold rotational symmetry ( $C_3$ ), additional selection rules arise which protect against intervalley scattering. (b) Atomic sulfur vacancy in 2D  $\text{MoS}_2$  showing the  $C_3$  symmetry of the vacancy site. The vacancy-dependent selection rules for  $K \leftrightarrow K'$  intervalley scattering in the conduction band are illustrated in the bottom part, showing that only  $M$  vacancies produce intervalley scattering (green arrow). This allows for a unique identification of the vacancy type with FT-STs.

WSe<sub>2</sub> was confirmed by the missing  $K \leftrightarrow K'$  intervalley peak in the FT-STs spectrum [18, 19]. Surprisingly, the intervalley peak was also missing in the conduction band where intervalley scattering should be allowed [18, 19] [see Fig. 1(a)].

Here, we demonstrate the effect of symmetry on quasi-particle scattering by atomic vacancies which are among the most common types of defects in 2D TMDs [32–38]. For this purpose, we perform atomistic density-functional (DFT)-based  $T$ -matrix calculations [39] of FT-STs and QPI spectra for vacancies in two archetypal TMDs: the direct gap [44], small SO split MoS<sub>2</sub>, and the indirect gap [17], large SO split [13, 14] WSe<sub>2</sub>. As we show, the  $K \leftrightarrow K'$  conduction-band intervalley FT-STs peak is strongly suppressed for  $X$  vacancies while it appears clearly for  $M$  vacancies, thus offering an appealing explanation for its conspicuous absence in experiments [18, 19]. Our findings furthermore show that FT-STs allows for a unique identification of the vacancy type, and indicate that the valley dynamics of carriers and excitons in 2D TMDs are not affected by disorder if  $M$ -type defects can be avoided.

#### *Symmetry-dependent intervalley scattering.*—

We consider first the effect of symmetry on intervalley scattering by defects in 2D TMDs. The selection rules can be deduced within the framework of the low-energy Hamiltonian [2],

$$\mathcal{H}(\mathbf{k}) = at(\tau k_x \hat{\sigma}_x + k_y \hat{\sigma}_y) + \frac{\Delta}{2} \hat{\sigma}_z + \tau \lambda \frac{\hat{1} - \hat{\sigma}_z}{2} \hat{s}_z, \quad (1)$$

describing the band structure in the  $K, K'$  valleys sketched in Fig. 1(a). Here,  $a$  is the lattice constant,  $t$  is a hopping parameter,  $\tau = \pm 1$  is the  $K, K'$  valley index,  $\Delta$  is the band gap,  $2\lambda$  is the SO splitting at the top of the valence band, and  $\hat{\sigma}$ ,  $\hat{\tau}$  and  $\hat{s}$  are Pauli matrices in the symmetry-adapted spinor basis, valley and spin space, respectively. The symmetry-adapted basis is spanned by the  $M$   $d$ -orbitals  $|\phi_{v\tau}\rangle = 1/\sqrt{2}(|d_{x^2-y^2}\rangle + i\tau|d_{xy}\rangle)$  and  $|\phi_{c\tau}\rangle = |d_{z^2}\rangle$  which dominate the states in the valence ( $v$ ) and conduction ( $c$ ) bands, respectively [45, 46].

In 2D TMDs, defects such as atomic vacancies have  $C_3$  symmetry, i.e.  $\hat{V}_i = C_3 \hat{V}_i C_3^\dagger$  where  $\hat{V}_i$  is the scattering potential for defect type  $i$  and  $C_3$  is the operator for threefold rotations by  $\pm 2\pi/3$  around the defect center. The intervalley matrix element ( $\tau \neq \tau'$ ) between the high-symmetry  $K, K'$  points can thus be written

$$\begin{aligned} \langle n\tau | \hat{V}_i | n\tau' \rangle &= \langle n\tau | C_3^\dagger C_3 \hat{V}_i C_3^\dagger C_3 | n\tau' \rangle \\ &= \langle n\tau | C_3^\dagger \hat{V}_i C_3 | n\tau' \rangle \equiv \gamma_{i,n}^{\tau\tau'} \langle n\tau | \hat{V}_i | n\tau' \rangle, \end{aligned} \quad (2)$$

where  $n$  is the band index (including spin) and  $\hat{I} = C_3^\dagger C_3$  is the identity operator. As  $C_3$  belongs to the group of the wave vector at the  $K, K'$  points ( $C_{3h}$ ), the Bloch functions transform according to the irreducible representation of  $C_{3h}$ ,  $C_3 | n\tau \rangle = w_{i,n\tau} | n\tau \rangle$  where  $w_{i,n\tau}$  denotes the

eigenvalues of  $C_3$ . The matrix element can thus be expressed in terms of the complex scalar  $\gamma_{i,n}^{\tau\tau'} = w_{i,n\tau}^* w_{i,n\tau'}$  as indicated in the last equality of (2). Our analysis shows that  $\gamma_{i,n}^{\tau\tau'} = 1$  only if the defect is centered on an  $M$  site and  $n = c$  [39]. In all other cases  $\gamma_{i,n}^{\tau\tau'} \neq 1$ , and the intervalley matrix element vanishes identically by virtue of Eq. (2).

The symmetry argument is completely general, and thus applies to all types of  $M, X$ -centered defects in 2D TMDs with  $C_3$  symmetry, e.g., complex defect structures [32, 36], adatoms, and substitutional atoms [37]. As Eq. (1) is diagonal in spin space, it furthermore holds for intervalley spin-flip scattering by magnetic defects.

**FT-STs theory.**—Next, we outline a general  $T$ -matrix based Green's function approach for the calculation of the FT-STs spectra. In STs, the measured real-space QPI pattern is related to the differential conductance  $dI/dV \propto \rho(\mathbf{r}, \varepsilon)$  [47], and hence the LDOS  $\rho(\mathbf{r}, \varepsilon) = -1/\pi \text{Im}[G(\mathbf{r}, \mathbf{r}; \varepsilon)]$  where  $G(\mathbf{r}, \mathbf{r}'; \varepsilon) = \langle \mathbf{r} | \hat{G}(\varepsilon) | \mathbf{r}' \rangle$  is the Green's function (GF) in real-space in the presence of a defect. Expressing the GF in a basis of Bloch states  $\psi_{n\mathbf{k}}(\mathbf{r})$ ,  $G(\mathbf{r}, \mathbf{r}'; \varepsilon) = \sum_{mn} \sum_{\mathbf{k}\mathbf{k}'} \psi_{n\mathbf{k}'}^*(\mathbf{r}) \psi_{m\mathbf{k}}(\mathbf{r}') G_{\mathbf{k}\mathbf{k}'}^{mn}(\varepsilon)$ , where  $\mathbf{k}$  is the wave vector and  $m, n$  band indices, the FT-STs spectrum given by the 2D Fourier transform of  $\rho(\mathbf{r}, \varepsilon)$  can be obtained as [39]

$$\begin{aligned} \rho(\mathbf{q} + \mathbf{G}, \varepsilon) &= \int d\mathbf{r} e^{-i(\mathbf{q} + \mathbf{G}) \cdot \mathbf{r}} \rho(\mathbf{r}, \varepsilon) \\ &= \frac{1}{2\pi i} \sum_{mn, \mathbf{k}} n_{\mathbf{k}, \mathbf{q}}^{mn}(\mathbf{G}) [G_{\mathbf{k}, \mathbf{k} + \mathbf{q}}^{mn}(\varepsilon)^* - G_{\mathbf{k} + \mathbf{q}, \mathbf{k}}^{mn}(\varepsilon)], \end{aligned} \quad (3)$$

where  $\mathbf{r} = (\mathbf{r}_\parallel, z)$ ,  $\mathbf{k}, \mathbf{q} \in$  1st Brillouin zone (BZ),  $\mathbf{G}$  is a reciprocal lattice vector, and  $G_{\mathbf{k}\mathbf{k}'}^{mn}(\varepsilon) = \langle \psi_{m\mathbf{k}} | \hat{G}(\varepsilon) | \psi_{n\mathbf{k}'} \rangle$  is the Bloch function representation of the GF. The matrix element  $n_{\mathbf{k}, \mathbf{q}}^{mn}(\mathbf{G}) = \langle \psi_{m\mathbf{k}} | e^{-i(\mathbf{q} + \mathbf{G}) \cdot \hat{\mathbf{r}}_\parallel} | \psi_{n\mathbf{k} + \mathbf{q}} \rangle$  is important in many aspects. For example, it describes the FT-STs Bragg peaks ( $\mathbf{G} \neq \mathbf{0}$ ), and hence the atomic modulation of the LDOS inside the unit cell. It also plays a central role in systems with (pseudo) spin texture, e.g., graphene and spin-orbit materials, as it contains the spinor overlap [48]. This is less important in 2D TMDs where the eigenstates of Eq. (1) are characterized by predominantly polarized spinor states [49] with trivial pseudospin,  $\hat{\sigma}$ , and spin,  $\hat{s}$ , textures.

For a single defect, the *exact* GF taking into account multiple scattering off the defect is given by the  $T$  matrix as

$$\mathbf{G}_{\mathbf{k}\mathbf{k}'}(\varepsilon) = \delta_{\mathbf{k}, \mathbf{k}'} \mathbf{G}_{\mathbf{k}}^0(\varepsilon) + \mathbf{G}_{\mathbf{k}}^0(\varepsilon) \mathbf{T}_{\mathbf{k}\mathbf{k}'}(\varepsilon) \mathbf{G}_{\mathbf{k}'}^0(\varepsilon), \quad (4)$$

where the boldface symbols denote matrices in band and spin indices, and the diagonal *bare* GF is given by the band energies,  $G_{n\mathbf{k}}^0(\varepsilon) = (\varepsilon - \varepsilon_{n\mathbf{k}} + i\eta)^{-1}$ . The last term in Eq. (4) comprises the nondiagonal, defect-induced correction  $\delta \mathbf{G}_{\mathbf{k}, \mathbf{k} + \mathbf{q}}$  to the GF. To isolate the FT-STs features related to the defect, we substitute  $G \rightarrow \delta G$  in Eq. (3) in our FT-STs calculations.

The  $T$  matrix obeys the integral equation

$$\mathbf{T}_{\mathbf{k}\mathbf{k}'}(\varepsilon) = \mathbf{V}_{\mathbf{k}\mathbf{k}'}^i + \sum_{\mathbf{k}''} \mathbf{V}_{\mathbf{k}\mathbf{k}''}^i \mathbf{G}_{\mathbf{k}''}^0(\varepsilon) \mathbf{T}_{\mathbf{k}''\mathbf{k}'}(\varepsilon), \quad (5)$$

where  $V_{i,\mathbf{k}\mathbf{k}'}^{mn}$  are matrix elements of the defect potential and the second term describes virtual transitions to intermediate states with wave vector  $\mathbf{k}''$ .

For nonmagnetic defects, we take  $\hat{V}_i = V_i(\hat{\mathbf{r}}) \otimes \hat{s}_0$  where  $\hat{s}_0$  is the identity operator in spin space. With the spin indices written out explicitly, the defect matrix elements can be expressed as

$$\begin{aligned} V_{i,\mathbf{k}\mathbf{k}'}^{mn}(s, s') &= \langle m\mathbf{k}s | \hat{V}_i | n\mathbf{k}'s' \rangle \\ &= \sum_{s_z} \langle m\mathbf{k}s; s_z | V_i(\hat{\mathbf{r}}) | n\mathbf{k}'s'; s_z \rangle, \end{aligned} \quad (6)$$

with  $|\cdot; s_z\rangle$  denoting the  $s_z = \pm 1$  spinor component of the wave function. Here, we use a DFT method based on an atomic supercell model for the defect site illustrated in Fig. 1(b) to calculate the defect matrix elements [39].

As an example, Fig. 2 shows the spin-diagonal conduction-band matrix elements for Mo and S vacancies in 2D MoS<sub>2</sub>. While the Mo vacancy gives rise to intravalley (short arrow) and intervalley (long arrow) couplings, the intervalley matrix element for the S vacancy vanishes, thus confirming the symmetry-based predictions in Eq. (2). Furthermore, we note that the matrix element in the  $K, K'$  valleys is an order of magnitude larger for Mo than for S vacancies. In a simple picture where only  $K, K'$  intra- and intervalley scattering with a constant matrix element  $V_0$  is considered, the  $T$  matrix becomes  $T(\varepsilon) = V_0/[1 - gV_0\bar{G}_0(\varepsilon)]$ , where  $\bar{G}_0(\varepsilon) = \int \frac{d\mathbf{k}}{(2\pi)^2} G_{c\mathbf{k}}^0(\varepsilon) \propto \rho_c$ ,  $\rho_c \approx 0.01 \text{ eV}^{-1} \text{ \AA}^{-2}$  is the density of states, and the valley multiplication factor  $g = 2$  ( $= 1$ ) for  $M$  ( $X$ ; only intravalley scattering) vacancies. Together with the values for  $V_0$  extracted from Fig. 2, this allows us to identify  $M$  ( $g\rho_c V_0 > 1$ ) and  $X$  ( $g\rho_c V_0 < 1$ ) vacancies as *strong* (unitary),  $T(\varepsilon) \approx -1/g\bar{G}_0(\varepsilon)$ , and *weak*,  $T(\varepsilon) \approx V_0$ , defects, respectively.

The FT-STs calculations presented below are based on full BZ  $\mathbf{k}, \mathbf{q}$ -point samplings of the band structures, defect matrix elements, and  $n_{\mathbf{k},\mathbf{q}}^{mn}(\mathbf{G})$  matrix elements, all obtained with DFT-LDA including SO interaction [39]. Our approach naturally goes beyond the low-energy description in Eq. (1), which is essential as both the  $K$  and  $Q$  valleys are relevant for quasiparticle scattering in 2D TMDs. As intervalley scattering in the valence band is suppressed by (i) the large spin-valley coupling, and (ii) the  $C_3$  symmetry of the vacancies, the valence-band FT-STs spectra are rather simple [18, 19], and we here limit the discussion to the conduction band. We furthermore focus on features related to the symmetry-forbidden intervalley scattering deferring a complete analysis to a forthcoming paper.

**FT-STs and QPI spectra.**—The calculated band structures and FT-STs spectra for atomic vacancies in

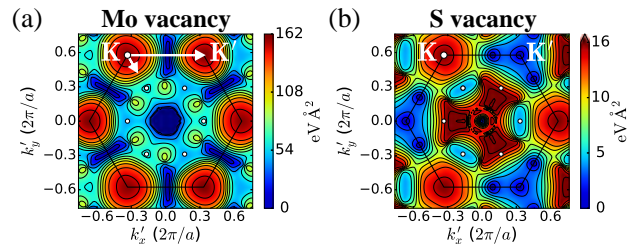


FIG. 2. Defect matrix elements for the conduction band in 2D MoS<sub>2</sub> calculated with our DFT-based supercell method. The plots show  $|V_{i,\mathbf{k}\mathbf{k}'}^{cc}(s, s)|$  for (a) a Mo, and (b) a S vacancy as a function of  $\mathbf{k}'$  with the initial state fixed to  $\mathbf{k} = \mathbf{K}$ . Note the different disorder strengths (colorbar scales) for the two types of vacancies as well as the vanishing intervalley matrix element [long arrow in (a)] for S vacancies.

MoS<sub>2</sub> and WSe<sub>2</sub> are summarized in Fig. 3. The different conduction-band structures in the two materials ( $K$  vs  $Q$  valley alignment and magnitude of the SO splitting) shown in the insets in Fig. 3(a) and the vacancy-dependent intervalley matrix element, result in markedly different spectra between the materials as well as the vacancy type.

In general, the FT-STs spectra close to the band edge ( $\varepsilon \approx 0$ ; see Ref. [39]) are characterized by featureless spots at the points in  $\mathbf{q}$  space corresponding to intravalley ( $\mathbf{q} = \mathbf{0}$ ) and intervalley scattering [ $\mathbf{q}_{1-5}$  in Fig. 3(b)]. The spot intensities are governed by the  $T$ -matrix scattering amplitude and valley degeneracy. For the Bragg peaks, the intensity is reduced compared to those in the first BZ due to the phase-factor matrix element  $n_{\mathbf{k},\mathbf{q}}^{mn}(\mathbf{G})$ .

In MoS<sub>2</sub> the SO splitting in the conduction band is small,  $\sim 3$  meV, thereby allowing for spin-conserving  $K \leftrightarrow K'$  intervalley scattering ( $\mathbf{q}_{1,2}$ ) near the band edge. Hence, intervalley peaks at  $\mathbf{q} = \mathbf{K}, \mathbf{K}'$  are to be expected. In WSe<sub>2</sub> the  $Q$  valley is lower than the  $K$  valley and the SO splitting is much larger ( $\sim 250$  meV in the  $Q$  valley and  $\sim 50$  meV the  $K$  valley), hence a  $\mathbf{q} \approx \mathbf{M}$  peak due to  $Q \leftrightarrow Q'$  intervalley processes ( $\mathbf{q}_3$ ) will appear instead.

The above is indeed the case in the FT-STs spectra for  $M$  vacancies shown in Fig. 3(c) for an energy  $\varepsilon = 75$  meV above the band edge [dashed lines in the insets in Fig. 3(a)]. At this energy, the spots have developed into features (see the zoomed insets) which are dominated by processes involving nesting vectors between parallel segments of the constant energy contour being probed. In MoS<sub>2</sub> with almost isotropic energy contours,  $\varepsilon(k) = \varepsilon$ , intravalley backscattering with  $q = 2k$  therefore produces circular features. Trigonal warping of the constant energy surfaces gives rise to additional approximate nesting vectors which produce starlike patterns with hexagonal symmetry around the  $\Gamma$  point and triangular symmetry near the  $K, K'$  points as in graphene [30]. The intervalley features are weaker than the intravalley

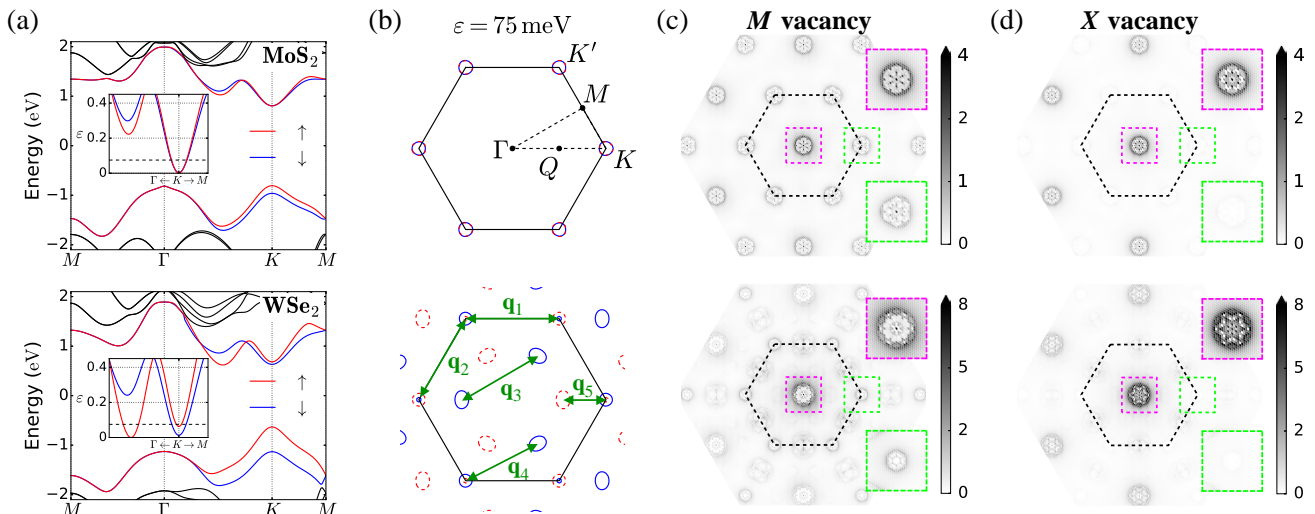


FIG. 3. Band structures and FT-STs spectra for atomic vacancies in MoS<sub>2</sub> (top) and WSe<sub>2</sub> (bottom). (a) Band structures including SO interaction. The insets show a zoom of the SO split conduction-band  $K, Q$  valleys with the energy  $\varepsilon = E - E_c$  measured relative to the band edge  $E_c$ . The dashed lines indicate the energy of the constant-energy surfaces in (b) and the FT-STs spectra in (c),(d). (b) Constant-energy surfaces in  $\mathbf{k}$  space for  $\varepsilon = 75$  meV, together with high-symmetry  $\mathbf{k}$  points in the Brillouin zone (top) and representative intervalley  $\mathbf{q}$  vectors (bottom). (c), (d) FT-STs spectra at  $\varepsilon = 75$  meV for (c)  $M = \text{Mo}, \text{W}$  and (d)  $X = \text{S}, \text{Se}$  vacancies. The boxes show zooms of the marked regions.

feature because intravalley processes in the  $K$  and  $K'$  valleys add up, while the two  $K \leftrightarrow K'$  intervalley processes have distinct wave vectors,  $\mathbf{q} \approx \pm \mathbf{K}$ . In WSe<sub>2</sub>, both the  $Q$  and  $K$  valleys are accessible at  $\varepsilon = 75$  meV, and therefore intervalley features around  $\mathbf{q} \approx \mathbf{M}$ ,  $\mathbf{q} \approx \mathbf{K}$  as well as  $\mathbf{q} \approx \mathbf{Q}$  are observed. They are associated with  $Q \leftrightarrow Q/K \leftrightarrow Q$  ( $\mathbf{q}_{3/4}$ ),  $K \leftrightarrow K'$  ( $\mathbf{q}_{1,2}$ ), and  $K \leftrightarrow Q$  ( $\mathbf{q}_5$ ) processes, respectively. The central intravalley feature in WSe<sub>2</sub> has more structure than in MoS<sub>2</sub> as it has contributions from both  $K$  and  $Q$  intravalley processes.

At even higher energies (not shown), the  $K$  and  $Q$  valleys are available in both MoS<sub>2</sub> and WSe<sub>2</sub>, and the FT-STs spectra become highly complex.

In contrast to the FT-STs spectra for  $M$  vacancies, the

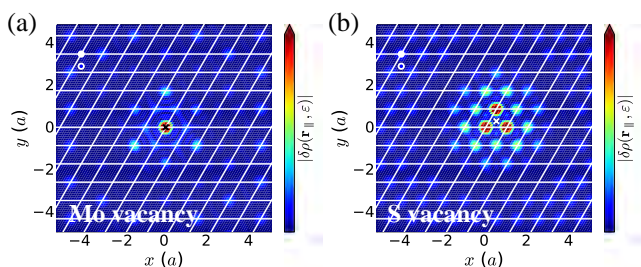


FIG. 4. Real-space QPI maps for 2D MoS<sub>2</sub> showing the defect-induced change in the LDOS  $\delta\rho(\mathbf{r}_{\parallel}, \varepsilon)$  around (a) a Mo, and (b) a S vacancy. The lines show the unit cells of the lattice with lattice constant  $a$ , and the atomic positions inside the unit cell and the position of the vacancy are indicated by the symbols (solid circle: Mo; open circle: S; cross: vacancy).

spectra for  $X$  vacancies in Fig. 3(d) show that the anticipated intervalley feature at  $\mathbf{q} \approx \mathbf{K}$  ( $\mathbf{q}_{1,2}$ ) is strongly suppressed for both MoS<sub>2</sub> and WSe<sub>2</sub>. This is a direct consequence of the symmetry-forbidden  $K \leftrightarrow K'$  intervalley matrix element which suppresses intervalley scattering also in the vicinity of the high-symmetry  $K, K'$  points [see Fig. 2(b)]. In WSe<sub>2</sub>, also the  $Q \leftrightarrow Q'$  ( $\mathbf{q}_3$ ) and  $Q \leftrightarrow K$  ( $\mathbf{q}_{4,5}$ ) intervalley features are much weaker for  $X$  vacancies, which can be traced back to overall small intervalley matrix elements.

The suppression of  $K \leftrightarrow K'$  intervalley scattering for  $X$  vacancies leaves a clear fingerprint in the real-space LDOS as demonstrated by the QPI maps in Fig. 4 for Mo and S vacancies in MoS<sub>2</sub>. They have been obtained by Fourier transforming the FT-STs spectra in Figs. 3(c) and 3(d),  $\rho(\mathbf{r}_{\parallel}, \varepsilon) = \sum_{\mathbf{G}} \int \frac{d\mathbf{q}}{(2\pi)^2} e^{i(\mathbf{q}+\mathbf{G})\cdot\mathbf{r}_{\parallel}} \rho(\mathbf{q}+\mathbf{G}, \varepsilon)$ . For both vacancies, the LDOS modulation has a threefold symmetry and decays away the vacancy site (marked by crosses). The observed atomic resolution can be attributed to the FT-STs Bragg peaks, and shows that the LDOS modulation is concentrated on the Mo sites of the lattice, in accordance with the Mo  $d$ -orbital character of the conduction-band states in the  $K, K'$  valleys [cf. Eq. (1)]. Noticeably, the QPI map for the S vacancy stands out by the absence of an intervalley-scattering-induced cell-to-cell modulation of the LDOS in the vicinity of the vacancy, which is clearly visible for the Mo vacancy. At larger distances from the vacancy site, a slower modulation with wave length  $2\pi/q$  ( $\approx 10a$  at  $\varepsilon = 75$  meV) due to intravalley backscattering,  $q = 2k$ , emerges.

**Conclusions and outlook.**—In conclusion, we have demonstrated (i) an unconventional symmetry-induced protection against intervalley scattering by atomic defects in 2D TMDs, and (ii) its fingerprint in conduction-band FT-STs spectra which allows for a unique identification of, e.g., the vacancy type. Our findings may offer an explanation why the  $K \leftrightarrow K'$  intervalley FT-STs peak has not been observed in experiments [18, 19], and are also relevant for FT-STs on metallic TMDs [50].

We are convinced that our work in conjunction with further experimental FT-STs studies can provide a complete understanding of defect scattering in 2D TMDs. In addition, FT-STs may shed important light on band-structure issues in 2D TMDs, such as the magnitude of SO splittings [18], the  $K, Q$ -valley ordering in the conduction band which is sensitive to the SO strength [13, 14], and the subband structure and valley ordering in few-layer TMDs [51, 52]. Besides our reported FT-STs signatures, the suppression of intervalley scattering is expected to have implications for a wide range of effects in disordered 2D TMDs, e.g., the optical conductivity [53], magnetotransport [54–58], the valley Hall effect [59], Elliot-Yafet spin relaxation [60], and disorder-induced valley pumping [61].

**Acknowledgements.**—We would like to thank an anonymous reviewer on a related work [62] for suggesting we investigate observable implications of our symmetry finding for intervalley scattering. K.K. acknowledges support from the European Union’s Horizon 2020 research and innovation programme under the Marie Skłodowska-Curie Grant Agreement No. 713683 (COFUNDfellows-DTU). T.L. acknowledges support from the National Science Foundation under Grant No. NSF/EFRI-1741660. The Center for Nanostructured Graphene (CNG) is sponsored by the Danish National Research Foundation, Project No. DNRFF103.

---

\* kkaa@nanotech.dtu.dk

- [1] X. Xu, W. Yao, D. Xiao, and T. F. Heinz, “Spin and pseudospins in layered transition metal dichalcogenides,” *Nature Phys.* **10**, 343 (2014).
- [2] D. Xiao, G.-B. Liu, W. Feng, X. Xu, and W. Yao, “Coupled spin and valley physics in monolayers of MoS<sub>2</sub> and other group-VI dichalcogenides,” *Phys. Rev. Lett.* **108**, 196802 (2012).
- [3] K. F. Mak, K. He, J. Shan, and T. F. Heinz, “Control of valley polarization in monolayer MoS<sub>2</sub> by optical helicity,” *Nature Nanotechnol.* **7**, 494 (2012).
- [4] H. Zeng, J. Dai, W. Yao, D. Xiao, and X. Cui, “Valley polarization in MoS<sub>2</sub> monolayers by optical pumping,” *Nature Nanotechnol.* **7**, 490 (2012).
- [5] T. Cao, G. Wang, W. Han, H. Ye, C. Zhu, J. Shi, Q. Niu, P. Tan, E. Wang, B. Liu, and J. Feng, “Valley-selective circular dichroism of monolayer molybdenum disulfide,” *Nature Commun.* **3**, 887 (2012).
- [6] A. Srivastava, M. Sidler, A. V. Allain, D. S. Lembke, A. Kis, and A. Imamoglu, “Valley Zeeman effect in elementary optical excitations of monolayer WSe<sub>2</sub>,” *Nature Phys.* **11**, 141 (2014).
- [7] G. Aivazian, Z. Gong, A. M. Jones, R.-L. Chu, J. Yan, D. G. Mandrus, C. Zhang, D. Cobden, W. Yao, and X. Xu, “Magnetic control of valley pseudospin in monolayer WSe<sub>2</sub>,” *Nature Phys.* **11**, 148 (2014).
- [8] Y. Li, J. Ludwig, T. Low, A. Chernikov, X. Cui, G. Arefe, Y. D. Kim, A. M. van der Zande, A. Rigosi, H. M. Hill, S. H. Kim, J. Hone, Z. Li, D. Smirnov, and T. F. Heinz, “Valley splitting and polarization by the Zeeman effect in monolayer MoSe<sub>2</sub>,” *Phys. Rev. Lett.* **113**, 266804 (2014).
- [9] D. MacNeill, C. Heikes, K. F. Mak, Z. Anderson, A. Kormányos, V. Zolyomi, J. Park, and D. C. Ralph, “Breaking of valley degeneracy by magnetic field in monolayer MoSe<sub>2</sub>,” *Phys. Rev. Lett.* **114**, 037401 (2015).
- [10] K. F. Mak, K. L. McGill, J. Park, and P. L. McEuen, “The valley Hall effect in MoS<sub>2</sub> transistors,” *Science* **344**, 1489 (2014).
- [11] L. Yang, N. A. Sinitsyn, W. Chen, J. Yuan, J. Zhang, J. Lou, and S. A. Crooker, “Long-lived nanosecond spin relaxation and spin coherence of electrons in monolayer MoS<sub>2</sub> and WS<sub>2</sub>,” *Nature Phys.* **11**, 830 (2015).
- [12] T. Yan, S. Yang, D. Li, and X. Cui, “Long valley relaxation time of free carriers in monolayer WSe<sub>2</sub>,” *Phys. Rev. B* **95**, 241406(R) (2017).
- [13] Z. Y. Zhu, Y. C. Cheng, and U. Schwingenschlöggl, “Giant spin-orbit-induced spin splitting in two-dimensional transition-metal dichalcogenide semiconductors,” *Phys. Rev. B* **84**, 153402 (2011).
- [14] K. Kosmider, J. W. González, and J. Fernández-Rossier, “Large spin splitting in the conduction band of transition metal dichalcogenide monolayers,” *Phys. Rev. B* **88**, 245436 (2013).
- [15] G.-B. Liu, H. Pang, Y. Yao, and W. Yao, “Intervalley coupling by quantum dot confinement potentials in monolayer transition metal dichalcogenides,” *New J. Phys.* **16**, 105011 (2014).
- [16] C.-P. Lu, G. Li, J. Mao, L.-M. Wang, and E. Y. Andrei, “Bandgap, mid-gap states, and gating effects in MoS<sub>2</sub>,” *Nano. Lett.* **14**, 4628 (2014).
- [17] C. Zhang, Y. Chen, A. Johnson, M.-Y. Li, L.-J. Li, P. C. Mendell, R. M. Feenstra, and C.-K. Shih, “Probing critical point energies of transition metal dichalcogenides: Surprising indirect gap of single layer WSe<sub>2</sub>,” *Nano. Lett.* **15**, 6494 (2015).
- [18] H. Liu, J. Chen, H. Yu, F. Yang, L. Jiao, G.-B. Liu, W. Ho, C. Gao, J. Jia, W. Yao, and M. Xie, “Observation of intervalley quantum interference in epitaxial monolayer tungsten diselenide,” *Nature Commun.* **6**, 8180 (2015).
- [19] M. Yankowitz, D. McKenzie, and B. J. LeRoy, “Local spectroscopic characterization of spin and layer polarization in WSe<sub>2</sub>,” *Phys. Rev. Lett.* **115**, 136803 (2015).
- [20] X. Zhou, K. Kang, S. Xie, A. Dadgar, N. R. Monahan, X.-Y. Zhu, J. Park, and A. N. Pasupathy, “Atomic-scale spectroscopy of gated monolayer MoS<sub>2</sub>,” *Nano. Lett.* **16**, 3148 (2016).
- [21] L. Simon, C. Bena, F. Vonau, M. Cranney, and D. Aubel, “Fourier transform scanning tunneling spectroscopy: The possibility to obtain constant energy maps and the band dispersion using a local measurement,” *J. Phys. D* **44**, 464010 (2011).

- [22] L. Chen, P. Cheng, and K. Wu, “Quasiparticle interference in unconventional 2D systems,” *J. Phys.: Condens. Matter* **29**, 103001 (2017).
- [23] G. M. Rutter, J. N. Crain, N. P. Guisinger, T. Li, P. N. First, and J. A. Stroscio, “Scattering and interference in epitaxial graphene,” *Science* **317**, 219 (2007).
- [24] P. Mallet, F. Varchon, C. Naud, L. Magaud, C. Berger, and J.-Y. Veuillen, “Electron states of mono- and bilayer graphene on SiC probed by scanning-tunneling microscopy,” *Phys. Rev. B* **76**, 041403(R) (2007).
- [25] C. Bena, “Effect of a single localized impurity on the local density of states in monolayer and bilayer graphene,” *Phys. Rev. Lett.* **100**, 076601 (2008).
- [26] I. Brihuega, P. Mallet, C. Bena, S. Bose, C. Michaelis, L. Vitali, F. Varchon, L. Magaud, K. Kern, and J.-Y. Veuillen, “Quasiparticle chirality in epitaxial graphene probed at the nanometer scale,” *Phys. Rev. Lett.* **101**, 206802 (2008).
- [27] T. Pereg-Barnea and A. H. MacDonald, “Chiral quasiparticle local density of states maps in graphene,” *Phys. Rev. B* **78**, 014201 (2008).
- [28] P. Mallet, I. Brihuega, S. Bose, M. M. Ugeda, J. M. Gómez-Rodríguez, K. Kern, and J.-Y. Veuillen, “Role of pseudospin in quasiparticle interferences in epitaxial graphene probed by high-resolution scanning tunneling microscopy,” *Phys. Rev. B* **86**, 045444 (2012).
- [29] M. Settnes, S. R. Power, D. H. Petersen, and A.-P. Jauho, “Theoretical analysis of a dual-probe scanning tunneling microscope setup on graphene,” *Phys. Rev. Lett.* **112**, 096801 (2014).
- [30] D. Dombrowski, W. Jolie, M. Petrović, S. Runte, F. Craes, J. Klinkhammer, M. Kralj, P. Lazić, E. Sela, and C. Busse, “Energy-dependent chirality effects in quasifree-standing graphene,” *Phys. Rev. Lett.* **118**, 116401 (2017).
- [31] B. Kiraly, N. Hauptmann, A. N. Rudenko, M. I. Katsnelson, and A. A. Khajetoorians, “Probing single vacancies in black phosphorus at the atomic level,” *Nano. Lett.* **17**, 3607 (2017).
- [32] W. Zhou, X. Zou, S. Najmaei, Z. Liu, Y. Shi, J. Kong, J. Lou, P. M. Ajayan, B. I. Yakobson, and J.-C. Idrobo, “Intrinsic structural defects in monolayer molybdenum disulfide,” *Nano. Lett.* **13**, 2615 (2013).
- [33] B. W. H. Baugher, H. O. H. Churchill, Y. Yang, and P. Jarillo-Herrero, “Intrinsic electronic transport properties of high-quality monolayer and bilayer MoS<sub>2</sub>,” *Nano. Lett.* **13**, 4212 (2013).
- [34] H. Schmidt, S. Wang, L. Chu, M. Toh, R. Kumar, W. Zhao, A. H. Castro Neto, J. Martin, S. Adam, B. Özyilmaz, and G. Eda, “Transport properties of monolayer MoS<sub>2</sub> grown by chemical vapor deposition,” *Nano. Lett.* **14**, 1909 (2014).
- [35] Z. Yu, Y. Pan, Y. Shen, Z. Wang, Z.-Y. Ong, T. Xu, R. Xin, L. Pan, B. Wang, L. Sun, J. Wang, G. Zhang, Y. W. Zhang, Y. Shi, and X. Wang, “Towards intrinsic charge transport in monolayer molybdenum disulfide by defect and interface engineering,” *Nature Commun.* **5**, 5290 (2014).
- [36] Y.-C. Lin, T. Björkman, H.-P. Komsa, P.-Y. Teng, C.-H. Yeh, F.-S. Huang, K.-H. Lin, J. Jadczyk, Y.-S. Huang, P.-W. Chiu, A. V. Krasheninnikov, and K. Suenaga, “Three-fold rotational defects in two-dimensional transition metal dichalcogenides,” *Nature Commun.* **6**, 6736 (2014).
- [37] J. Hong, Z. Hu, M. Probert, K. Li, D. Lv, X. Yang, L. Gu, N. Mao, Q. Feng, L. Xie, J. Zhang, D. Wu, Z. Zhang, C. Jin, W. Ji, X. Zhang, J. Yuan, and Z. Zhang, “Exploring atomic defects in molybdenum disulphide monolayers,” *Nature Commun.* **6**, 6293 (2015).
- [38] S. Zhang, C.-G. Wang, M.-Y. Li, D. Huang, L.-J. Li, W. Ji, and S. Wu, “Defect structure of localized excitons in a WSe<sub>2</sub> monolayer,” *Phys. Rev. Lett.* **119**, 046101 (2017).
- [39] See Supplemental Material for details on (i) the derivation of Eq. (3), (ii) the DFT-based calculations of the FT-STs spectra and the involved quantities, (iii) additional FT-STs spectra at the band edge, and (iv) the symmetry analysis of the defect matrix elements, which includes Refs. [40–43].
- [40] J. J. Mortensen, L. B. Hansen, and K. W. Jacobsen, “Real-space grid implementation of the projector augmented wave method,” *Phys. Rev. B* **71**, 035109 (2005).
- [41] A. H. Larsen, M. Vanin, J. J. Mortensen, K. S. Thygesen, and K. W. Jacobsen, “Localized atomic basis set in the projector augmented wave method,” *Phys. Rev. B* **80**, 195112 (2009).
- [42] J. Enkovaara *et al.*, “Electronic structure calculations with GPAW: a real-space implementation of the projector augmented-wave method,” *J. Phys.: Condens. Matter* **22**, 253202 (2010).
- [43] T. Olsen, “Designing in-plane heterostructures of quantum spin Hall insulators from first principles: 1T'-MoS<sub>2</sub> with adsorbates,” *Phys. Rev. B* **94**, 235106 (2016).
- [44] K. F. Mak, C. Lee, J. Hone, J. Shan, and T. F. Heinz, “Atomically thin MoS<sub>2</sub>: A new direct-gap semiconductor,” *Phys. Rev. Lett.* **105**, 136805 (2010).
- [45] E. Cappelluti, R. Roldán, J. A. Silva-Guillén, P. Ordejón, and F. Guinea, “Tight-binding model and direct-gap/indirect-gap transition in single-layer and multilayer MoS<sub>2</sub>,” *Phys. Rev. B* **88**, 075409 (2013).
- [46] G.-B. Liu, W.-Y. Shan, Y. Yao, W. Yao, and D. Xiao, “Three-band tight-binding model for monolayers of group-VIB transition metal dichalcogenides,” *Phys. Rev. B* **88**, 085433 (2013).
- [47] G. A. Fiete and E. J. Heller, “Colloquium: Theory of quantum corrals and quantum mirages,” *Rev. Mod. Phys.* **75**, 933 (2003).
- [48] Y. Kohsaka, T. Machida, K. Iwaya, M. Kanou, T. Hanaguri, and T. Sasagawa, “Spin-orbit scattering visualized in quasiparticle interference,” *Phys. Rev. B* **95**, 115307 (2017).
- [49] W.-Y. Shan, H.-Z. Lu, and D. Xiao, “Spin Hall effect in spin-valley coupled monolayers of transition metal dichalcogenides,” *Phys. Rev. B* **88**, 125301 (2013).
- [50] T. Machida, Y. Kohsaka, K. Iwaya, R. Arita, T. Hanaguri, R. Suzuki, M. Ochi, and Y. Iwasa, “Orbital-dependent quasiparticle scattering interference in 3R-NbS<sub>2</sub>,” *Phys. Rev. B* **96**, 075206 (2017).
- [51] R. Roldán, J. A. Silva-Guillén, M. P. López-Sancho, F. Guinea, E. Cappelluti, and P. Ordejón, “Electronic properties of single-layer and multilayer transition metal dichalcogenides MX<sub>2</sub> (M=Mo,W and X=S,Se),” *Annalen der Physik* **526**, 347 (2014).
- [52] A. M. Jones, H. Yu, J. S. Ross, P. Klement, N. J. Ghimire, J. Yan, D. G. Mandrus, W. Yao, and X. Xu, “Spin-layer locking effects in optical orientation of exciton spin in bilayer WSe<sub>2</sub>,” *Nature Phys.* **10**, 130 (2014).
- [53] S. Yuan, R. Roldán, M. I. Katsnelson, and F. Guinea,

- “Effect of point defects on the optical and transport properties of MoS<sub>2</sub> and WS<sub>2</sub>,” *Phys. Rev. B* **90**, 041402 (2014).
- [54] H.-Z. Lu, W. Yao, D. Xiao, and S.-Q. Shen, “Intervalley scattering and localization behaviors of spin-valley coupled Dirac fermions,” *Phys. Rev. Lett.* **110**, 016806 (2013).
- [55] H. Ochoa, F. Finocchiaro, F. Guinea, and V. I. Fal’ko, “Spin-valley relaxation and quantum transport regimes in two-dimensional transition-metal dichalcogenides,” *Phys. Rev. B* **90**, 235429 (2014).
- [56] A. Kormányos, P. Rakyta, and G. Burkard, “Landau levels and Shubnikov-de Haas oscillations in monolayer transition metal dichalcogenide semiconductors,” *New J. Phys.* **17**, 103006 (2015).
- [57] H. Schmidt, I. Yudhistira, L. Chu, A. H. Castro Neto, B. Özyilmaz, S. Adam, and G. Eda, “Quantum transport and observation of Dyakonov-Perel spin-orbit scattering in monolayer MoS<sub>2</sub>,” *Phys. Rev. Lett.* **116**, 046803 (2016).
- [58] B. Fallahazad, H. C. P. Movva, K. Kim, S. Larentis, T. Taniguchi, K. Watanabe, S. K. Banerjee, and E. Tutuc, “Shubnikov-de Haas oscillations of high mobility holes in monolayer and bilayer WSe<sub>2</sub>: Landau level degeneracy, effective mass, and negative compressibility,” *Phys. Rev. Lett.* **116**, 086601 (2016).
- [59] T. Olsen and I. Souza, “Valley Hall effect in disordered monolayer MoS<sub>2</sub> from first principles,” *Phys. Rev. B* **92**, 125146 (2015).
- [60] H. Ochoa and R. Roldán, “Spin-orbit-mediated spin relaxation in monolayer MoS<sub>2</sub>,” *Phys. Rev. B* **87**, 245421 (2013).
- [61] X.-T. An, J. Xiao, M. W.-Y. Tu, H. Yu, V. I. Fal’ko, and W. Yao, “Realization of valley and spin pumps by scattering at nonmagnetic disorders,” *Phys. Rev. Lett.* **118**, 096602 (2017).
- [62] K. Kaasbjerg, T. Low, and A.-P. Jauho, (2017), arXiv:1612.00469.

# Supplemental material for “Symmetry-forbidden intervalley scattering by defects in monolayer transition-metal dichalcogenides”

Kristen Kaasbjerg,<sup>1,\*</sup> Johannes H. J. Martiny,<sup>1</sup> Tony Low,<sup>2</sup> and Antti-Pekka Jauho<sup>1</sup>

<sup>1</sup>Center for Nanostructured Graphene (CNG), Dept. of Micro- and Nanotechnology, Technical University of Denmark, DK-2800 Kongens Lyngby, Denmark

<sup>2</sup>Department of Electrical and Computer Engineering, University of Minnesota, Minneapolis, MN 55455, USA

(Dated: December 4, 2017)

## S1. THEORETICAL FT-STTS CALCULATIONS

Under the assumption that the density of states of the STM tip varies slowly with energy, the  $dI/dV$  characteristics at position  $\mathbf{r}$  and voltage  $eV = \varepsilon$  is proportional to the local density of states  $\rho(\mathbf{r}, \varepsilon)$  of the sample<sup>1</sup>,

$$\frac{dI(\mathbf{r}, \varepsilon)}{dV} \propto \rho(\mathbf{r}, \varepsilon) = -\frac{1}{2\pi i} [G(\mathbf{r}, \mathbf{r}; \varepsilon) - G^*(\mathbf{r}, \mathbf{r}; \varepsilon)], \quad (\text{S1})$$

where  $G(\mathbf{r}, \mathbf{r}'; \varepsilon) = \langle \mathbf{r} | \hat{G}(\varepsilon) | \mathbf{r}' \rangle$ ,  $\hat{G}(\varepsilon) = [\varepsilon - \hat{H} + i\eta]^{-1}$ , is the real-space Green’s function (GF) for a defect in the 2D material.

For a numerical evaluation of the FT-STTS spectrum, it is convenient to express the GF in terms of Bloch states  $\psi_{m\mathbf{k}}$  of the pristine lattice. By inserting the identity  $I = \sum_{m\mathbf{k}} |\psi_{m\mathbf{k}}\rangle \langle \psi_{m\mathbf{k}}|$ , the GF can be written as

$$\begin{aligned} G(\mathbf{r}, \mathbf{r}'; \varepsilon) &= \langle \mathbf{r} | \hat{G}(\varepsilon) | \mathbf{r}' \rangle = \sum_{mn} \sum_{\mathbf{k}\mathbf{k}'} \langle \mathbf{r} | \psi_{m\mathbf{k}} \rangle \langle \psi_{m\mathbf{k}} | \hat{G}(\varepsilon) | \psi_{n\mathbf{k}'} \rangle \langle \psi_{n\mathbf{k}'} | \mathbf{r}' \rangle \\ &= \sum_{mn} \sum_{\mathbf{k}\mathbf{k}'} \psi_{m\mathbf{k}}(\mathbf{r}) \psi_{n\mathbf{k}'}^*(\mathbf{r}') G_{\mathbf{k}\mathbf{k}'}^{mn}(\varepsilon), \end{aligned} \quad (\text{S2})$$

where  $G_{\mathbf{k}\mathbf{k}'}^{mn}(\varepsilon) = \langle \psi_{m\mathbf{k}} | \hat{G}(\varepsilon) | \psi_{n\mathbf{k}'} \rangle$  is its Bloch function representation and the  $\mathbf{k}, \mathbf{k}'$  sums are over the first Brillouin zone (BZ), here sampled with a discrete, equidistant  $N_k \times N_k$   $\mathbf{k}$ -point grid as illustrated in Fig. S1.

The FT-STTS spectrum is given by the 2D Fourier transform (FT) of the LDOS in Eq. (S1). Here, we consider the  $z$ -integrated LDOS, which is a reasonable approach for 2D materials. Plugging in the Bloch function expansion of the GF and setting  $\mathbf{r} = (\mathbf{r}_{\parallel}, z)$  where  $\mathbf{r}_{\parallel}$  is the inplane component of the position, the  $z$ -integrated FT becomes

$$\begin{aligned} \rho(\mathbf{q} + \mathbf{G}, \varepsilon) &= \int d\mathbf{r} e^{-i(\mathbf{q} + \mathbf{G}) \cdot \mathbf{r}_{\parallel}} \rho(\mathbf{r}, \varepsilon) \\ &= -\frac{1}{2\pi i} \int d\mathbf{r} e^{-i(\mathbf{q} + \mathbf{G}) \cdot \mathbf{r}_{\parallel}} [G(\mathbf{r}, \mathbf{r}; \varepsilon) - G^*(\mathbf{r}, \mathbf{r}; \varepsilon)] \\ &= -\frac{1}{2\pi i} \sum_{mn} \sum_{\mathbf{k}\mathbf{k}'} \underbrace{\int d\mathbf{r} \psi_{m\mathbf{k}}^*(\mathbf{r}) e^{-i(\mathbf{q} + \mathbf{G}) \cdot \mathbf{r}_{\parallel}} \psi_{n\mathbf{k}'}(\mathbf{r}')}_{\delta_{\mathbf{k}', \mathbf{k} + \mathbf{q}} n_{\mathbf{k}, \mathbf{q}}^{mn}(\mathbf{G})} [G_{\mathbf{k}', \mathbf{k}}^{mn}(\varepsilon) - G_{\mathbf{k}, \mathbf{k}'}^{mn}(\varepsilon)^*] \\ &= \frac{1}{2\pi i} \sum_{mn} \sum_{\mathbf{k}} n_{\mathbf{k}, \mathbf{q}}^{mn}(\mathbf{G}) \times [G_{\mathbf{k}, \mathbf{k} + \mathbf{q}}^{mn}(\varepsilon)^* - G_{\mathbf{k} + \mathbf{q}, \mathbf{k}}^{mn}(\varepsilon)], \end{aligned} \quad (\text{S3})$$

where  $\mathbf{q} \in 1. \text{BZ}$ ,  $\mathbf{G}$  is a reciprocal lattice vector, and  $n_{\mathbf{k}, \mathbf{q}}^{mn}(\mathbf{G}) = \langle \psi_{m\mathbf{k}} | e^{-i(\mathbf{q} + \mathbf{G}) \cdot \hat{\mathbf{r}}_{\parallel}} | \psi_{n\mathbf{k} + \mathbf{q}} \rangle = \langle u_{m\mathbf{k}} | e^{-i\mathbf{G} \cdot \hat{\mathbf{r}}_{\parallel}} | u_{n\mathbf{k} + \mathbf{q}} \rangle$ , where  $u_{m\mathbf{k}}$  is the periodic part of the Bloch functions, is a phase-factor matrix element. The latter is important in both technical and practical aspects. In numerical calculations, it cancels the arbitrary phase on the wave functions in  $G_{\mathbf{k}\mathbf{k}'}^{mn}(\varepsilon)$ , thus leaving the expression (S3) gauge invariant as it should be. In the FT-STTS spectra, it may affect the structure of the intra- and intervalley features, and is the reason that the Bragg peaks,  $\mathbf{G} \neq \mathbf{0}$ , in general, must be expected to differ from the corresponding  $\mathbf{G} = \mathbf{0}$  peaks inside the first BZ.

All results presented in the main manuscript are based on the general expression for the FT-STTS spectrum in Eq. (S3). However, we note that simpler variants which follow from this general expression are often encountered in the literature. For example, if we disregarding the reciprocal lattice vector and assume that the periodic parts of the Bloch functions are orthogonal, i.e.  $\langle u_{m\mathbf{k}} | u_{n\mathbf{k} + \mathbf{q}} \rangle = \delta_{mn}$ , the expression reduces to

$$\rho(\mathbf{q}, \varepsilon) \approx \frac{1}{2\pi i} \sum_{\mathbf{k}} \text{Tr} [\mathbf{G}_{\mathbf{k}, \mathbf{k} + \mathbf{q}}(\varepsilon)^* - \mathbf{G}_{\mathbf{k} + \mathbf{q}, \mathbf{k}}(\varepsilon)]. \quad (\text{S4})$$

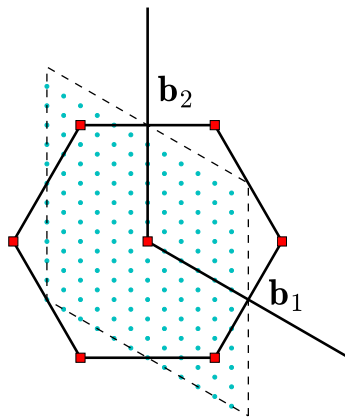


FIG. S1. Equidistant  $N_k \times N_k$  grid used for the  $\mathbf{k}, \mathbf{q}$ -point samplings of the rhombic BZ in the numerical calculation of the defect GF and the FT-STs spectra. The plot shows a  $12 \times 12$  BZ grid while a  $75 \times 75$  grid was used in the actual calculations presented in this work.

Depending on the approximation used for the defect GF, e.g., the Born approximation, this may be simplified further. Note that since  $\rho(\mathbf{r})$  is real-valued, it follows that  $\rho(\mathbf{q}) = \rho^*(-\mathbf{q})$  regardless of the approximation used for the defect GF.

### A. Single-defect Green's function

For the single-defect problem, the *exact* GF can be expressed in terms of the  $T$  matrix as

$$\mathbf{G}_{\mathbf{k}\mathbf{k}'}(\varepsilon) = \delta_{\mathbf{k},\mathbf{k}'}\mathbf{G}_{\mathbf{k}}^0(\varepsilon) + \mathbf{G}_{\mathbf{k}}^0(\varepsilon)\mathbf{T}_{\mathbf{k}\mathbf{k}'}(\varepsilon)\mathbf{G}_{\mathbf{k}'}^0(\varepsilon), \quad (\text{S5})$$

where the boldface symbols denote matrices in the band ( $n$ ) and spin  $s_z$  indices,  $\mathbf{k}$  is the electronic wave vector, the matrix  $\mathbf{G}^0$  for the *bare* Green's function is diagonal with elements  $G_{n\mathbf{k}}^0(\varepsilon) = (\varepsilon - \varepsilon_{n\mathbf{k}} + i\eta)^{-1}$ , and the  $\mathbf{k}''$  sum is over the BZ. Note that the sum rule  $\int d\varepsilon \rho(\varepsilon) = N_{\mathbf{k}} \times N_b$ , where  $\rho(\varepsilon) = -1/\pi \sum_{\mathbf{k}} \text{Tr}[\text{Im} \mathbf{G}_{\mathbf{k}\mathbf{k}}(\varepsilon)]$ ,  $N_{\mathbf{k}} = N_k \times N_k$  is the number of  $\mathbf{k}$  points and  $N_b$  is the number of bands, is fulfilled by the bare GF alone, and hence the trace of the correction to the GF in the second term must integrate to zero.

The  $T$  matrix describes multiple scattering off a single defect and is given by,

$$\mathbf{T}_{\mathbf{k}\mathbf{k}'}(\varepsilon) = \mathbf{V}_{\mathbf{k}\mathbf{k}'} + \sum_{\mathbf{k}''} \mathbf{V}_{\mathbf{k}\mathbf{k}''}\mathbf{G}_{\mathbf{k}''}^0(\varepsilon)\mathbf{T}_{\mathbf{k}''\mathbf{k}'}(\varepsilon). \quad (\text{S6})$$

The defect matrix elements  $\mathbf{V}_{\mathbf{k}\mathbf{k}'}$  are given by the matrix elements of the defect-induced scattering potential with respect to the Bloch functions of the pristine lattice (see below). Note that in contrast to  $\mathbf{V}_{\mathbf{k}\mathbf{k}'}$ , the  $T$  matrix is, in general, not hermitian.

#### 1. Numerical details

To solve for the  $T$  matrix in Eq. (S6), we recast it as a matrix equation,

$$[\mathbf{I} - \mathbf{V}\mathbf{G}_0(\varepsilon)]\mathbf{T}(\varepsilon) = \mathbf{V}, \quad (\text{S7})$$

where the boldface symbols now denote matrices in the band, spin and  $\mathbf{k}$ -vector indices, and the Green's function matrix  $\mathbf{G}_0$  is diagonal. Rather than solving this equation by direct inversion of the matrix  $[\mathbf{I} - \mathbf{V}\mathbf{G}_0(\varepsilon)]$ , it is numerically more stable and accurate to regard it as a system of coupled linear equation (one set of coupled equations for each column in  $\mathbf{T}$  and  $\mathbf{V}$ ) and solve it with a standard linear solver. This requires one factorization followed by a matrix-vector multiplications and scales as  $O(M^3)$  where  $M$  denotes the matrix dimension.

The calculations presented in the main manuscript are based on  $75 \times 75$   $\mathbf{k}$ -point samplings of the BZ and include the six lowest spin-orbit split conduction bands. This amounts to a matrix dimension of  $M = 6 \times 75^2 = 33750$ . With the matrix elements represented as 128-bit complex floating-point numbers, the memory requirement for each of the dense complex matrices in Eq. (S7) becomes  $33750^2 \times 128/8 \text{ bytes} \approx 17 \text{ GBs}$ . To tackle the large matrix dimensions and memory requirements in the solution of the matrix equation (S7), we exploit the automatic openMP multithreading of the LAPACK linear solvers and run the calculations as serial jobs on a multicore platform setting `OMP_NUM_THREADS=$NPROCS` where `NPROCS` specifies the number of CPUs to be used for multithreading.

## B. Details of the atomistic DFT calculations

All the quantities entering the calculation of the defect GF and the FT-STs spectra, i.e. band structures, defect matrix elements, and phase-factor matrix elements, have been obtained on the above-mentioned  $\mathbf{k}, \mathbf{q}$ -point BZ grids with the GPAW electronic-structure code<sup>2-4</sup>, using DFT-LDA within the projector augmented-wave (PAW) method, a DZP LCAO basis, and including spin-orbit interaction<sup>5</sup>. The implementation will be made available in the GPAW software package, and a full account including details of the PAW specific aspects will be published in a forthcoming paper.

In the following two subsections section, we give a brief overview of: 1. the atomistic DFT-based supercell method for the calculation of the defect matrix elements, and 2. the calculation of the phase-factor matrix elements.

### 1. Defect matrix elements

For nonmagnetic defects of type  $i$ , we consider a scattering potential of the form

$$\hat{V}_i = V_i(\hat{\mathbf{r}}) \otimes \hat{s}_0 \quad (\text{S8})$$

where  $\hat{s}_0$  is the identity operator in spin space. For the present purpose, spin-orbit scattering, which is not included in Eq. (S8), can be safely neglected as the spin-orbit terms are small compared to the main contribution to the scattering potential in Eq. (S8).

The real-space part of the scattering potential is taken as the difference in the crystal potential between the lattice with a defect site and the pristine lattice, i.e.

$$V_i(\mathbf{r}) = V_{\text{dis}}^i(\mathbf{r}) - V_{\text{pris}}(\mathbf{r}). \quad (\text{S9})$$

In practice, this is obtained in a large supercell constructed by repetition of the primitive cell and with the defect site located in the center. Due to periodic boundary conditions in the inplane directions, the supercell must be chosen large enough that defects in neighboring supercells do not interact. A common reference for the two potentials on the right-hand side of Eq. (S9) is ensured by imposing Dirichlet boundary conditions on the cell boundaries in the direction perpendicular to the material plane.

In the basis of the Bloch states and with the spin indices written out explicitly, the defect matrix elements can be expressed as

$$V_{i, \mathbf{k}\mathbf{k}'}^{mn}(s, s') = \langle m\mathbf{k}s | \hat{V}_i | n\mathbf{k}'s' \rangle = \sum_{s_z} \langle m\mathbf{k}s; s_z | V_i(\hat{\mathbf{r}}) | n\mathbf{k}'s'; s_z \rangle, \quad (\text{S10})$$

with  $|\cdot; s_z\rangle$  denoting the  $s_z$  component of the wave function.

The numerical evaluation of the defect matrix element in Eq. (S10) is based on an LCAO expansions of the Bloch functions of the pristine lattice,  $|m\mathbf{k}s\rangle = \sum_{s_z\nu} c_{m\mathbf{k}s}^{\nu s_z} |\nu\mathbf{k}s_z\rangle$ , where  $\nu = (\alpha, \mu)$  is a composite index for atomic site ( $\alpha$ ) and orbital index ( $\mu$ ) and

$$|\nu\mathbf{k}s_z\rangle = \frac{1}{\sqrt{N}} \sum_l e^{i\mathbf{k}\cdot\mathbf{R}_l} |\nu\mathbf{R}_l\rangle, \quad (\text{S11})$$

are Bloch expansions of the spin-independent LCAO basis orbitals  $|\nu\mathbf{R}_l\rangle$ , with  $N$  denoting the number of unit cells in the lattice and  $\mathbf{R}_l$  is the lattice vector to the  $l$ 'th unit cell.

Inserting in the expression for the matrix element in Eq. (S10), we find

$$\begin{aligned} V_{i,\mathbf{k}\mathbf{k}'}^{mn}(s,s') &= \sum_{s_z} \sum_{\nu\nu'} (c_{m\mathbf{k}s}^{\nu s_z})^* c_{n\mathbf{k}'s'}^{\nu' s_z} \langle \nu\mathbf{k} | V_i(\hat{\mathbf{r}}) | \nu'\mathbf{k}' \rangle \\ &= \frac{1}{N} \sum_{s_z} \sum_{\nu\nu'} (c_{m\mathbf{k}s}^{\nu s_z})^* c_{n\mathbf{k}'s'}^{\nu' s_z} \sum_{kl} e^{i(\mathbf{k}'\cdot\mathbf{R}_l - \mathbf{k}\cdot\mathbf{R}_k)} \langle \nu\mathbf{R}_k | V_i(\hat{\mathbf{r}}) | \nu'\mathbf{R}_l \rangle, \end{aligned} \quad (\text{S12})$$

where the factor of  $1/N$  stems from the normalization of the Bloch sums in Eq. (S11) to the lattice area  $A$ , the last factor in the second line is the LCAO representation of the defect potential  $V_i(\mathbf{r})$  in the supercell and the  $k, l$  sums are over the lattice cells in the supercell. With this, the defect matrix elements can be calculated for arbitrary  $\mathbf{k}, \mathbf{k}' = \mathbf{k} + \mathbf{q}$  values.

Note that the factor of  $1/N$  in the defect matrix element, which in the context of Eqs. (S6) and (S3) for the  $T$  matrix and FT-STs spectra, respectively, should be associated with the number of  $\mathbf{k}$ -points, i.e.  $N \rightarrow N_{\mathbf{k}}$ , ensures that the wave-vector sums in those equations are independent of the BZ sampling.

The matrix elements shown in Fig. 2 of the main manuscript, have a different unit from the one defined in Eq. (S10) above. Using that the lattice area can be written  $A = N \times A_{\text{cell}}$  where  $A_{\text{cell}}$  is the unit cell area, the matrix element in Eq. (S10) can be expressed as

$$V_{i,\mathbf{k}\mathbf{k}'}^{mn}(s,s') = \frac{N A_{\text{cell}}}{A} V_{i,\mathbf{k}\mathbf{k}'}^{mn}(s,s') \equiv \frac{1}{A} \bar{V}_{i,\mathbf{k}\mathbf{k}'}^{mn}(s,s') \quad (\text{S13})$$

where  $\bar{V}_i$  has units of the 2D Fourier transform of a scattering potential and is independent on  $N$ .

## 2. Phase-factor matrix element

The matrix element of the phase factor in Eq. (S3),

$$n_{\mathbf{k},\mathbf{q}}^{mn}(\mathbf{G}) = \langle \psi_{m\mathbf{k}} | e^{-i(\mathbf{q}+\mathbf{G})\cdot\hat{\mathbf{r}}} | \psi_{n\mathbf{k}+\mathbf{q}} \rangle = \langle u_{m\mathbf{k}} | e^{-i\mathbf{G}\cdot\hat{\mathbf{r}}} | u_{n\mathbf{k}+\mathbf{q}} \rangle, \quad (\text{S14})$$

can be reduced to an integral over the primitive unit cell as both the  $u_{m\mathbf{k}}$ s and  $\exp(-i\mathbf{G}\cdot\mathbf{r})$  are cell-periodic functions,

$$n_{\mathbf{k},\mathbf{q}}^{mn}(\mathbf{G}) = N \int_{\Omega} d\mathbf{r} u_{m\mathbf{k}}^*(\mathbf{r}) e^{-i\mathbf{G}\cdot\mathbf{r}} u_{n\mathbf{k}+\mathbf{q}}(\mathbf{r}), \quad (\text{S15})$$

where  $\Omega$  is the unit-cell volume.

In practice, the matrix elements are evaluated by integrating the first expression in Eq. (S14), i.e. the product of the LCAO Bloch functions and the full phase factor  $\exp[-i(\mathbf{q} + \mathbf{G}) \cdot \mathbf{r}]$ . Note that the factor of  $N$  in Eq. (S15) is cancelled by the inverse factor originating from the normalization of the Bloch sums in Eq. (S11).

## C. Computational details

All DFT calculations presented in the main manuscript have been performed with the electronic structure code GPAW<sup>2-4</sup> within the projector augmented-wave method, using LDA, an LCAO double-zeta polarized basis set, and including spin-orbit interaction<sup>5</sup>. The ground-state densities were obtained using a  $21 \times 21$   $\mathbf{k}$ -point sampling of the BZ with 7.5 Å vacuum to the cell boundaries in the vertical direction. The defect matrix elements were obtained using a  $11 \times 11$  supercell. The phase-factor matrix elements were obtained on a  $3 \times 3$   $\mathbf{G}$ -point grid with  $\mathbf{G}_i = m_i \mathbf{b}_1 + n_i \mathbf{b}_2$ ,  $m_i, n_i = -1, 0, 1$ . Finally, the calculation of the  $T$  matrix and FT-STs spectra are grid on  $75 \times 75$   $\mathbf{k}, \mathbf{q}$ -point samplings of the BZ with a broadening  $\eta = 5$  meV.

## D. FT-STs spectra at the band edge

To support our discussion of the energy dependence of the FT-STs spectra in the main manuscript, we show here in Fig. S2 the spectra for MoS<sub>2</sub> at the conduction-band edge. At the conduction-band edge in MoS<sub>2</sub>, quasiparticle scattering can only take place between the states at the bottom of the  $K, K'$  valleys. As a consequence, the FT-STs features in Fig. 3(c)+(d) of the main manuscript are reduced to featureless spots at the  $\mathbf{q}$  vectors corresponding to intra- ( $\mathbf{q} = \mathbf{0}$ ) and intervalley scattering. Due to the small spin-orbit splitting in the conduction band of MoS<sub>2</sub>

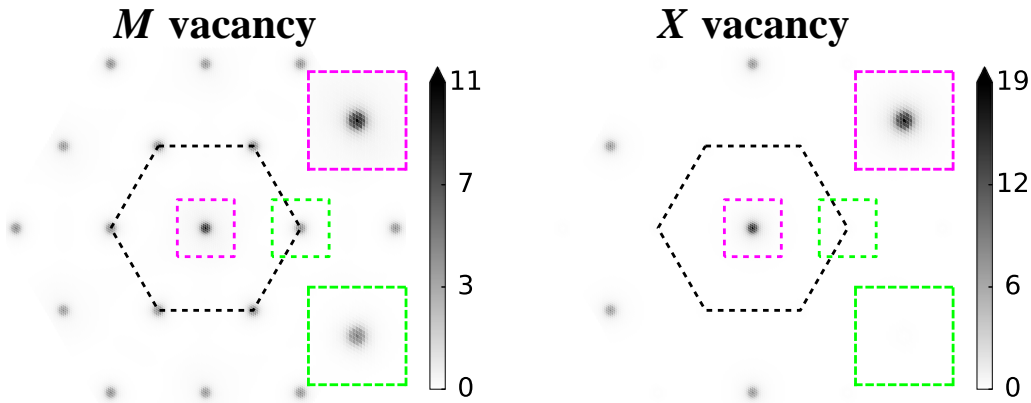


FIG. S2. FT-STs spectra for  $M = \text{Mo}$  (left) and  $X = \text{S}$  (right) vacancies in  $\text{MoS}_2$  at the band edge,  $\varepsilon = E - E_c = 0$  meV. The boxes show zooms of the marked regions.

( $\sim 3$  meV), spin-conserving intervalley scattering with  $\mathbf{q} = \mathbf{K}, \mathbf{K}'$  is possible at the band edge in the presence of a finite linewidth broadening which in our calculations are given by the numerical  $\eta$  broadening of the bands. This is indeed the case for the Mo vacancy as shown in Fig. S2. However, the intervalley peak is completely absent for the S vacancy as the intervalley matrix element, according to our symmetry analysis below, in this case vanishes identically between the two high-symmetry  $K, K'$  points.

## S2. SYMMETRY ANALYSIS OF THE DEFECT MATRIX ELEMENTS

The selection rules for the matrix elements between states at high-symmetry points in the Brillouin zone can be deduced from the symmetries of the space group which for monolayer  $\text{MX}_2$  is  $D_{3h}$ . At the  $K, K'$  points, the group of the wave vector is  $C_{3h}$  which is formed by the space-group operations  $C_3$  (rotation by  $\pm 2\pi/3$  around an axis perpendicular to the plane of the monolayer) and  $\sigma_h$  (reflection in the horizontal mirror plane defined by the monolayer). Each state at  $\mathbf{k} = \pm \mathbf{K}$  can thus be labeled by two quantum numbers which express the phase picked up by the Bloch wavefunction under rotations by  $\pm 2\pi/3$  and reflections in the mirror plane, respectively.

When the perturbing defect potential is invariant under one or more of the symmetries forming the group of the wave vector, selection rules for its matrix elements arise. Focusing here on defects with  $C_3$  symmetry, the matrix elements in (S10) between the  $K, K'$ -point Bloch functions labelled by a band ( $n = v, c$ ) and valley ( $\tau = \pm 1$ ) index, can be written

$$\begin{aligned} \langle n\tau | V_i | n\tau' \rangle &= \langle n\tau | C_3^\dagger C_3 V_i C_3^\dagger C_3 | n\tau' \rangle \\ &= \langle n\tau | C_3^\dagger V_i C_3 | n\tau' \rangle \\ &\equiv \gamma_{i,n}^{\tau\tau'} \langle n\tau | V_i | n\tau' \rangle, \end{aligned} \quad (\text{S16})$$

where  $\gamma_{i,n}^{\tau\tau'} = w_{i,n\tau}^* w_{i,n\tau'}$  is given by the product of the phase factors which describe the transformation of the Bloch functions under  $C_3$ . As we shall see below, the phase factors also depend on the position of the  $C_3$  symmetry axis, which is here fixed by the defect type indexed by  $i$  ( $= M, X$  for  $M$  and  $X$  centered defects, respectively). From Eq. (S16), it is clear that the matrix element must vanish in case  $\gamma_{i,n}^{\tau\tau'} \neq 1$ .

The transformation of the symmetry-adapted basis functions<sup>6</sup> defined in the main paper under the  $C_3$  symmetry operation can be inferred from their Bloch form,

$$\phi_{n\tau}^K(\mathbf{r}) = \frac{1}{\sqrt{N}} \sum_l e^{i\tau \mathbf{K} \cdot \mathbf{R}_l} \phi_{n\tau}(\mathbf{r} - \mathbf{t}_i - \mathbf{R}_l), \quad (\text{S17})$$

where the sum is over unit cells  $l$ ,  $\phi_{n\tau}$  is given by the  $d$ -orbitals on  $M$ , and  $\mathbf{t}_i$  is the position of the  $M$  site in the primitive unit cell with respect to the defect center [see Eq. (S19) below].

Operating on the Bloch functions with  $C_3$ , we find

$$C_3\phi_{n\tau}^K(\mathbf{r}) = \frac{1}{\sqrt{N}} \sum_l e^{i\tau\mathbf{K}\cdot\mathbf{R}_l} \phi_{n\tau}(C_3^{-1}\mathbf{r} - \mathbf{R}_l - \mathbf{t}_i) \quad (\text{S18a})$$

$$= \frac{1}{\sqrt{N}} e^{-i\tau\mathbf{K}\cdot\mathbf{t}_i} \sum_l e^{i\tau\mathbf{K}\cdot(\mathbf{R}_l+\mathbf{t}_i)} \phi_{n\tau}(C_3^{-1}[\mathbf{r} - C_3(\mathbf{R}_l + \mathbf{t}_i)]) \quad (\text{S18b})$$

$$= \frac{1}{\sqrt{N}} e^{-i\tau\mathbf{K}\cdot\mathbf{t}_i} \sum_l e^{i\tau C_3\mathbf{K}\cdot C_3(\mathbf{R}_l+\mathbf{t}_i)} \phi_{n\tau}(C_3^{-1}[\mathbf{r} - C_3(\mathbf{R}_l + \mathbf{t}_i)]) \quad (\text{S18c})$$

$$= \frac{1}{\sqrt{N}} e^{-i\tau\mathbf{K}\cdot\mathbf{t}_i} \sum_l e^{i\tau C_3\mathbf{K}\cdot(\mathbf{R}_l+\mathbf{t}_i)} \phi_{n\tau}(C_3^{-1}[\mathbf{r} - \mathbf{R}_l - \mathbf{t}_i]) \quad (\text{S18d})$$

$$= \frac{1}{\sqrt{N}} e^{i\tau(C_3\mathbf{K}-\mathbf{K})\cdot\mathbf{t}_i} \sum_l e^{i\tau\mathbf{K}\cdot\mathbf{R}_l} w_{n\tau} \phi_{n\tau}(\mathbf{r} - \mathbf{R}_l - \mathbf{t}_i) \quad (\text{S18e})$$

$$= e^{i\tau(C_3\mathbf{K}-\mathbf{K})\cdot\mathbf{t}_i} w_{n\tau} \phi_{n\tau}^K(\mathbf{r}) \equiv w_{i,\tau} w_{n\tau} \phi_{n\tau}^K(\mathbf{r}) \equiv w_{i,\tau n} \phi_{n\tau}^K(\mathbf{r}). \quad (\text{S18f})$$

Here we have carried out the following steps: (S18a) apply  $C_3$ ; (S18b) insert identity in the form of phase factor; (S18c) inner product invariant under unitary transformation of both vectors; (S18d) summing over  $C_3(\mathbf{R}_l + \mathbf{t}_i)$  is the same summing over  $\mathbf{R}_l + \mathbf{t}_i$  when the rotation axis is centered on a lattice site; (S18e)  $C_3$  is an element in the group of  $\mathbf{K} \Rightarrow C_3\mathbf{K}$  and  $\mathbf{K}$  are equivalent, and  $C_3$  element in the space group  $\Rightarrow \phi_{n\tau}(C_3^{-1}[\cdot]) = C_3\phi_{n\tau}(\mathbf{r}) = w_{n\tau}\phi_{n\tau}(\mathbf{r})$ , where  $w_{n\tau} = e^{2\pi i|m_n|\tau/3}$  originates from the rotation of the orbital around its own center and  $m_n$  ( $= 0, \pm 2$  for  $n = c, v$ ) is the magnetic quantum number.

Finally, we evaluate the phase factors defined in Eq. (S18f). In terms of the primitive vectors  $\mathbf{a}_{1,2}$  and  $\mathbf{b}_{1,2}$  of the direct and reciprocal lattice, respectively, the vectors in (S18f) are given by

$$\mathbf{t}_M = \mathbf{0} \quad \text{or} \quad \mathbf{t}_X = \frac{1}{3}\mathbf{a}_1 + \frac{1}{3}\mathbf{a}_2, \quad (\text{S19})$$

and

$$\mathbf{K} = -\frac{1}{3}\mathbf{b}_1 + \frac{1}{3}\mathbf{b}_2 \quad (\text{S20})$$

$$C_3\mathbf{K} = +\frac{2}{3}\mathbf{b}_1 + \frac{1}{3}\mathbf{b}_2. \quad (\text{S21})$$

For the  $C_3$  symmetry axis positioned at the  $M$  ( $X$ ) site, we then find  $w_{M,\tau} = 1$  ( $w_{X,\tau} = e^{2\pi i\tau/3}$ ). The phase factors from the rotation of the orbitals around their own centers are  $w_{v\tau} = e^{4\pi i\tau/3}$  and  $w_{c\tau} = 1$ .

The  $\gamma_{i,n}^{\tau\tau'}$  factor in Eq. (S16) can now be obtained. For the intravalley ( $\tau = \tau'$ ) matrix element,  $\gamma_{i,n}^{\tau\tau} = 1$  in all cases implying that the matrix element is finite. On the other hand, for the intervalley ( $\tau \neq \tau'$ ) matrix element we find,

$$\gamma_{M,c}^{\tau\tau'} = 1 \quad , \quad \gamma_{X,c}^{\tau\tau'} = e^{\pm 4\pi i/3}, \quad (\text{S22})$$

$$\gamma_{M,v}^{\tau\tau'} = e^{\pm 8\pi i/3} \quad , \quad \gamma_{X,v}^{\tau\tau'} = e^{\pm 4\pi i/3}, \quad (\text{S23})$$

stating that the intervalley matrix element vanishes identically in all cases except for  $M$ -centered defects where the matrix element in the conduction band is finite. This is in excellent agreement with our atomistic calculations of the matrix elements in Fig. 2 of the main text.

\* kkaa@nanotech.dtu.dk

<sup>1</sup> G. A. Fiete and E. J. Heller, Rev. Mod. Phys. **75**, 933 (2003).

<sup>2</sup> J. J. Mortensen, L. B. Hansen, and K. W. Jacobsen, Phys. Rev. B **71**, 035109 (2005).

<sup>3</sup> A. H. Larsen, M. Vanin, J. J. Mortensen, K. S. Thygesen, and K. W. Jacobsen, Phys. Rev. B **80**, 195112 (2009).

<sup>4</sup> J. . E. *et al.*, J. Phys.: Condens. Matt. **22**, 253202 (2010).

<sup>5</sup> T. Olsen, Phys. Rev. B **94**, 235106 (2016).

<sup>6</sup> D. Xiao, G.-B. Liu, W. Feng, X. Xu, and W. Yao, Phys. Rev. Lett. **108**, 196802 (2012).

## Paper II

### Theoretical study of impurity-induced magnetism in FeSe

Johannes H. J. Martiny, Andreas Kreisel, Brian M. Andersen

*Physical Review B* **99** (1), 014509 (2018)

# Theoretical study of impurity-induced magnetism in FeSe

Johannes H. J. Martiny,<sup>1</sup> Andreas Kreisel,<sup>2</sup> and Brian M. Andersen<sup>3</sup>

<sup>1</sup>*Center for Nanostructured Graphene (CNG), Dept. of Micro- and Nanotechnology, Technical University of Denmark, DK-2800 Kongens Lyngby, Denmark*

<sup>2</sup>*Institut für Theoretische Physik, Universität Leipzig, D-04103 Leipzig, Germany and*

<sup>3</sup>*Niels Bohr Institute, University of Copenhagen, Lyngbyvej 2, DK-2100 Copenhagen, Denmark*

(Dated: November 5, 2018)

Experimental evidence suggests that FeSe is close to a magnetic instability, and recent scanning tunneling microscopy (STM) measurements on FeSe multilayer films have revealed stripe order locally pinned near defect sites. Motivated by these findings, we perform a theoretical study of locally induced magnetic order near nonmagnetic impurities in a model relevant for FeSe. We find that relatively weak repulsive impurities indeed are capable of generating short-range magnetism, and explain the driving mechanism for the local order by resonant  $e_g$ -orbital states. In addition, we investigate the importance of orbital-selective self-energy effects relevant for Hund's metals, and show how the structure of the induced magnetization cloud gets modified by orbital selectivity. Finally, we make concrete connection to STM measurements of iron-based superconductors by symmetry arguments of the induced magnetic order, and the basic properties of the Fe Wannier functions relevant for tunneling spectroscopy.

## I. INTRODUCTION

The understanding of the electronic properties of the material FeSe continues to pose an interesting challenge to the research community of iron-based superconductors. Controversial current topics include the reasons for its modified electronic structure (compared to DFT calculations), the nature of the nematic phase, and the origin of the highly anisotropic superconducting gap structure.<sup>1</sup> There is considerable interest in resolving these issues both for our general understanding of correlated superconductors in general, and FeSe in particular due to the ability to significantly enhance its superconducting transition temperature  $T_c$  by pressure, intercalation, or dosing.<sup>2-8</sup> In addition, while bulk FeSe exhibits a  $T_c \sim 9$  K, a single monolayer of FeSe on STO has been shown to superconduct up to  $\sim 65$  K.<sup>9</sup> On the other hand, thicker films suppress superconductivity and exhibit a strong nematic phase for reasons that remain unclear at present.<sup>10</sup>

A striking difference between FeSe and most of the iron-based superconductors is the lack of magnetic ordering in FeSe. Even though the tetragonal to orthorhombic transition takes place around  $T_s \sim 90$  K, there is no evidence for long-range static magnetic order setting in at lower temperatures. However, there is experimental evidence that FeSe is close to a magnetic instability at low temperatures, as seen by the diverging spin-lattice relaxation rate  $1/T_1T$  versus  $T$  by NMR.<sup>11</sup> For example, modest pressures exceeding  $\sim 0.8$  GPa induce static stripe antiferromagnetism indicating that FeSe at ambient pressure is parametrically close to the ordered magnetic phase.<sup>2-5</sup> The resulting temperature-pressure phase diagram describing the pressure dependence of nematic, magnetic, and superconducting orders has been recently described theoretically in terms of pressure-dependent electronic interactions.<sup>12</sup> The importance of low-energy magnetic fluctuations in FeSe (at ambient pressure) has

been also pointed out by recent inelastic neutron scattering experiments revealing a rich temperature and momentum dependence of the scattering intensity.<sup>13-16</sup> As a function of temperature, spectral weight is shifted from Néel-like fluctuations to stripe-like  $(\pi, 0)$  fluctuations. Thus at low temperatures the magnetic fluctuations at low energies are entirely dominated by the stripe-like fluctuations.

The proximity to a stripe magnetic instability suggests the possibility of disorder-induced magnetism in FeSe. Naively various imperfections such as impurities and twin boundaries may relatively easily induce weak local magnetic order by the presence of a nearby magnetic quantum critical point.<sup>17</sup> Despite the fact that very high quality FeSe crystals can be made<sup>18</sup>, and disorder-generated magnetism does not appear to be widespread in those samples, a number of recent experimental results do find evidence of local magnetism. For example, the close similarity in the behavior of the magnetostriction and uniform susceptibility between  $\text{BaFe}_2\text{As}_2$  and FeSe in the nematic phase, led He *et al.*<sup>19</sup> to propose that short-range stripe magnetic order exists in FeSe. Evidence of dilute static magnetism possibly arising from impurities has also been recently put forward by  $\mu\text{SR}$  measurements on high quality single crystals.<sup>20</sup> Earlier  $\mu\text{SR}$  studies of  $\text{FeSe}_{0.85}$  also found evidence of a dilute and randomly distributed static magnetic signal.<sup>21</sup> Related to these findings, an STM study of FeSe multilayer films found clear evidence of charge stripe order centered near Fe vacancy sites.<sup>22</sup> This study reveals a clear example of impurity-induced local order, and it was suggested by the authors that the observed charge stripes are the natural associated charge modulations induced by the magnetic fluctuations pinned by the defect sites.<sup>22</sup> The presence of disorder-pinned antiferromagnetic order was also recently suggested to be at play in parent as-grown films of FeSe on STO.<sup>23</sup> Finally, we point out recent NMR studies of FeSe finding evidence of static short-range ne-

matic order above  $T_s$ .<sup>24,25</sup> It remains an interesting question if and how local magnetic order may be connected to these NMR observations.

From a theoretical perspective, the low-energy magnetic fluctuations in bulk FeSe have been described within an itinerant approach which successfully captured the temperature and momentum dependence of the spin excitations.<sup>26–28</sup> However, this is only true if one includes so-called orbital-selective effects in the theory, i.e. the fact that distinct orbitals experience different self-energy renormalizations leading to orbital-dependent mass enhancements and quasi-particle weights.<sup>29–39</sup> These properties are characteristics of Hund’s metals, and agree with recent STM quasi-particle interference measurements both in the normal state and superconducting phases.<sup>40–42</sup>

In terms of impurity-physics in unconventional superconducting materials, a number of theoretical works have pointed out the interesting role of electronic interactions in dressing bare impurity potentials.<sup>43–52</sup> In addition, there are nontrivial effects from the multi-band electronic structure of this family of materials. For example, in the nematic state, nonmagnetic disorder may lead to short-range anisotropic magnetic order which has been proposed to explain unusual transport phenomena in Co-doped BaFe<sub>2</sub>As<sub>2</sub>.<sup>53</sup> Regarding the superconducting state, there are also novel suggested impurity effects including disorder-enhanced  $T_c$  due to local density of states (LDOS) enhancements from bound states generated in off-Fermi level bands.<sup>54</sup>

In this paper, we combine realistic microscopic modeling of FeSe with impurity studies to address the role of local nucleated short-range magnetic order in this material. We apply the so-called Chebyshev Bogoliubov-de Gennes method to study large real-space systems, and map out the phase diagram of local magnetic order as a function of onsite Coulomb repulsion  $U$  and impurity potential  $V_0$ . We find a favorable impurity potential range for induced local order. In addition, we discuss the role of orbital selectivity in the self-consistency equations, and show how the associated self-energy effects are directly tied to the local internal structure of the induced magnetization clouds surrounding impurity sites with favor-

able potentials able to generate induced order. We suggest that the experimental evidence of local magnetism in FeSe may be caused by a particular class of disorder in this material.

## II. METHOD

We start from a fitted tight binding model for the nematic phase of FeSe with the Hamiltonian

$$\mathcal{H}_0 = \sum_{ij,\mu\nu,\sigma} (t_{ij}^{\mu\nu} - \delta_{ij}\delta_{\mu\nu}\mu_0) c_{i\mu\sigma}^\dagger c_{j\nu\sigma} + H.c., \quad (1)$$

where  $\mu, \nu$  span the d-orbitals of the two inequivalent iron atoms in the unit cell, and  $t_{ij}^{\mu\nu}$  denote the hopping elements detailed in Ref. 42. A point-like impurity at a site  $i'$  is described by the term

$$\mathcal{H}_{imp} = V_0 \sum_{\mu,\sigma} c_{i'\mu\sigma}^\dagger c_{i'\mu\sigma}, \quad (2)$$

where the sum now spans the orbitals of a single iron site. Interactions are initially included using the usual multiorbital Hubbard-Hund model

$$\begin{aligned} \mathcal{H}_{int} = & U \sum_{i,\mu} n_{i\mu\uparrow} n_{i\mu\downarrow} + U' \sum'_{i,\mu<\nu,\sigma} n_{i\mu\sigma} n_{i\nu\bar{\sigma}} \quad (3) \\ & + (U' - J) \sum'_{i,\mu<\nu,\sigma} n_{i\mu\sigma} n_{i\nu\sigma} \\ & + J \sum'_{i,\mu<\nu,\sigma} c_{i\mu\sigma}^\dagger c_{i\nu\bar{\sigma}}^\dagger c_{i\mu\bar{\sigma}} c_{i\nu\sigma} \\ & + J' \sum'_{i,\mu\neq\nu} c_{i\mu\uparrow}^\dagger c_{i\mu\downarrow}^\dagger c_{i\nu\downarrow} c_{i\nu\uparrow}, \end{aligned}$$

where we set  $J = J' = U/4$  and use spin-rotational invariant interactions,  $U' = U - 2J$ , and the sums  $\sum'$  only give a contribution when the indices  $\mu$  and  $\nu$  label an orbital on the same iron atom.

The interactions are included at the mean field level, yielding the mean field Hamiltonian

$$\begin{aligned} \mathcal{H}_{int}^{MF} = & \sum_{i,\nu,\sigma} \left[ U \langle n_{i\nu\bar{\sigma}} \rangle + \sum'_{\mu\neq\nu} \left\{ U' \langle n_{i\mu\bar{\sigma}} \rangle + (U' - J) \langle n_{i\mu\sigma} \rangle \right\} \right] c_{i\nu\sigma}^\dagger c_{i\nu\sigma} \quad (4) \\ & - \sum'_{i,\mu\neq\nu,\sigma} \left[ (U' - J) \langle c_{i\nu\sigma}^\dagger c_{i\mu\sigma} \rangle - J' \langle c_{i\mu\bar{\sigma}}^\dagger c_{i\nu\bar{\sigma}} \rangle - J \langle c_{i\nu\bar{\sigma}}^\dagger c_{i\mu\bar{\sigma}} \rangle \right] c_{i\mu\sigma}^\dagger c_{i\nu\sigma} \\ & - \sum_{i,\nu,\sigma} \left[ U \langle c_{i\nu\sigma}^\dagger c_{i\nu\bar{\sigma}} \rangle + J \sum'_{\mu\neq\nu} \langle c_{i\mu\sigma}^\dagger c_{i\mu\bar{\sigma}} \rangle \right] c_{i\nu\bar{\sigma}}^\dagger c_{i\nu\sigma} - \sum'_{i,\mu\neq\nu,\sigma} \left[ U' \langle c_{i\nu\sigma}^\dagger c_{i\mu\bar{\sigma}} \rangle + J' \langle c_{i\mu\sigma}^\dagger c_{i\nu\bar{\sigma}} \rangle \right] c_{i\mu\bar{\sigma}}^\dagger c_{i\nu\sigma}. \end{aligned}$$

The Hamiltonian  $\mathcal{H} = \mathcal{H}_0 + \mathcal{H}_{imp} + \mathcal{H}_{int}^{MF}$  defines the

“bare” version of our model, where effects of orbital se-

lectivity (discussed further below) are not included. The results derived from this bare model will serve as a comparison basis for another model defined below which includes the effects of orbital selectivity.

Unrestricted self-consistent calculations of the density and magnetization mean fields for the tight binding models are performed using the Chebyshev Bogoliubov-de Gennes (CBdG) method,<sup>55</sup> wherein the electronic Greens function of a Hamiltonian  $\mathcal{H}$  is expanded in a series of orthogonal polynomials. We will provide a brief outline of this procedure below. The starting point of the expansion procedure is the estimation of extremal eigenvalues  $E_{\min}, E_{\max}$  which are obtained by explicitly diagonalizing the Hamiltonian in a small system. We can then define the rescaled Hamiltonian

$$\tilde{\mathcal{H}} = (\mathcal{H} - b)/a, \quad (5)$$

with  $b = (E_{\max} + E_{\min})/2$  and  $a = (E_{\max} - E_{\min})/(2 - \delta)$ , where  $\delta = 0.001$  is a small parameter introduced to avoid divergence at the edges of the domain. The rescaled Hamiltonian  $\tilde{\mathcal{H}}$  has eigenvalues in the interval  $(-1, 1)$ , which coincides with the domain of the Chebyshev polynomials.

Defining the rescaled energy  $\tilde{\omega} = (\omega - b)/a \in (-1, 1)$ , the Greens function can then be expanded as

$$\begin{aligned} G_{\mu\nu}^{\sigma\sigma'}(i, j, \tilde{\omega}) &= \lim_{\eta \rightarrow 0} \left\langle c_{i\mu\sigma} \left| \frac{1}{\tilde{\omega} + i\eta - \tilde{\mathcal{H}}} \right| c_{j\nu\sigma'}^\dagger \right\rangle \\ &= \frac{-2i}{\sqrt{1 - \tilde{\omega}^2}} \sum_{n=0}^{N-1} a_{\mu\nu,n}^{\sigma\sigma'}(i, j) \exp(-in \arccos(\tilde{\omega})), \end{aligned} \quad (6)$$

with  $|c_{j\nu\sigma'}^\dagger\rangle = c_{j\nu\sigma'}^\dagger |0\rangle$ , and expansion coefficients

$$a_{\mu\nu,n}^{\sigma\sigma'}(i, j) = \frac{1}{1 + \delta_{0,n}} \left\langle c_{i\mu\sigma} \left| T_n(\tilde{\mathcal{H}}) \right| c_{j\nu\sigma'}^\dagger \right\rangle \quad (7)$$

where  $T_n$  is the  $n$ th Chebyshev polynomial of the first kind. The problem has therefore been reduced to finding the expansion coefficients, which are obtained using the recursion relation of the Chebyshev polynomials. Defining the intermediate states  $|j_n\rangle = T_n(\tilde{\mathcal{H}}) |c_{j\nu\sigma'}^\dagger\rangle$ , we can generate coefficients recursively starting from an initial state

$$|j_0\rangle = |c_{j\nu\sigma'}^\dagger\rangle, \quad (8a)$$

$$|j_1\rangle = \tilde{\mathcal{H}} |c_{j\nu\sigma'}^\dagger\rangle, \quad (8b)$$

$$|j_{n+1}\rangle = 2\tilde{\mathcal{H}} |j_n\rangle - |j_{n-1}\rangle. \quad (8c)$$

The full expansion coefficients can be then obtained as the inner product  $a_{\mu\nu,n}^{\sigma\sigma'}(i, j) = \langle c_{i\mu\sigma} | j_n \rangle$ . An artificial broadening of  $\eta = 1$  meV is included in the Greens function by applying the Lorentz kernel during the expansion.<sup>55</sup>

The mean fields in Eq. (5) and the local density of

states (LDOS) then follow from

$$\left\langle c_{i\mu\sigma}^\dagger c_{i\nu\sigma'} \right\rangle = \int_{-1}^1 d\tilde{\omega} \text{Im} G_{\mu\nu}^{\sigma\sigma'}(i, i, \tilde{\omega}) f(\tilde{\omega}), \quad (9)$$

$$\rho_\mu^\sigma(i, \omega) = -\frac{1}{\pi} \text{Im} G_{\mu\mu}^{\sigma\sigma}(i, i, \omega), \quad (10)$$

with  $f(\tilde{\omega})$  the Fermi-Dirac distribution function which is evaluated at a temperature of 1K in all following calculations. (For the study of FeSe below this implies that we are deep within the nematic phase in the undoped system.) The energy integrals for the mean fields can be obtained efficiently using Chebyshev-Gauss quadrature in a similar fashion as Ref. 55, leaving the sparse matrix-vector products as the limiting part of the full calculation. We find that these mean fields are converged at  $N = 1000$  expansion coefficients, and use this value for all calculations apart from when we plot the LDOS at high energy resolution (then,  $N = 20000$ ). In agreement with Ref. 55, we find that this procedure is extremely efficient for selfconsistent calculations in large multi-orbital systems such as our considered ten orbital model, while yielding results consistent with the conventional BdG method. We stress that all calculations below are fully unrestricted in all orbitals and sites.

### III. RESULTS

The phase diagram of magnetization versus  $V_0$  and  $U$  is obtained by initializing a  $12 \times 12$  system with a central impurity surrounded by a small uniformly spin polarized region, and then converging the mean fields for given Hubbard  $U$  and impurity potentials  $V_0$ . Convergence is defined as a maximal variation of the set of mean fields  $n$  of Eq. (9) of  $\max(n_{m-1} - n_m) < 10^{-7}$  between iteration steps  $m-1$  and  $m$ , for at least 100 iteration steps. This is usually accomplished within 1500 iteration steps of the CBdG procedure. Consistent with previous susceptibility calculations,<sup>42</sup> we find that the homogeneous system ( $V_0 = 0$ ) displays a transition to a global  $(\pi, \pi)$  antiferromagnetic phase at a critical  $U_c = 295$ meV. Approaching this transition from below, we find the possibility of local magnetic order nucleated by the impurity site for a range of potentials  $V_0$  displayed in Fig. 1 (a). At the phase boundary the local order sets in at  $V_0 = 70$ meV, and extends until  $V_0 = 560$ meV, with only repulsive potentials being able to induce local magnetic order. The local magnetic structure inside this phase mirrors the bulk  $(\pi, \pi)$  phase as demonstrated in Fig. 1(b-c), displaying the real space magnetization (b) and its Fourier transform (c). The orbital splitting included in  $\mathcal{H}_0$  to describe the nematic order of FeSe at low  $T$ , induces a negligible degree of  $C_4$ -symmetry breaking in the magnetization, and hence the results in Fig. 1(b-c) appear  $C_4$  symmetric even though they are, strictly speaking, only  $C_2$  symmetric.

We now turn to the underlying reason for stabilization of local magnetic order. Previous studies of

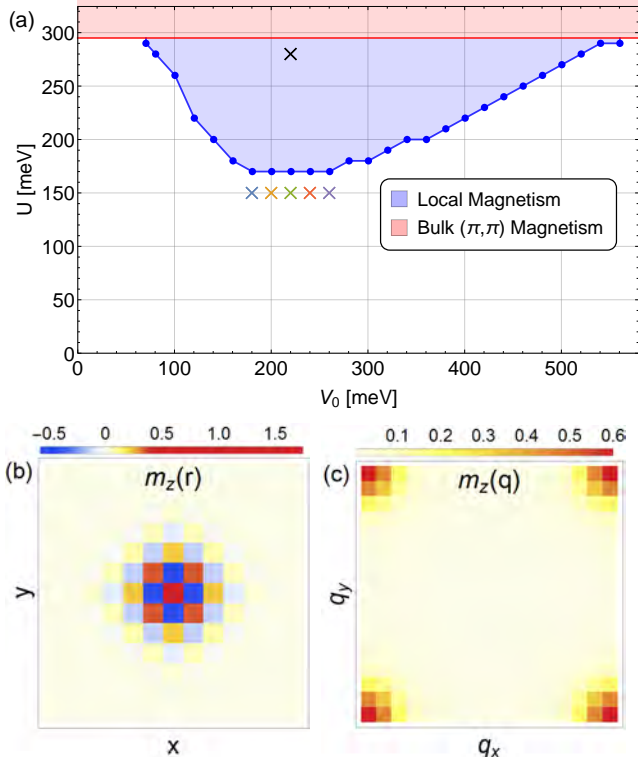


FIG. 1. (a) Phase diagram of impurity-induced magnetization as a function of the impurity potential strength  $V_0$  and Hubbard  $U$ . The phase diagram shows the bulk  $(\pi, \pi)$  phase above  $U_c = 295\text{meV}$  (red), and a region of impurity nucleated local magnetic order (blue) just below the bulk order. The system is most susceptible to the formation of local magnetic order for impurity potentials close to  $V_0 \approx 220\text{meV}$ . (b) Magnetization for  $V_0 = 220\text{meV}$ ,  $U = 280\text{meV}$  deep in the pocket of local magnetic order (indicated by the black cross in the phase diagram (a)), alongside (c) the Fourier transform showing the local  $(\pi, \pi)$  order.

impurity-induced magnetization have found a link between local magnetic order and impurity resonant states formed at the Fermi level just below the local magnetic transition.<sup>51,56</sup> This suggests a mechanism of locally enhanced LDOS providing a local Stoner transition to a magnetic state.<sup>57</sup> In Fig. 2 (a) we investigate this local Stoner scenario. We fix  $U = 150\text{meV}$ , i.e. just below the local magnetic transition and show the LDOS near the Fermi level for varying values of the impurity potential  $V_0$ , as marked by the line of colored crosses in Fig. 1 (a). We find that the point in  $(U, V_0)$ -phase space where the system is most susceptible to local magnetic order, i.e. where the critical coupling line  $U_c(V_0)$  has its lowest value, corresponds exactly to the impurity potential where the resonant state crosses the Fermi level ( $V_0 \approx 220\text{meV}$ ). This indicates that the onset of local magnetic order can be understood as a local Stoner transition. The role of these resonant states in inducing local magnetism, and enhancing superconductivity, has been

recently discussed in Refs. 52 and 58.

The emergence of these resonant states can in turn be understood from the real space Greens function in the presence of a point-like impurity at the origin ( $r = 0$ )

$$G(r, \omega) = G_0(r, \omega) + G_0(r - 0, \omega)T(\omega)G_0(0 - r, \omega), \quad (11)$$

where each quantity is a matrix containing the spin and orbital components of Eq. (7), and we have defined the impurity T-matrix

$$T(\omega) = \frac{V_0}{\mathbb{I} - V_0 \sum_k G_0(k, \omega)} = \frac{\mathbb{I}}{(V_0)^{-1} - g_0(\omega)}, \quad (12)$$

with the shortened notation  $g_0(\omega) = G_0(0, \omega)$  for the local Greens function in the absence of impurities. The impurity-induced change in the LDOS can then be defined using Eq. (10)

$$\begin{aligned} \delta\rho(r, \omega) &= \rho(r, \omega) - \rho_0(r, \omega) \\ &= -\frac{1}{\pi} \text{Im} [G_0(r - 0, \omega)T(\omega)G_0(0 - r, \omega)], \end{aligned} \quad (13)$$

from which we see that impurity bound states correspond to poles of the T-matrix. If the impurity and local Greens function are diagonal matrices, we find five independent criteria for the formation of bound states

$$\det[(V_0)^{-1} - g_0(\omega)] = \prod_{\mu} \left( \frac{1}{V_0} - g_0^{\mu}(\omega) \right) = 0, \quad (14)$$

i.e. a bound state appears at an energy  $\omega = \xi$  if for any orbital  $\mu$

$$0 = -\pi\rho_0^{\mu}(0, \xi), \quad (15a)$$

$$\frac{1}{V_0} = \text{Re} g_0^{\mu\mu}(\xi). \quad (15b)$$

Solutions to these equations for any energy  $\xi$  correspond to true bound states with impurity site LDOS  $\delta\rho(0, \xi) \propto \delta(\xi)$ , while resonant states are allowed as complex solutions  $\xi = \xi' + i\xi''$  with a broadened Lorentzian shape in the impurity site LDOS.<sup>56</sup> If we consider a quasi-gapped region where  $\rho_0^{\mu}(0, \omega) \approx 0$  for some orbital  $\mu$ , the T-matrix solution predicts resonant states with orbital character  $\mu$ , and the resonant state energy  $\xi$  determined by the impurity strength  $V_0$ .

Fig. 2 (b) shows the graphical solution to these equations obtained from a converged homogeneous system ( $V_0 = 0, U = 150\text{meV}$ ). The three  $t_{2g}$  orbitals all have finite spectral weight at the Fermi level, leaving only the two quasi-gapped  $e_g$  orbitals,  $d_{z^2}, d_{x^2-y^2}$ , as candidates for the resonant state. Of these only the  $d_{z^2}$  real part of the Greens function fulfills the second condition in this energy interval. This results in resonant states of purely  $d_{z^2}$  character as shown in (c) where each orbital component of the LDOS is plotted. Since the  $d_{z^2}$  LDOS is quasi-gapped in an extended energy interval, the location

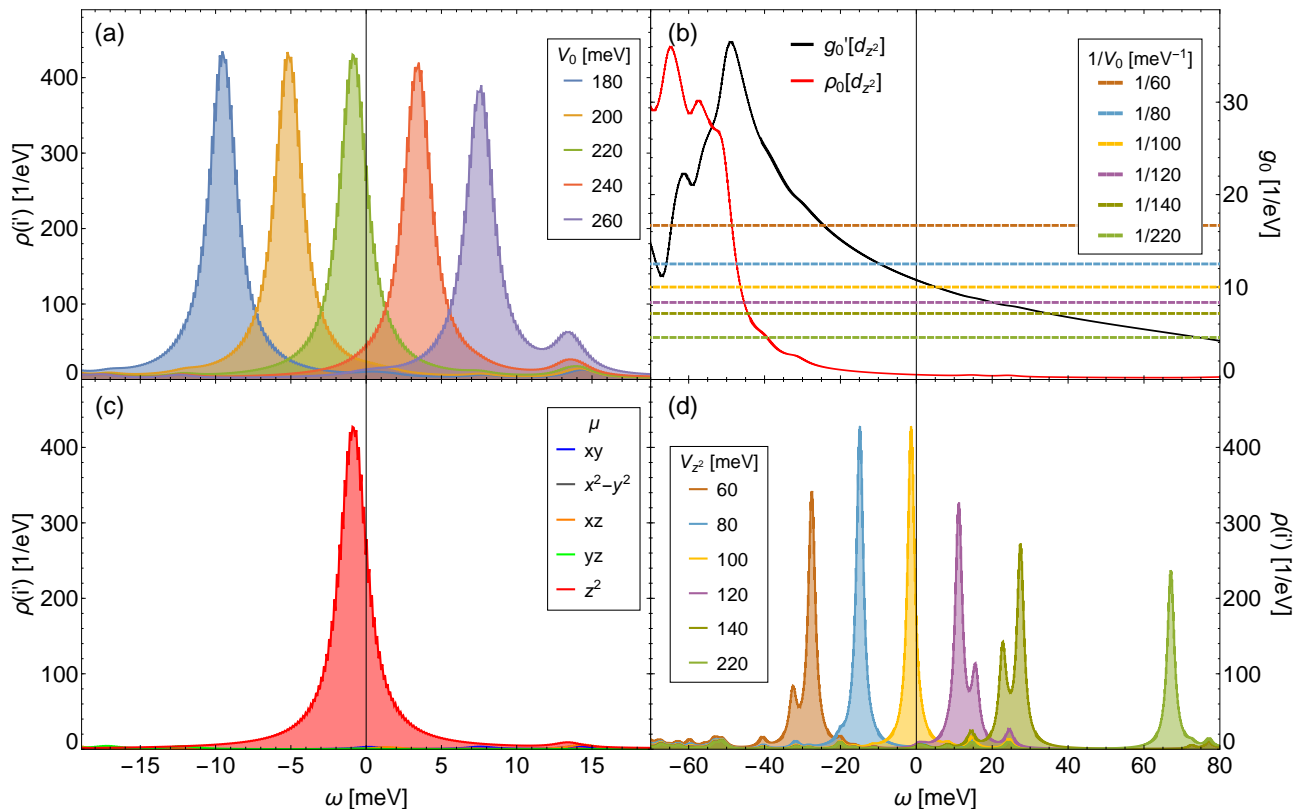


FIG. 2. (a) LDOS at the impurity site  $i'$  for  $U = 150\text{meV}$  just below the local magnetic transition, displaying a clear progression of bound states with varying  $V_0$ . As the bound state approaches the Fermi level, the local magnetic transition sets in as a local Stoner transition. (b) Real (black line) and imaginary (red line,  $\propto \text{LDOS}$ ) part of the  $d_{z^2}$  component of the Greens function. Resonant states are expected at energies where the inverse impurity potential (dashed lines) matches the real part of the Greens function while the LDOS is gapped. (c) Orbitally resolved LDOS of a single impurity potential  $V = 220\text{meV}$ , demonstrating that the resonant state is almost purely of  $d_{z^2}$  character due to the negligible density of states for this orbital. (d) Removing selfconsistency and using a purely  $d_{z^2}$  impurity in the tight binding calculation yields resonant states matching the T-matrix solution within the broadening.

of the resonant state varies smoothly with the impurity potential as evident in (a).

We note that while the progression of resonant state energies matches the quasi-gapped region and the slope of the real part of the orbital Greens function, a discrepancy of  $\approx 80\text{meV}$  in the exact position of the resonant state predicted from the T-matrix solution and the result of our selfconsistent procedure exists. This shift stems from the fact that the T-matrix solution only applies exactly for a purely  $d_{z^2}$  impurity  $V_0^\mu = \delta_{\mu,z^2}V_0$  and neglects the effect of selfconsistent density modulations, while the CBdG result includes a multiorbital impurity and selfconsistently converged the mean fields. Repeating the CBdG procedure without selfconsistency and assuming a pure  $d_{z^2}$  impurity exactly reproduces the expected resonant state positions as seen in 2 (d). The close correspondence between the T-matrix predictions of resonant states and the obtained phase diagrams indicate that these regions of local order can be efficiently obtained by first considering the homogeneous Greens

function. The search of pockets of local magnetic order in  $(U, V_0)$  space is thus made much simpler as approximate phase diagrams can be obtained from a single calculation in the clean system.

#### IV. EFFECTS OF ORBITAL SELECTIVITY

The physics of orbital selectivity has been studied quite extensively in correlated multi-orbital models relevant for FeSCs<sup>37–39</sup>. In particular several groups have applied DMFT<sup>29,30</sup> and slave-spin methods<sup>31,34</sup> to investigate self-energy effects on e.g. the band-structure. Such studies have found strong orbital dependent mass renormalizations and quasi-particle weights  $Z_\mu$ . Motivated by the recent experimental evidence for orbital selectivity in FeSe, we construct also a “dressed” version of the above mean-field model. This can be done most simply by the

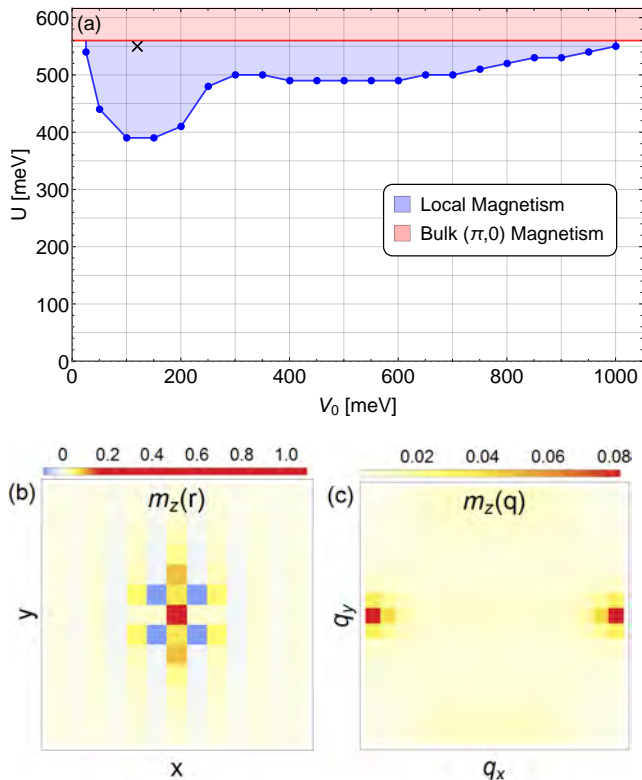


FIG. 3. (a) Phase diagram of the orbital-selective model showing the transition to a bulk  $(\pi, 0)$  phase above  $U_c = 560$  meV (red), and the region of local magnetic order (blue) as a function of the impurity potential strength  $V_0$  and interaction  $U$ . Apart from shifting the phase boundaries, the orbitally selective interaction parameters also fundamentally alter the bulk and local magnetic orderings. (b) Zoom of the local magnetic structure nucleated around the impurity site for potentials close to the bulk transition,  $U = 550$  meV and  $V = 120$  meV (black cross in the phase diagram). (c) Fourier transform of the local magnetic order revealing the highly anisotropic local  $(\pi, 0)$  structure.

prescription

$$c_{i\mu}^\dagger \rightarrow \sqrt{Z_\mu} c_{i\mu}^\dagger, \quad (16)$$

where  $Z_\mu$  denotes the quasi-particle weight for the orbital  $\mu$ . The orbitally selective ansatz in Eq. (16) leads to a modified mean-field theory where all effects of orbital selectivity are contained in dressed interaction parameters

$$U_\mu \rightarrow Z_\mu^2 U_\mu, \quad (17)$$

$$U'_{\mu\nu} \rightarrow Z_\mu Z_\nu U'_{\mu\nu}, \quad (18)$$

with similar expressions for  $J, J'$ . Based on earlier studies of FeSe, in the following we fix the values of the quasi-particle weights  $\{\sqrt{Z_\mu}\} = \{0.2715, 0.9717, 0.4048, 0.9236, 0.5916\}$  for the five Fe 3d orbitals  $\{d_{xy}, d_{x^2-y^2}, d_{xz}, d_{yz}, d_{z^2}\}$ . We note that these values are within the confidence interval of the experimentally extracted values of  $Z_\mu$ .<sup>28,42</sup>

Making this orbitally selective ansatz and including the quasi-particle weights  $Z_\mu$  defined above changes the magnetic phase diagram as shown in Fig. 3 (a). In Ref. 42 the splitting of  $Z_{yz}, Z_{xz}$  quasiparticle weights was shown to result in a leading  $(\pi, 0)$  stripe order instability, in agreement with the  $(\pi, 0)$  ordered bulk phase of our selfconsistent calculations. Close to the phase transition we again find local magnetic order as displayed in Fig. 3 (b), which inherits the bulk  $(\pi, 0)$  structure as seen in the Fourier transform of the magnetization in (c) that exhibits only a peak at  $(\pi, 0)$  and is strongly  $C_2$  symmetric. We find the ordering structure of this local magnetism to vary with the Hubbard  $U$ , starting out strongly  $C_2$ -symmetric just below the bulk phase transition, and then transitioning to a nearly  $C_4$ -symmetric  $(\pi, 0) + (0, \pi)$  structure when approaching the lower local order boundary line. This result is in sharp contrast to the omnipresent nearly  $C_4$ -symmetric magnetization exhibited by the bare model. Similar to the results from the bare model, we find that this region of local magnetic order can be understood from the emergence of resonant states just below the transition.

## V. DETECTION AND DIFFERENTIATION OF LOCAL MAGNETISM

Specifically for the material FeSe, there exists evidence for local magnetism from bulk experimental probes as discussed in the introduction.<sup>19–21</sup> However, given the high quality of the available crystals<sup>18</sup>, local probes like STM may be more suitable for direct investigation of the nature of the electronic state in the vicinity of impurities. For the appearance of static local magnetic order, an obvious experimental technique would be spin-polarized STM measurements. While such approaches have been carried out and are developed recently, it is worth pointing out that also a non-spin polarized experiment can be used to discriminate between the two scenarios of local magnetization which we have investigated. At this point, we do not intend to perform a quantitative simulation of topographies and conductance maps,<sup>59,60</sup> but instead utilize simple symmetry based arguments that hold true also in the case of a correlated electron system. In order to calculate the tunneling current as measured in STM experiments, one needs to consider the LDOS at the position of the STM tip.<sup>61</sup> If the underlying model Hamiltonian is constructed on a lattice, as in the present case, see Eq. (1), the connection to the relevant quantity above the surface of the material, i.e. in the vacuum, can be made by a basis transformation where Wannier functions of the electronic states enter as matrix elements.<sup>59,60</sup> For single impurities, it has been shown that the properties of the elementary cell have imprints on the observed shapes in topographies and conductance maps<sup>59,60,62–64</sup>. In Fig. 4 (a), we show the positions of the atoms at a cleaved surface of FeSe, where the Fe atoms form the lattice as used in our Hamiltonian, while

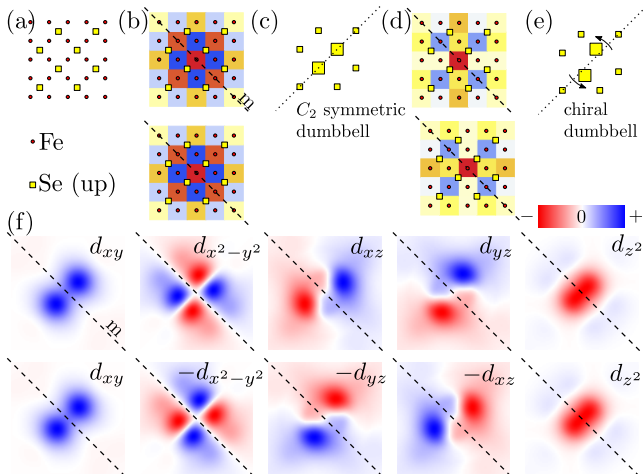


FIG. 4. Symmetries of the order parameter and the Wannier functions on the surface of FeSe. (a) Positions of the Fe atoms (red circles) and the Se atoms (yellow squares) at the surface of FeSe. (b) Magnetic order parameter around an impurity for the case without orbital selectivity which exhibits an (approximate) symmetry for a mirror plane  $m$  along the diagonals (dashed lines). (c) Expected pattern of the local density of states at the STM tip position for case (b). (d) Magnetic order parameter in the orbital selective case which does not exhibit the mirror symmetry such that the expected pattern in an STM experiment shows deviations of the maxima from the symmetry axis (dotted line) (e). (f) Cuts through the five Wannier functions for FeSe<sup>59,60</sup> (red/blue: negative/positive) centered at one Fe atom which have definite symmetry properties with respect to mirror plane  $m$  (lower row: mirror operation applied to function).

the Se atoms above the Fe plane are arranged in a rotated lattice with larger lattice constant which is also observed in STM experiments<sup>22,40,41</sup>. For the case of FeSe, a Fe centered impurity, leads to the observation of a dumbbell originating from the tails of the Wannier functions that have weights close the positions of the Se atoms at the surface of the material.<sup>59</sup>

Now, let us turn to the symmetries of the magnetic order parameter as presented in Figs. 1 and 3 by considering a mirror plane  $m$  along the diagonals of the Fe lattice, as shown by the dashed line in Fig. 4. The Wannier functions of the five relevant states at one Fe atom, of course have definite symmetry properties under this operation which is shown explicitly in Fig. 4 (f) where in the top row, maps of Wannier functions in FeSe above the surface, i.e. at the STM tip are presented and in the lower row, a mirror operation has been applied. First,

we note that the shape of the wavefunctions have lower symmetry than the corresponding atomic wavefunctions and second, the  $d_{xz}$  and  $d_{yz}$  Wannier functions exhibit a chiral structure of opposite direction. Turning now to the two patterns of local magnetic order, we see that for the order of  $(\pi, \pi)$  type, Fig. 4 (b), the mirror plane is a symmetry and therefore the expected pattern in an STM experiment will be symmetric with respect to the mirror plane  $m$  as well, such that one should expect that enhancements at Se positions should be along the diagonal (dotted line) as presented schematically in Fig. 4 (c)<sup>65</sup>. As for the chiral components of the  $d_{xz}$  and  $d_{yz}$  Wannier functions, these will enter with equal weights in the calculation of the LDOS such that the final pattern does not exhibit any chiral character. This situation is different for the local magnetic order parameter of  $(\pi, 0)$  type which obviously does not have a definite symmetry under the mirror operation  $m$ , Fig. 4 (d) and therefore should produce a pattern in the LDOS where the maxima are away from the dotted line in Fig. 4 (e). Similar features have been found in bulk FeSe<sup>40</sup> and have been recently analyzed quantitatively in experiments reporting local impurity-induced magnetization in thin films of FeSe<sup>22</sup>. The direction of the deviation depends on the details of the orbital structure of the local order parameter, and could also switch as a function of bias voltage.

## VI. CONCLUSIONS

In summary, we have explored theoretically the induction of local static magnetic order by nonmagnetic impurity potentials in a model relevant for FeSe. We have mapped out the regions of the phase diagram where such order is present, and investigated the role of orbital-selectivity. The latter may strongly alter the magnetic structure of both long-range and short-range magnetism. Finally we discussed the detection of local magnetic order by non-spin-polarized STM measurements and provided simple symmetry-based arguments to illustrate how this technique may be used to differentiate between distinct forms of induced local magnetic order.

## VII. ACKNOWLEDGEMENTS

We acknowledge useful discussions with M. N. Gastiasoro, P. J. Hirschfeld, and Daniel D. Scherer. The Center for Nanostructured Graphene is supported by the Danish National Research Foundation, Project DNRF103.

<sup>1</sup> Anna E. Böhrer and Andreas Kreisel, “Nematicity, magnetism and superconductivity in FeSe,” *J. Phys. C* **30**, 023001 (2018).

<sup>2</sup> S. Medvedev, T. M. McQueen, I. A. Troyan, T. Palasyuk, M. I. Erements, R. J. Cava, S. Naghavi, F. Casper, V. Ksenofontov, G. Wortmann, and C. Felser, “Electronic and magnetic phase diagram of  $\beta$ -Fe<sub>1.01</sub> with superconduct-

- tivity at 36.7 K under pressure,” *Nature Mat.* **8**, 630–633 (2009).
- <sup>3</sup> M. Bendele, A. Ichsanow, Yu. Pashkevich, L. Keller, Th. Strässle, A. Gusev, E. Pomjakushina, K. Conder, R. Khasanov, and H. Keller, “Coexistence of superconductivity and magnetism in  $\text{FeSe}_{1-x}$  under pressure,” *Phys. Rev. B* **85**, 064517 (2012).
  - <sup>4</sup> J. P. Sun, K. Matsuura, G. Z. Ye, Y. Mizukami, M. Shimozawa, K. Matsubayashi, M. Yamashita, T. Watashige, S. Kasahara, Y. Matsuda, J. Q. Yan, B. C. Sales, Y. Uwatoko, J. G. Cheng, and T. Shibauchi, “Dome-shaped magnetic order competing with high-temperature superconductivity at high pressures in FeSe,” *Nat. Commun.* **7**, 12146 (2016).
  - <sup>5</sup> K. Kothapalli, A. E. Böhmer, W. T. Jayasekara, B. G. Ueland, P. Das, A. Sapkota, V. Taufour, Y. Xiao, E. E. Alp, S. L. Bud’ko, P. C. Canfield, A. Kreyssig, and A. I. Goldman, “Strong cooperative coupling of pressure-induced magnetic order and nematicity in FeSe,” *Nat. Commun.* **7**, 12728 (2016).
  - <sup>6</sup> Matthew Burrard-Lucas, David G. Free, Stefan J. Sedlmaier, Jack D. Wright, Simon J. Cassidy, Yoshiaki Hara, Alex J. Corkett, Tom Lancaster, Peter J. Baker, Stephen J. Blundell, and Simon J. Clarke, “Enhancement of the superconducting transition temperature of FeSe by intercalation of a molecular spacer layer,” *Nat. Mater.* **12**, 15–19 (2013).
  - <sup>7</sup> T. P. Ying, X. L. Chen, G. Wang, S. F. Jin, T. T. Zhou, X. F. Lai, H. Zhang, and W. Y. Wang, “Observation of superconductivity at 30~46K in  $\text{A}_x\text{Fe}_2\text{Se}_2$  ( $\text{A} = \text{Li, Na, Ba, Sr, Ca, Yb, and Eu}$ ),” *Scientific Reports* **2**, 426 (2012).
  - <sup>8</sup> A. Krzton-Maziopa, V. Svitlyk, E. Pomjakushina, R. Puzniak, and K. Conder, “Superconductivity in alkali metal intercalated iron selenides,” *J. Phys. C* **28**, 293002 (2016).
  - <sup>9</sup> Qing-Yan Wang, Zhi Li, Wen-Hao Zhang, Zuo-Cheng Zhang, Jin-Song Zhang, Wei Li, Hao Ding, Yun-Bo Ou, Peng Deng, Kai Chang, Jing Wen, Can-Li Song, Ke He, Jin-Feng Jia, Shuai-Hua Ji, Ya-Yu Wang, Li-Li Wang, Xi Chen, Xu-Cun Ma, and Qi-Kun Xue, “Interface-induced high-temperature superconductivity in single unit-cell FeSe films on  $\text{SrTiO}_3$ ,” *Chin. Phys. Lett.* **29**, 037402 (2012).
  - <sup>10</sup> Y. Zhang, M. Yi, Z.-K. Liu, W. Li, J. J. Lee, R. G. Moore, M. Hashimoto, M. Nakaajima, H. Eisaki, S.-K. Mo, Z. Hussain, T. P. Devereaux, Z.-X. Shen, and D. H. Lu, “Distinctive orbital anisotropy observed in the nematic state of a FeSe thin film,” *Phys. Rev. B* **94**, 115153 (2016).
  - <sup>11</sup> T. Imai, K. Ahilan, F. L. Ning, T. M. McQueen, and R. J. Cava, “Why does undoped FeSe become a high- $T_c$  superconductor under pressure?” *Phys. Rev. Lett.* **102**, 177005 (2009).
  - <sup>12</sup> Daniel D. Scherer, A. C. Jacko, Christoph Friedrich, Ersoy Şaşıoğlu, Stefan Blügel, Roser Valentí, and Brian M. Andersen, “Interplay of nematic and magnetic orders in FeSe under pressure,” *Phys. Rev. B* **95**, 094504 (2017).
  - <sup>13</sup> M. C. Rahn, R. A. Ewings, S. J. Sedlmaier, S. J. Clarke, and A. T. Boothroyd, “Strong  $(\pi, 0)$  spin fluctuations in  $\beta$ -FeSe observed by neutron spectroscopy,” *Phys. Rev. B* **91**, 180501 (2015).
  - <sup>14</sup> Qisi Wang, Yao Shen, Bingying Pan, Xiaowen Zhang, K. Ikeuchi, K. Iida, A. D. Christianson, H. C. Walker, D. T. Adroja, M. Abdel-Hafez, Xiaojia Chen, D. A. Chareev, A. N. Vasiliev, and Jun Zhao, “Magnetic ground state of FeSe,” *Nat. Comm.* **7**, 12182 (2016).
  - <sup>15</sup> Q. Wang, Y. Shen, B. Pan, Y. Hao, M. Ma, F. Zhou, P. Steffens, K. Schmalzl, T. R. Forrest, M. Abdel-Hafez, X. Chen, D. A. Chareev, A. N. Vasiliev, P. Bourges, Y. Sidis, H. Cao, and J. Zhao, “Strong interplay between stripe spin fluctuations, nematicity and superconductivity in FeSe,” *Nat. Mater.* **15**, 159–163 (2016).
  - <sup>16</sup> Mingwei Ma, Philippe Bourges, Yvan Sidis, Yang Xu, Shiyan Li, Biaoyan Hu, Jiarui Li, Fa Wang, and Yuan Li, “Prominent role of spin-orbit coupling in FeSe revealed by inelastic neutron scattering,” *Phys. Rev. X* **7**, 021025 (2017).
  - <sup>17</sup> Brian M. Andersen, Siegfried Graser, and P. J. Hirschfeld, “Disorder-induced freezing of dynamical spin fluctuations in underdoped cuprate superconductors,” *Phys. Rev. Lett.* **105**, 147002 (2010).
  - <sup>18</sup> A. E. Böhmer, F. Hardy, F. Eilers, D. Ernst, P. Adelman, P. Schweiss, T. Wolf, and C. Meingast, “Lack of coupling between superconductivity and orthorhombic distortion in stoichiometric single-crystalline FeSe,” *Phys. Rev. B* **87**, 180505 (2013).
  - <sup>19</sup> Mingquan He, Liran Wang, Frédéric Hardy, Liping Xu, Thomas Wolf, Peter Adelman, and Christoph Meingast, “Evidence for short-range magnetic order in the nematic phase of FeSe from anisotropic in-plane magnetotriaxion and susceptibility measurements,” *Phys. Rev. B* **97**, 104107 (2018).
  - <sup>20</sup> V. Grinenko, R. Sarkar, P. Materne, S. Kamusella, A. Yamashita, Y. Takano, Y. Sun, T. Tamegai, D. V. Efremov, S.-L. Drechsler, J.-C. Orain, T. Goko, R. Scheuermann, H. Luetkens, and H.-H. Klauss, “Low-temperature breakdown of antiferromagnetic quantum critical behavior in FeSe,” *Phys. Rev. B* **97**, 201102 (2018).
  - <sup>21</sup> R. Khasanov, K. Conder, E. Pomjakushina, A. Amato, C. Baines, Z. Bukowski, J. Karpinski, S. Katrych, H.-H. Klauss, H. Luetkens, A. Shengelaya, and N. D. Zhigadlo, “Evidence of nodeless superconductivity in  $\text{FeSe}_{0.85}$  from a muon-spin-rotation study of the in-plane magnetic penetration depth,” *Phys. Rev. B* **78**, 220510 (2008).
  - <sup>22</sup> Wei Li, Yan Zhang, Peng Deng, Zhilin Xu, S.-K. Mo, Ming Yi, Hao Ding, M. Hashimoto, R. G. Moore, D.-H. Lu, Xi Chen, Z.-X. Shen, and Qi-Kun Xue, “Stripes developed at the strong limit of nematicity in FeSe film,” *Nat. Phys.* **13**, 957 (2017).
  - <sup>23</sup> Y. Zhou, L. Miao, P. Wang, F. F. Zhu, W. X. Jiang, S. W. Jiang, Y. Zhang, B. Lei, X. H. Chen, H. F. Ding, Hao Zheng, W. T. Zhang, Jin-feng Jia, Dong Qian, and D. Wu, “Antiferromagnetic order in epitaxial FeSe films on  $\text{SrTiO}_3$ ,” *Phys. Rev. Lett.* **120**, 097001 (2018).
  - <sup>24</sup> P. S. Wang, P. Zhou, S. S. Sun, Y. Cui, T. R. Li, Hechang Lei, Ziqiang Wang, and Weiqiang Yu, “Robust short-range-ordered nematicity in FeSe evidenced by high-pressure NMR,” *Phys. Rev. B* **96**, 094528 (2017).
  - <sup>25</sup> P. Wiecki, M. Nandi, A. E. Böhmer, S. L. Bud’ko, P. C. Canfield, and Y. Furukawa, “NMR evidence for static local nematicity and its cooperative interplay with low-energy magnetic fluctuations in FeSe under pressure,” *Phys. Rev. B* **96**, 180502 (2017).
  - <sup>26</sup> Shantanu Mukherjee, A. Kreisel, P. J. Hirschfeld, and Brian M. Andersen, “Model of electronic structure and superconductivity in orbitally ordered FeSe,” *Phys. Rev. Lett.* **115**, 026402 (2015).
  - <sup>27</sup> A. Kreisel, Shantanu Mukherjee, P. J. Hirschfeld, and Brian M. Andersen, “Spin excitations in a model of FeSe with orbital ordering,” *Phys. Rev. B* **92**, 224515 (2015).

- <sup>28</sup> A. Kreisel, B. M. Andersen, and P. J. Hirschfeld, “Itinerant approach to magnetic neutron scattering of FeSe: effect of orbital selectivity,” ArXiv e-prints (2018), arXiv:1807.09482 [cond-mat.supr-con].
- <sup>29</sup> K. Haule and G. Kotliar, “Coherence-incoherence crossover in the normal state of iron oxypnictides and importance of Hund’s rule coupling,” New J. Phys. **11**, 025021 (2009).
- <sup>30</sup> Z. P. Yin, K. Haule, and G. Kotliar, “Kinetic frustration and the nature of the magnetic and paramagnetic states in iron pnictides and iron chalcogenides,” Nat. Mater. **10**, 932 (2011).
- <sup>31</sup> Luca de’ Medici, Jernej Mravlje, and Antoine Georges, “Janus-faced influence of Hund’s rule coupling in strongly correlated materials,” Phys. Rev. Lett. **107**, 256401 (2011).
- <sup>32</sup> Nicola Lanatà, Hugo U. R. Strand, Gianluca Giovannetti, Bo Hellsing, Luca de’ Medici, and Massimo Capone, “Orbital selectivity in Hund’s metals: The iron chalcogenides,” Phys. Rev. B **87**, 045122 (2013).
- <sup>33</sup> Antoine Georges, Luca de’ Medici, and Jernej Mravlje, “Strong correlations from Hund’s coupling,” Ann. Rev. Cond. Mat. Phys. **4**, 137–178 (2013).
- <sup>34</sup> Luca de’ Medici, Gianluca Giovannetti, and Massimo Capone, “Selective Mott physics as a key to iron superconductors,” Phys. Rev. Lett. **112**, 177001 (2014).
- <sup>35</sup> L. Fanfarillo and E. Bascones, “Electronic correlations in Hund metals,” Phys. Rev. B **92**, 075136 (2015).
- <sup>36</sup> Luca de’ Medici and Massimo Capone, “Modeling many-body physics with slave-spin mean-field: Mott and Hund’s physics in Fe-superconductors,” in *The Iron Pnictide Superconductors: An Introduction and Overview*, edited by Ferdinando Mancini and Roberta Citro (Springer International Publishing, Cham, 2017) pp. 115–185.
- <sup>37</sup> Ambroise van Roekeghem, Pierre Richard, Hong Ding, and Silke Biermann, “Spectral properties of transition metal pnictides and chalcogenides: Angle-resolved photoemission spectroscopy and dynamical mean-field theory,” C. R. Phys. **17**, 140 (2016), iron-based superconductors / Supraconducteurs à base de fer.
- <sup>38</sup> Daniel Guterding, Steffen Backes, Milan Tomić, Harald O. Jeschke, and Roser Valentí, “Ab initio perspective on structural and electronic properties of iron-based superconductors,” Phys. Status. Solidi B **254**, 1600164–n/a (2017), 1600164.
- <sup>39</sup> L. de Medici, *Iron-Based Superconductivity, Weak and Strong Correlations in Fe Superconductors*, edited by Peter D. Johnson, Guangyong Xu, and Wei-Guo Yin, Springer Series in Materials Science (Springer, 2015).
- <sup>40</sup> A. Kostin, P. O. Sprau, A. Kreisel, Yi Xue Chong, A. E. Böhrer, P. C. Canfield, P. J. Hirschfeld, B. M. Andersen, and J. C. Séamus Davis, “Visualizing orbital-selective quasiparticle interference in the Hund’s metal state of FeSe,” Nat. Mater. **17**, 869–874 (2018).
- <sup>41</sup> P. O. Sprau, A. Kostin, A. Kreisel, A. E. Böhrer, V. Taufour, P. C. Canfield, S. Mukherjee, P. J. Hirschfeld, B. M. Andersen, and J. C. Séamus Davis, “Discovery of orbital-selective Cooper pairing in FeSe,” Science **357**, 75–80 (2017).
- <sup>42</sup> Andreas Kreisel, Brian M. Andersen, P. O. Sprau, A. Kostin, J. C. Séamus Davis, and P. J. Hirschfeld, “Orbital selective pairing and gap structures of iron-based superconductors,” Phys. Rev. B **95**, 174504 (2017).
- <sup>43</sup> H. Alloul, J. Bobroff, M. Gabay, and P. J. Hirschfeld, “Defects in correlated metals and superconductors,” Rev. Mod. Phys. **81**, 45–108 (2009).
- <sup>44</sup> Hiroki Tsuchiura, Yukio Tanaka, Masao Ogata, and Satoshi Kashiwaya, “Local magnetic moments around a nonmagnetic impurity in the two-dimensional  $t$ - $J$  model,” Phys. Rev. B **64**, 140501 (2001).
- <sup>45</sup> Ziqiang Wang and Patrick A. Lee, “Local moment formation in the superconducting state of a doped Mott insulator,” Phys. Rev. Lett. **89**, 217002 (2002).
- <sup>46</sup> Jian-Xin Zhu, Ivar Martin, and A. R. Bishop, “Spin and charge order around vortices and impurities in high- $T_c$  superconductors,” Phys. Rev. Lett. **89**, 067003 (2002).
- <sup>47</sup> Yan Chen and C. S. Ting, “States of local moment induced by nonmagnetic impurities in cuprate superconductors,” Phys. Rev. Lett. **92**, 077203 (2004).
- <sup>48</sup> J. W. Harter, B. M. Andersen, J. Bobroff, M. Gabay, and P. J. Hirschfeld, “Antiferromagnetic correlations and impurity broadening of NMR linewidths in cuprate superconductors,” Phys. Rev. B **75**, 054520 (2007).
- <sup>49</sup> Hiroshi Kontani and Masanori Ohno, “Effect of a nonmagnetic impurity in a nearly antiferromagnetic Fermi liquid: Magnetic correlations and transport phenomena,” Phys. Rev. B **74**, 014406 (2006).
- <sup>50</sup> Maria N. Gastiasoro, P. J. Hirschfeld, and Brian M. Andersen, “Impurity states and cooperative magnetic order in Fe-based superconductors,” Phys. Rev. B **88**, 220509 (2013).
- <sup>51</sup> Maria N. Gastiasoro and Brian M. Andersen, “Local magnetization nucleated by non-magnetic impurities in Fe-based superconductors,” Journal of Superconductivity and Novel Magnetism **28**, 1321–1324 (2015).
- <sup>52</sup> Maria N. Gastiasoro, Fabio Bernardini, and Brian M. Andersen, “Unconventional disorder effects in correlated superconductors,” Phys. Rev. Lett. **117**, 257002 (2016).
- <sup>53</sup> Maria N. Gastiasoro, I. Paul, Y. Wang, P. J. Hirschfeld, and Brian M. Andersen, “Emergent defect states as a source of resistivity anisotropy in the nematic phase of iron pnictides,” Phys. Rev. Lett. **113**, 127001 (2014).
- <sup>54</sup> M. N. Gastiasoro and B. M. Andersen, “Enhancing superconductivity by disorder,” ArXiv e-prints (2017), arXiv:1712.02656 [cond-mat.supr-con].
- <sup>55</sup> Alexander Weiße, Gerhard Wellein, Andreas Alvermann, and Holger Fehske, “The kernel polynomial method,” Rev. Mod. Phys. **78**, 275–306 (2006).
- <sup>56</sup> M. N. Gastiasoro, *Emergent disorder phenomena in correlated Fe-based superconductors*, Ph.D. thesis, University of Copenhagen (2016).
- <sup>57</sup> Maria N. Gastiasoro and Brian M. Andersen, “Competing magnetic double- $q$  phases and superconductivity-induced reentrance of  $C_2$  magnetic stripe order in iron pnictides,” Phys. Rev. B **92**, 140506 (2015).
- <sup>58</sup> M. N. Gastiasoro and B. M. Andersen, “Enhancing Superconductivity by Disorder,” ArXiv e-prints (2017), arXiv:1712.02656 [cond-mat.supr-con].
- <sup>59</sup> Peayush Choubey, T. Berlijn, A. Kreisel, C. Cao, and P. J. Hirschfeld, “Visualization of atomic-scale phenomena in superconductors: Application to FeSe,” Phys. Rev. B **90**, 134520 (2014).
- <sup>60</sup> A. Kreisel, R. Nelson, T. Berlijn, W. Ku, Ramakrishna Aluru, Shun Chi, Haibiao Zhou, Udai Raj Singh, Peter Wahl, Ruixing Liang, Walter N. Hardy, D. A. Bonn, P. J. Hirschfeld, and Brian M. Andersen, “Towards a quantitative description of tunneling conductance of superconductors: Application to LiFeAs,” Phys. Rev. B **94**, 224518 (2016).

- <sup>61</sup> J. Tersoff and D. R. Hamann, “Theory of the scanning tunneling microscope,” *Phys. Rev. B* **31**, 805–813 (1985).
- <sup>62</sup> A. Kreisel, Peayush Choubey, T. Berlijn, W. Ku, B. M. Andersen, and P. J. Hirschfeld, “Interpretation of scanning tunneling quasiparticle interference and impurity states in cuprates,” *Phys. Rev. Lett.* **114**, 217002 (2015).
- <sup>63</sup> Shun Chi, Ramakrishna Aluru, Udai Raj Singh, Ruixing Liang, Walter N. Hardy, D. A. Bonn, A. Kreisel, Brian M. Andersen, R. Nelson, T. Berlijn, W. Ku, P. J. Hirschfeld, and Peter Wahl, “Impact of iron-site defects on superconductivity in LiFeAs,” *Phys. Rev. B* **94**, 134515 (2016).
- <sup>64</sup> Dennis Huang and Jennifer E. Hoffman, “Monolayer FeSe on SrTiO<sub>3</sub>,” *Ann. Rev. Cond. Mat. Phys.* **8**, 311–336 (2017).
- <sup>65</sup> Strictly speaking, the magnetization profile in Fig. 4(c) breaks  $C_4$  symmetry since it is generated from the nematic FeSe bandstructure. This, however, is a tiny effect not important for the general arguments for differentiation between different magnetization patterns by STM.

## Paper III

### Tunable valley Hall effect in graphene superlattices

Johannes H. J. Martiny, Kristen Kaasbjerg, and Antti-Pekka Jauho

*Physical Review B* **00**, 005400 (2019)

# Tunable valley Hall effect in gate-defined graphene superlattices

Johannes H. J. Martiny,\* Kristen Kaasbjerg, and Antti-Pekka Jauho  
*Center for Nanostructured Graphene (CNG), Department of Physics,  
Technical University of Denmark, DK-2800 Kongens Lyngby, Denmark*  
(Dated: October 21, 2019)

We theoretically investigate gate-defined graphene superlattices with broken inversion symmetry as a platform for realizing tunable valley dependent transport. Our analysis is motivated by recent experiments [C. Forsythe *et al.*, Nat. Nanotechnol. **13**, 566 (2018)] wherein gate-tunable superlattice potentials have been induced on graphene by nanostructuring a dielectric in the graphene/patterned-dielectric/gate structure. We demonstrate how the electronic tight-binding structure of the superlattice system resembles a gapped Dirac model with associated valley dependent transport using an unfolding procedure. In this manner we obtain the valley Hall conductivities from the Berry curvature distribution in the superlattice Brillouin zone, and demonstrate the tunability of this conductivity by the superlattice potential. Finally, we calculate the valley Hall angle relating the transverse valley current and longitudinal charge current and demonstrate the robustness of the valley currents against irregularities in the patterned dielectric.

## I. INTRODUCTION

The electronic structure of graphene hosts well-separated degenerate minima in momentum space which are labeled as the  $K, K'$  valleys.<sup>1</sup> Electrons in graphene are thus described not only by their charge and spin but also by their valley degree of freedom which is conserved when intervalley scattering is absent. In recent years this new degree of freedom has been proposed as a stable carrier of information in so-called valleytronics.<sup>2–6</sup>

In hexagonal materials lacking inversion symmetry, control of the valley degree of freedom can be accomplished by generating opposite transverse currents of carriers with different valley index when applying an in-plane electric field. This valley Hall effect is the result of a nonzero Berry curvature of opposite sign in each valley which acts as a valley dependent magnetic field in momentum space.<sup>7</sup> Indirect measurements of valley currents in such materials have been suggested in e.g. bilayer graphene under transverse electric field,<sup>8–10</sup> or in graphene superlattices defined by an underlying hexagonal boron nitride (hBN) substrate aligned commensurately with the graphene sheet.<sup>11</sup> These observations have been made in nonlocal transport measurements where a current flowing between two terminals in a Hall bar induces a nonlocal voltage between two different terminals through a combination of the direct and indirect valley Hall effects.

The valley Hall effect and the associated valley currents are absent in pristine graphene unless perturbations break the sublattice symmetry of the bipartite lattice. The electronic properties of graphene have previously been engineered using e.g. strain,<sup>10,12,13</sup> substrate effects,<sup>14–16</sup> or lithographic etching of a periodic array of holes in the graphene sheet.<sup>17–19</sup> Recently, a new approach to band structure engineering has been demonstrated where holes or indentations are made not in the graphene sheet but in an underlying dielectric instead.<sup>20</sup> This procedure avoids introducing any short range disorder to the graphene sheet, and thus limits intervalley

scattering while effectively inducing a superlattice potential on the graphene sheet by a gate under the dielectric. As such, this nanostructuring approach seems very well suited for valleytronic applications.

In this work we theoretically investigate the electronic structure and valley dependent properties of a graphene superlattice geometrically structured for valleytronics. We define a superlattice by a periodic external potential corresponding to a graphene sheet gated through a nanostructured dielectric with a regular array of indentations or holes. Symmetry analysis of this structure reveals that a finite valley Hall effect is possible when these holes do not have an inversion center. Our choice of superlattice structure is supported by earlier studies demonstrating extremely stable band gaps with respect to disorder when perturbations break the graphene A/B sublattice symmetry,<sup>21,22</sup> and by the natural formation of such deformations in hBN.<sup>23</sup>

We study the electronic band structure of these systems within a tight-binding model and show the emergence of tunable band gaps in the energy spectrum as the superlattice potential is applied. Using an unfolding procedure for the spectral weight and electronic Berry curvature,<sup>24</sup> the superlattice results are mapped to the graphene Brillouin zone where we recover a gapped  $K, K'$  valley structure with Berry curvature distributions of opposite sign in each valley. We compare these supercell tight-binding results with an analytical model of graphene with sublattice asymmetry and an overall shift in the Fermi energy, and find a close resemblance at small superlattice potentials. We furthermore compute the valley-resolved transverse conductivities arising from the finite Berry curvature distributions in each valley, and demonstrate the tunability of these conductivities with the strength of the applied superlattice potential, as well as the position of the Fermi energy. Finally, a Boltzmann equation approach for the longitudinal conductivity enables us to calculate the valley Hall angle at different electronic fillings and make predictions for experimental observations in nonlocal transport experiments.<sup>25</sup>

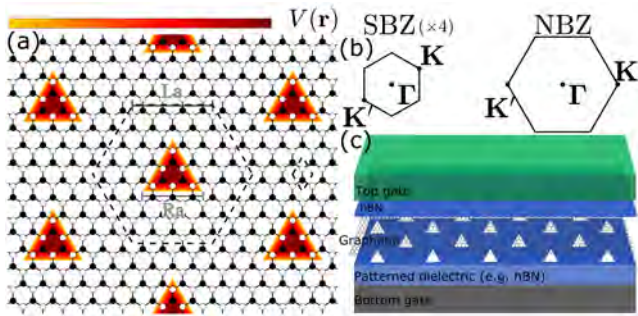


FIG. 1. (a) The superlattice system considered in this work: a graphene sheet (empty and filled circles) gated through a patterned dielectric with triangular zigzag-edged holes yielding an effective superlattice potential (red-to-black gradient). The supercell is marked by the dashed lines (left), alongside the normal (graphene) unit cell (right). The lack of inversion center and the sublattice asymmetric structure of the gated regions induce the valley Hall effect under in-plane electric field. The geometry is characterized by the supercell hexagon side length  $L$  and the triangle side length  $R$ . (b) The corresponding supercell (SBZ) and normal (NBZ) Brillouin zone. The SBZ is shown enlarged four times for clarity. (c) Sketch of the considered graphene/nanostructured dielectric/gate structure. Here we show nanopatterned hBN with the naturally occurring triangular zigzag edges holes nucleated on boron sites.

## II. METHOD

We consider a graphene sheet under the effect of a periodic superlattice potential, providing a model for graphene on top of a patterned dielectric. We posit a triangular array of holes etched into the dielectric, and thus a similar structure for the induced superlattice potential in the graphene monolayer as shown in Fig. 1. The hexagonal unit cell of this superlattice is shown in Fig. 1(a), with the induced gate potential indicated by the gradient. The geometries considered can be uniquely described by the supercell hexagon side length  $L$ , and the triangular superlattice potential side length  $R$ . We model the superlattice by a tight-binding Hamiltonian which includes onsite terms arising from the gate induced potential

$$H = \sum_{i,\sigma} V(\mathbf{r}_i) c_{i\sigma}^\dagger c_{i\sigma} + \sum_{\langle ij \rangle, \sigma} t_{ij} c_{i\sigma}^\dagger c_{j\sigma} \quad (1)$$

where  $t_{ij} = -t\delta_{\langle ij \rangle}$ , with  $t = 3.033$  eV, includes nearest neighbor hopping, and  $V(\mathbf{r})$  is the gate-induced potential, defined here along a zigzag edge in the graphene sheet since this edge profile minimizes intervalley scattering.<sup>26,27</sup> The potential corresponds to a zigzag edged triangle etched into e.g. hBN as the dielectric, where such perforations appear naturally nucleated on a single sublattice.<sup>23</sup> In our calculations we consider both perfectly sharp (flat) and smoothly varying spatial profiles of the potential, as well as some degree of armchair

edges caused by edge disorder in the dielectric nanostructuring. In the following we ignore the possible lattice constant mismatch between the hBN and graphene, and the resulting moiré structure. Other inversion symmetry breaking shapes of the induced superlattice potential can also lead to the valley Hall effect in the superlattice. Here we restrict ourselves to the  $C_3$  structures outlined above, wherein stable band gaps and lack of intervalley scattering lead directly to characteristic plateaus of finite valley Hall conductivity.

Our main goal is to calculate the transverse conductivity arising from the valley Hall effect. This effect can be understood from wave-packet dynamics.<sup>28,29</sup> The equation of motion for such a wave-packet composed of states from a single band  $n$ , can in the presence of an electric field be written ( $\hbar = 1$ )

$$\dot{\mathbf{r}}_n(\mathbf{k}) = \partial_{\mathbf{k}} \epsilon_n(\mathbf{k}) - e\mathbf{E} \times \boldsymbol{\Omega}_n(\mathbf{k}) \quad (2)$$

where we recognize the first term on the right-hand side as the conventional band velocity, while the second term is responsible for various anomalous transport phenomena, determined by the electronic Berry curvature

$$\boldsymbol{\Omega}_n(\mathbf{k}) = \nabla_{\mathbf{k}} \times i \langle u_{n\mathbf{k}} | \nabla_{\mathbf{k}} | u_{n\mathbf{k}} \rangle, \quad (3)$$

written here in terms of the periodic part of the Bloch state,  $|u_{n\mathbf{k}}\rangle = e^{-i\mathbf{k}\cdot\mathbf{r}} |\psi_{n\mathbf{k}}\rangle$ . In particular, when an in-plane  $E$ -field is applied to a perturbed graphene lattice with broken inversion symmetry, electrons in each valley have opposite Berry curvature and thus acquire transverse anomalous velocity components depending on their valley index, leading to the valley Hall effect.

Valley resolved conductivities follow from the Berry curvature of occupied states by integrating over each valley region separately

$$\sigma_{xy}^{K(K')}(E_F) = -\frac{2e^2}{h} \int_{K(K')} \frac{d^2k}{2\pi} \Omega_{xy}(\mathbf{k}, E_F). \quad (4)$$

Here, the integration region in each case is exactly half the Brillouin zone with the  $\Gamma \rightarrow M$  symmetry lines as the borders,<sup>24</sup> and we have defined the Berry curvature of occupied states

$$\Omega_{xy}(\mathbf{k}, E_F) = \sum_n f_n(\mathbf{k}) \Omega_n(\mathbf{k}), \quad (5)$$

with  $f_n(\mathbf{k}) = [e^{(E_{n\mathbf{k}} - E_F)/k_B T} + 1]^{-1}$  the Fermi-Dirac distribution. We fix a low temperature of  $T = 1$  K in the following in order to clearly distinguish the step in the valley resolved conductivity near the band edges.

The valley Hall conductivity is then defined as the difference between the valley-resolved conductivities

$$\sigma_{xy}^v = \sigma_{xy}^K - \sigma_{xy}^{K'}. \quad (6)$$

In the presence of time-reversal symmetry only half the Brillouin zone needs to be considered in the calculation of the valley Hall conductivity since  $\sigma_{xy}^K = -\sigma_{xy}^{K'}$  and thus  $\sigma_{xy}^v = 2\sigma_{xy}^K = -2\sigma_{xy}^{K'}$ .<sup>28</sup>

### A. Unfolding

We now turn to the calculation of the valley-resolved conductivities from the tight-binding supercell results. Diagonalization of the tight-binding Hamiltonian yields the supercell eigenenergies and Bloch states  $E_{n\mathbf{k}}, |\psi_{n\mathbf{k}}\rangle$ , from which we can also obtain the spectral function

$$A(\mathbf{k}, \omega) = \sum_{n\mathbf{k}} \frac{\eta/\pi}{(\omega - E_{n\mathbf{k}})^2 + \eta^2}, \quad (7)$$

where  $\eta$  is a numerical broadening.

The valley-resolved conductivities are not immediately available since the Berry curvature folds into the superlattice Brillouin zone (SBZ) in a nontrivial way, which prohibits the direct application of Eq. (4). Our approach is thus to unfold the Berry curvature obtained in the SBZ back into the graphene (normal) Brillouin zone (NBZ) and recover information about the valley degree of freedom.<sup>30</sup> We note that the considered superlattice potential is a perturbation clearly described in terms of the underlying ordered graphene lattice, and that the unfolded Berry curvature and associated valley Hall conductivity thus remain well-defined.<sup>24,31</sup> Details of this unfolding procedure can be found in Appendix A, and we provide here a short summary.

The central quantity in the unfolding procedure is the overlap between a normal cell orbital  $|\chi_{i\mathbf{k}}\rangle$  with  $\mathbf{k} \in \text{NBZ}$  and a supercell Bloch state  $|\psi_{N\mathbf{K}}\rangle$  with  $\mathbf{K} \in \text{SBZ}$ ,

$$\lambda_{iN\mathbf{k}} = \langle \chi_{i\mathbf{k}} | \psi_{N\mathbf{K}} \rangle, \quad (8)$$

which we can calculate directly from the tight-binding Bloch states.

Quantities in the SBZ can then be unfolded to the NBZ by convolution with the overlap  $\lambda$ , and, e.g., the unfolded spectral function becomes

$$A^{(u)}(\mathbf{k}, \omega) = \sum_i \sum_{N\mathbf{K}} |\lambda_{iN\mathbf{k}}|^2 \frac{\eta/\pi}{(\omega - E_{N\mathbf{K}})^2 + \eta^2}. \quad (9)$$

where the sum over  $i = A, B$  spans the sublattices of graphene, and  $E_{N\mathbf{K}}$  are the band energies of the superlattice. The unfolding of the Berry curvature [Eq. (3)] from the tight-binding result follows in a similar manner but requires a more extensive treatment, since the analogous expression to Eq. (9) becomes gauge dependent.<sup>24,31</sup> Once the unfolded Berry curvature  $\Omega^{(u)}(\mathbf{k}, E_F)$  is obtained by this procedure, the valley-resolved conductivities follow by a simple application of Eq. (4).

### B. Valley Hall angle

We characterize the relative magnitude of the response associated with the valley Hall effect by calculating the valley Hall angle

$$\tan \theta_v = \frac{\sigma_{xy}^v}{\sigma_{xx}}. \quad (10)$$

This angle is finite only close to the band edges where the valley Hall conductivity is nonzero. We obtain the longitudinal conductivity  $\sigma_{xx}$  from a DC Boltzmann equation approach in the relaxation time approximation<sup>32</sup>

$$\sigma_{xx} = 2e^2 \frac{1}{A} \sum_{n\mathbf{k}} \tau_{n\mathbf{k}} v_{n\mathbf{k},x}^2 \delta(E_F - E_{n\mathbf{k}}) \quad (11)$$

where  $A$  is the sample area, and  $\mathbf{v}_{n\mathbf{k}} = (1/\hbar)\nabla_{\mathbf{k}}\epsilon_{n\mathbf{k}}$  is the band velocity component in the  $\hat{x}$  direction. Here, we calculate this analytically from the tight-binding Hamiltonian.

$$\mathbf{v}_{n\mathbf{k}} = \frac{1}{\hbar} \langle n\mathbf{k} | \nabla_{\mathbf{k}} H_{\mathbf{k}} | n\mathbf{k} \rangle. \quad (12)$$

For numerical evaluation of the longitudinal conductivity at low temperatures we approximate the delta function by a Lorentzian  $\delta(E_F - E_{n\mathbf{k}}) \rightarrow \frac{1}{\pi}(\eta/2)[(E_F - E_{n\mathbf{k}})^2 + (\eta/2)^2]^{-1}$  with a constant broadening  $\eta = 3$  meV.

We extract the relaxation time from a typical mobility near the charge neutrality point in hBN encapsulated graphene  $\mu \approx 10^5$  cm<sup>2</sup> V<sup>-1</sup> s<sup>-1</sup> at the given temperature. If we consider the conduction to be limited by charged impurities, the relaxation time varies linearly with the Fermi energy<sup>33</sup>

$$\tau_{k_F} = C_{ci,\tau} E_F, \quad (13)$$

where the proportionality constant is  $C_{ci,\tau} \approx 10$  ps/eV at the chosen mobility. For gapped systems we set  $\tau_{n\mathbf{k}} = C_{ci,\tau} \delta E_{n\mathbf{k}}$  in Eq. (11) where  $\delta E_{n\mathbf{k}}$  is the energy measured from the band edge of the gapped region.

## III. RESULTS

### A. Band structure and Berry curvature in the supercell

We first consider the electronic structure of the superlattice of Fig. 1(a) ( $L = 4, R = 3$ ) directly in the SBZ. For  $V = 0$  we recover the usual graphene band structure folded into the superlattice Brillouin zone [dashed lines in Fig. 2(a)]. For the geometry considered here the  $K, K'$  points are both folded in to the superlattice  $\Gamma_{SC}$  point, resulting in nearly degenerate linear bands around this symmetry point. The splitting of these curves at larger  $|k_x^{SBZ}|$  depends on the choice of the specific cut in  $\mathbf{k}$ -space. When the finite superlattice potential is applied, an effective sublattice asymmetry is obtained on top of a constant overall shift of the bands. Thus, for  $V \neq 0$  a gap opens continuously in the spectrum, with a simultaneous shift of the bands upwards in energy as shown in Fig. 2(a)-(b). For the structures considered in this work the sublattice asymmetry is an intrinsic feature which is not removed by smoothly varying gate potentials, and we thus find these band gaps to be stable with respect to the smoothness of the applied potential

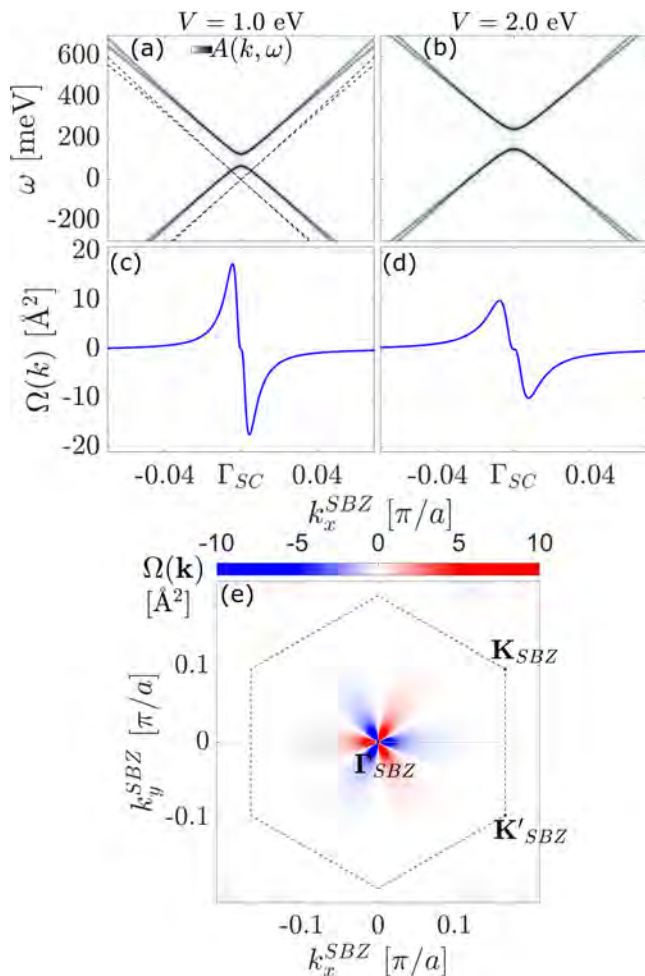


FIG. 2. (a)-(b) Spectral weight (gray surface,  $\eta = 3\text{meV}$ ) close to the SBZ  $\Gamma$  point for different values of the constant superlattice potential  $V(\mathbf{r}_i) = 1\text{ eV}, 2\text{ eV}$ . The dashed lines in (a) show the  $V = 0$  (pristine graphene) band structure. (c)-(d) Corresponding line-cuts of the occupied Berry curvature when the Fermi energy is fixed in the gap at each potential. (e) Supercell Berry curvature in the SBZ with the valence band filled. The pristine system  $K$  and  $K'$  valleys fold to the SBZ  $\Gamma$  point, yielding a sign changing peak centered on this symmetry point. The horizontal dotted line indicates the cut in  $\mathbf{k}$ -space shown above.

with only a minor decrease in the gap magnitude (see Sec. III D. below). We note that the gap may close at larger values of  $|V| \sim t$  depending on the specific geometry of the gated region and supercell width, but the gap formation at  $|V| < t$  considered here is universal to all geometries, as predicted previously for potentials of  $C_3$  symmetry.<sup>22</sup> We demonstrate this universal gap formation in Figure 3(a) where the density of states (DOS) is shown for different extents of the superlattice potential in the supercell. The inset shows the corresponding band gap size ( $\Delta$ ), and the shift in the center of the band gap ( $E_s$ ) as a function of the superlattice potential mag-

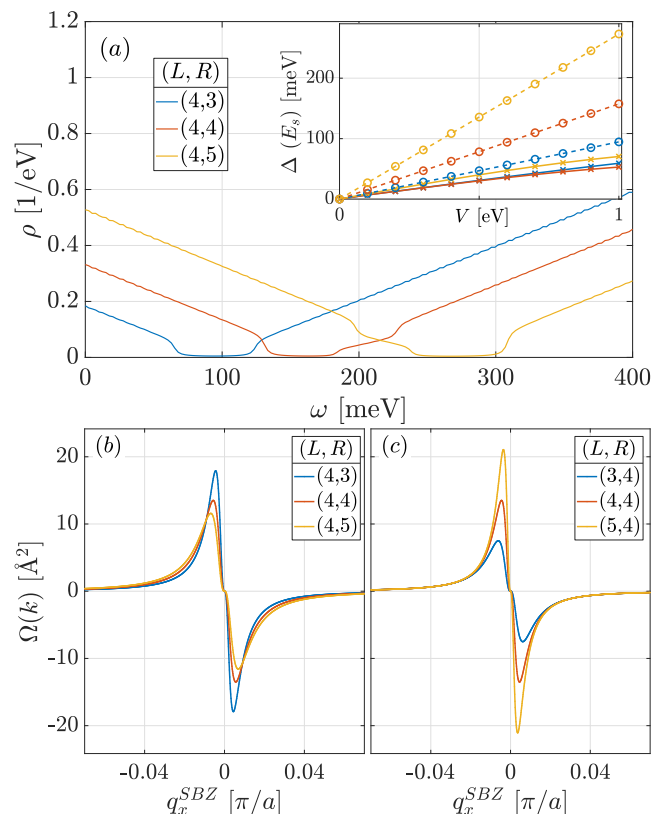


FIG. 3. (a) Density of states for different geometries of the superlattice at  $V = 1\text{ eV}$ . Inset: Band gaps as a function of the superlattice potential magnitude (full lines) for different geometries of the gated region ( $L = 4$ ). The band gap widens as the superlattice potential is increased in all considered geometries. Dashed lines show the corresponding shift ( $E_s$ ) of the center of the band gap as the superlattice potential is increased. This shift increases linearly with increasing superlattice potential, with the slope determined by the size of the gated region ( $R$ ). (b) Linecut of the SBZ Berry curvature in the gap for different geometries of the gated regions ( $L = 4, V = 1\text{ eV}$ ). The shape of the Berry curvature distribution broadens for increasing size of the gated region  $R$ , mirroring the broadening with increasing superlattice potential magnitude  $V$ . (c) The SBZ Berry curvature when the supercell size is varied instead, demonstrating the opposite scaling in the width.

nitude  $V$ . The effect of varying the magnitude of the superlattice potential is similar to that of changing the ratio between the gated region (triangle side length  $R$ ) and the supercell size (hexagon side length  $L$ ), as investigated further in Appendix B. Similar gap openings have been demonstrated previously within the tight-binding model for gated superlattices in Ref. 34, where circular potentials were considered instead. However, the gap opening in Ref. 34 was attributed to the local sublattice asymmetry near the edge, and thus these band gaps were found to be quickly decaying with increasing smoothness of the gate potential due to the disappearance of the local edge asymmetry.

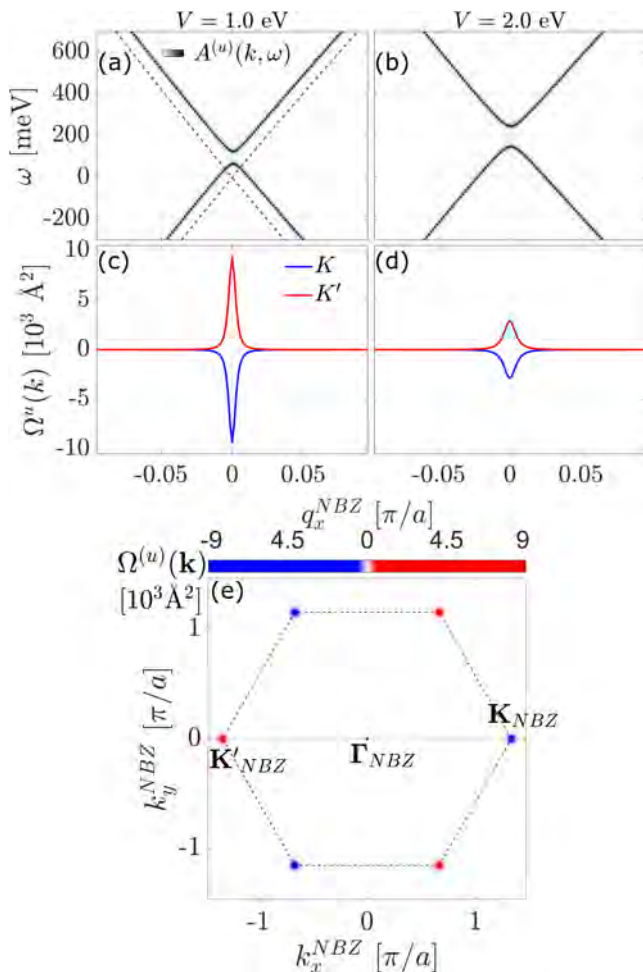


FIG. 4. (a)-(b) Line-cuts of the unfolded spectral weight (gray surface) close to the NBZ  $K$  point for different values of the constant superlattice potential  $V(\mathbf{r}_i) = 1$  eV, 2 eV. The result at the  $K'$  point along this same cut in  $\mathbf{k}$ -space can be found by reflection around the central point  $\Gamma_\tau$ , and thus has similar structure. (c)-(d) Corresponding line-cuts of the unfolded occupied Berry curvature in the  $K$  (blue) and  $K'$  (red) valley with the Fermi energy fixed in the gap at each potential. (e) Unfolded Berry curvature in the NBZ demonstrating equal peaks of opposing signs, indicating the presence of transverse valley currents. The dotted line indicates the cut in  $\mathbf{k}$ -space shown above.

In Fig. 2(c)-(d) we show the supercell Berry curvature along the same cut in  $\mathbf{k}$ -space as in (a)-(b). The distribution displays a double peaked structure, with a clear sign change appearing exactly at the  $\Gamma_{SC}$  point. As the superlattice potential is increased, this distribution is noticeably broadened but retains its shape. A similar result is obtained if the supercell and potential geometries are changed instead as shown in Fig. 3(b). The full threefold symmetry of this distribution arising from the supercell folding is shown in Fig. 2(e) where the Berry curvature is shown in the full SBZ. The rotational symmetry of this distribution follows from the specific folding of the NBZ

valleys into the SBZ. The same symmetrical distribution is found when other superlattice geometries are considered, the only variation being in the width of the Berry curvature peaks. This effect is illustrated in Fig. 3(b).

## B. Unfolded Berry curvature and valley Hall conductivity

Prior to our consideration of the unfolded result, it is instructive to compare the superlattice tight-binding calculations with results from a well-known model of the valley Hall effect in graphene. For this purpose, we consider a model which neglects confinement due to the periodic structure of the applied potentials, and simply considers the average potential on the A and B sites of the graphene system, leading to an effective sublattice asymmetry. This corresponds to a gapped Dirac model,

$$H_\tau(\mathbf{q}) = \frac{\sqrt{3}}{2} at(\tau q_x \sigma_x + q_y \sigma_y) + \frac{\Delta}{2} \sigma_z, \quad (14)$$

with  $\tau = \pm 1$  the valley index,  $\mathbf{q} = \mathbf{k} - \tau \mathbf{K}$  measured with respect to the  $K, K'$  points, and  $a$  the graphene lattice constant. The Berry curvature in the  $K, K'$  region close to the gap edge can be derived analytically, e.g. for the conduction band<sup>7</sup>

$$\Omega_{xy}(\mathbf{q}) = \tau \frac{3a^2 t^2 \Delta}{2(\Delta^2 + 3a^2 t^2 |\mathbf{q}|^2)^{3/2}}, \quad (15)$$

with associated Berry phases approaching  $\pm\pi$  for small  $\Delta$ , and hence a quantized valley Hall conductivity following from Eq. (4-6) of  $\sigma_{xy}^v = 2e^2/h$  at the top of the valence band. This simple model with Berry curvature peaks of opposite sign in each valley and quantized valley Hall conductivity will serve as the comparison point for the superlattice results. We note that the utilized full tight-binding model goes beyond the simple decomposition into distinct valleys in the massive Dirac model above, since the tight-binding model includes both valleys and thus the effects of intervalley scattering.<sup>35</sup>

We now turn to the unfolded quantities  $A^{(u)}, \Omega^{(u)}$ , which are shown in Fig. 4. The spectral weight of the nearly degenerate bands in the supercell around the  $\Gamma_{SC}$  point now unfold into the NBZ  $K, K'$  valleys as seen from the line-cut through the  $K$  point in (a)-(b). As such, the unfolded spectral weight resembles the valley structure of the massive Dirac model introduced above. Correspondingly, the unfolded Berry curvature peaks exactly at the center of each valley, but with opposite signs as shown in Fig. 4(c)-(d). The full distribution is shown in Fig. 4(e). Here, we observe sharp peaks around each symmetry point with opposite signs in the entire valley regions. It now becomes clear how the rotational symmetry of the supercell Berry curvature arises. The unfolded Berry curvature peaks of each valley fold into separate regions of the SBZ around the  $\Gamma_{SC}$  point, yielding the flower structure in Fig. 2(e).

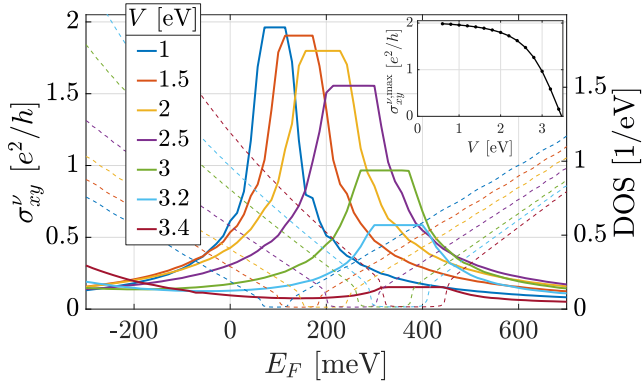


FIG. 5. Valley Hall conductivity as a function of filling (full lines) for varying values of the superlattice potential  $V$ , shown alongside the density of states (dotted lines). Berry curvature accumulated near the band edges causes a saturation of the valley Hall conductivity as the gap is approached, and for small  $V$  the quantized  $2e^2/h$  value of the massive Dirac model is approached. The inset shows the plateau value in the gap as the superlattice potential is tuned. The valley Hall conductivity decays for larger superlattice potentials, as the supercell bands flatten and the unfolded valley structure is lost.

A finite valley Hall effect in these systems is evident from the unfolded Berry curvature distribution, since integration of this quantity around each valley yields finite valley-resolved conductivities of opposite signs. The result of the integration procedure [Eq. (4-6)] is shown in Fig. 5 as a function of the Fermi energy for different values of the superlattice potential. As demonstrated above, the band edges act as Berry curvature hot spots causing a saturation of the valley Hall conductivity as the Fermi energy approaches the gap from below. This plateau then decays when states in the bands above the gap start contributing Berry curvature of opposite sign. In the limit of small  $V$  we found above that the unfolded electronic structure and Berry curvature distribution closely resembles an effective massive Dirac model, and in this case we also find that the valley Hall conductivity approaches a quantized plateau value of  $2e^2/h$  as predicted from Eq. (15). When the superlattice potential is increased this plateau widens as the gap expands and a small variation in the plateau value appears. We note that the numbers of  $k$  points needed to converge the valley Hall conductivity increase dramatically as the potential is decreased since the Berry curvature distribution becomes more sharply peaked. All calculations in this work are performed with  $N_{\mathbf{k}} = 230 \times 230$   $k$ -points.

In the limit of larger superlattice potentials the simple resemblance to the shifted massive Dirac model breaks down, and the valley Hall conductivity decays from the quantized plateau value of  $2e^2/h$  as demonstrated in Fig. 5, ultimately vanishing at  $V = 3.4$  eV. In this limit the superlattice potential approaches the energy scale of the hopping  $t$  and the electronic structure is strongly per-

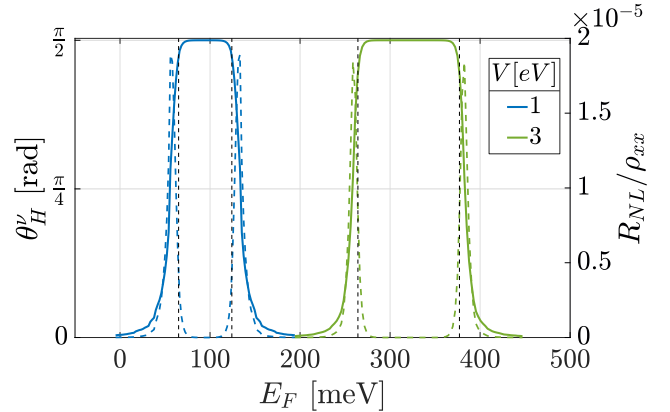


FIG. 6. Valley Hall angle (full lines) and expected nonlocal resistance signal (dashed lines) close to the band edge for two values of the superlattice potential  $V = 1$  eV, 3 eV. The band gap is indicated by the vertical dashed lines. The valley Hall angle is only finite close to the band edge where  $\sigma_{xy} \sim \sigma_{xx}$ , and approaches  $\pi/2$  in the gap. The predicted nonlocal resistance close to the band edges is obtained using the expression of Ref. 25. The peaks in the ratio  $R_{NL}/\rho_{xx}$  occur exactly at the  $\theta_v = \pi/4$  point, i.e. when the valley Hall and longitudinal conductivities are equal,  $\sigma_{xy}^v = \sigma_{xx}$ . These peaks in the nonlocal response shift as the superlattice potential is tuned.

turbed, resulting in a Berry curvature distribution diverging from the simple model. In particular, the valence and conduction bands flatten and the valley-structure of the unfolded spectral weight is lost.

### C. Valley Hall angle and associated nonlocal response

In Fig. 6(a) we show the valley Hall angle  $\theta_H^v = \arctan \sigma_{xy}^v / \sigma_{xx}$ , which is the ratio of the magnitude of the transverse valley and longitudinal charge currents. The angle is finite only close to the band edge where the valley Hall conductivity peaks and exceeds the longitudinal conductivity in a small interval. Following Ref. 25, we estimate the valley Hall contribution to the nonlocal resistance from the valley Hall angle in, e.g., a Hall bar of width  $W$ , with inter-terminal distance  $d$ , and valley diffusion length  $l_v$ :

$$\Delta R_{NL}/\rho_{xx} = \frac{W}{2L_v} \frac{\tan^2 \theta_v}{1 + \tan^2 \theta_v} e^{-|d|/L_v}, \quad (16)$$

where  $L_v = l_v \sqrt{1 + \tan^2 \theta_v}$  is a renormalized valley diffusion length.

We note that this interpretation relies on the picture of bulk valley currents carried by subgap states,<sup>25,36</sup> which is but one interpretation of nonlocal measurements in valley Hall systems. In particular, these currents are missing when the Fermi energy is placed in the gap in Landauer-Büttiker calculations,<sup>37</sup> and only reappear as edge currents when detailed modeling of the electronic structure

and edge profiles are considered.<sup>38</sup> In this work we thus restrict ourselves to making predictions close to the band edge outside the gapped region where the interpretation as bulk valley currents is valid.

The expected nonlocal signal for varying values of the superlattice potential is displayed in Fig. 6(b), for  $W, d, l_v = 100, 10^3, 10^5$  nm. The nonlocal response is shifted as the the superlattice potential is varied, since it peaks near the band edge where the valley Hall angle  $\theta_v$  approaches  $\pi/4$ . This tunability of the nonlocal response with the external potential provides an unambiguous way of separating stray current and valley Hall contributions to the nonlocal resistance.

#### D. Robustness with respect to the dielectric environment

In what follows we consider more realistic potentials based on the specific dielectric environment in patterned dielectric superlattices. In particular, we consider potentials varying smoothly with the distance  $r$  from the edge of the side of the nanostructured indentation in the dielectric to the center, here parametrized by  $V(r)/V_{max} = [\exp((r-1)/u) + 1]^{-1} - 1/2$ , with  $u \in [0, 1]$  a continuous parameter setting the smoothness of the potential,  $u = 0$  being the flat potential considered so far, and  $u = 1$  the extreme case of a linearly decreasing potential. Line profiles of this potential are shown in the inset of Fig. 7, and the full 2D potential for  $u = 0.2$  is shown in the gradient of Fig. 1(a). Further details of the spatial profile of the smoothly varying potential are included in Appendix C.

The valley Hall conductivity obtained for this potential is shown in Fig. 7. The result is similar to that obtained above for the flat potential, although with slightly narrower plateau regions. Additionally, new features appear away from the band edge since degeneracies are lifted and thus the integrated Berry curvature varies in small increments when each band edge is reached. For small potentials we again approach the quantized value in the gap.

Finally, we conclude our analysis of realistic potentials by considering irregularities in the edge of the dielectric etching, which modulates the potential near the edge. We simulate this effect by adding a random potential to the edges of the gated region in the supercell, disrupting the perfect zigzag edges considered thus far which were expected to minimize coupling of the valleys. At each site which is a nearest neighbor to the gate region on edge we add a random potential  $w_{edge} \in [-0.5, 0.5]$  eV, and consider the resulting valley Hall conductivity for different random configurations at a fixed superlattice potential ( $V = 2$  eV,  $u = 0.2$ ). The result of this procedure is shown in Fig. 8 (gray lines), together with the clean limit result (full black line), and the average of the irregular configurations (red dashed line). The application of these random edge potentials does not substantially modify the valley Hall conductivity, which displays a shifted

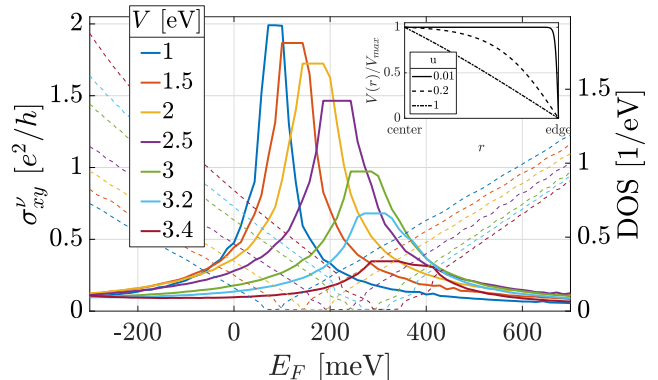


FIG. 7. Valley Hall conductivity as a function of filling for different values of the superlattice potential for a smoothly varying potential ( $u = 0.2$ ), the profile of which is displayed in the inset. The results are similar to the flat potential case, with some additional structure in the peak structure due to the lifting of degeneracies of bands near the band edge.

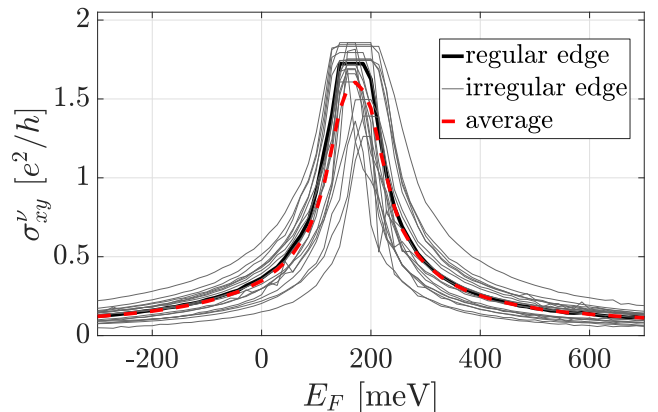


FIG. 8. Variation of the valley Hall conductivity with respect to irregularities in the edge profile of the superlattice potential, corresponding to irregularities in the dielectric etching. The regular limit for a smoothly varying potential ( $V = 2$  eV,  $u = 0.2$ ) is shown in the full black line, alongside the same calculation with random edge profiles at the superlattice potential boundary (gray lines). The average of all such configurations is shown in the red dotted line. The finite valley Hall conductivity does not require a perfectly symmetrical induced potential, and is thus a general prediction in these superlattices.

peak structure for all configurations with a small variation in the plateau value. The average tracks the clean result peak, with a rounded plateau due to the different shifts of the gapped region in different configurations.

## IV. DISCUSSION AND CONCLUSIONS

We have theoretically investigated graphene superlattices defined by periodic gating as a platform for valleytronics. For zigzag edged triangular potentials where

inversion symmetry is broken and intervalley scattering is suppressed, a gate-tunable valley Hall effect appears. This effect stems from the accumulation of Berry curvature near the band edge of the superlattice band structure, which unfolds to curvature of opposite sign in the  $K$  and  $K'$  valleys of the graphene Brillouin zone. For small potentials the system resembles a gapped Dirac model with quantized valley Hall conductivity, yet when the gate-tunable potential is increased this valley Hall conductivity decreases continuously, resulting in a platform for valleytronics where both the magnitude and width of the valley Hall conductivity plateau can be tuned by an external gate. Finally, we have considered experimental signatures of the gate-tunable valley Hall effect when the Fermi energy is tuned close to the band edge in nonlocal transport experiments, and determined how this response varies with the external potential.

In this work we have considered the maximum of the externally induced potential as the tunable parameter. In addition to this degree of freedom the effect of alignment between the substrate and the graphene sheet, with a corresponding rotation and shift in the induced potential, can also have a profound impact on the valley Hall conductivity.<sup>39</sup> For the atomically-resolved model considered here the result will in general depend on the size of the gated region, with sign changes in the valley Hall conductivity when the sublattice is shifted.

Our idealized model of irregularities at the edge of the induced potential implies a periodic structure with the same edge profile, and as such we are limited to calculating modifications to the intrinsic part of the valley Hall conductivity. In general the valley Hall conductivity also has contributions from disorder, commonly classified as the side-jump and skew scattering corrections.<sup>40</sup> We note that these corrections occur outside the gapped region, and do not substantially modify tunable properties of the valley Hall conductivity in these systems.<sup>41</sup>

The main measurable consequence of the nonzero Berry curvature in time-reversal invariant systems, such as the superlattice considered in this work, is a finite correction to the nonlocal resistance. Recently, additional measurable consequences have been predicted, including applications in current rectification,<sup>42</sup> and direct detection via the so-called Magnus Hall effect.<sup>43</sup> The gate-tunable Berry curvature predicted in this work could define a controllable platform for further investigations of these effects.

## V. ACKNOWLEDGMENTS

We acknowledge useful discussions with S. Power. The Center for Nanostructured Graphene is supported by the Danish National Research Foundation, Project D NRF103.

## Appendix A: Unfolding procedure

We unfold quantities calculated in the supercell Brillouin zone (SBZ) back into the pristine graphene, or normal, Brillouin zone (NBZ) following Ref. 30.

Real space and reciprocal lattice vectors in the normal- and supercell are related by<sup>44</sup>

$$\mathbf{A} = \underline{\mathbf{M}} \cdot \mathbf{a}, \quad (\text{A1})$$

$$\mathbf{B} = \underline{\mathbf{M}}^{-1} \cdot \mathbf{b}, \quad (\text{A2})$$

with  $\underline{\mathbf{M}}$  a matrix of integers.

For the triangular superlattices considered here, the general form of this matrix is<sup>45</sup>

$$\underline{\mathbf{M}} = L \begin{pmatrix} 2 & 1 \\ 1 & 2 \end{pmatrix}, \quad (\text{A3})$$

with  $L$  the side length of the supercell hexagon. The determinant of this matrix is the ratio of unit cell volumes.

A given wavevector  $\mathbf{k} \in \text{NBZ}$  is folded into a unique  $\mathbf{K} \in \text{SBZ}$  by a reciprocal lattice vector<sup>44</sup>

$$\mathbf{K} = \mathbf{k} - \mathbf{G}_0, \quad (\text{A4})$$

with  $\mathbf{G}_0 = \sum_i q_i \mathbf{B}_i$ , where the  $q_i$  are integers. We define  $\mathbf{K}'(\mathbf{k})$  as the unique  $\mathbf{K}$  point to which a given  $\mathbf{k}$  point folds.

A wavevector in the SBZ unfolds into multiple values

$$\mathbf{k}_i = \mathbf{K} + \mathbf{G}_i, \quad (\text{A5})$$

with a number of elements  $N_k$  in  $\{\mathbf{G}_i\}$  given by  $N_k = \det \underline{\mathbf{M}}$ .<sup>44</sup>

We employ a tight-binding calculation using localized orbitals  $|\phi_{i\mathbf{r}}\rangle$ , and find the Bloch states. These are characterized by quantum number  $n$  and wavevector  $\mathbf{k}$  in the normal (pristine) cell, and by quantum number  $N$  and wavevector  $\mathbf{K}$  in the supercell

$$|n\mathbf{k}\rangle = \sum_i C_{in\mathbf{k}} |i\mathbf{k}\rangle \quad (\text{A6})$$

$$= \sum_{i\mathbf{r}} C_{in\mathbf{k}} e^{i\mathbf{k}\cdot(\mathbf{r}+\boldsymbol{\tau}_i)} |\phi_{i\mathbf{r}}\rangle, \quad (\text{A7})$$

$$|N\mathbf{K}\rangle = \sum_{I\mathbf{R}} C_{IN\mathbf{K}} e^{i\mathbf{K}\cdot(\mathbf{R}+\boldsymbol{\tau}_I)} |\phi_{I\mathbf{R}}\rangle, \quad (\text{A8})$$

with  $\mathbf{r}, \mathbf{R}$  lattice vectors in the normal cell and supercell, and  $\boldsymbol{\tau}_{i/I}$  the relative position of each orbital in the unit cell and supercell, respectively.

Given an quantity  $\mathcal{O}_{N\mathbf{K}}$  defined in the SBZ, we now define the corresponding unfolded quantity in the NBZ:

$$\mathcal{O}_{i\mathbf{k}}^{(u)} = \sum_{N\mathbf{K}} |\langle i\mathbf{k} | N\mathbf{K} \rangle|^2 \mathcal{O}_{N\mathbf{K}} \quad (\text{A9})$$

$$= \sum_N \lambda_{iN\mathbf{k}} \mathcal{O}_{N\mathbf{K}'(\mathbf{k})}. \quad (\text{A10})$$

Unfolding then boils down to finding the Bloch state overlap  $\lambda_{iN\mathbf{k}}$ , which we will derive within a tight-binding scheme below. Note that the unfolding becomes more complicated for the Berry curvature since a derivative with respect to  $\mathbf{k}$  is included in the definition of this quantity (see Ref. 31 eq. 31).

Define a map  $I \rightarrow \mathbf{R} + \mathbf{r}'(I)$ ,  $i'(I)$  uniquely identifying a localized orbital in the supercell ( $I$ ) with a similar orbital in the normal cell [ $i'(I)$ ], where  $\mathbf{r}'(I)$  is a normal cell lattice vector giving the relative position between unit cells. We can then calculate the overlap between a given supercell and normal cell orbital:

$$\langle \phi_{i\mathbf{r}} | \phi_{I\mathbf{R}} \rangle = \langle \phi_{i\mathbf{r}} | \phi_{i'(I)\mathbf{R} + \mathbf{r}'(I)} \rangle \quad (\text{A11})$$

$$= \delta_{ii'(I)} \delta_{\mathbf{r}, \mathbf{R} + \mathbf{r}'(I)}, \quad (\text{A12})$$

where the final equality follows from orthogonality of the normal cell orbitals. This simple form of the orbital overlap enables a calculation the Bloch state overlap

$$\lambda_{iN\mathbf{k}} = \langle i\mathbf{k} | N\mathbf{K} \rangle \quad (\text{A13})$$

$$= \sum_{I, \mathbf{r}\mathbf{R}} C_{IN\mathbf{K}} e^{-i\mathbf{k} \cdot (\mathbf{r} + \boldsymbol{\tau}_i)} e^{i\mathbf{K} \cdot (\mathbf{R} + \boldsymbol{\tau}_I)} \langle \phi_{i\mathbf{r}} | \phi_{I\mathbf{R}} \rangle \quad (\text{A14})$$

$$= \sum_{I, \mathbf{R}} C_{IN\mathbf{K}} e^{-i\mathbf{k} \cdot (\mathbf{R} + \mathbf{r}'(I) + \boldsymbol{\tau}_i)} e^{i\mathbf{K} \cdot (\mathbf{R} + \boldsymbol{\tau}_I)} \delta_{ii'(I)} \quad (\text{A15})$$

$$= \sum_I C_{IN\mathbf{K}} e^{-i\mathbf{k} \cdot (\mathbf{r}'(I) + \boldsymbol{\tau}_i)} e^{i\mathbf{K} \cdot \boldsymbol{\tau}_I} \delta_{ii'(I)} \delta_{\mathbf{K}[\mathbf{k}]}, \quad (\text{A16})$$

where  $[\mathbf{k}]$  is the set of wavevectors  $\mathbf{k}$  which downfold to  $\mathbf{K}$ . Note that for a given  $\mathbf{k}$  the value of  $\mathbf{K}$  for which this delta function is finite is unique. This enables us to collapse all sums over  $\mathbf{K}$  when unfolding, picking out the value  $\mathbf{K}'(\mathbf{k})$ .

Calculation of the unfolded Berry curvature proceeds from this formalism using the gauge-invariant approach of Ref. 31, and its extension to tight-binding in Ref. 24.

### Appendix B: Band gap and shift for different geometries

In this appendix we provide further information on the evolution of the gap in the spectrum  $\Delta = |E_1 - E_0|$ , and the shift in the center of this gap  $E_s = E_0 + \Delta/2$ , where  $E_{1,0}$  indicate the band edges with  $E_1 > E_0$ . Fig. 9 displays further calculations of these quantities for different geometries (a)-(b), and their evolution with the superlattice geometry parameters  $L, R$  (c)-(d). The shift in the center of the gap ( $E_s$ ) is seen to vary linearly with the superlattice potential, as might be expected from considering the average potential in the unit cell. Indeed, calculating this average potential as  $V_{avg} = V (N_V/N_{SC}) \propto$

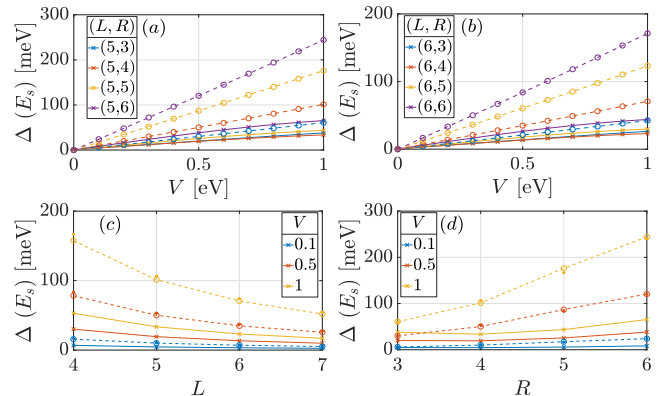


FIG. 9. (a)-(b) Band gap variation with the superlattice potential magnitude for different geometries. (c)-(d) Band gap ( $\Delta$ ) and shift ( $E_s$ ) variation with the supercell size ( $L, R = 4$ ) and extent of the superlattice potential ( $L = 5, R$ ), respectively, shown here for multiple values of the superlattice potential magnitude ( $V$ ). The small asterisks indicate the average potential on each site in the supercell, which matches the numerically calculated shift ( $E_s$ ). The same general result is obtained for different configurations: The band gap widens for either greater magnitude of the superlattice potential, or for increasing ratio between gated region and supercell size.

( $R^2/L^2$ ), where  $N_V = R^2$  is the number of sites with shifted onsite potentials from the superlattice potential and  $N_{SC} = 6L^2$  is the total number of sites in the supercell, we find a close match with the obtained value of the shift. This average potential is shown (small asterisks) alongside the obtained shifts in Fig. 9 (c)-(d).

Similar simple models for the band gap ( $\Delta$ ) in the electronic spectrum of a given geometry based on, e.g., the average graphene A/B site asymmetry do not match the calculated band gap in these systems. This follows from the fact that band gap formation can be driven both by the periodic structure of the superlattice potential itself, which can result in band gaps even for circular potentials, and effects associated with local symmetry of the potential structure such as A/B asymmetry on the edges of the potential. The former of these mechanism can yield extreme sensitivity to small variations in the superlattice size  $L$ , as seen in, e.g., antidot lattices.<sup>17</sup> For the potentials of  $C_3$  symmetry considered in this work we thus restrict ourselves to the general observations, as found in similar superlattices,<sup>17,34</sup> that the size of the induced band gap is directly proportional to the magnitude of the superlattice potential and the extent of this potential  $R$ , and inversely proportional to the supercell size ( $L$ ), i.e., the distance between gated regions, as demonstrated in Fig. 9.

A full picture of a typical band gap and the minibands closest to the gap is provided in Fig. 10 (a)-(b), alongside the DOS in the same region. The gap formation in real space can be observed by calculating the local density of states (LDOS) as a projection of the spectral weight on

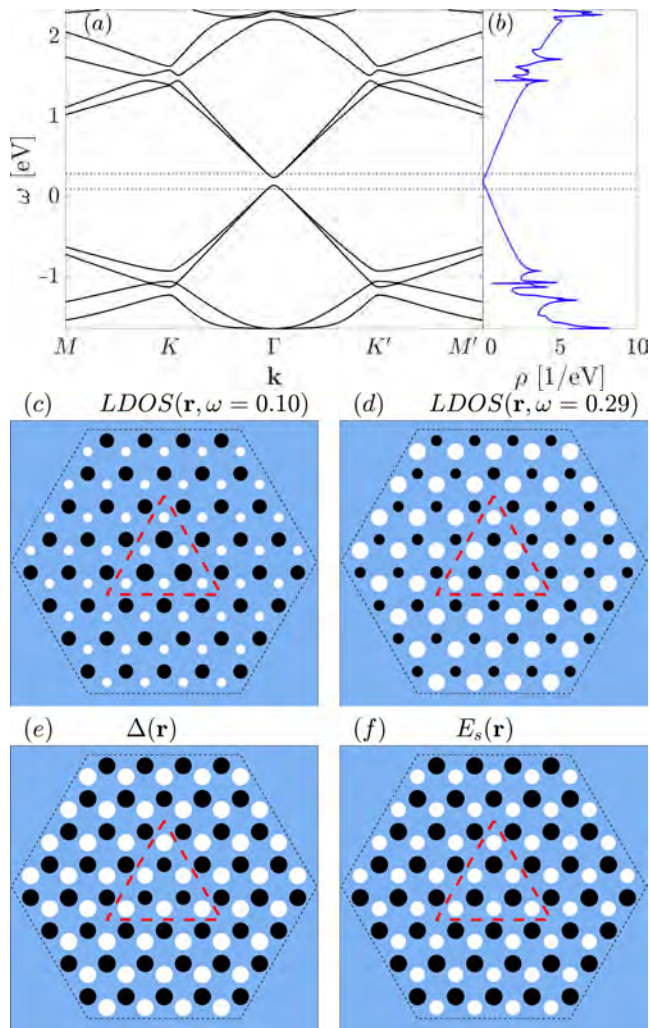


FIG. 10. (a) Extended view of the band structure  $E_N(\mathbf{k})$  showing the gap and miniband formation of the supercell. The symmetry points are those of the SBZ. (b) Corresponding density of states, demonstrating the shifted band gap. (c)-(d) LDOS, plotted using the radii of black (white) disks to indicate the value at A (B) sites, sampled just above and below the gap at  $\omega = 0.1, 0.29$  eV (dashed lines in (a)). The superlattice potential breaks inversion symmetry and causes a splitting of the A/B weight at these sites. (e) Local gap magnitude at each site in the supercell as derived from the local density of states (variations enhanced  $\times 5$ ), showing a small variation at the potential edge. (f) Corresponding shift in the center of this local gap (variations enhanced  $\times 5$ ), showing a small difference between A/B sites in the supercell. All plots are for a representative configuration of  $(L = 4, R = 3, V = 2$  eV).

a given orbital  $\phi_{I\mathbf{R}}$  in the supercell

$$LDOS(\mathbf{R}_I, \omega) = \frac{1}{N_{\mathbf{K}}} \sum_{N\mathbf{K}} |\langle \phi_{I\mathbf{R}} | N\mathbf{K} \rangle|^2 A_{N\mathbf{K}}(\omega). \quad (\text{B1})$$

The LDOS above and below the band edge is displayed in Fig. 10 (c)-(d) at energies as shown by the dashed lines in (a), and demonstrates the opposite splitting of the LDOS on the A/B sublattices above and below the band edge caused by the inversion-symmetry-breaking superlattice potential. In these plots the LDOS is plotted on A (B) sites as black (white) disks, with the radius indicating the magnitude of the LDOS normalized to the maximal value in the supercell. From the LDOS around the gap region we can define the local gap and shift ( $\Delta(\mathbf{r}), E_S(\mathbf{r})$ ) using the band edges of the local gap in the LDOS at a given site. These quantities are shown in Fig. 10 (e)-(f), using a similar plotting scheme similar to that for the LDOS. In these cases the maximal variation from the mean is much smaller (7%, 6% for the gap and shift, respectively) than for the LDOS, and we have thus enhanced the variation fivefold in these plots. The local gap is almost homogeneous, and the only variation of the local gap magnitude  $\Delta(\mathbf{r})$  is seen to take place close to the superlattice potential edge where the potential locally breaks A/B symmetry. The shift  $E_S(\mathbf{r})$  is also homogenous apart from a minor constant A/B variation due to the different number of A/B sites enclosed by the superlattice potential.

### Appendix C: Spatial profile of the superlattice potential

\* johmar@dtu.dk

<sup>1</sup> A. H. Castro Neto, F. Guinea, N. M. R. Peres, K. S. Novoselov, and A. K. Geim, “The electronic properties of graphene,” *Rev. Mod. Phys.* **81**, 109–162 (2009).

<sup>2</sup> A. Rycerz, J. Tworzydło, and C. W.J. Beenakker, “Valley filter and valley valve in graphene,” *Nat. Phys.* **3**, 172–175 (2007).

<sup>3</sup> John R. Schaibley, Hongyi Yu, Genevieve Clark, Pasqual

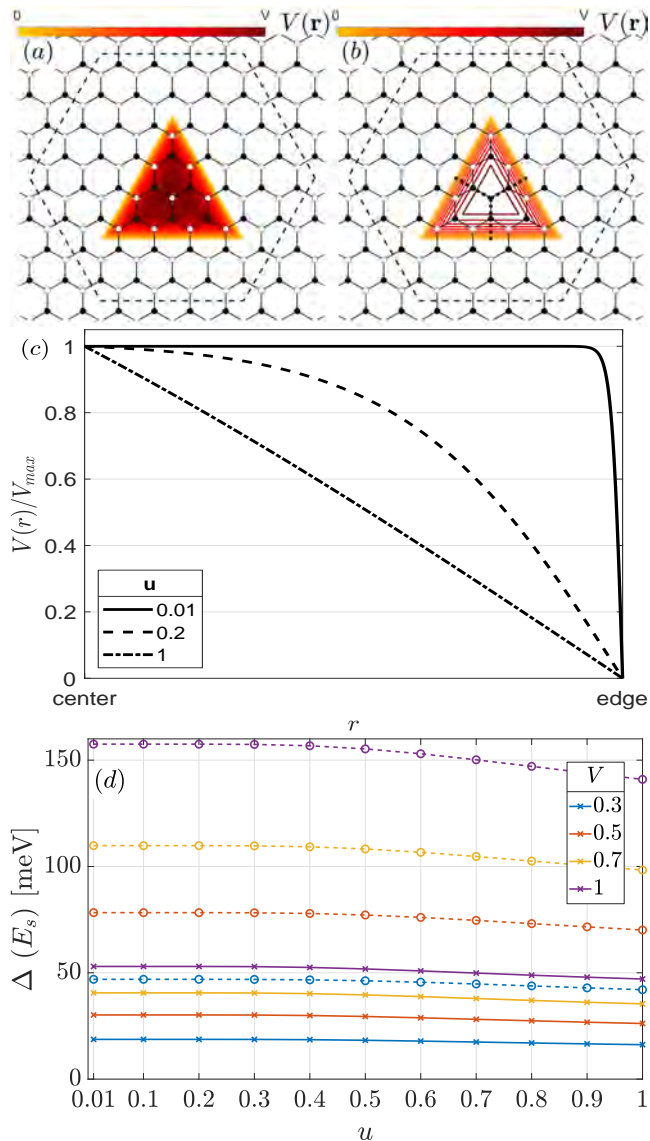


FIG. 11. Spatial variation of the superlattice potential ( $[L, R, u] = [4, 4, 0.2]$ ), shown as (a) a color gradient, (b) a contour plot. (c) The equivalent linecuts indicated by the black dotted lines in (b) for different values of the smoothness parameter  $u = [0.01, 0.2, 1]$ , which interpolates between the extreme cases of flat and linearly decreasing potentials. (d) Variation of the induced band gap (full lines) and shift (dashed lines) with the smoothness parameter  $u$  for the  $(L, R) = (4, 4)$  geometry outlined above. There is only a small decay in the gap magnitude.

Rivera, Jason S. Ross, Kyle L. Seyler, Wang Yao, and Xiaodong Xu, “Valleytronics in 2D materials,” *Nat. Rev. Mater.* **1**, 16055 (2016).

<sup>4</sup> Michihisa Yamamoto, Yuya Shimazaki, Ivan V. Borzenets, and Seigo Tarucha, “Valley Hall effect in two-dimensional hexagonal lattices,” *Journal of the Physical Society of Japan* **84**, 121006 (2015).

<sup>5</sup> K. F. Mak, K. L. McGill, J. Park, and P. L. McEuen, “The valley Hall effect in MoS2 transistors,” *Science* **344**,

1489–1492 (2014).

- <sup>6</sup> Steven A. Vitale, Daniel Nezich, Joseph O. Varghese, Philip Kim, Nuh Gedik, Pablo Jarillo-Herrero, Di Xiao, and Mordechai Rothschild, “Valleytronics: Opportunities, Challenges, and Paths Forward,” *Small* **14**, 1801483 (2018).
- <sup>7</sup> Di Xiao, Wang Yao, and Qian Niu, “Valley-contrasting physics in graphene: Magnetic moment and topological transport,” *Phys. Rev. Lett.* **99**, 236809 (2007).
- <sup>8</sup> Y. Shimazaki, M. Yamamoto, I. V. Borzenets, K. Watanabe, T. Taniguchi, and S. Tarucha, “Generation and detection of pure valley current by electrically induced Berry curvature in bilayer graphene,” *Nat. Phys.* **11**, 1032–1036 (2015).
- <sup>9</sup> Jing Li, Ke Wang, Kenton J. McFaul, Zachary Zern, Yafei Ren, Kenji Watanabe, Takashi Taniguchi, Zhenhua Qiao, and Jun Zhu, “Gate-controlled topological conducting channels in bilayer graphene,” *Nat. Nanotechnol.* **11**, 1060–1065 (2016).
- <sup>10</sup> Chen Si, Zhimei Sun, and Feng Liu, “Strain engineering of graphene: a review,” *Nanoscale* **8**, 3207–3217 (2016).
- <sup>11</sup> R. V. Gorbachev, J. C. W. Song, G. L. Yu, A. V. Kretinin, F. Withers, Y. Cao, A. Mishchenko, I. V. Grigorieva, K. S. Novoselov, L. S. Levitov, and A. K. Geim, “Detecting topological currents in graphene superlattices,” *Science* **346**, 448–451 (2014).
- <sup>12</sup> Xian Peng Zhang, Chunli Huang, and Miguel A. Cazalilla, “Valley Hall effect and nonlocal transport in strained graphene,” *2D Mater.* **4** (2017), 10.1088/2053-1583/aa5e9b.
- <sup>13</sup> Mikkel Settnes, Jose H. Garcia, and Stephan Roche, “Valley-polarized quantum transport generated by gauge fields in graphene,” *2D Mater.* **4**, 031006 (2017).
- <sup>14</sup> Justin C. W. Song, Polnop Samutpraphoot, and Leonid S. Levitov, “Topological Bloch bands in graphene superlattices,” *Proceedings of the National Academy of Sciences* **112**, 10879–10883 (2015).
- <sup>15</sup> Tobias M. R. Wolf, Oded Zilberberg, Ivan Levkivskyi, and Gianni Blatter, “Substrate-induced topological minibands in graphene,” *Phys. Rev. B* **98**, 125408 (2018).
- <sup>16</sup> Chen Hu, Vincent Michaud-Rioux, Wang Yao, and Hong Guo, “Moiré Valleytronics: Realizing Dense Arrays of Topological Helical Channels,” *Phys. Rev. Lett.* **121**, 186403–186404 (2018).
- <sup>17</sup> Thomas G. Pedersen, Christian Flindt, Jesper Pedersen, Niels Asger Mortensen, Antti-Pekka Jauho, and Kjeld Pedersen, “Graphene antidot lattices: Designed defects and spin qubits,” *Phys. Rev. Lett.* **100**, 136804 (2008).
- <sup>18</sup> Andreas Sandner, Tobias Preis, Christian Schell, Paula Giudici, Kenji Watanabe, Takashi Taniguchi, Dieter Weiss, and Jonathan Eroms, “Ballistic transport in graphene antidot lattices,” *Nano Letters* **15**, 8402–8406 (2015).
- <sup>19</sup> Bjarke S. Jessen, Lene Gammelgaard, Morten R. Thomsen, David M.A. Mackenzie, Joachim D. Thomsen, José M. Caridad, Emil Duegaard, Kenji Watanabe, Takashi Taniguchi, Timothy J. Booth, Thomas G. Pedersen, Antti Pekka Jauho, and Peter Bøggild, “Lithographic band structure engineering of graphene,” *Nat. Nanotechnol.* (2019), 10.1038/s41565-019-0376-3.
- <sup>20</sup> Carlos Forsythe, Xiaodong Zhou, Kenji Watanabe, Takashi Taniguchi, Abhay Pasupathy, Pilkyung Moon, Mikito Koshino, Philip Kim, and Cory R. Dean, “Band structure engineering of 2D materials using patterned dielectric superlattices,” *Nat. Nanotechnol.* **13**, 566–571 (2018).

- <sup>21</sup> Søren Schou Gregersen, Jose H Garcia, Antti-Pekka Jauho, Stephan Roche, and Stephen R Power, “Charge and spin transport anisotropy in nanopatterned graphene,” *J. Phys. Mater.* **1**, 015005 (2018).
- <sup>22</sup> D. Malterre, B. Kierren, Y. Fagot-Revurat, C. Didiot, F. J. García De Abajo, F. Schiller, J. Cordon, and J. E. Ortega, “Symmetry breaking and gap opening in two-dimensional hexagonal lattices,” *New Journal of Physics* **13** (2011), 10.1088/1367-2630/13/1/013026.
- <sup>23</sup> Gyeong Hee Ryu, Hyo Ju Park, Junga Ryou, Jinwoo Park, Jongyeong Lee, Gwangwoo Kim, Hyeon Suk Shin, Christopher W. Bielawski, Rodney S. Ruoff, Suklyun Hong, and Zonghoon Lee, “Atomic-scale dynamics of triangular hole growth in monolayer hexagonal boron nitride under electron irradiation,” *Nanoscale* **7**, 10600–10605 (2015).
- <sup>24</sup> Thomas Olsen and Ivo Souza, “Valley Hall effect in disordered monolayer MoS<sub>2</sub> from first principles,” *Phys. Rev. B* **92**, 125146 (2015).
- <sup>25</sup> Michael Beconcini, Fabio Taddei, and Marco Polini, “Non-local topological valley transport at large valley Hall angles,” *Phys. Rev. B* **94**, 121408(R) (2016).
- <sup>26</sup> Luis Brey and H. A. Fertig, “Edge states and the quantized Hall effect in graphene,” *Phys. Rev. B* **73**, 195408 (2006).
- <sup>27</sup> A. Orlof, J. Ruseckas, and I. V. Zozoulenko, “Effect of zigzag and armchair edges on the electronic transport in single-layer and bilayer graphene nanoribbons with defects,” *Phys. Rev. B* **88**, 125409 (2013).
- <sup>28</sup> Di Xiao, Ming-Che Chang, and Qian Niu, “Berry phase effects on electronic properties,” *Rev. Mod. Phys.* **82**, 1959–2007 (2010).
- <sup>29</sup> Dimitrie Culcer, Yugui Yao, and Qian Niu, “Coherent wave-packet evolution in coupled bands,” *Phys. Rev. B* **72**, 085110 (2005).
- <sup>30</sup> Wei Ku, Tom Berlijn, and Chi-Cheng Lee, “Unfolding first-principles band structures,” *Phys. Rev. Lett.* **104**, 216401 (2010).
- <sup>31</sup> Raffaello Bianco, Raffaele Resta, and Ivo Souza, “How disorder affects the Berry-phase anomalous Hall conductivity: A reciprocal-space analysis,” *Phys. Rev. B* **90**, 125153 (2014).
- <sup>32</sup> H. Smith and H. Højgaard Jensen, *Transport phenomena* (Oxford [England] : Clarendon Press ; New York : Oxford University Press, 1989).
- <sup>33</sup> E. H. Hwang, S. Adam, and S. Das Sarma, “Carrier transport in two-dimensional graphene layers,” *Phys. Rev. Lett.* **98**, 186806 (2007).
- <sup>34</sup> Jesper Goor Pedersen and Thomas Garm Pedersen, “Band gaps in graphene via periodic electrostatic gating,” *Phys. Rev. B* **85**, 235432 (2012).
- <sup>35</sup> A. Cresti, B. K. Nikolić, J. H. García, and S. Roche, “Charge, spin and valley Hall effects in disordered graphene,” *Riv. del Nuovo Cim.* **39**, 587–667 (2016).
- <sup>36</sup> Yuri D. Lensky, Justin C. W. Song, Polnop Samutpraphoot, and Leonid S. Levitov, “Topological valley currents in gapped Dirac materials,” *Phys. Rev. Lett.* **114**, 256601 (2015).
- <sup>37</sup> George Kirczenow, “Valley currents and nonlocal resistances of graphene nanostructures with broken inversion symmetry from the perspective of scattering theory,” *Phys. Rev. B* **92**, 125425 (2015).
- <sup>38</sup> J M Marmolejo-Tejada, J H García, M D Petrović, P-H Chang, X-L Sheng, A Cresti, P Plecháč, S Roche, and B K Nikolić, “Deciphering the origin of nonlocal resistance in multiterminal graphene on hexagonal-boron-nitride with ab initio quantum transport: Fermi surface edge currents rather than Fermi sea topological valley currents,” *Journal of Physics: Materials* **1**, 015006 (2018).
- <sup>39</sup> Minwoo Jung, Zhiyuan Fan, and Gennady Shvets, “Midinfrared plasmonic valleytronics in metagate-tuned graphene,” *Phys. Rev. Lett.* **121**, 086807 (2018).
- <sup>40</sup> N. A. Sinitsyn, A. H. MacDonald, T. Jungwirth, V. K. Dugaev, and Jairo Sinova, “Anomalous Hall effect in a two-dimensional Dirac band: The link between the Kubo-Streda formula and the semiclassical Boltzmann equation approach,” *Phys. Rev. B* **75**, 045315 (2007).
- <sup>41</sup> Tsuneya Ando, “Valley Hall conductivity in graphene: Effects of higher-order scattering,” *Journal of the Physical Society of Japan* **87**, 044702 (2018).
- <sup>42</sup> Hiroki Isobe, Su-Yang Xu, and Liang Fu, “High-frequency rectification via chiral Bloch electrons,” *arXiv e-prints*, arXiv:1812.08162 (2018), arXiv:1812.08162 [cond-mat.mtrl-sci].
- <sup>43</sup> Michal Papaj and Liang Fu, “Magnus Hall Effect,” *arXiv e-prints*, arXiv:1904.00013 (2019), arXiv:1904.00013 [cond-mat.mes-hall].
- <sup>44</sup> Voicu Popescu and Alex Zunger, “Extracting  $E$  versus  $k$  effective band structure from supercell calculations on alloys and impurities,” *Phys. Rev. B* **85**, 085201 (2012).
- <sup>45</sup> F. Guinea and Tony Low, “Band structure and gaps of triangular graphene superlattices,” *Philos. Trans. R. Soc. A Math. Phys. Eng. Sci.* **368**, 5391–5402 (2010).

## Paper IV

### Quantum phase transition of iron-based superconductivity in $\text{LiFe}_{1-x}\text{Co}_x\text{As}$

J.-X. Yin, S. S. Zhang, G. Dai, Y. Zhao, A. Kreisel, G. Macan, X. Wu, H. Miao, Z.-Q. Huang, Johannes H. J. Martiny, B. M. Andersen, N. Shumiya, D. Multer, M. Litskevich, Z. Cheng, X. Yang, T. A. Cochran, G. Chang, I. Belopolski, L. Xing, X. Wang, Y. Gao, F.-G. Chuang, H. Lin, Z. Wang, C. Jin, Y. Bang, and M. Z. Hasan

*Physical Review Letters* **123**, 217004 (2019)

# Quantum phase transition of correlated iron-based superconductivity in $\text{LiFe}_{1-x}\text{Co}_x\text{As}$

**Authors:** Jia-Xin Yin<sup>1\*†</sup>, Songtian S. Zhang<sup>1\*</sup>, Guangyang Dai<sup>2\*</sup>, Yuanyuan Zhao<sup>3\*</sup>, Andreas Kreisel<sup>4\*</sup>, Genevieve Macam<sup>5\*</sup>, Xianxin Wu<sup>2</sup>, Hu Miao<sup>6</sup>, Zhi-Quan Huang<sup>5</sup>, Johannes H. J. Martiny<sup>7</sup>, Brian M. Andersen<sup>8</sup>, Nana Shumiya<sup>1</sup>, Daniel Multer<sup>1</sup>, Maksim Litskevich<sup>1</sup>, Zijia Cheng<sup>1</sup>, Xian Yang<sup>1</sup>, Tyler A. Cochran<sup>1</sup>, Guoqing Chang<sup>1</sup>, Ilya Belopolski<sup>1</sup>, Lingyi Xing<sup>2</sup>, Xiancheng Wang<sup>2</sup>, Yi Gao<sup>9</sup>, Feng-Chuan Chuang<sup>5</sup>, Hsin Lin<sup>10</sup>, Ziqiang Wang<sup>11</sup>, Changqing Jin<sup>2</sup>, Yunkyu Bang<sup>12</sup>, M. Zahid Hasan<sup>1,13†</sup>

## Affiliations:

<sup>1</sup>Laboratory for Topological Quantum Matter and Advanced Spectroscopy (B7), Department of Physics, Princeton University, Princeton, New Jersey, USA.

<sup>2</sup>Institute of Physics, Chinese Academy of Sciences, Beijing, China.

<sup>3</sup>School of Physics and Optoelectronic Engineering, Nanjing University of Information Science and Technology, Nanjing, China.

<sup>4</sup>Institut für Theoretische Physik, Universität Leipzig, Leipzig, Germany.

<sup>5</sup>Department of Physics, National Sun Yat-Sen University, Kaohsiung, Taiwan.

<sup>6</sup>Brookhaven National Laboratory, Upton, New York, USA.

<sup>7</sup>Center for Nanostructured Graphene (CNG), Dept. of Micro- and Nanotechnology, Technical University of Denmark, DK-2800 Kongens Lyngby, Denmark.

<sup>8</sup>Niels Bohr Institute, University of Copenhagen, Copenhagen, Denmark.

<sup>9</sup>Center for Quantum Transport and Thermal Energy Science, Jiangsu Key Lab on Opto-Electronic Technology, School of Physics and Technology, Nanjing Normal University, Nanjing, China.

<sup>10</sup>Institute of Physics, Academia Sinica, Taipei, Taiwan.

<sup>11</sup>Department of Physics, Boston College, Chestnut Hill, Massachusetts, USA.

<sup>12</sup>Asia Pacific Center for Theoretical Physics and Department of Physics, POSTECH, Pohang, Gyeongbuk, Korea.

<sup>13</sup>Lawrence Berkeley National Laboratory, Berkeley, California, USA.

†Corresponding author, E-mail: [mzhasan@princeton.edu](mailto:mzhasan@princeton.edu); [jiaxiny@princeton.edu](mailto:jiaxiny@princeton.edu)

\*These authors contributed equally to this work.

**Abstract: The interplay between unconventional Cooper pairing and quantum states associated with atomic scale defects is a frontier of research with many open questions. So far, only a few of the high-temperature superconductors allow this intricate physics to be studied in a widely tunable way. We use scanning tunneling microscopy (STM) to image the electronic impact of Co atoms on the ground state of the  $\text{LiFe}_{1-x}\text{Co}_x\text{As}$  system. We observe that impurities progressively suppress the global superconducting gap and introduce low energy states near the gap edge, with the superconductivity remaining in the strong-coupling limit. Unexpectedly, the fully opened gap evolves into a nodal state before the Cooper pair coherence is fully destroyed. Our systematic theoretical analysis shows that these new observations can be quantitatively understood by the nonmagnetic Born-limit scattering effect in a  $s_{\pm}$ -wave superconductor, unveiling the driving force of the superconductor to metal quantum phase transition.**

In the research of high- $T_c$  superconductors, chemical substitution is a powerful way to manipulate electronic phases [1-5]. Meanwhile, chemical substitution also creates imperfections at the atomic scale, which break the unconventional Cooper pairing [4,5]. Although the single atomic impurity pair-breaking effect has been demonstrated in certain superconducting systems [4,5], it is challenging to study its collective many-body manifestation (the finite-density-impurity problem) in a widely tunable way, due to the existence of competing orders or inhomogeneity from strong electron correlation [1-5]. In this regard, the  $\text{LiFe}_{1-x}\text{Co}_x\text{As}$  is a rare case in which Co substitution monotonically suppresses the homogeneous superconductivity in  $\text{LiFeAs}$  without generating other competing orders [6-12], making it a versatile platform to quantitatively test many-body theories. Intriguingly, photoemission, optical and magnetic response experiments [7-11] reveal that Co substitution changes the Fermi surface and enhances the Fermi surface nesting along with the associated low-energy spin fluctuation, while the spin fluctuation is generally believed to be beneficial for the Cooper pairing in this material [13-15]. This contrast implies a striking, yet not understood de-pairing mechanism associated with Co substitution. Unexpectedly, previous STM experiments found no detectable local pair-breaking effects associated with a single Co impurity [16,17]. There is also no direct spectroscopic data measured deep in the superconducting state demonstrating how a finite density of Co impurities collectively suppresses Cooper pairing. Therefore, a systematic microscopic examination of the effect of the Co substitution on the ground state of  $\text{LiFe}_{1-x}\text{Co}_x\text{As}$  across the whole superconducting phase diagram is demanded.

$\text{LiFeAs}$  crystallizes in a tetragonal unit cell ( $P4/nmm$ ) as shown in Fig. 1(a) with a superconducting transition temperature  $T_C$  of  $\sim 17\text{K}$ . In momentum space, it features hole-like Fermi surfaces at the Brillouin zone center and electron-like Fermi surfaces around the zone boundary, with two extra Dirac cones at the zone center being recently observed [12] (Figs. 1(b)). We first probe the superconducting ground state of the pristine material at  $T = 0.4\text{K}$ . Our atomically resolved high resolution STM image reveals a tetragonal lattice which is the Li-terminating surface (Fig. 1(c)). A line-cut of the differential conductance spectra probing the local density of state (DOS) shows a spatially homogenous double-gap structure, with a larger gap of  $6.0\text{meV}$  and a smaller gap of  $3.3\text{meV}$  (Fig. 1(d)). Based on previous photoemission data [18] measured at  $8\text{K}$ , the large gap likely arises from the electron bands and the inner hole-like band, and the smaller gap likely arises from the outer hole-like band.

As the Fe lattice is systematically substituted with Co atoms, the  $T_C$  decreases linearly and reaches zero around  $x = 16\%$  (Fig. 2(a)) [6-11]. Based on the photoemission data [12], the Fermi level can be systematically tuned by increasing Co concentration as illustrated in the inset of Fig. 2(a). Upon bulk substitution of 1% Co atoms, STM topographical scans reveal new dumbbell-like defects randomly scattered on the surface (Fig. 2(b)) that are different from various native defects in LiFeAs. The concentration of these defects is consistent with the nominal Co substitution. The dumbbell-like defects are also randomly aligned along two orthogonal directions, with its local two-fold symmetry arising from the structural geometry. The center of each such defect is located at the middle of two Li atoms (Fig. 2(c)), which corresponds to the position of the Co atom in the underlying (Fe, Co) lattice (Fig. 2(d) inset), and altogether they possess a local two-fold symmetry. Thus, these defects are likely caused by the atomic Co substitution [17]. Directly above these dumbbell defects, we observe a state near the smaller gap at the positive energy while the overall gap structure remains almost unchanged compared with the far away spectrum (Fig. 2(d)). The weak in-gap state is consistent with earlier calculations [19] based on the band structure and impurity potentials of Co obtained from density functional theory. We note that the observation of the small local electronic variation may benefit from our lower temperature (0.4K) and more dilute impurity concentration compared with previous STM studies [16,17]. Our observation indicates that the dilute Co substitution has a limited local impact on the superconducting order parameter or causes only very weak pair-breaking scattering.

With increasing Co concentration, the Co induced weak in-gap states overlap spatially, making them difficult to be visualized individually [16,17]. On the other hand, the finite concentration of Co impurities collectively suppresses bulk superconductivity. To study the global effects on the superconducting ground state, we systematically probe the spectra away from the apparent surface defects for a wide range of Co concentrations at base temperature 0.4K. We observe a strong variation of the superconducting gap structure in the tunneling conductance which correlates strongly with the  $T_C$  reduction (Fig. 2(e)). As the Co concentration increases, the large superconducting gap size decreases progressively until no gap remains at  $x = 16\%$  where  $T_C = 0$ . Meanwhile, the superconducting coherence peak grows progressively weaker. Evidently, the spectral bottom evolves from a U-shape to a V-shape and then gradually elevates to the normal state value.

The Co induced gap reduction and scattering can also be qualitatively reflected in the vortex excitation. We extensively study the vortices (Fig. 3) for different Co concentrations at 0.4K with *c*-axis magnetic fields. In the pristine sample (Fig. 3 (a)), the vortices form an ordered hexagonal lattice under a zero-field cooling method [20,21], as can be clearly seen in the autocorrelation of the real-space mapping at 2T (Fig. 3(a) inset). As the Co concentration  $x$  increases, we find the vortex lattice symmetry to remain hexagonal like (Figs. 3(b) inset), while the vortex core size increases. The persistent hexagonal vortex lattice symmetry indicates that the randomly distributed Co dopants do not distort the vortex lattice significantly. As the core size is related with the coherence length which is proportional to the reverse of the gap in the BCS theory, the increment of the vortex core size is consistent with the aforementioned gap reduction. Moreover, measuring the conductance within a vortex under an applied *c*-axis field of 0.5T reveals sharp in-gap bound states at  $|E| \approx 1\text{meV}$  (Figs. 3(b)) [20,21], in agreement with the estimate of vortex core states energies in the quantum limit, which should be on the order of a non-topological superconducting vortex state (in the energy order of  $\pm\Delta^2/E_F$ ). As the doping concentration increases, these sharp bound states become gradually less pronounced (Figs. 3(b)), consistent with the aforementioned

increased scattering. For each concentration, we carefully examine at least six vortex core states, but do not find any that exhibits a pronounced zero-energy peak. This absence of localized zero-energy states is consistent with the detailed band topology of  $\text{LiFe}_{1-x}\text{Co}_x\text{As}$ . According to the photoemission study [12] and first-principles calculations (Fig. 1(b) and Fig. 2(a) inset), the surface Dirac cone (lower cone) is buried below the Fermi level in the three-dimensional bulk states, and hence does not form surface helical Cooper pairing and distinct Majorana bound states localized at the ends of the vortex line [22]. Moreover, the expected spectra of the vortex lines in superconductors with bulk Dirac states are not yet fully understood. Recently, there have been theoretical studies of the expected Majorana modes [23,24]. However, details of the vortex properties leave the possibility that these states are not localized at the vortex ends and the system might not feature zero energy bound states. These conclusions are not inconsistent with our experimental data, and we want to stress that it is a challenge to unambiguously distinguish the non-localized Majorana state by STM technique alone [23,24].

To quantify the Co induced gap reduction and scattering, we extract two key parameters from the raw data: the large energy gap size  $\Delta_L$  and global zero-energy density of state  $N(E=0)$ . Remarkably, we find that  $\Delta_L$  decreases linearly as a function of  $x$  and reaches zero around 16%, which scales linearly with the reducing  $T_C$  (Fig. 4(a)). In other words, the coupling strength  $2\Delta_L/k_B T_C$  remains a constant (inset of Fig. 4(a)). In particular,  $\text{LiFe}_{1-x}\text{Co}_x\text{As}$  remains in the strong coupling limit for all  $x$  as evidenced by  $2\Delta_L/k_B T_C \approx 7.7$ , much larger than the BCS value 3.5. These results suggest that the superconductivity is destroyed via a mechanism which decreases the pair susceptibility strength, but not the coupling strength. On the other hand, the extracted zero-energy state  $N(E=0)$  exhibits an exponential like growth as shown in Fig. 4(b). The comparatively smaller rate of growth increase of  $N(E=0)$  at low concentrations is consistent with the local effect of each Co atom individually (Fig. 2(d)) that each Co induces weak impurity state near the superconducting gap edge (Fig. 2(d)). As the concentration increases, the interference of their impurity wave functions becomes stronger and the global impurity states spread further in energy, and their tail states eventually contribute to the rapid rise of the global zero-energy state.

In our systematic first-principles calculations, we find that the Co dopants are essentially nonmagnetic with a relatively weak on-site potential of -0.43eV (Supplementary), consistent with previous experiments showing that they do not introduce a local magnetic moment [6,10,11,25]. According to the Anderson theorem, nonmagnetic impurities have little effect on the conventional s-wave superconductor. With a sign change in the order parameter, nonmagnetic impurity is then able to break the Cooper pairs [4,5,26-29]. Considering previous phase sensitive experiments [21] in this compound, the strongest pairing wave-function candidate is  $s_{\pm}$  (where the sign changes between the ordinary hole and electron Fermi surfaces). Crucially, the variation of the gap structure from U-shape to V-shape due to nonmagnetic scattering in the  $s_{\pm}$  pairing state has been predicted using the T-matrix theory [26]. Taking this two-band model from Ref. 26, we set both linear gap reduction and linear scattering rate enhancement with increasing  $x$  (Supplementary), and compute  $N(E=0)$  under the Born (weak scattering) limit and the unitary (strong scattering) limit [4,5] with the results shown in Fig. 4(b). We find that the experimental data is consistent with the former condition and deviates substantially from the latter. Figure 4(d) displays the calculated DOS in the Born limit, which gradually evolves from a fully opened gap to a less coherent V-shaped structure, in consistency with our experimental observation (Fig. 2(e)). In this model, such behavior is due to the impurity states residing near the gap edge (which can be qualitatively identified from the imaginary part of the quantum many-body self-energy, as detailed in supplementary) with their

tail states gradually moving towards zero-energy. Therefore, this theory offers a heuristic understanding of our experiment, demonstrating the Born limit nonmagnetic scattering nature of Co and sign reversal of the gap symmetry.

To acquire a self-consistent and quantitative understanding of the quantum many-body effect of the Co dopants, we further perform real-space calculations using the Bogoliubov–de Gennes (BdG) approach. We first take a two-orbital effective model capturing the essence of its low energy multi-band structure and consider randomly distributed electron dopants with weak potential scattering as Co impurities in reference to first-principles calculation (Supplementary). The next-nearest-neighbor intra-orbital attraction is considered to cause the  $s_{\pm}$  wave Cooper pairing. The calculated DOS indeed shows a clear U-shape to a V-shape evolution as demonstrated in Fig. 4(f). This encourages us to further perform a fully realistic calculation with complete five-orbitals. The five-orbital model has successfully explained the vortex core states<sup>20</sup> and weak Co impurity states in pristine LiFeAs<sup>16,19</sup>, where the  $s_{\pm}$  wave Cooper pairing is self-consistently obtained within spin-fluctuation mediated pairing. Considering similarly weak potential scattering, the calculated DOS and phase diagram are shown in Fig. 4(e), which reasonably agrees with the experiment in realistic energy units. We stress that the latter five-band theoretical study contains no free fitting parameters since the band, gap structure, and impurity potential are fixed by either experiment or first-principles calculations. In this respect, it constitutes a new level of quantitative disorder modelling of unconventional superconductors. Therefore, these realistic self-consistent calculations capture the essence of the experiments and embrace the same spirit of the T-matrix calculation, unambiguously demonstrating the scattering nature of Co in iron-based superconductivity. Our systematic experimental-theoretical analysis of the impurity effect from a single impurity to the finite density case microscopically uncovers that the Born-limit nonmagnetic scattering is the driving force of the superconducting quantum phase transition in LiFe<sub>1-x</sub>Co<sub>x</sub>As. Future characterization of the Co impurity effect by Bogoliubov quasi-particle interference imaging will be important for further exploring the orbital and band selectivity of the Born-limit nonmagnetic scattering.

## References and Notes:

1. B. Keimer and J. E. Moore, The physics of quantum materials. *Nature Physics* **13**, 1045 (2017).
2. E. Fradkin, S. A. Kivelson and J. M. Tranquada, Colloquium: Theory of intertwined orders in high temperature superconductors. *Rev. Mod. Phys.* **87**, 457 (2015).
3. G. R. Stewart, Superconductivity in iron compounds. *Rev. Mod. Phys.* **83**, 1589-1652 (2011).
4. A. V. Balatsky, I. Vekhter and J-X. Zhu, Impurity-induced states in conventional and unconventional superconductors. *Rev. Mod. Phys.* **78**, 373-433 (2006).
5. H. Alloul, J. Bobroff, M. Gabay and P. J. Hirschfeld, Defects in correlated metals and superconductors. *Rev. Mod. Phys.* **81**, 45 (2009).

6. M. J. Pitcher *et al.* Compositional Control of the Superconducting Properties of LiFeAs. *J. Am. Chem. Soc.* **132**, 10467 (2010).
7. S. V. Borisenko *et al.* Superconductivity without Nesting in LiFeAs. *Phys. Rev. Lett.* **105**, 067002 (2010).
8. S. Aswartham *et al.* Suppressed superconductivity in charge-doped Li(Fe<sub>1-x</sub>Co<sub>x</sub>)As single crystals. *Phys. Rev. B* **84**, 054534 (2011).
9. Z. R. Ye *et al.* Extraordinary Doping Effects on Quasiparticle Scattering and Bandwidth in Iron-Based Superconductors. *Phys. Rev. X* **4**, 031041 (2014).
10. Y. M. Dai *et al.* Spin-fluctuation-induced non-Fermi-liquid behavior with suppressed superconductivity in Li(Fe<sub>1-x</sub>Co<sub>x</sub>)As. *Phys. Rev. X* **5**, 031035 (2015).
11. Yu Li *et al.* Orbital Selective Spin Excitations and their Impact on Superconductivity of LiFe<sub>1-x</sub>Co<sub>x</sub>As. *Phys. Rev. Lett.* **116**, 247001 (2016).
12. P. Zhang *et al.* Multiple topological states in iron-based superconductors. *Nat. Phys.* **15**, 41-47 (2019).
13. A. E. Taylor *et al.* Antiferromagnetic spin fluctuations in LiFeAs observed by neutron scattering. *Phys. Rev. B* **83**, 220514 (2011).
14. M. P. Allan *et al.* Identifying the ‘fingerprint’ of antiferromagnetic spin fluctuations in iron pnictide superconductors. *Nature Physics* **11**, 177–182 (2015).
15. P. J. Hirschfeld, M. M. Korshunov, I. I. Mazin. Gap symmetry and structure of Fe-based superconductors. *Rep. Prog. Phys.* **74**, 124508 (2011).
16. S. Chi *et al.* Impact of iron-site defects on superconductivity in LiFeAs. *Phys. Rev. B* **94**, 134515 (2016).
17. H. Yang *et al.* Unexpected weak spatial variation in the local density of states induced by individual Co impurity atoms in superconducting Na(Fe<sub>1-x</sub>Co<sub>x</sub>)As crystals revealed by scanning tunneling spectroscopy. *Phys. Rev. B* **86**, 214512 (2012).
18. K. Umezawa *et al.* Unconventional Anisotropic s-Wave Superconducting Gaps of the LiFeAs Iron-Pnictide Superconductor. *Phys. Rev. Lett.* **108**, 037002 (2012).
19. M. N. Gastiasoro, P. J. Hirschfeld, B. M. Andersen. Impurity states and cooperative magnetic order in Fe-based superconductors. *Phys. Rev. B* **88**, 220509(R) (2013).
20. T. Hanaguri *et al.* Scanning Tunneling Microscopy/Spectroscopy of Vortices in LiFeAs. *Phys. Rev. B* **85**, 214505 (2012). B. M. Urange, *et al.* Electronic vortex structure of Fe-based superconductors: Application to LiFeAs. *Phys. Rev. B* **93**, 224503 (2016).
21. S. Z. Song *et al.* Vector field controlled vortex lattice symmetry in LiFeAs using scanning tunneling microscopy. *Phys. Rev. B* **99**, 161103(R) (2019).
22. L. Fu and C. L. Kane, Superconducting Proximity Effect and Majorana Fermions at the Surface of a Topological Insulator. *Phys. Rev. Lett.* **100**, 096407 (2008).
23. E. J. König and P. Coleman, Helical Majorana modes in iron based Dirac superconductors. *Phys. Rev. Lett.* **122**, 207001 (2019).

24. S. Qin *et al.* Quasi 1D topological nodal vortex line phase in doped superconducting 3D Dirac Semimetals. *Phys. Rev. Lett.* **123**, 027003 (2019).
25. L. Y. Xing *et al.* Observation of non-Fermi liquid behavior in hole-doped  $\text{LiFe}_{1-x}\text{V}_x\text{As}$ . *Phys. Rev. B* **94**, 094524 (2016).
26. Y. Bang, H. Y. Choi and H. Won, Impurity effects on the  $\pm s$ -wave state of the iron-based superconductors. *Phys. Rev. B* **79**, 054529 (2009).
27. S. Onari and H. Kontani, Violation of Anderson's theorem for the sign-reversing s-wave state of iron-pnictide superconductors. *Phys. Rev. Lett.* **103**, 177001 (2009).
28. D. Zhang, Nonmagnetic Impurity Resonances as a Signature of Sign-Reversal Pairing in FeAs-Based Superconductors. *Phys. Rev. Lett.* **103**, 186402 (2009).
29. Mizukami, Y. *et al.* Disorder-induced topological change of the superconducting gap structure in iron pnictides. *Nature Communications* **5**, 5657 (2014).

**Acknowledgments:** Experimental and theoretical work at Princeton University was supported by the Gordon and Betty Moore Foundation (GBMF4547/ Hasan) and the United States Department of energy (US DOE) under the Basic Energy Sciences programme (grant number DOE/BES DE-FG-02-05ER46200). M.Z.H. acknowledges support from Lawrence Berkeley National Laboratory and the Miller Institute of Basic Research in Science at the University of California, Berkeley in the form of a Visiting Miller Professorship. We also acknowledge Korea NRF (Grant No. 2016-R1A2B4-008758), the Natural Science Foundation from Jiangsu Province of China (Grant No. BK20160094). Computations for this work were partially done with resources of Leipzig University Computing Centre. Z.W and K.J. acknowledge US DOE grant DE-FG02-99ER45747.

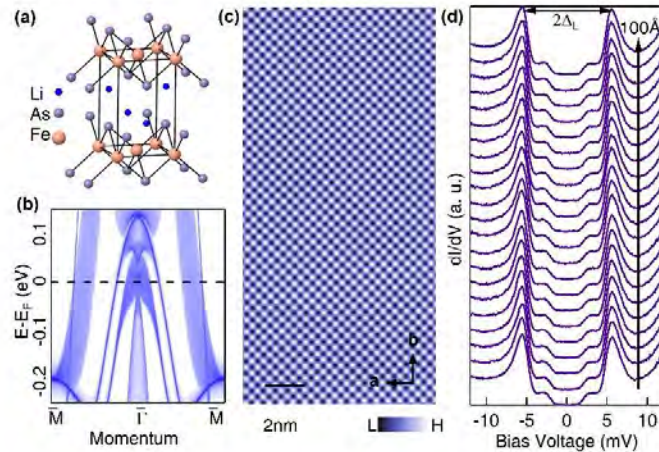


**Fig. 1.** (a) Crystal structure of LiFeAs. (b) First-principles calculation of the band structure for (001) surface. The zoom-in image shows the two Dirac cones at the zone center, with the upper one from bulk and the lower one from the surface. (c) Atomically-resolved topographic image of pristine LiFeAs showing clean tetragonal lattice. (d) Line-cut differential conductance spectra on pristine LiFeAs, showing a spatially homogeneous double-gap structure.

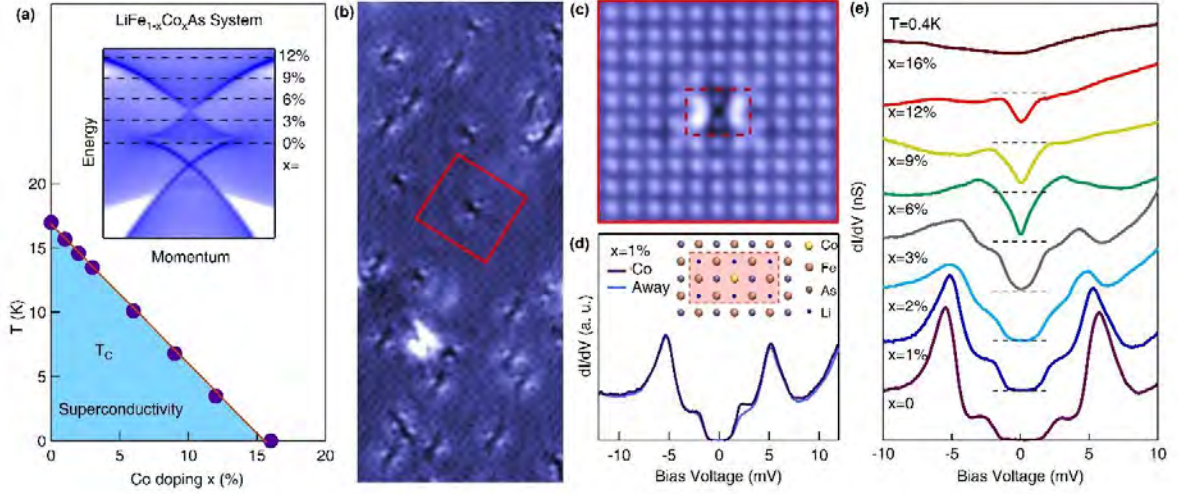


**Fig. 2.** (a) Phase diagram of  $\text{LiFe}_{1-x}\text{Co}_x\text{As}$ . The superconducting transition temperature is determined by the onset of zero resistivity. Inset: illustration of the Co doping effect on the bulk Dirac cone based on Ref. 12. (b) Atomically resolved topographic image of a sample with 1% Co substitution, showing randomly scattered dumbbell-like defects that do not exist in the pristine sample and with concentration consistent with the Co substitution level. (c) Enlarged image of single reproducible dumbbell-like defect. The center of the defect geometrically corresponds to a Co substitution atom in the Fe layer (in reference to Fig. 2D inset). (d) Differential conductance spectrum taken at the defect and far from the defect. Inset: crystal structure from top view. (e) Co concentration dependence on spatially averaged superconducting gap structure. The spectra are offset for clarity. The dashed lines mark the zero-intensity value for each case. 30 to 50  $dI/dV$  curves taken away from apparent surface impurities with the same junction set up ( $V = -15\text{mV}$ ,  $I = 750\text{pA}$ ) were averaged to obtain the  $dI/dV$  curve for each concentration.

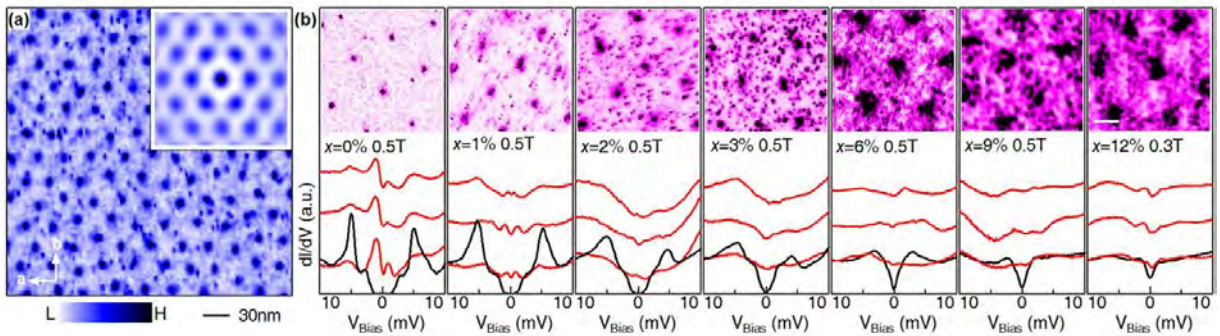


**Fig. 3.** (a) Left: real space mapping of vortices at the Fermi energy on pristine  $\text{LiFeAs}$  at  $B = 2\text{T}$ . Inset: auto-correlation of vortex mapping showing hexagonal lattice symmetry. (b) Spectra in the zero-field state (black) and at three representative vortices offset for clarity (red) for each concentration. The inset image in each panel shows the respective vortex lattice (the bar marks a length of  $35\text{nm}$ ).

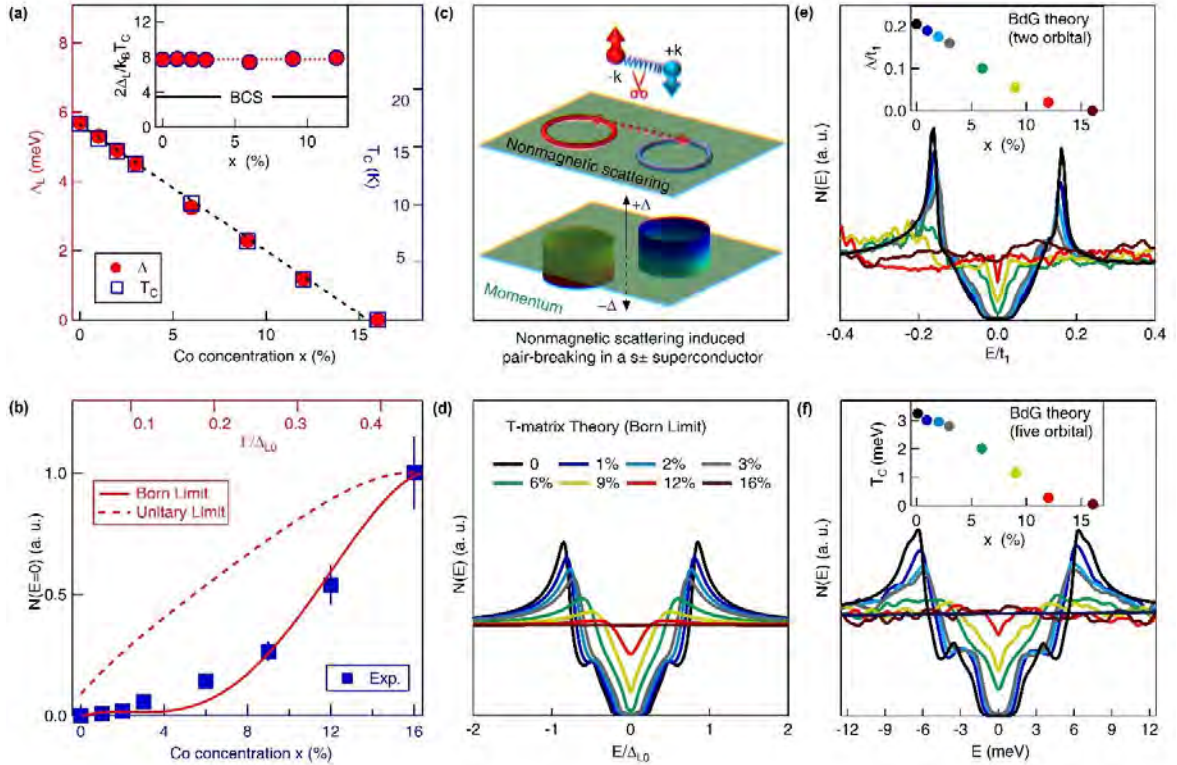


**Fig. 4.** (a) The large gap size  $\Delta_L$  (left axis, red) and  $T_c$  (right axis, blue) both decrease linearly as a function of concentration  $x$ . Inset:  $2\Delta_L/k_B T_c$  remains constant ( $\sim 7.7$ ) as a function of Co concentration. (b) Differential conductance at zero energy  $N(E=0)$  as a function of Co concentration  $x$  in  $\text{LiFe}_{1-x}\text{Co}_x\text{As}$ . The experimental data is normalized by the normal state value. The red solid and dashed lines denote  $N(E=0)$  calculated based on Born and unitary limit scattering, respectively. (c) Schematic showing a sign reversal  $s_{\pm}$  wave pairing on two Fermi surfaces (lower panel,  $s_{\pm}$  gap symmetry) and the nonmagnetic impurities induced interband scattering causing pair-breaking (upper panel). (d) Calculated density of states evolution of the  $s_{\pm}$  pairing state with nonmagnetic scattering at the Born limit with T-matrix theory. (e) (f) Calculated averaged DOS evolution with increasing Co concentration by BdG theory with two-orbital and five-orbital models, respectively. The inset shows the phase diagram plot.

# Supplementary Materials

## Materials and Methods

Single crystals of  $\text{LiFe}_{1-x}\text{Co}_x\text{As}$  grown using the self-flux method of up to  $5\text{mm} \times 5\text{mm} \times 0.5\text{mm}$  were used in this study. All preparation work was carried out in an Ar filled glove box in order to protect the samples from air. Samples were cleaved mechanically *in situ* at 77K in ultra-high vacuum conditions, and then immediately inserted into the STM head, already at He4 base temperature (4.2K). The STM head that includes the sample was subsequently cooled to 0.4K with He3 cooling and stabilized, after which the magnetic field was slowly applied, with maximum temperature fluctuations of 0.2K during ramping. We waited for 1 h before performing spectroscopic imaging so that there was no noticeable vortex creep in the differential conductance map. This zero-field-cooling technique was adopted throughout this work. Tunneling conductance spectra were obtained with an Ir/Pt tip using standard lock-in amplifier techniques with a root mean square oscillation voltage of  $100\mu\text{V}$  and a lock-in frequency of 973Hz. The conductance maps are taken with tunneling junction set up:  $V = -15\text{mV}$ ,  $I = 50\text{-}150\text{pA}$ , while the tunneling spectra are taken with junction set up:  $V = -15\text{mV}$ ,  $I = 750\text{pA}$ .

High-quality single crystals of  $\text{LiFe}_{1-x}\text{Co}_x\text{As}$  are grown with the self-flux method. The precursor of  $\text{Li}_3\text{As}$  is prepared by sintering Li foil and an As lump at about  $700^\circ\text{C}$  for 10 h in a Ti tube filled with Ar atmosphere.  $\text{Fe}_{1-x}\text{Co}_x\text{As}$  is prepared by mixing the Fe, Co, and As powders thoroughly, and then sealed in an evacuated quartz tube, and sintered at  $700^\circ\text{C}$  for 30 h. To ensure the homogeneity of the product, these pellets are reground and heated for a second time. The  $\text{Li}_3\text{As}$ ,  $\text{Fe}_{1-x}\text{Co}_x\text{As}$ , and As powders are mixed according to the elemental ratio  $\text{Li}(\text{Fe}_{1-x}\text{Co}_x)_{0.3}\text{As}$ . The mixture is put into an alumina oxide tube and subsequently sealed in a Nb tube and placed in a quartz tube under vacuum. The sample is heated at  $650^\circ\text{C}$  for 10 h and then heated up to  $1000^\circ\text{C}$  for another 10 h. Finally, it is cooled down to  $750^\circ\text{C}$  at a rate of  $2^\circ\text{C}$  per hour. Crystals with a size up to 5 mm are obtained. The entire process of preparing the starting materials and the evaluation of the final products are carried out in a glove box purged with high-purity Ar gas. The molar ratio of Co and Fe of the  $\text{LiFe}_{1-x}\text{Co}_x\text{As}$  single crystals is checked by energy-dispersive x-ray spectroscopy (EDS) at several points on one or two selected samples for each Co concentration. For each doping, the Co concentration measured by EDS is consistent with the nominal value.

## Nonmagnetic nature of Co dopants

### Magnetization characterization

We measure the magnetic susceptibility of  $\text{LiFe}_{1-x}\text{Co}_x\text{As}$  using a vibrating sample magnetometer with a magnetic field of 1T to study their effective magnetic moment. As shown in Fig. S1, the measured magnetic susceptibility for different concentrations are within the same order of magnitude. Their low temperature magnetization can be described by the Curie–Weiss law [31]:  $\frac{1}{\chi - \chi_0} = (T + T_\theta)/C$ , and from the fitting parameter  $C = \mu_0 \mu_{ef}^2 / 3k_B$  we can extract the effective local magnetic moment per Fe/Co as shown in the inset of Fig. S1. We find that in contrast to the giant enhancement of local moment for Mn and V dopants [31,25], the local moment for  $\text{LiFe}_{1-x}$

$x\text{Co}_x\text{As}$  fluctuates around  $0.2\mu_B$  per Fe/Co and the Co dopants do not substantially enhance the effective moment, thus it is more suitable to treat them as nonmagnetic impurities.

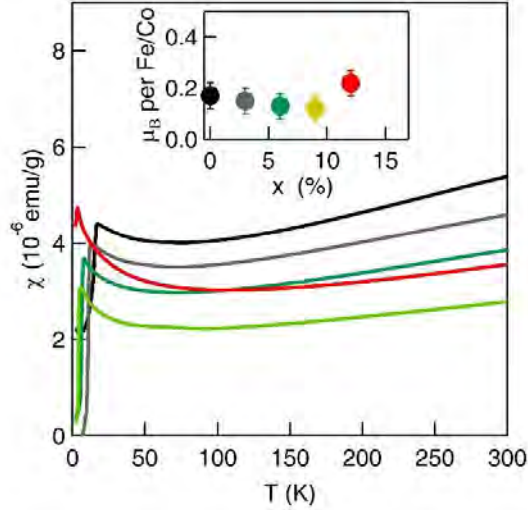


**Fig. S1** Temperature dependence of the dc magnetic susceptibility in a 1 T magnetic field for different Co concentrations. The inset shows the extracted effective local magnetic moment.

### First-principles calculation

First-principles calculations were performed in the density functional theory [32,33] framework as implemented in the Vienna Ab initio Simulation Package (VASP) [34]. Generalized gradient approximation in Perdew–Burke–Ernzerhof (PBE) functional [35][36] was applied to describe electron exchange–correlation interaction with the projector augmented wave (PAW) potentials [37]. The energy cutoff was set at 500 eV. The energies in self-consistent calculations were converged until  $10^{-5}$  eV. Striped antiferromagnetic, ferromagnetic and non-magnetic states are simulated via non-collinear self-consistent calculations of  $\sqrt{2} \times \sqrt{2} \times 1$  LiFeAs supercell for undoped and Co-doped,  $\text{LiFe}_{(1-x)}\text{Co}_x\text{As}$  where  $x = 0.5$ . The Brillouin zone was sampled using a  $16 \times 16 \times 10$  Monkhorst-Pack [38] grid.

We explored the effect of Co substitution on the magnetism of LiFeAs, and investigated ferromagnetic (FM), striped antiferromagnetic (AFM), and nonmagnetic (NM) orientations. DFT calculations show that Co substitution suppresses the magnetism in LiFeAs. In Table S1, undoped LiFeAs have three distinct magnetic configurations – FM, AFM and NM. Striped AFM is the most stable magnetic orientation, with 0.156 eV and 0.167 eV per  $\sqrt{2}$  supercell lower than FM and NM cases. The non-striped type of antiferromagnetic configuration is degenerate with the NM case. The system energies and magnetic moments are summarized in Table S1.

However, after partial Co substitution, the system becomes unstable as the magnetic states are no longer distinguishable. From Table S2, we can find that the ferromagnetic states are suppressed, and the striped AFM states become degenerate with NM states. At concentration  $x = 0.5$ , two possible arrangements of Co doping arise, i.e., (i). Fe atoms with two and (ii). four nearest-

neighbor Co atoms denoted as A1(Linear) and A2 (Alternating), respectively. The A2 configuration is generally the preferred atomic arrangement by 0.05 eV per  $\sqrt{2}$  supercell. In these configurations, the FM calculations converge to NM and the net magnetic moments become zero.

The AFM orientations shown in Fig. S2 present two types of striped AFM, labeled as parallel and crossed. Parallel stripes occur when the magnetic moments are along a line of nearest-neighbor doped atoms having the same direction. On the other hand, in the crossed stripes orientation, the nearest-neighbor doped atoms have an opposite direction from each other. This is schematically shown in the rightmost panel of Fig. S2. Table S2 shows that the energies of both types of striped AFM and NM cases are degenerate.

Examining the local magnetic moments, we found that Co doping reduced the magnetic moments of each atom as listed in Table S3. Specifically, in the linear Co doping arrangement, A1, with crossed stripes, the local magnetic moment of Co and Fe atoms are  $0.071\mu_B$  and  $0.381\mu_B$ , respectively. This is a substantial reduction as compared to the undoped LiFeAs where Fe atoms have a larger local magnetic moment of  $1.213\mu_B$ . Clearly, these results confirm that in partially Co-doped LiFeAs, Co dopants exhibit a non-magnetic nature.

Finally, we estimate the on-site potential of Co dopants. We first calculate the orbital resolved DOS for  $\text{LiFe}_{0.5}\text{Co}_{0.5}\text{As}$ . As shown in Fig. S3, the DOS of Co  $3d$  orbitals overlaps substantially with that of Fe  $3d$  orbitals without apparent sharp bound state, indicating weak potential scattering nature of the Co dopants. We then calculate the "center of mass" for each partial DOS. The energy for the center of mass is used to estimate the on-site energy of the orbital as  $U = \int_{-6\text{eV}}^{+3\text{eV}} \text{DOS}(E)E / \int_{-6\text{eV}}^{+3\text{eV}} \text{DOS}(E)$ , where  $\text{DOS}(E)$  is the partial density of state as a function of  $E$ . The calculated on-site energies for Co  $3d$  and Fe  $3d$  as  $-1.52\text{eV}$  and  $-1.09\text{eV}$ , respectively. The on-site potential of Co is then estimated by their difference to be  $-0.43\text{eV}$ , which is of the same sign and order of magnitude with previous on-site potential estimation [39] of Co dopants in  $\text{LaOFeAs}$ .

<b>Magnetic Orientation</b>	<b>Undoped LiFeAs</b>	
	<b>Energy (eV)</b>	<b>Mag. (<math>\mu_B</math>)</b>
<b>Striped AFM</b>	-64.816	0.000
<b>FM</b>	-64.660	1.338
<b>NM</b>	-64.649	0.000

**Table S1.** System energies and net magnetic moments undoped LiFeAs with different magnetic orientations.

Arrangement of Co and Fe atoms					
Magnetic Orientation		A1 - Linear		A2 - Alternating	
		Energy (eV)	Mag. ( $\mu_B$ )	Energy (eV)	Mag. ( $\mu_B$ )
FM		<i>converged to NM</i>		<i>converged to NM</i>	
AFM Stripes	Parallel	-62.812	0.000	-62.863	0.000
AFM Stripes	Crossed	-62.811	0.000	-62.863	0.026
NM		-62.811	0.000	-62.863	0.000

**Table S2.** System energies and net magnetic moments for partial Co substitution,  $x = 0.5$ , with different magnetic orientations.

Co Concentration, $x$	Antiferromagnetic orientation	Magnetic moment per atom ( $\mu_B$ )	
		Fe	Co
0.0	Undoped LiFeAs	1.213	N/A
0.5	Linear – parallel stripes	0.003	-0.003
0.5	Linear – crossed stripes	$\pm 0.381$	$\pm 0.071$
0.5	Alternating – parallel stripes	$\pm 0.043$	0.001
0.5	Alternating – crossed stripes	0.035	-0.022

**Table S3.** Local magnetic moments of Fe and Co atoms for undoped and Co-doped LiFeAs.

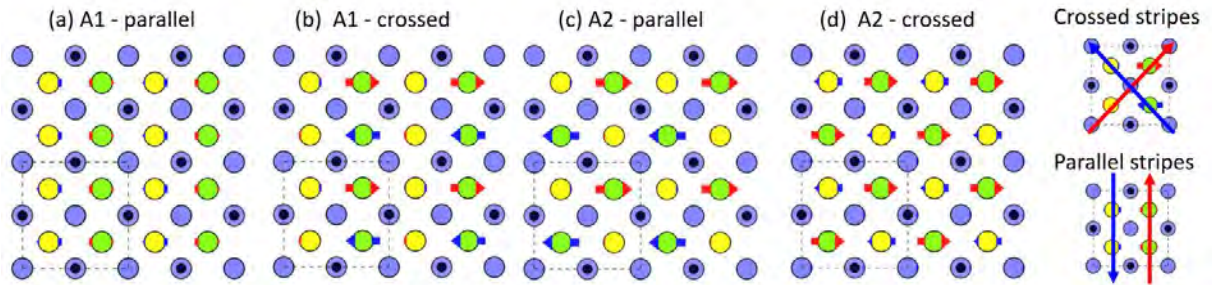


**Figure S2.** The non-collinear striped AFM orientations of LiFeAs with Co concentration of  $x = 0.5$ . The parallel and crossed AFM stripes of linearly (A1) arranged Co and Fe atoms are shown in (a) and (b), respectively. The 3<sup>rd</sup> and 4<sup>th</sup> panels show the alternating (A2) arrangement for (c)

parallel and (d) crossed AFM strips. The rightmost panel shows the schematic difference between crossed and parallel AFM strips.

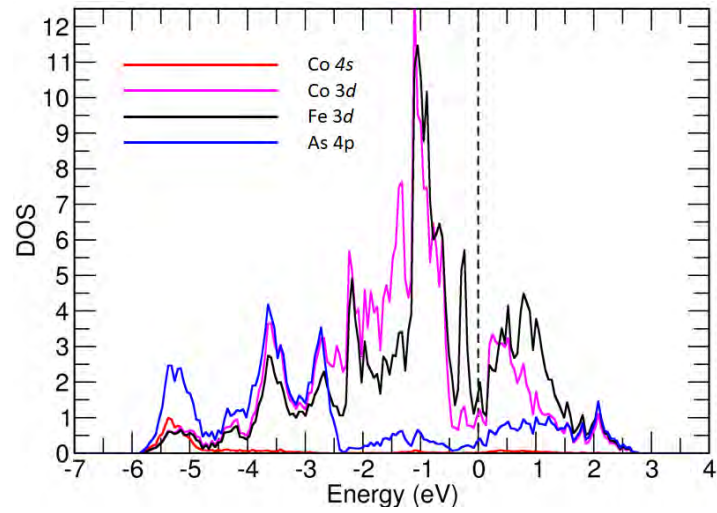


**Figure S3.** Calculated orbital resolved DOS for LiFe<sub>0.5</sub>Co<sub>0.5</sub>As.

## Theoretical simulation finite density of Co on the superconducting ground state

### T-matrix calculation

We use the  $\mathcal{T}$ -matrix approximation [26,40] generalized to the  $s^\pm$ -wave state of the two band model, to study the effects of impurities on the evolution of the experimentally measured local DOS with a systematic Co doping. In this study we freely tuned the strength of the impurity potential from the weak (Born limit) to the strong (unitary limit) coupling to fit the experimental data. We also tested a magnetic impurity potential on the assumed  $s^{++}$ -wave state, and found that the weak non-magnetic impurity scatterers on the  $s^\pm$ -wave state can describe the experimental DOS  $N(\omega)$  and its evolution with Co-doping.

The impurity induced self-energies are calculated with the  $\mathcal{T}$ -matrix generalized to a two-band superconductivity as

$$T_a^i(\omega_n) = \frac{G_a^i(\omega_n)}{D} \quad (i = 0,1; a = h, e) \quad (1)$$

$$D = c^2 + |G_h^0 + G_e^0|^2 + |G_h^1 + G_e^1|^2 \quad (2)$$

$$G_a^0(\omega_n) = \frac{N_a}{N_{tot}} \left\langle \frac{\tilde{\omega}_n}{\sqrt{\tilde{\omega}_n^2 + \tilde{\Delta}_a^2(k)}} \right\rangle \quad (3)$$

$$G_a^1(\omega_n) = \frac{N_a}{N_{tot}} \left\langle \frac{\tilde{\Delta}_n}{\sqrt{\tilde{\omega}_n^2 + \tilde{\Delta}_a^2(k)}} \right\rangle \quad (4)$$

where  $\omega_n = T\pi(2n + 1)$  is the Matsubara frequency, and  $N_{tot} = N_h(0) + N_e(0)$  is the total DOS.  $c = \cot \delta_0 = \frac{1}{\pi N_{tot} I_{imp}}$  is a convenient measure of scattering strength  $I_{imp}$ , with  $c = 0$  for the unitary limit and  $c > 1$  for the Born limit scattering.  $\langle \dots \rangle$  denotes the Fermi surface average. The subscript  $a$  stands for the electron band and hole band, respectively, and the superscript  $i$  stands for the normal ( $i = 0$ ) and anomalous ( $i = 1$ ) part of Green's functions, respectively.

The above four  $\mathcal{T}$ -matrices,  $\mathcal{T}_a^i$ , are numerically solved and the corresponding impurity induced self-energies are obtained as

$$\Sigma_{h,e}^{0,1}(\omega_n) = \Gamma \cdot T_{h,e}^{0,1}(\omega_n), \quad \Gamma = \frac{n_{imp}}{\pi N_{tot}} \quad (5)$$

where  $\Gamma$  is the impurity concentration parameter with  $n_{imp}$  the impurity density per unit cell. The normal/anomalous self-energy corrections to the Green's functions are then:

$$\widetilde{\omega}_n = \omega_n + \Sigma_h^0(\omega_n) + \Sigma_e^0(\omega_n) \quad (6)$$

$$\widetilde{\Delta}_{h,e} = \Delta_{h,e} + \Sigma_h^1(\omega_n) + \Sigma_e^1(\omega_n) \quad (7)$$

The important part for an impurity bound state is  $D$  in Eq.(2). Being a denominator of  $\mathcal{T}$ -matrices,  $\mathcal{T}_a^i$ , it signals a formation of a bound state when it goes to zero; otherwise, no bound state exists. The last term in  $D$ , namely,  $|G_h^1 + G_e^1|$  would exactly vanish for a d-wave superconductor because the FS average over the d-wave order parameter becomes zero, hence a zero energy bound state forms when  $c = 0$ . For the  $s\pm$ -wave case, a cancellation still occurs because  $G_h^1$  and  $G_e^1$  have opposite signs. However, this cancellation is never perfect unless  $|\Delta_e| = |\Delta_h|$  and  $N_h(0) = N_e(0)$ . With an incomplete cancellation, this finite remnant  $|G_h^1 + G_e^1|$  acts as a weakening impurity scattering strength (increasing the effective value of  $c$ ). Therefore, the impurity bound state in the  $s\pm$ -wave state forms at finite energies symmetrically split relative to the zero energy even with unitary impurity  $c = 0$ . Decreasing the impurity scattering strength towards a Born limit, these split in-gap bound states move towards the gap edges and merge to the quasi-particle continuum.

By fitting the experimental DOS (we use  $N_L=N_e$ , and  $N_S=N_h$  as in the main text), we can effectively determine the nature of the impurities and its coupling strength. We set realistic parameters: DOS ratio:  $N_L/N_S=2.5$ ; gap size ratio:  $\Delta_S/\Delta_L=-0.55$ , with a sign reversal; the scattering rate is set to be proportional to the Co concentration with a small offset:  $\Gamma/\Delta_{L0}=0.05+0.4(x/x_C)$  where  $x_C=16\%$ ; and  $\Delta_L=\Delta_{L0}(x_C-x)/x_C$  in reference to Fig. 4a. Figure S4 shows the quantum many body self-energy (the imaginary part) for different Co concentrations at the Born limit.

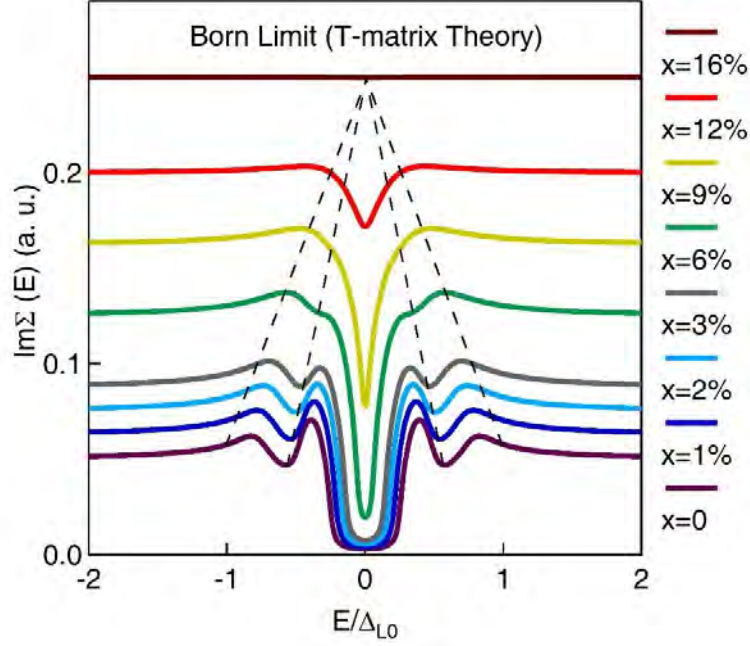


**Figure. S4** Nonmagnetic impurity induced many-body self-energies (imaginary part) for different concentrations at the Born limit. The dashed lines illustrate the reduction of the two gaps.

## Bogoliubov–de Gennes self-consistent calculation

### Two-orbital model

We adopted a two-orbital tight-binding model proposed in Ref. 28. Based on this model, there are many numerical results [41-44] consistent with experiments. Thus, this model may be a starting point to study the low-energy excitations for the iron-based superconductors. Here we also apply this model while considering the results from the photoemission experiment and the first-principles calculations in Co-doped LiFeAs.

This model is given by

$$\begin{aligned}
H = & - \sum_{i\mu j\nu\sigma} (t_{i\mu j\nu} c_{i\mu\sigma}^\dagger c_{j\nu\sigma} + H. c.) - \mu_c \sum_{i\mu\sigma} c_{i\mu\sigma}^\dagger c_{i\mu\sigma} \\
& + \sum_{i\mu j\nu\sigma} (\Delta_{i\mu j\nu} c_{i\mu\sigma}^\dagger c_{j\nu\bar{\sigma}}^\dagger + H. c.) + U \sum_{i\mu\sigma \neq \bar{\sigma}} \langle n_{i\mu\bar{\sigma}} \rangle n_{i\mu\sigma} + U' \sum_{i,\mu \neq \nu, \sigma \neq \bar{\sigma}} \langle n_{i\mu\bar{\sigma}} \rangle n_{i\nu\sigma} \\
& + (U' - J_H) \sum_{i,\mu \neq \nu, \sigma} \langle n_{i\mu\sigma} \rangle n_{i\nu\sigma} + \sum_{i_m\mu\sigma} V_{imp} c_{i_m\mu\sigma}^\dagger c_{i_m\mu\sigma}
\end{aligned} \tag{8}$$

Where  $i = (i_x, i_y), j = (j_x, j_y)$  are the site indices in two-dimensional plane,  $\mu, \nu = 1, 2$  are the orbital indices, and  $n_{i\mu\sigma}$  is the density operator at site  $i$  and orbital  $\mu$ ,  $U$  ( $U'$ ) is the on-site intraorbital (interorbital) Coulomb interaction and  $J_H$  is the Hund's rule coupling. The quantity  $U'$  is taken to be  $U - 2J_H$ , assuming the orbital rotation symmetry [43]. For a nonmagnetic impurity located at site  $i_m$ , we consider the intra-orbital scattering with the strength  $V_{imp}$ . In addition,  $\mu_c$  is the chemical potential, which is determined by the electron filling, corresponding to different doping level  $x$ . Considering the two-orbital tight-binding model here,  $x$  is related to the band filling as  $n = 2 + x$ . The hopping constants  $t_{i\mu j\nu}$  are chosen as follows:

$$\begin{aligned}
t_{i1, i\pm\hat{x}1} &= t_{i2, i\pm\hat{y}2} = t_1, \\
t_{i1, i\pm\hat{y}1} &= t_{i2, i\pm\hat{x}2} = t_2, \\
t_{i\mu, i\pm(\hat{x}+\hat{y})\mu} &= \frac{1 + (-1)^i}{2} t_3 + \frac{1 - (-1)^i}{2} t_4, \\
t_{i\mu, i\pm(\hat{x}-\hat{y})\mu} &= \frac{1 + (-1)^i}{2} t_4 + \frac{1 - (-1)^i}{2} t_3, \\
t_{i\mu, i\pm\hat{x}\pm\hat{y}\nu} &= t_5, (\mu \neq \nu)
\end{aligned} \tag{9}$$

The mean-field Hamiltonian can be diagonalized by solving the Bogoliubov-de-Gennes (BdG) equations,

$$H = \sum_j \sum_\nu \begin{pmatrix} H_{i\mu j\nu\sigma} & \Delta_{i\mu j\nu} \\ \Delta_{i\mu j\nu}^* & -H_{i\mu j\nu\bar{\sigma}}^* \end{pmatrix} \begin{pmatrix} u_{j\nu\sigma}^n \\ v_{j\nu\bar{\sigma}}^n \end{pmatrix} = E_n \begin{pmatrix} u_{i\mu\sigma}^n \\ v_{i\mu\bar{\sigma}}^n \end{pmatrix} \tag{10}$$

where

$$H_{i\mu j\nu\sigma} = -t_{i\mu j\nu} + (U \langle n_{i\mu\bar{\sigma}} \rangle + (U - 2J_H) \langle n_{i\bar{\mu}\bar{\sigma}} \rangle + (U - 3J_H) \langle n_{i\bar{\mu}\sigma} \rangle + V_{imp} \delta_{i, i_m} - \mu_c) \delta_{ij} \delta_{\mu\nu} \tag{11}$$

and

$$\Delta_{i\mu j\nu} = \frac{V_{i\mu j\nu}}{4} \sum_n (u_{i\mu\uparrow}^n v_{j\nu\downarrow}^{n*} + u_{j\nu\uparrow}^n v_{i\mu\downarrow}^{n*}) \tanh\left(\frac{E_n}{2k_B T}\right) \tag{12}$$

$$\langle n_{i\mu\uparrow} \rangle = \sum_n |u_{i\mu\uparrow}^n|^2 f(E_n) \tag{13}$$

$$\langle n_{i\mu\downarrow} \rangle = \sum_n |v_{i\mu\downarrow}^n|^2 (1 - f(E_n)) \tag{14}$$

$$\langle n_{i\mu} \rangle = \langle n_{i\mu\uparrow} \rangle + \langle n_{i\mu\downarrow} \rangle \tag{15}$$

here,  $f(E_n)$  is the Fermi-Dirac distribution function, and  $V_{i\mu j\nu}$  is the pairing strength. Here we consider the  $s_{\pm}$ - wave symmetry (see main text) and choose the next-nearest-neighbor (NNN) intraorbital pairing with strength  $V_{i\mu j\nu} = V_{ij} = V_{NNN}$  as a constant [21-26, 44]. In addition, we define the local magnetization and  $s_{\pm}$ - wave projection of the superconductivity order parameter at each site  $i$ , respectively as:  $m_i = \frac{1}{2} \sum_{\mu} (\langle n_{i\mu\uparrow} \rangle - \langle n_{i\mu\downarrow} \rangle)$ ,  $\Delta_i = \frac{1}{8} \sum_{\mu\delta} \Delta_{i\mu, i+\delta\mu}$ , where  $\delta = \pm\hat{x} \pm \hat{y}$ . When determining the strength of the pairing symmetry for a given different doping level  $x$ , we take an average over the whole lattice positions and disorder configurations for each local pairing amplitude shown in Eq. (12).

Throughout this work, the energies are measured in units of  $t_1$ , the temperature is set to be  $T = 0.0001$ , the hopping constants are chosen as  $t_{1-5} = (1, 0.7, 0.5, -2.0, 0.16)$ . The band energy and fermi surface without interaction has been depicted in Fig. S5. With electron doping the Fermi surface nesting condition is enhanced, consistent with the photoemission data in Ref. 9. The intraorbital Coulomb interaction  $U$  and the pairing strength  $V_{NNN}$  are set to be 3.4 and 1.4, respectively, the Hund's rule coupling  $J_H = U/4$ . Based on our first-principles calculation mentioned above, the on-site potential of Co is estimated to be as weak as -0.43eV. In model calculation, a further renormalization factor around 2 is often used to taking the correlations into account [19]. Thus here  $V_{imp}$  is set to be -2 (which amounts to  $\sim -0.2$ eV much smaller than the total bandwidth  $\sim 1.2$ eV in the model). With these realistic parameters, we calculated the BdG equations self-consistently with different doping level. The numerical calculations are performed on a  $28 \times 28$  square lattice with periodic boundary conditions. At each doping level, the calculations are performed on 25 different configurations, in each of which Co dopants are distributed randomly and homogeneously. Co dopants not only provide the onsite scattering, but also contribute extra electrons into the system. With these considerations, we obtain the linear decreasing trend of the superconductivity order parameter with increasing Co concentration, as shown in Fig. 4. To investigate the local dopant effect, we calculate the local DOS at  $x = 1\%$  around the Co dopant, and compare the results with that far away from the dopant (Fig. S6). The LDOS can be expressed as

$$\rho_i(\omega) = \sum_{n,\mu} \left[ |u_{i\mu\sigma}^n|^2 \delta(E_n - \omega) + |v_{i\mu\bar{\sigma}}^n|^2 \delta(E_n + \omega) \right] \quad (16)$$

where the  $\delta$  function is taken as  $\Gamma/\pi(x^2 + \Gamma^2)$ , with the quasiparticle damping  $\Gamma = 0.003$ . In addition, the averaged DOS at each doping level are calculated. A  $32 \times 32$  supercell is used to calculate the averaged DOS.

In the presence of a magnetic field  $B$  perpendicular to the plane, the hopping integral can be expressed as  $t'_{i\mu j\nu} = t_{i\mu j\nu} \exp \left[ i(\pi/\Phi_0) \int_i^j \vec{A}(\vec{r}) \cdot d\vec{r} \right]$ , where  $\Phi_0 = h_c/2e$  is the superconducting flux quantum, and  $\vec{A}(\vec{r}) = (-By, 0, 0)$  is the vector potential in the Landau gauge. In our calculation, magnetic unit cells are introduced where each unit cell accommodates two superconducting flux quantum and the linear dimension is  $N_x \times N_y = 64 \times 32$ . A  $16 \times 32$  supercell is used to calculate the local density of states. The vortex core state is shown in Fig. S6 inset.

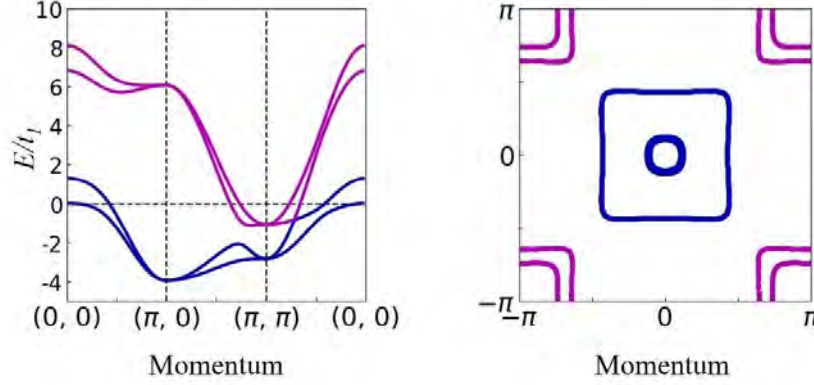


**Figure S5.** The two-orbital model calculated band structure (left) and Fermi surface (right) for LiFeAs.

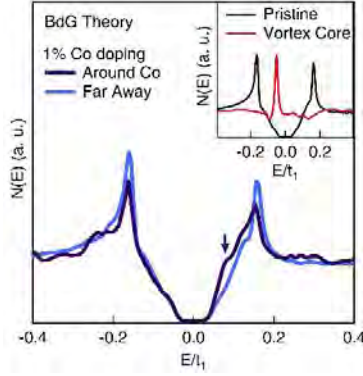


**Figure S6.** The two-orbital model calculated single Co impurity effect and vortex core states.

### Five-orbital model

We use the tight binding model as deduced earlier from spectral positions of the band structure as measured in photoemission [45]. This model was obtained by fitting the symmetry allowed hoppings [46] at short ranges such that the orbital content at the Fermi level matches experimental evidences as well. The band structure and the Fermi surface of that model for the pristine LiFeAs is presented in Fig. S7. The superconducting order parameter has been obtained self-consistently using a real space implementation of the BdG approach using pairing interactions in real space (where the pairing has been cut at a distance of three lattice spacings in x and y direction) that have been calculated from a modified spin-fluctuation approach [47] within the same tight binding model. Upon Co doping, the pairing interaction itself is kept constant. For the homogeneous case one obtains a superconducting order parameter with a structure as shown in Fig. S8 (where the real space structure, its Fourier transform and the corresponding projection to the Fermi surface is presented). Next, random impurity configurations are taken to simulate Co substituting for Fe in the system. The impurity potential is chosen to be  $V_{\text{imp}} = -0.15\text{eV}$ , which is in agreement with the value as found from ab initio calculations by taking into account a quasiparticle renormalization factor of  $Z=1/2$  [19].

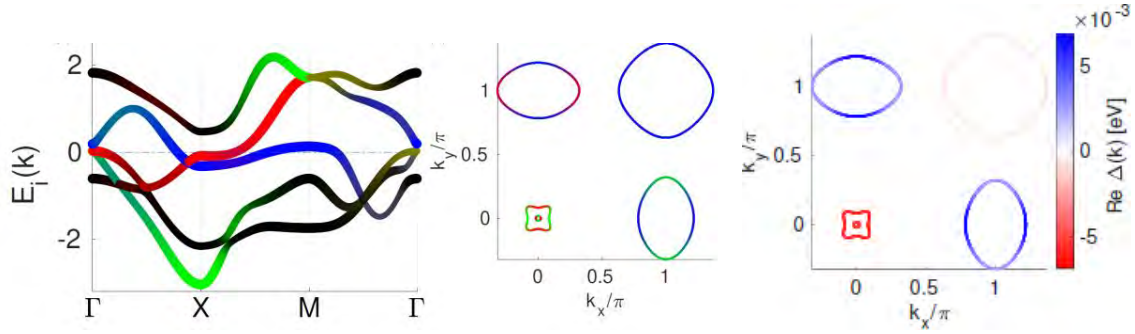


**Figure S7.** Bands along high symmetry directions together with the orbital character (left) and Fermi surface of the 2D version of the electronic structure (middle) and gap structure (right) for LiFeAs. Color code: red  $dxz$ , green  $dyz$ , blue  $dxy$ , black (other).

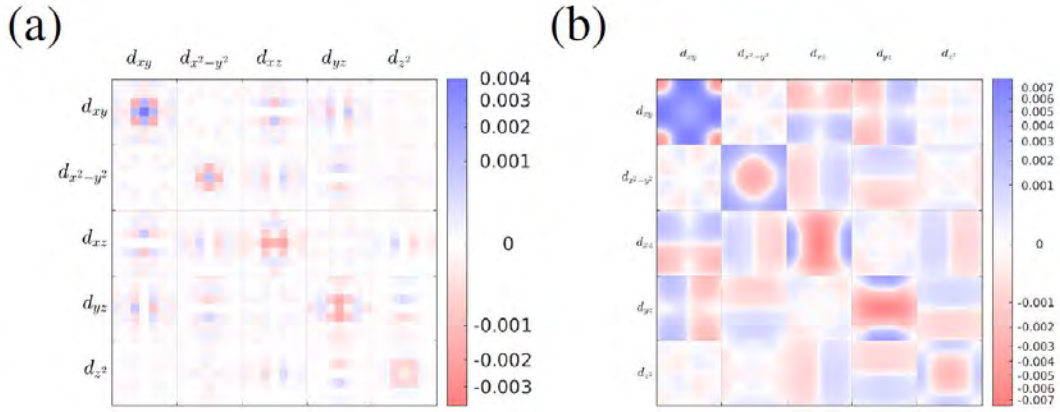


**Figure S8.** Plot of the mean fields as obtained in the self-consistent calculation of a homogeneous system. Structure of gap for all combinations of the orbitals in the real space (a) and in momentum space (b). Projection of the order parameter in band space shown on the Fermi surface.

### Further discussion of pairing on the bulk Dirac bands

In addition, the electron doping also causes the system's Fermi level to cross the bulk Dirac cone (Fig. 2a inset) and there will be two corresponding spherical Fermi surfaces along the  $\Gamma$ -Z direction [12]. Due to the intrinsic orbit-momentum locking in such Fermi surfaces [48,49], its gap function can be either nodeless or nodal. When we assume its pairing is induced from the  $s_{\pm}$  state of the ordinary bands, the most natural pairing on the bulk Dirac bands should be spin-singlet and intra-orbital, which is a s-wave gap. In principle, the spin triplet inter-orbital pairing is also allowed for the bulk Dirac Fermi surfaces, and the associated gap function has point nodes along the  $k_z$  axis [48,49], which is incompatible with the  $s_{\pm}$  gap function. The frustration in pairing symmetry, in this case, can suppress the Cooper pairing, and its impact can be non-monotonic when the Fermi level systematically crosses the bulk Dirac cone via Co doping. However, experimentally both the

gap and  $T_C$  are linearly suppressed, which does not directly support the latter case. Therefore, we conclude that the main source of the linear  $T_C$  reduction may still come from a finite density of nonmagnetic scatters in a  $s\pm$  superconductor.

## References

31. Q. Deng et al. The effect of impurity and the suppression of superconductivity in  $\text{Na}(\text{Fe}_{0.97-x}\text{Co}_{0.03}\text{T}_x)\text{As}$  ( $T = \text{Cu, Mn}$ ). *New J. Phys.* **16**, 063020 (2014).
32. P. Hohenberg, W. Kohn. Inhomogeneous Electron Gas. *Phys. Rev.* **136**, B864 (1964).
33. W. Kohn, L. J. Sham. Self-Consistent Equations Including Exchange and Correlation Effects. *Phys. Rev.* **140**, A1133 (1965).
34. G. Kresse, J. Hafner. Ab initio molecular dynamics for liquid metals. *Phys. Rev. B* **47**, 558 (1993).
35. G. Kresse, J. Furthmüller. Efficient iterative schemes for ab initio total-energy calculations using plane-wave basis set. *Phys. Rev. B* **54**, 11169 (1996).
36. J. P. Perdew, K. Burke, M. Ernzerhof. Generalized gradient approximation made simple. *Phys. Rev. Lett.* **77**, 3865 (1996).
37. G. Kresse, D. Joubert. From ultrasoft pseudopotentials to the projector augmented-wave method. *Phys. Rev. B* **59**, 1758 (1999).
38. H. J. Monkhorst, J. D. Pack. Special points for Brillouin-zone integrations. *Phys Rev B* **13**, 5188–5192 (1976).
39. K. Nakamura et al. First-principles calculation of transition-metal impurities in  $\text{LaFeAsO}$ . *Phys. Rev. B* **83**, 144512 (2011).
40. P. J. Hirschfeld, P. Wolfle, D. Einzel. Consequences of resonant impurity scattering in anisotropic superconductors: Thermal and spin relaxation properties. *Phys Rev. B.* **37**, 83 (1988).
41. T. Zhou et al. Electronic structure around a vortex core in iron-based superconductors: Numerical studies of a two-orbital model. *Phys. Rev. B* **84**, 174524 (2011).
42. T. Zhou et al. Quasiparticle states around a nonmagnetic impurity in electron-doped iron-based superconductors with spin-density-wave order. *Phys. Rev. B* **83**, 214502 (2011).
43. Y. Y. Zhao et al. Effects of single- and multi-substituted Zn ions in doped 122-type iron-based superconductors. *Phys. Rev. B* **93**, 144510 (2016).
44. Y. Gao et al. Possible pairing symmetry in the FeSe-based superconductors determined by quasiparticle interface. *Phys. Rev. Lett.* **121**, 267005 (2018).
45. Y. Wang et al. Superconducting gap in  $\text{LiFeAs}$  from three-dimensional spin-fluctuation pairing calculations. *Phys. Rev. B* **88**, 174516 (2013).
46. H. Eschrig and K. Koepernik, Tight-binding models for the iron-based superconductors, *Phys. Rev. B* **80**, 104503 (2009).
47. A. Kreisler et al. Orbital selective pairing and gap structures of iron-based superconductors. *Phys. Rev. B* **95**, 174504 (2017).
48. S. Kobayashi, M. Sato. Topological Superconductivity in Dirac Semimetals. *Phys. Rev. Lett.* **115**, 187001 (2015).
49. T. Hashimoto, S. Kobayashi, Y. Tanaka, M. Sato. Superconductivity in doped Dirac semimetals. *Phys. Rev. B* **94**, 014510 (2016).

## Paper V

### Visualization of local magnetic moments emerging from impurities in the Hund's metal states of FeSe

S. Y. Song, Johannes H. J. Martiny, A. Kreisel, B. M. Andersen, J. Seo

*Currently under review*

*Preprint: arXiv:1909.13515*

# Visualization of local magnetic moments emerging from impurities in the Hund's metal states of FeSe

Sang Yong Song,<sup>1</sup> J. H. J. Martiny,<sup>2</sup> A. Kreisel,<sup>3</sup> B. M. Andersen,<sup>4</sup> and Jungpil Seo<sup>1,†</sup>

<sup>1</sup>*Department of Emerging Materials Science, DGIST, 333 Techno-Jungang-daero, Hyeonpung-Eup, Dalseong-Gun, Daegu 42988, Korea*

<sup>2</sup>*Center for Nanostructured Graphene (CNG), Department of Micro- and Nanotechnology, Technical University of Denmark, DK-2800 Kongens Lyngby, Denmark*

<sup>3</sup>*Institut für Theoretische Physik, Universität Leipzig, D-04103 Leipzig, Germany*

<sup>4</sup>*Niels Bohr Institute, University of Copenhagen, Lyngbyvej 2, DK-2100 Copenhagen, Denmark*

## Abstract

Understanding the origin of the magnetism of high temperature superconductors is crucial for establishing their unconventional pairing mechanism. Recently, theory predicts that FeSe is close to a magnetic quantum critical point, and thus weak perturbations such as impurities could induce local magnetic moments. To elucidate such quantum instability, we have employed scanning tunneling microscopy and spectroscopy. In particular, we have grown FeSe film on superconducting Pb(111) using molecular beam epitaxy and investigated magnetic excitation caused by impurities in the proximity-induced superconducting gap of FeSe. Our study provides a deep insight into the origin of the magnetic ordering of FeSe by showing the way local magnetic moments develop in response to impurities near the magnetic quantum critical point.

PACS number: 74.25.Dw, 07.79.Cz, 68.35.Rh

FeSe presents intriguing properties in terms of the interplay among the lattice, charge, and spin degree of freedom. Its nematic phase transition occurs at  $T_S = 90$  K, below which the  $C_4$  lattice symmetry is reduced to  $C_2$  symmetry [1-3]. Unlike other iron-based superconductors, however, the long-range magnetic ordering is absent in FeSe down to the superconducting transition temperature  $T_c = 8$  K for bulk material, making the degree of freedom that drives the nematic order ambiguous among lattice, charge, and spin [3-10].

Although long-range magnetic ordering is absent in FeSe, there are experiments that suggest the ground state of FeSe is close to the magnetic quantum phase transition point. First of all, the hydrostatic pressure of  $\sim 1$  GPa readily induces static stripe antiferromagnetic (AFM) orders in FeSe which are typically observed in other iron-based superconductors [11-14]. There is also evidence of local magnetism in FeSe. For example, a muon spin resonance ( $\mu$ SR) study of FeSe<sub>0.85</sub> measured an exponential decay of the muon polarization, which might hint at the presence of randomly oriented local magnetic moments [15]. The magnetostriction and susceptibility experiment shows strong in-plane anisotropy in FeSe, inferring the coupling of the local magnetic ordering and spin-orbit coupling [16]. Recently, a scanning tunneling microscopy (STM) study observed a signature of local spin fluctuations near the Fe defect in multi-layer FeSe on SrTiO<sub>3</sub> substrate [17]. Such magnetic instability, as pointed out in recent theory papers, suggests the possibility that the magnetism can be triggered by impurities in FeSe [18,19].

Despite intensive efforts in understanding the magnetism in FeSe, the direct observation of local magnetic moments emerging from impurities, which results from

the quantum instability, has been challenging mostly owing to the lack of spatial magnetic resolution in the experiments. Here, we use a novel experimental approach to investigate the impurity-induced local magnetic moments in FeSe. Using molecular beam epitaxy (MBE), we grow FeSe film on Pb(111) substrate which is known to be an s-wave superconductor. We have observed a clear signature of the s-wave superconducting gap on the FeSe film, which is proximity-induced from the Pb substrate. When local magnetic moments develop near crystalline imperfections, they respond to the s-wave superconductivity giving rise to Cooper pair breaking. This leads to a strong bound state known as Yu-Shiba-Rusinov (YSR) excitation within the superconducting gap [20-24]. We used these YSR excitations as probes of induced magnetic moments in FeSe. Thanks to the extreme sensitivity of superconductivity to magnetism, the energy and spatial resolutions in our study for observing the local magnetic moments are unprecedented. All data are taken at the temperature of 4.3 K in the experiment.

In the growth of FeSe, we first grew a single layer (SL) of PbSe on Pb(111). We then deposited Fe atoms on the PbSe at 490 K, which resulted in the formation of FeSe islands on Pb(111) (see Supplemental Material for detail). Figure 1a shows a typical STM image of the FeSe island grown on Pb(111). The FeSe island is surrounded by the PbSe layer and several bare Pb patches whose identity is confirmed by scanning tunneling spectroscopy (STS). The hexagonal-shaped defects in the island and near the island are Ar gas bubbles trapped inside the Pb substrate, which are introduced during the Ar gas sputtering process for cleaning the substrate [25]. The inset shows the atomic structure of FeSe. A rectangular lattice structure is clearly resolved and is distinguished from the crystal structure of Pb(111).

Figure 1b shows the Fourier transform (FT) of the topography of the FeSe. The strong lattice peaks are present at the position of  $(k_x, k_y) = (\pm 1.2, \pm 1.2) \text{ \AA}^{-1}$ , whose numbers translate into the lattice constant of 3.7 Å. Figure 1c depicts the atomic model of FeSe forming tri-layer (TL) structure. The blue-filled circles, the red-filled circles, and the blue open circles represent the Se atoms in the top layer, the Fe atoms in the middle layer and the Se atoms in the bottom layer, respectively. As STM mostly measures the top-most Se atoms [26], the obtained lattice structure should conform to the Se lattice in the top layer (solid box in Fig. 1c). For bulk FeSe, the Se lattice constant is known to be  $\sim 3.75 \text{ \AA}$  [27-29], which agrees well with the measured value.

The apparent height of FeSe islands with respect to the Pb substrate is found to be  $\sim 1.7 \text{ \AA}$  (Fig. 1d). This is smaller than the 1 TL of bulk FeSe ( $\sim 5.33 \text{ \AA}$ ), indicating that most of the FeSe is embedded inside Pb. Similar growth has been reported when FeSe film is grown on soft substrates [30-32]. The lattice modeling of FeSe and Pb estimates the thickness of our FeSe is 3 TL (see Supplemental Material) although it cannot be precisely determined by STM. A Moiré pattern found in the FeSe (Fig. 1a), which is due to the lattice mismatch between FeSe and Pb(111), confirms that the FeSe is in the thin film limit.

To study the electronic property of the FeSe, we performed a differential conductance ( $dI/dV$ ) spectroscopy using a standard lock-in technique [25]. To maximize the energy resolution in measuring  $dI/dV$  spectrum at our experiment temperature, we used a Pb-coated superconducting tip [21,25]. Figure 1e shows the

dl/dV spectra measured in the FeSe and Pb. For the FeSe spectrum, there is a characteristic peak near the bias voltage ( $V_{\text{bias}}$ ) of -0.3 V, which is consistent with the spectra of FeSe in literature [29,33].

When the spectrum is zoomed in around the Fermi energy, a superconducting gap is found (the inset of Fig. 1e). According to following three facts, we conclude that the superconductivity of our FeSe is proximity-induced from the Pb substrate. First, the superconducting coherence length ( $\xi$ ) of Pb ( $\sim 830 \text{ \AA}$ ) is much larger than the thickness of the FeSe ( $\sim 16 \text{ \AA}$  for 3 TL). Second, the gap is fully developed revealing the s-wave nature in superconductivity. Third, the phonon peaks associated with Pb superconductivity are clearly seen in the spectrum of FeSe (marked by arrows in the inset of Fig. 1e) [34,35]. No hint of unconventional superconductivity is observed. The gap size (4.6 meV) is twice that of the Pb superconducting gap ( $2\Delta \approx 2.3 \text{ meV}$ ) because the tip is coated with Pb. Under the  $T_c$  of Pb superconductivity ( $\sim 7.2 \text{ K}$ ), all electrons of FeSe are forced to participate in the proximity-induced s-wave pairing. Any electron pairs which are not in a time reversal symmetry (TRS) relationship will form YSR excitation states within the superconducting gap [20,21,36].

We have investigated the response of FeSe to proximity-induced s-wave superconductivity. Figure 2b shows spectra measured at different FeSe sites marked with A, B, C, and R in Fig. 2a. The spectrum on PbSe (Position R) is first measured as a reference because PbSe is not an intrinsic superconductor and thus its superconductivity is undoubtedly induced by proximity to the Pb. Remarkably, the spectrum measured inside the FeSe island (Position B) exhibits no YSR excitation, indicating that the expected magnetic moment  $\langle M_i \rangle$  is zero for the ground state,

where  $i$  is the site index for Fe atoms. This is direct microscopic evidence of the absence of static magnetic ordering in FeSe. In contrast to the spectrum at B, the spectra measured at the boundary of the FeSe island (Position A and C) show strong YSR excitation states, suggesting local magnetic moments are developed along the boundary. Therefore, it should be remarked that FeSe itself is far from non-magnetic although its ground state preserves TRS [9,12,13,37-39]. Figure 2c displays the  $dI/dV$  plot along the dashed line marked in Fig. 2a. We barely observed a variation in superconductivity inside the FeSe island.

To study the impurity-induced quantum instability in FeSe, we have deposited Ag atoms onto the sample at 20 K (Fig. 3a). The height of Ag atoms is  $\sim 0.7$  Å on the FeSe (Fig. 3b). By careful FT analysis, we determined that the Ag atoms are located on the center of top Se lattice in the FeSe (Fig. 3c and also see Supplemental Material). Non-magnetic atoms, such as Ag, will not break TRS and thus the s-wave superconductivity should not respond to them. Accordingly, the  $dI/dV$  spectrum of the Ag atom on the Pb surface exhibits no YSR excitation (Fig. 3d). We only observed a slight variation in gap size, which might be related to the double Fermi surface of Pb but is not caused by magnetism [40]. By contrast, when we measured the  $dI/dV$  spectrum on the Ag atom placed on the FeSe, strong YSR excitation is detected, showing that local magnetic moments are developed (also see Supplemental Material). It is remarkable that such non-magnetic atoms induce local magnetism in FeSe. This supports the assertion that the ground state of FeSe is near a magnetic quantum critical point.

To understand the pattern of local magnetic moments, we measured  $dI/dV$  maps at the various energies ( $E = eV_{\text{bias}}$ ) of YSR states. Figure 3e shows the topography of the Ag atom and simultaneously obtained  $dI/dV$  maps. The most striking feature in the  $dI/dV$  maps is the splitting of the  $dI/dV$  patterns. The  $dI/dV$  patterns at  $E = -1.85$  meV and  $E = -1.3$  meV are split along up-and-down. The  $dI/dV$  pattern at  $E = 1.48$  meV is slightly tilted from the up-and-down splitting. These are representative magnetic patterns induced by Ag atoms in FeSe (see Supplemental Material).

Three notable features are present regarding the magnetic patterns. First, the tendency of splitting is the same among the Ag atoms placed on the FeSe in Fig. 3a. No Ag atom showed a splitting along the left-and-right. This symmetry breaking can be attributed to the nematic order in our FeSe. Second, the in-gap states are strongly localized near the Ag atom. We barely observed long-range magnetic ordering near the Ag atom, which is in contrast to the STM experiment in which Fe defects of FeSe are argued to pin the long-range charge oscillations associated with  $(\pi, 0)$  spin fluctuations [17]. Third, the magnetic patterns only satisfy  $C_2$  symmetry. They do not follow the full symmetry of the crystal lattice, which implies there is a hidden rule that restricts the symmetry of magnetic patterns.

Before proceeding further, the reliability of the  $C_2$  symmetry of the magnetic patterns is discussed. We have found that the direction of Moiré pattern does not match the splitting direction of the magnetic patterns (see Supplemental Material). This excludes the Moiré pattern as a possible origin of the splitting. The magnetic patterns varied slightly depending on the Ag atom, but the overall  $C_2$  symmetry was

maintained for the majority of Ag atoms we measured in the experiment (see Supplemental Material).

Recent theory predicts that the local magnetic moments in FeSe reflect the momentum structure of the magnetic fluctuations in the bulk [19]. To confirm this, we compared the measured magnetic patterns with two bulk models for FeSe in terms of symmetry. Figure 3f shows the collinear AFM (cAFM) model (left panel) and the Néel AFM model (right panel). The cAFM model preserves the  $C_2$  symmetry of FeSe, which agrees with our magnetic patterns. The Néel AFM model can be ruled out because it does not have  $C_2$  symmetry and it has a definite mirror symmetry plane (the dashed line in Fig. 3f) that contradicts the symmetry of the magnetic patterns at  $E = -1.85$  meV and  $E = -1.3$  meV. Therefore, the magnetic patterns observed in the experiment reflect the symmetry of the  $(\pi, 0)$  AFM ordering. Note that the spin angle of  $45^\circ$  in our models is supported by recent  $\mu$ SR measurement [41]. For the spin angle of  $0^\circ$  which is another high symmetry direction, however, the magnetic patterns are also consistent with the symmetry of the cAFM ordering (see Supplemental Material).

Now we turn to a discussion of the origin of impurity-induced local magnetic moments in FeSe. Electron interactions are strong in FeSe and almost drive the material magnetism. A recent theoretical study, based on a multi-orbital Hubbard model with a band structure relevant for FeSe, mapped out the phase diagram of local impurity-induced magnetism [19]. Importantly, as shown in Ref. [19] the orbital-selectivity characteristic of Hund's metals [27,42] is directly imprinted on the local impurity-induced order, yielding local  $(\pi, 0)$  AFM structure versus  $(\pi, \pi)$  AFM local

order when orbital-selectivity is included or disregarded, respectively. These calculations reveal that strongly anisotropic magnetic fluctuations dictate the detailed structure of induced local magnetic order [19]. A similar transmutation of the structure of the bulk magnetic fluctuations and superconducting pairing, takes place when including orbital selectivity [39,43,44]. While the results from Ref. [19] focused on impurities centered on Fe sites, we show in Supplemental Material (Note S2) that Se-centered disorder (like Ag) also induce local  $(\pi, 0)$ -structured magnetic order. In addition, we have applied the same theoretical machinery to sample edges, and found that FeSe is very susceptible to induce magnetism strongly localized near the edges (Note S2 in Supplemental Material), in agreement with the STM findings reported here.

We occasionally found a dumbbell-shaped local defect in the FeSe before the deposition of Ag atoms (Fig. 4a). The center of the defect is located at the Fe site as guided by the two dashed lines depicted in Fig. 4a, suggesting it is an Fe vacancy [45-47]. When the  $dI/dV$  spectrum is measured off the Fe defect, no YSR excitation is observed. However, when it is measured on the defect, strong YSR excitation is observed, indicating that an Fe defect also induces local magnetic moments in FeSe.

Figure 4c-f shows the topography of the Fe defect and simultaneously measured  $dI/dV$  maps. The dashed line depicted in Fig. 4e represents the mirror symmetry plane imposed by the crystal lattice. The topography is naturally symmetric with respect to this mirror symmetry (Fig. 4c). Interestingly, the magnetic patterns (Fig. 4d-f) are not symmetric under the mirror operation [17,42]. Recent theory shows that orbital-selectivity can give rise to chiral patterns in the conductance maps from local

magnetic ordering near Fe defects, upon which the mirror symmetry is broken [19]. In fact, Fig. 4d shows the axis of the magnetic pattern (yellow dotted line) is tilted from the mirror symmetry axis according to the theory. We find that the observed magnetic patterns are again consistent with the symmetry of the cAFM model. Figure 4g shows the cAFM model with the Fe defect. The cAFM ordering directly breaks the mirror symmetry of the crystal lattice. Furthermore, the cAFM ordering breaks the  $C_2$  symmetry of FeSe when a defect exists in the Fe site, which is in contrast to the case of the Ag on FeSe. Two green-colored sites in Fig. 4g are then no longer equivalent in terms of symmetry. In the experiment, the magnetic excitation at these sites indeed appears at different energies as shown in Fig. 4e and 4f.

Our STM experiment provides a novel method to study local magnetism in correlated superconductors, here exemplified through FeSe. The results lead to several important remarks. First, the magnetic quantum phase transition by non-magnetic impurities is microscopically observed in FeSe. Second, we show that the magnetic patterns of the local magnetic moments are consistent with the  $(\pi, 0)$  AFM phase, implying that the orbital-selectivity is at play. Third, our experiment reveals the magnetic characteristics of impurities in FeSe. The  $s_{\pm}$  superconductivity responds to both magnetic and non-magnetic impurities, whereas the  $s_{++}$  superconductivity only responds to magnetic impurities [24,48]. It is therefore important to characterize the magnetic property of impurities before they are used to probe the symmetry of superconductivity. Our experiment unambiguously reveals that the crystalline defects like crystal boundary and Fe vacancy are magnetic in FeSe. Furthermore, it should be noted that the local magnetism could also be induced by non-magnetic impurities in FeSe.

The data analysis described here is based on a simple and powerful symmetry argument. A theoretical work deserving further investigation is identifying the Fe orbitals responsible for each magnetic pattern observed in the experiment. This will reveal the origin of the local magnetism in FeSe in conjunction with the orbital-selectivity. In future STM works, it will be interesting to study how the local magnetism develops into the bulk magnetism when the Ag impurities form networks, which can be accomplished by the STM atom manipulation. Nearby, it might be possible to detect strong orbital-selective spin fluctuations through inelastic tunneling spectroscopy (IETS), which could be in turn related to the anisotropic Cooper pairing in FeSe.

This work was supported by the Samsung Science & Technology Foundation under Project Number SSTF-BA1502-04.

tjseo@dgist.ac.kr

## References

- [1] A. I. Coldea and M. D. Watson, *Annual Review of Condensed Matter Physics* **9**, 125 (2018).
- [2] A. E. Böhrer and A. Kreisel, *Journal of Physics: Condensed Matter* **30**, 023001 (2018).
- [3] T. M. McQueen, A. J. Williams, P. W. Stephens, J. Tao, Y. Zhu, V. Ksenofontov, F. Casper, C. Felser, and R. J. Cava, *Physical Review Letters* **103**, 057002 (2009).
- [4] M. Bendele *et al.*, *Physical Review Letters* **104**, 087003 (2010).
- [5] T. Imai, K. Ahilan, F. L. Ning, T. M. McQueen, and R. J. Cava, *Physical Review Letters* **102**, 177005 (2009).
- [6] J.-H. She, M. J. Lawler, and E.-A. Kim, *Physical Review Letters* **121**, 237002 (2018).
- [7] F. Wang, S. A. Kivelson, and D.-H. Lee, *Nature Physics* **11**, 959 (2015).
- [8] J. K. Glasbrenner, I. I. Mazin, H. O. Jeschke, P. J. Hirschfeld, R. M. Fernandes, and R.

- Valentí, *Nature Physics* **11**, 953 (2015).
- [9] R. M. Fernandes, A. V. Chubukov, and J. Schmalian, *Nature Physics* **10**, 97 (2014).
- [10] S. H. Baek, D. V. Efremov, J. M. Ok, J. S. Kim, J. van den Brink, and B. Büchner, *Nature Materials* **14**, 210 (2014).
- [11] M. Bendele *et al.*, *Physical Review B* **85**, 064517 (2012).
- [12] J. P. Sun *et al.*, *Nature Communications* **7**, 12146 (2016).
- [13] K. Kothapalli *et al.*, *Nature Communications* **7**, 12728 (2016).
- [14] T. Terashima *et al.*, *J Phys Soc Jpn* **84**, 063701 (2015).
- [15] R. Khasanov *et al.*, *Physical Review B* **78**, 220510(R) (2008).
- [16] M. He, L. Wang, F. Hardy, L. Xu, T. Wolf, P. Adelmann, and C. Meingast, *Physical Review B* **97**, 104107 (2018).
- [17] W. Li *et al.*, *Nature Physics* **13**, 957 (2017).
- [18] M. N. Gastiasoro and B. M. Andersen, *Journal of Superconductivity and Novel Magnetism* **28**, 1321 (2014).
- [19] J. H. J. Martiny, A. Kreisel, and B. M. Andersen, *Physical Review B* **99**, 014509 (2019).
- [20] A. Yazdani, B. A. Jones, C. P. Lutz, M. F. Crommie, and E. D. M., *Science* **275**, 1767 (1997).
- [21] K. J. Franke, G. Schulze, and J. I. Pascual, *Science* **332**, 940 (2011).
- [22] H. Shiba, *Progress of Theoretical Physics* **40**, 435 (1968).
- [23] M. I. Salkola, A. V. Balatsky, and J. R. Schrieffer, *Physical Review B* **55**, 12648 (1997).
- [24] A. V. Balatsky, I. Vekhter, and J.-X. Zhu, *Reviews of Modern Physics* **78**, 373 (2006).
- [25] S. Y. Song and J. Seo, *Scientific Reports* **7**, 12177 (2017).
- [26] C. L. Song *et al.*, *Science* **332**, 1410 (2011).
- [27] A. Kostin, P. O. Sprau, A. Kreisel, Y. X. Chong, A. E. Böhmer, P. C. Canfield, P. J. Hirschfeld, B. M. Andersen, and J. C. S. Davis, *Nature Materials* **17**, 869 (2018).
- [28] F. S. Li *et al.*, *2d Mater* **3**, 024002 (2016).
- [29] X. Liu *et al.*, *Journal of Physics: Condensed Matter* **27**, 183201 (2015).
- [30] A. Cavallin *et al.*, *Surface Science* **646**, 72 (2016).
- [31] A. Eich *et al.*, *Physical Review B* **94**, 125437 (2016).
- [32] U. R. Singh, J. Warmuth, V. Markmann, J. Wiebe, and R. Wiesendanger, *Journal of Physics: Condensed Matter* **29**, 025004 (2017).
- [33] Y. H. Yuan *et al.*, *Nano Letters* **18**, 7176 (2018).
- [34] M. Schackert, T. Märkl, J. Jandke, M. Hölzer, S. Ostanin, E. K. U. Gross, A. Ernst, and W. Wulfhekel, *Physical Review Letters* **114**, 047002 (2015).
- [35] W. L. McMillan and J. M. Rowell, *Physical Review Letters* **14**, 108 (1965).
- [36] D. J. Choi, C. Rubio-Verdu, J. de Bruijckere, M. M. Ugeda, N. Lorente, and J. I. Pascual,

- Nature Communications **8**, 15175 (2017).
- [37] Q. Wang *et al.*, Nature Communications **7**, 12182 (2016).
- [38] Q. Wang *et al.*, Nature Materials **15**, 159 (2015).
- [39] T. Chen *et al.*, Nature Materials **18**, 709 (2019).
- [40] M. Ruby, B. W. Heinrich, J. I. Pascual, and K. J. Franke, Physical Review Letters **114**, 157001 (2015).
- [41] R. Khasanov, Z. Guguchia, A. Amato, E. Morenzoni, X. Dong, F. Zhou, and Z. Zhao, Physical Review B **95**, 180504(R) (2017).
- [42] P. O. Sprau *et al.*, Science **357**, 75 (2017).
- [43] A. Kreisel, B. M. Andersen, P. O. Sprau, A. Kostin, J. C. S. Davis, and P. J. Hirschfeld, Physical Review B **95**, 174504 (2017).
- [44] A. Kreisel, B. M. Andersen, and P. J. Hirschfeld, Physical Review B **98**, 214518 (2018).
- [45] P. Choubey, T. Berlijn, A. Kreisel, C. Cao, and P. J. Hirschfeld, Physical Review B **90**, 134520 (2014).
- [46] S. Chi *et al.*, Physical Review B **94**, 134515 (2016).
- [47] D. Huang, T. A. Webb, C.-L. Song, C.-Z. Chang, J. S. Moodera, E. Kaxiras, and J. E. Hoffman, Nano Letters **16**, 4224 (2016).
- [48] S. Onari and H. Kontani, Physical Review Letters **103**, 177001 (2009).

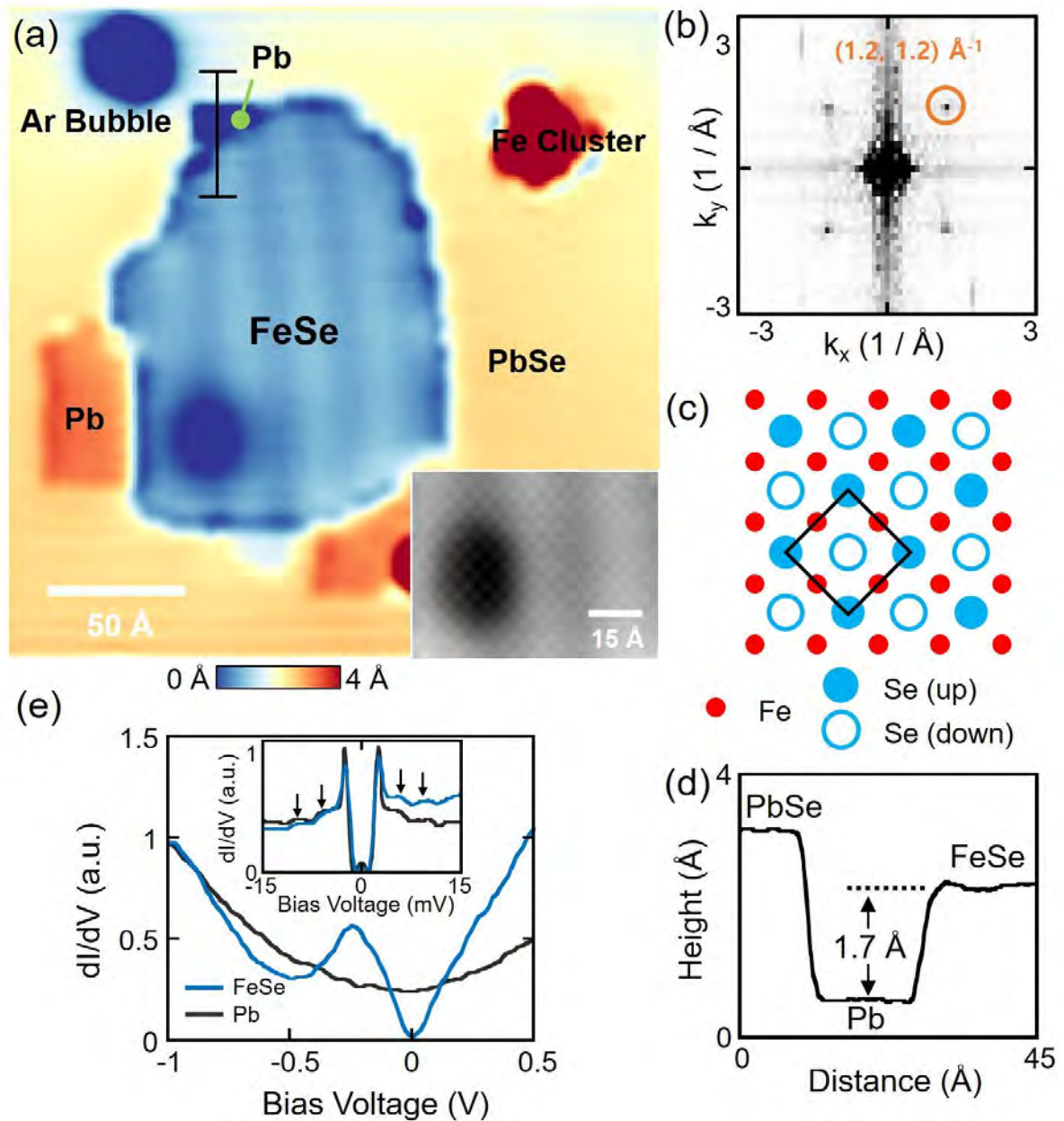


**Figure 1.** (a) The topography of FeSe island grown on Pb(111).  $V_{\text{bias}} = -0.1$  V and  $I = 50$  pA. The inset shows the atomically resolved image.  $V_{\text{bias}} = -50$  mV and  $I = 50$  pA. (b) Fourier transform of the FeSe image. (c) Atomic model of the FeSe that consists of tri-layer. The solid box represents the Se lattice in the top layer. (d) The height profile along the vertical line in (a). (e) The  $dI/dV$  spectra measured in the FeSe island and bare Pb.  $V_{\text{bias}} = -1$  V and  $I = 50$  pA. Lock-in modulation: frequency  $f = 463.0$  Hz and root-mean-square (rms) amplitude  $V_{\text{rms}} = 10$  mV. The inset shows the spectra around the Fermi energy.  $V_{\text{bias}} = -15$  mV and  $I = 50$  pA. Lock-in modulation:  $f = 463.0$  Hz and  $V_{\text{rms}} = 0.3$  mV. The arrows indicate the phonon peaks derived from the Pb superconductivity.

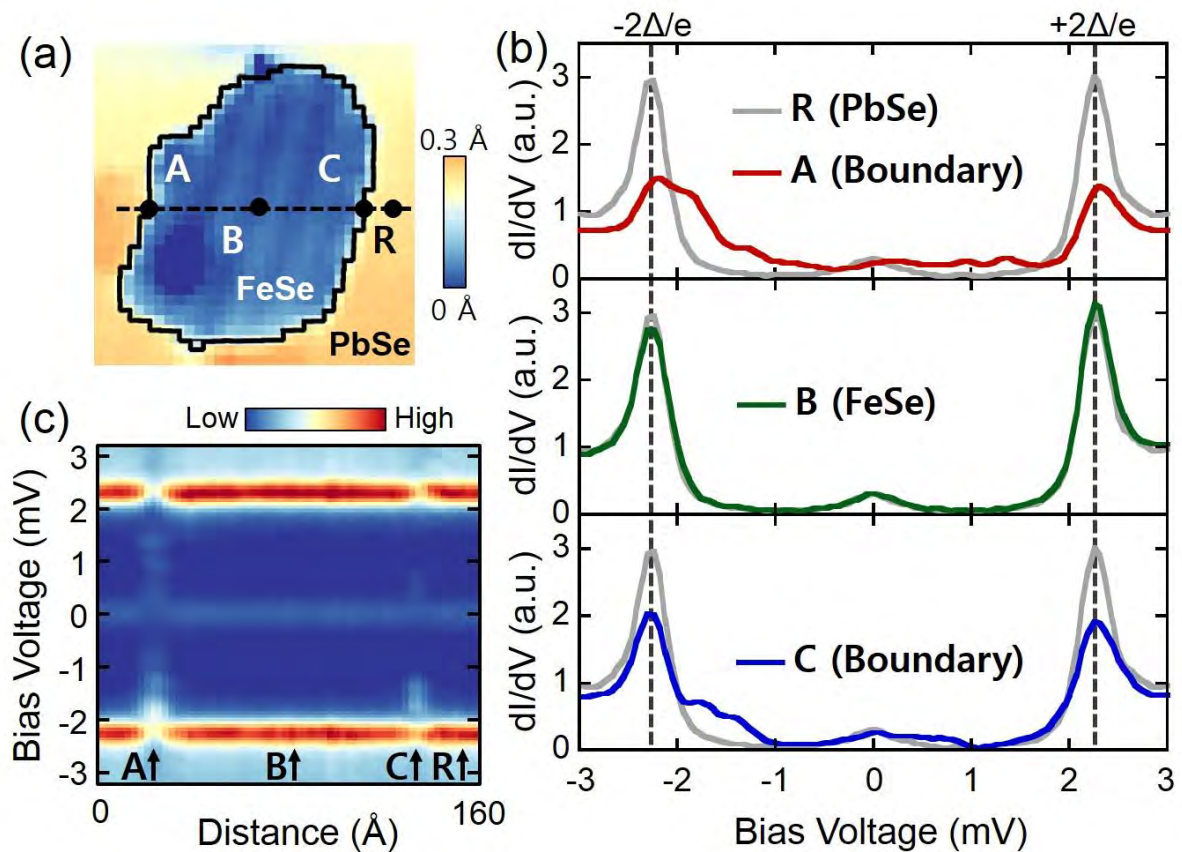


**Figure 2.** (a) The topography of FeSe grown on Pb(111) substrate.  $V_{\text{bias}} = -0.1$  V and  $I = 50$  pA. (b) The  $dI/dV$  spectrum measured at Point B marked in (a) shows no in-gap states excitation compared to the reference spectrum measured at point R. When measured at the edges of the FeSe island (Point A and C), strong in-gap states excitation is observed.  $V_{\text{bias}} = -3.0$  mV and  $I = 50$  pA. Lock-in modulation:  $f = 463.0$  Hz and  $V_{\text{rms}} = 60$   $\mu$ V. Because the Pb-coated superconducting tip is used in the experiment, the coherent peaks are located at  $E = \pm 2\Delta$ . The broad peak around  $V_{\text{bias}} = 0$  mV is due to the thermal effect at 4.3 K. (c) Line  $dI/dV$  spectroscopy measured along the dashed line marked in (a).

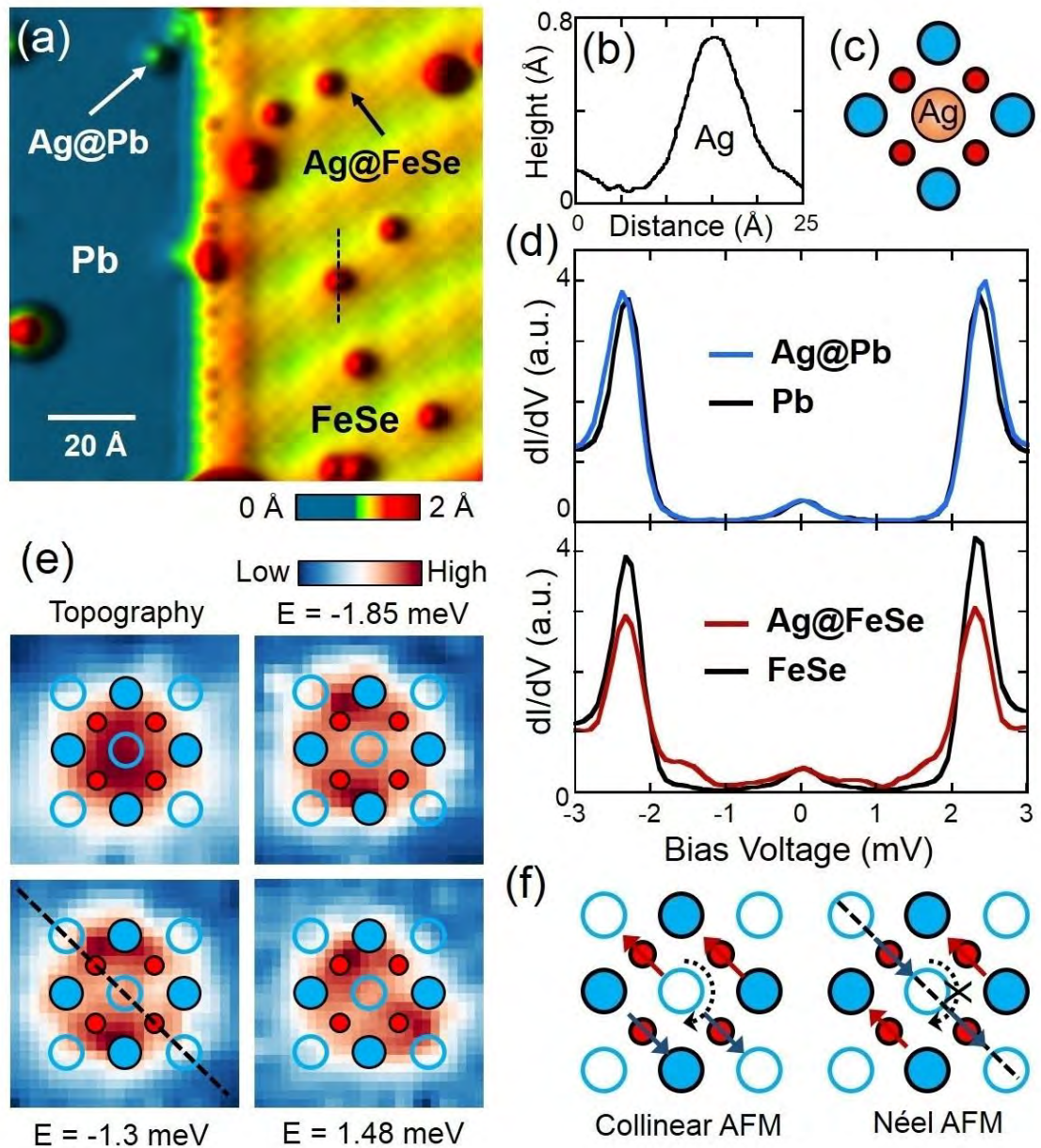


**Figure 3.** (a) Topography of Ag atoms on the FeSe and Pb surfaces. The Moiré pattern is seen in the FeSe along diagonal direction.  $V_{\text{bias}} = -0.1$  V and  $I = 50$  pA. (b) The height profile along the dashed line in (a). (c) The Ag atom (orange ball) is placed on the center of top Se lattice. (d) The Ag atom on bare Pb surface do not show in-gap states excitation. By contrast, the Ag atoms on the FeSe show strong in-gap states excitation.  $V_{\text{bias}} = -3.0$  mV and  $I = 50$  pA. Lock-in modulation:  $f = 463.0$  Hz and  $V_{\text{rms}} = 60$   $\mu$ V. (e) Topography of the Ag atom and the  $dI/dV$  maps (size:  $9.5 \text{ \AA} \times 9.5 \text{ \AA}$ ). (f) Two spin models; collinear AFM model preserves the  $C_2$  symmetry imposed by the lattice, as indicated by the dotted arrow. The Néel AFM model breaks the  $C_2$  symmetry while it maintains mirror symmetry marked with the dashed line.

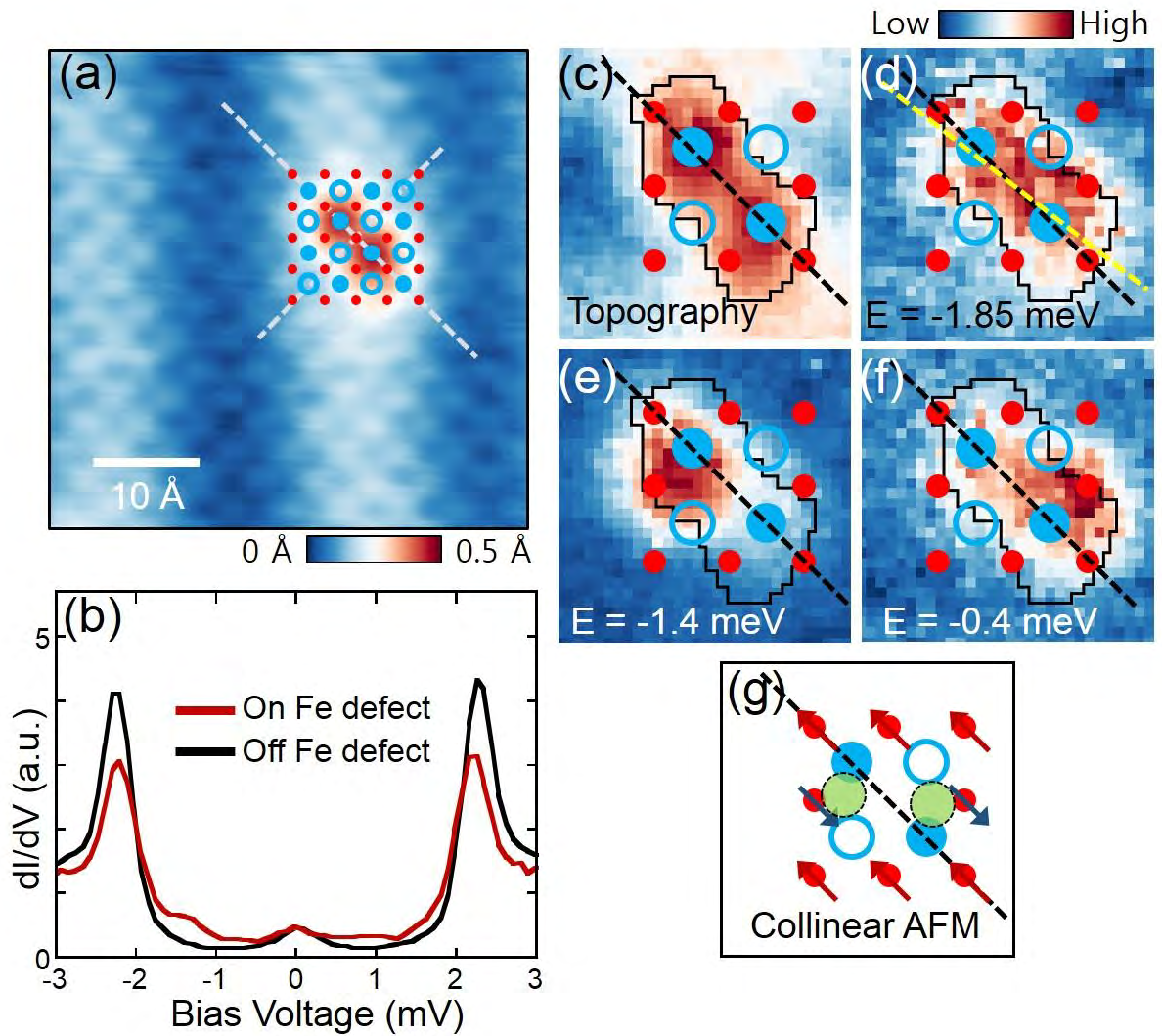


**Figure 4.** (a) Topography of a dumbbell-shaped defect in the FeSe.  $V_{\text{bias}} = -30$  mV and  $I = 50$  pA. (b) On the defect site, strong in-gap states excitation is observed. No in-gap states excitation is present off the defect site.  $V_{\text{bias}} = -3.0$  mV and  $I = 50$  pA. Lock-in modulation:  $f = 463.0$  Hz and  $V_{\text{rms}} = 60$   $\mu\text{V}$ . (c) A zoomed-in image of the Fe defect. The dashed line represents the mirror symmetry plane in topography. (d-f) The  $dI/dV$  maps at the energy of in-gap states. The yellow dashed line in (d) denotes the axis of the magnetic pattern. (g) The collinear AFM model breaks the  $C_2$  symmetry around the defect as well as the mirror symmetry.

# Supplemental Material

## Visualization of local magnetic moments emerging from impurities in the Hund's metal states of FeSe

Sang Yong Song,<sup>1</sup> J. H. J. Martiny,<sup>2</sup> A. Kreisel,<sup>3</sup> B. M. Andersen,<sup>4</sup> and Jungpil Seo<sup>1,†</sup>

<sup>1</sup>*Department of Emerging Materials Science, DGIST, 333 Techno-Jungang-daero, Hyeonpung-Eup, Dalseong-Gun, Daegu 42988, Korea*

<sup>2</sup>*Center for Nanostructured Graphene (CNG), Department of Micro- and Nanotechnology, Technical University of Denmark, DK-2800 Kongens Lyngby, Denmark*

<sup>3</sup>*Institut für Theoretische Physik, Universität Leipzig, D-04103 Leipzig, Germany*

<sup>4</sup>*Niels Bohr Institute, University of Copenhagen, Lyngbyvej 2, DK-2100 Copenhagen, Denmark*

†jseo@dgist.ac.kr

## Contents

Note S1. Growth of FeSe on Pb(111) substrate.

Figure S1. Examples of FeSe islands grown on Pb(111) substrate.

Figure S2. Thickness of FeSe grown on Pb(111) substrate.

Figure S3. Comparison among the  $dI/dV$  spectra of Pb, PbSe and FeSe.

Figure S4. Response of impurities to the proximity-induced superconductivity in PbSe.

Figure S5. Identification of the location of Ag atoms on the FeSe.

Figure S6. Magnetic patterns induced by Ag atoms on the FeSe.

Figure S7. Moiré pattern and the splitting pattern induced by Ag atoms in  $dI/dV$  maps.

Figure S8.  $dI/dV$  spectra measured on Ag atoms in FeSe.

Figure S9. Magnetic patterns for various Ag atoms on the FeSe.

Figure S10. Symmetry of Collinear AFM and Néel AFM models with spin angle of  $0^\circ$ .

Note S2. Theory results for local magnetic order around Se centered impurities and FeSe island edges

Figure S11. Theoretical results for local magnetic order near impurity sites and edges.

### Note S1. Growth of FeSe on Pb(111) substrate.

We grew the FeSe film on Pb(111) substrate in a molecular beam epitaxy (MBE) chamber under ultra-high vacuum (UHV) condition. First, the substrate was cleaned by repeated cycles of 2 kV Ar<sup>+</sup> sputtering for 10 minutes in Ar pressure of  $4.5 \times 10^{-5}$  torr and annealing at 500 K for 12 minutes (min). To form a single layer of PbSe on Pb(111), we evaporated Se atoms for 200 seconds (s) with the speed of  $\sim 1 \text{ \AA}/\text{min}$  onto the substrate at 490 K. The sample was then cooled down to 300 K. Subsequently, we heated the sample to 490 K again and Fe atoms were deposited onto the sample for 100 s with the speed of  $\sim 1 \text{ \AA}/\text{min}$ . After the Fe deposition, the sample was cooled down to 300 K. The examples of grown FeSe film are provided in Fig. S1.

During the growth of FeSe, Se atoms are supplied from the PbSe layer, which induces the exposure of Pb surface. We observed such Pb surface next to the grown FeSe film and near the step edges of PbSe layer.

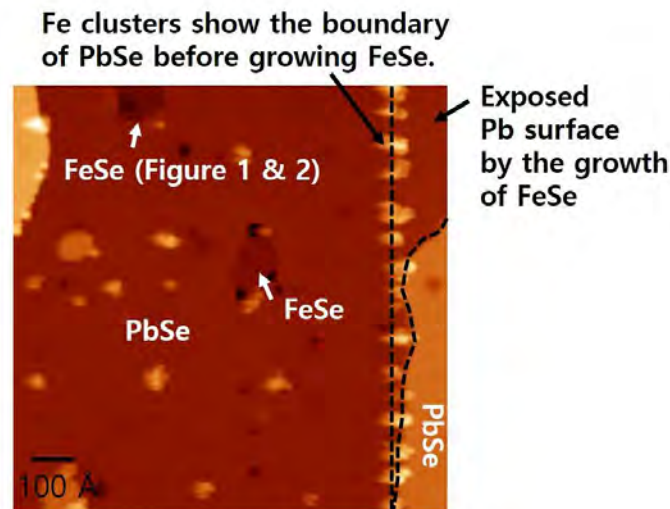
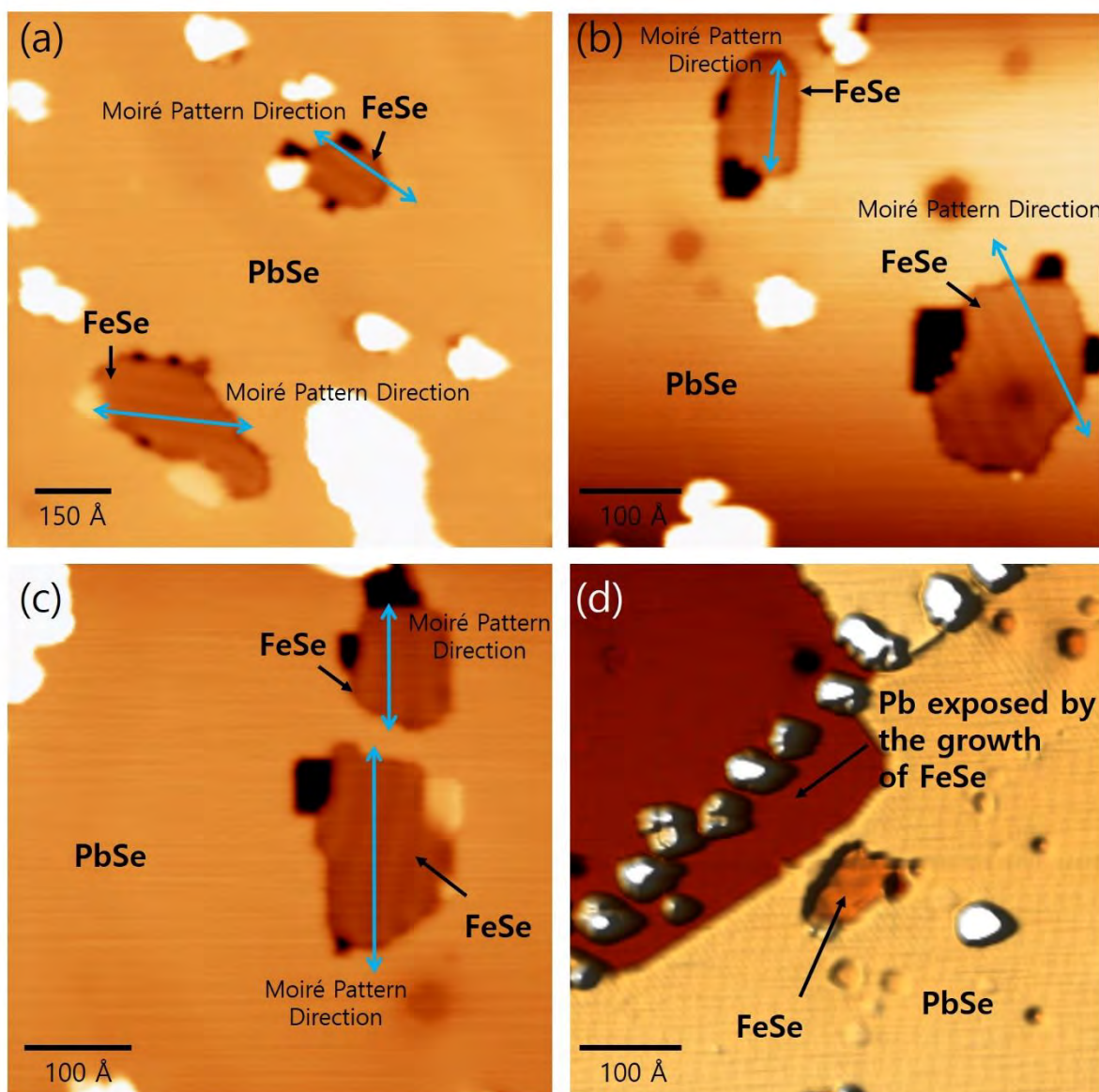
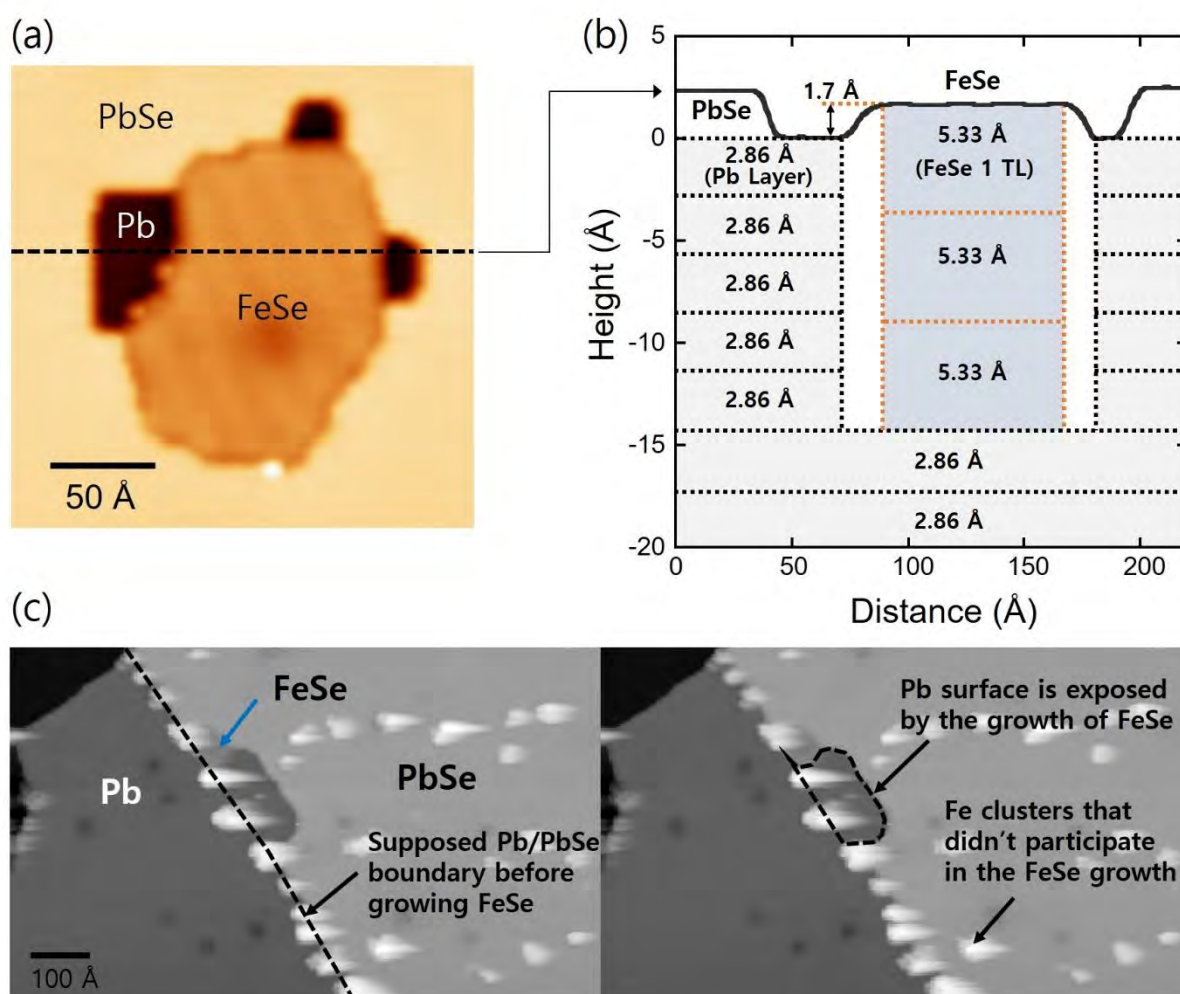


Figure Note S1. The exposure of Pb surface by the growth of FeSe. The growth of FeSe leads to exposure of Pb surface from PbSe because Se atoms needed for the growth are supplied from the PbSe.



**Figure S1. Examples of FeSe islands grown on Pb(111) substrate.** The size of the grown FeSe islands is typically less than  $200 \text{ \AA} \times 200 \text{ \AA}$ . The islands larger than this size was rarely found in our growth condition. (a-c) The Moiré pattern depends on the relative crystal angle between the FeSe layer and Pb substrate. (d) A 3-dimensional rendered image of FeSe/PbSe/Pb(111). The growth of FeSe induced the exposure of Pb surface near the step edge of PbSe.



**Figure S2. Thickness of FeSe grown on Pb(111) substrate.** (a) The topography of FeSe grown on Pb(111) substrate. (b) The height profile along the dashed line in (a). The height of FeSe with respect to the Pb is found to be  $\sim 1.7$  Å. This value corresponds to the height difference between FeSe film of 3 tri-layer (TL) and 5 layered Pb, as illustrated by sketched stacking units of FeSe and Pb (Phys. Rev. B 84, 125437 (2016); Surf. Sci. 646, 72 (2016); J. Phys.: Condens. Matter 29, 025004 (2017)). The inter-layer distance of Pb(111) is 2.86 Å. The height of 1 TL of FeSe is 5.33 Å. (c) The FeSe island grown near the edge of PbSe. The growth of FeSe induces exposure of Pb surface in the PbSe. The newly exposed Pb area is about 4 times larger than the area of FeSe island. Taking into account the Se densities of 1 mono-layer (ML) PbSe ( $0.08 \text{ atom}/\text{Å}^2$ ) and 1 tri-layer (TL) FeSe ( $0.14 \text{ atom}/\text{Å}^2$ ), we calculate the thickness of the grown FeSe film is approximately 3 TL.

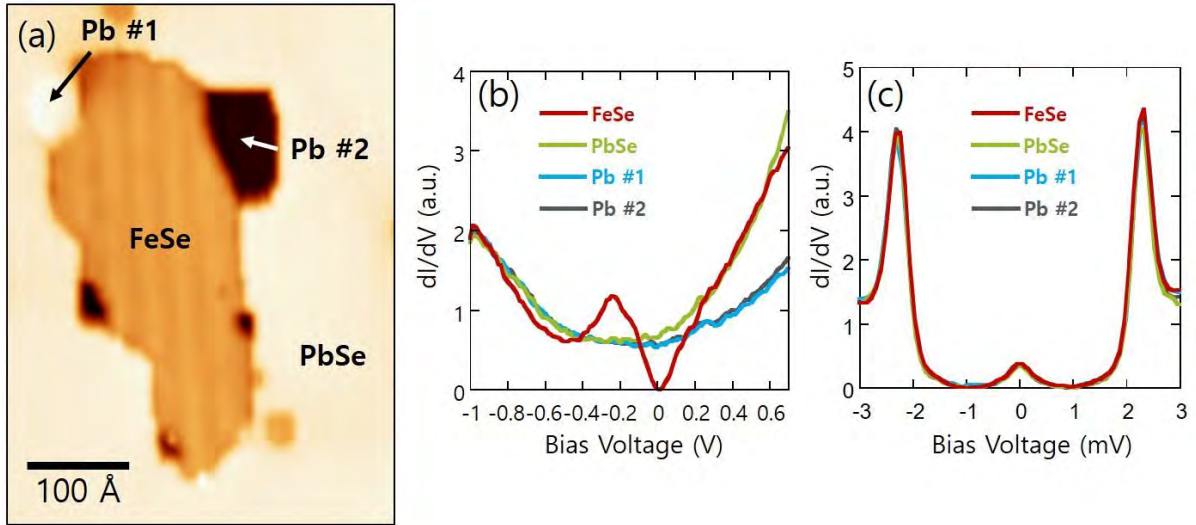


**Figure S3. Comparison among the  $dI/dV$  spectra of Pb, PbSe and FeSe.** (a) Topographic image of an FeSe grown on Pb(111).  $V_{\text{bias}} = -0.1$  V and  $I = 50$  pA. The  $dI/dV$  spectra were taken in FeSe, PbSe and Pb surfaces. (b) The  $dI/dV$  spectra in the wide bias voltage range.  $V_{\text{bias}} = -1$  V and  $I = 50$  pA. (c) The  $dI/dV$  spectra in the superconducting gap regime.  $V_{\text{bias}} = -3$  mV and  $I = 50$  pA.

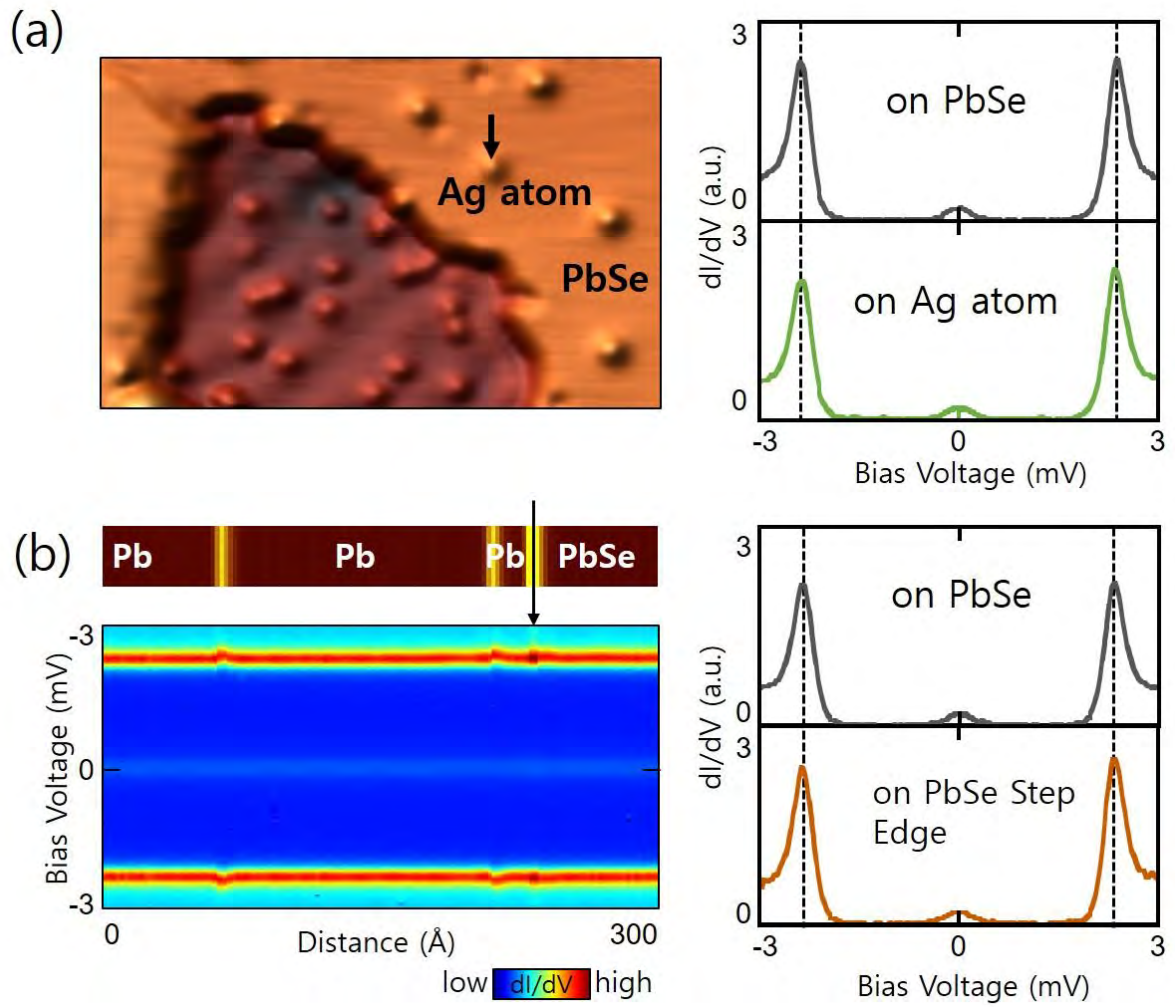


**Figure S4. Response of impurities to the proximity-induced superconductivity in PbSe.** In the main text, we show the crystal imperfections induce magnetic moments in FeSe. In this figure, we show Ag atoms and crystal edge do not induce magnetic moments in PbSe. (a) dI/dV spectra measured on/off Ag atoms on PbSe. (b) Line spectroscopy is taken across the PbSe step. The step edge is marked by the vertical arrow. No in-gap excitation is observed for the Ag atoms and the PbSe step.  $V_{\text{bias}} = -3$  mV and  $I = 50$  pA.

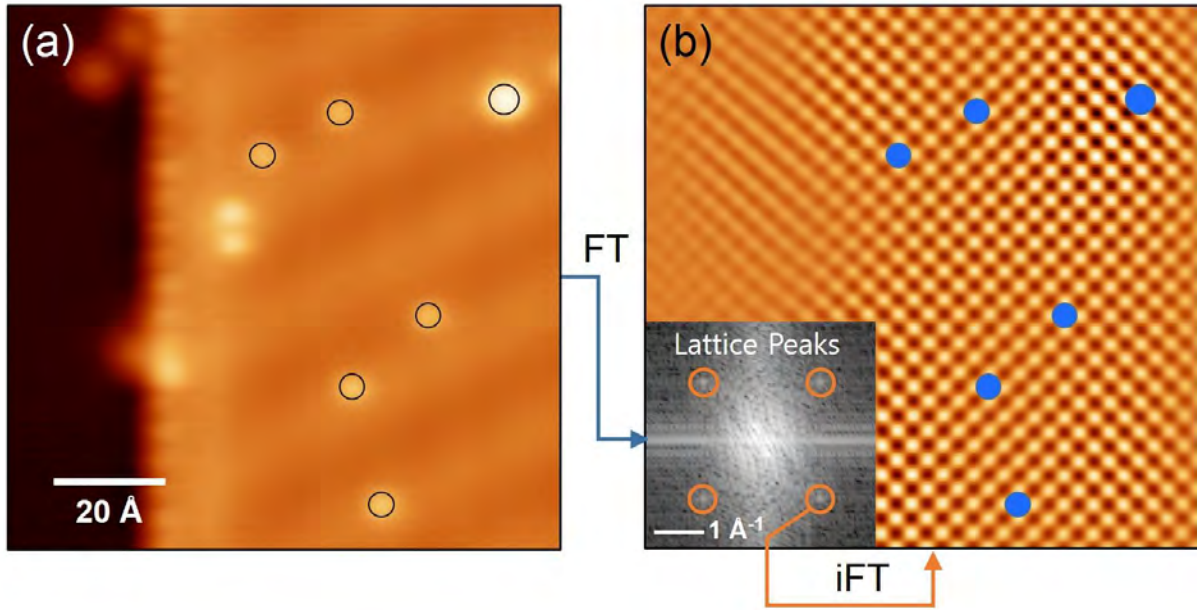


**Figure S5. Identification of the location of Ag atoms on the FeSe. (a)**

Topography image of Ag atoms on the FeSe. The open circles represent the location of Ag atoms. (b) The Fourier transform image of the topography is shown in the inset. The orange circles show the lattice peaks of the top Se atoms in the FeSe. By the inverse Fourier transform of the peaks, the position of Se atoms is revealed. The blue filled circles denote the Ag atoms of which location are exactly copied from the location of the open circles in (a). The FT analysis shows the Ag atoms are located on the center of the Se lattice.

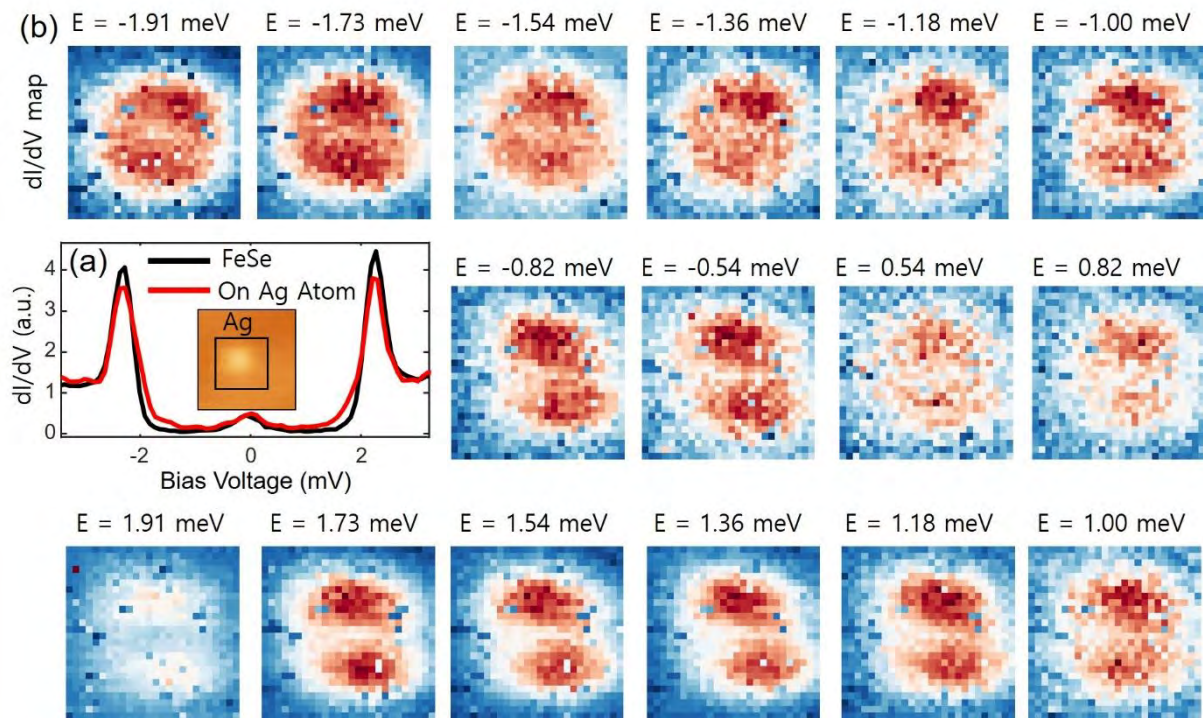


**Figure S6. Magnetic patterns induced by Ag atoms on the FeSe.** (a) The  $dI/dV$  spectra measured on FeSe (black curve) and the Ag atom (red curve). This Ag atom is different from the Ag atom in Fig. 4d and 4e. Inset shows the topography of the Ag atom. (c) The  $dI/dV$  maps for the Ag atom are displayed (the size is  $8.5 \text{ \AA} \times 8.5 \text{ \AA}$ ). Every magnetic pattern shows the  $C_2$  symmetry.

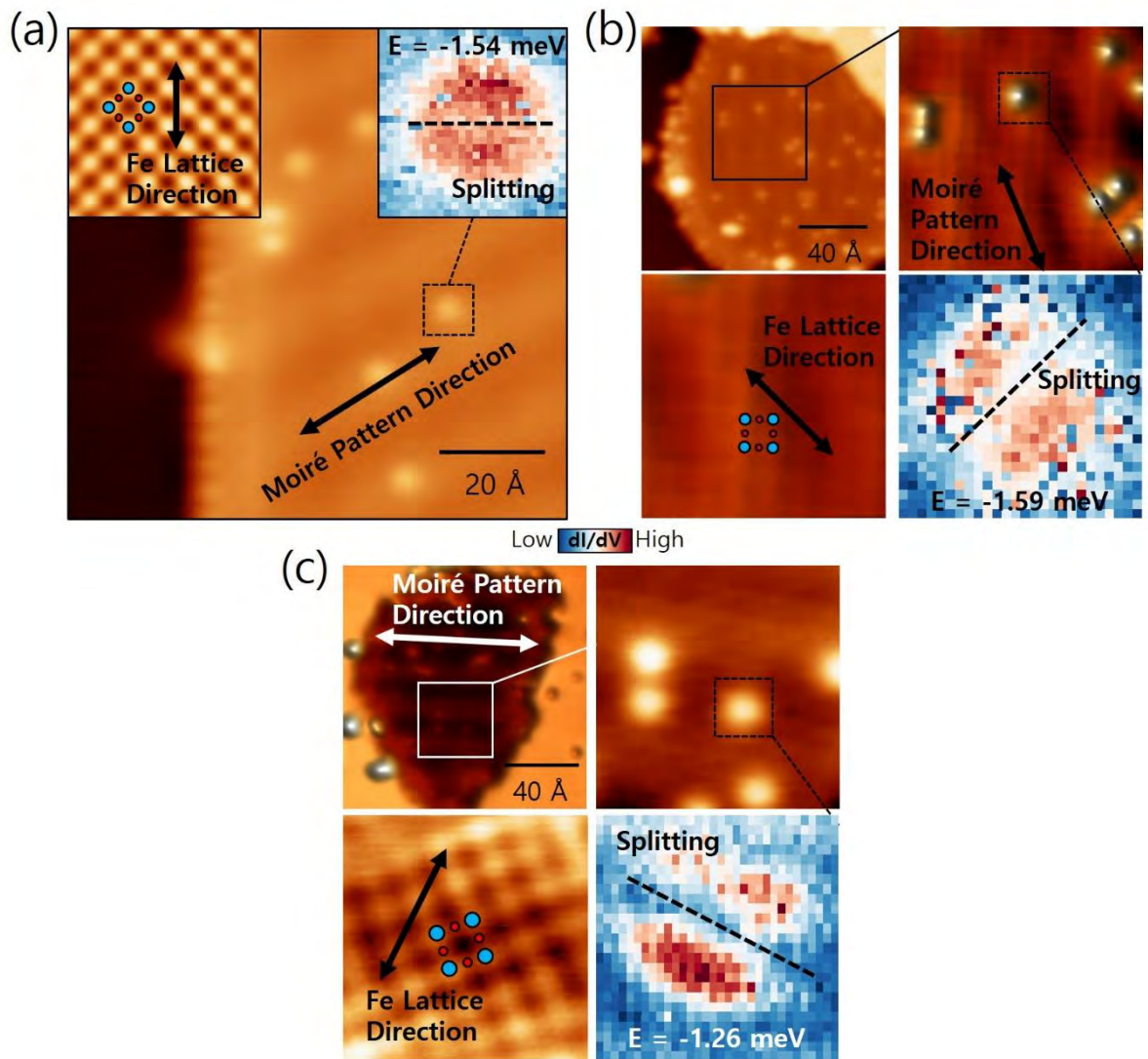


**Figure S7. Moiré pattern and the splitting pattern induced by Ag atoms in dI/dV maps.** The angle between Fe lattice and Moiré pattern is 60°, 20° and 70° for (a), (b), and (c), respectively. (a) The dI/dV map (top-right inset) is taken for the Ag atom at the energy of  $E = -1.54$  meV. The dashed line shows the splitting of dI/dV intensity. The atomic structure (top-left inset) is obtained by Fourier transform analysis. The blue balls and red balls represent the Se lattice and Fe lattice, respectively. (b) The dI/dV map is taken at the energy of  $E = -1.59$  meV. (c) The dI/dV map is taken at the energy of  $E = -1.26$  meV. Regardless of the Moiré pattern, the splitting in the dI/dV maps is aligned along the Fe lattice direction, which rules out the Moiré pattern as a possible origin of the splitting in the dI/dV maps. The data shown here were obtained using different tips in the separate experiments.

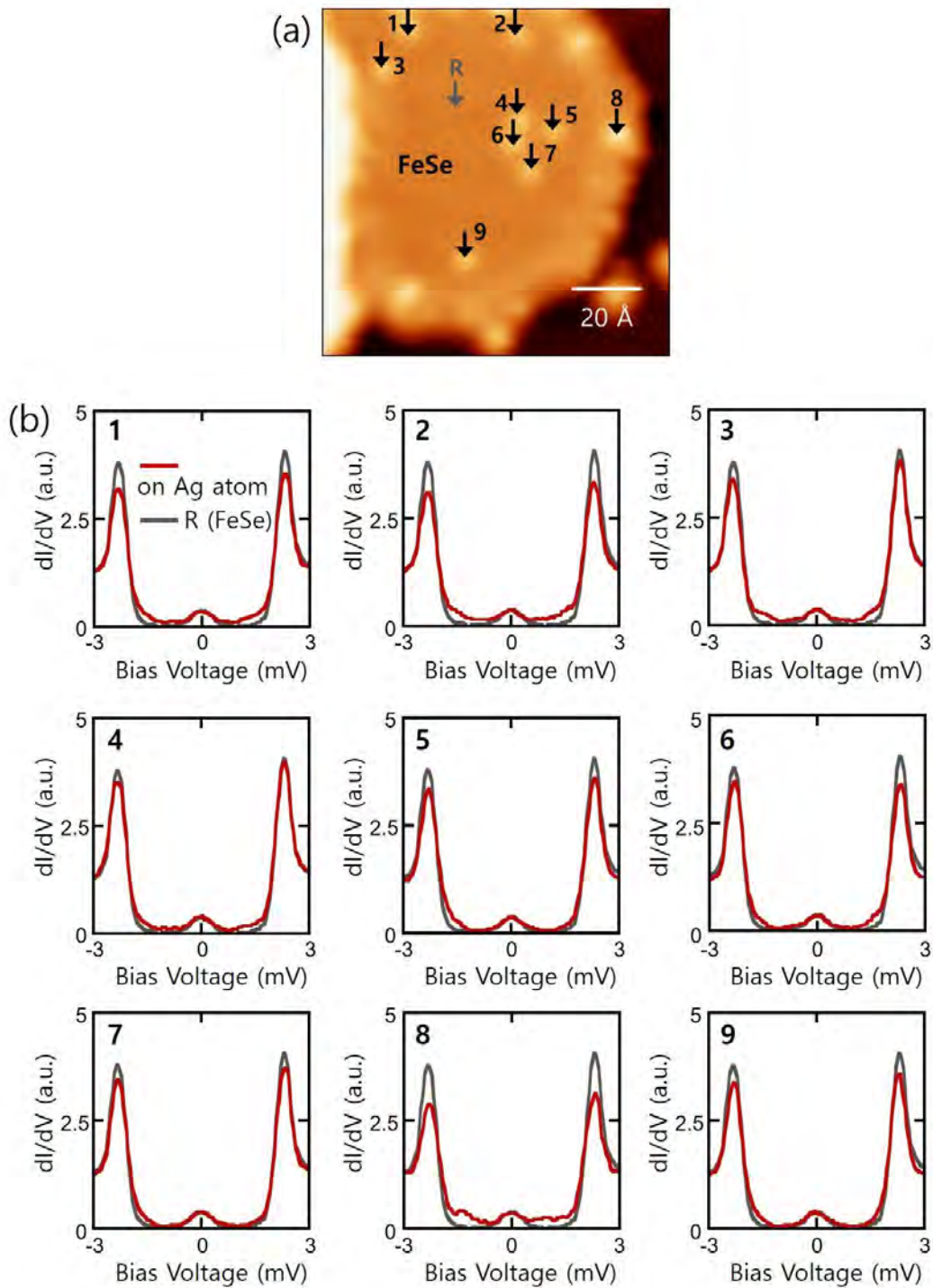


**Figure S8.  $dI/dV$  spectra measured on Ag atoms in FeSe.** (a) Ag atoms on the FeSe island. Imaging condition:  $V_{\text{bias}} = -0.1$  V and  $I = 50$  pA. (b) The  $dI/dV$  spectrum for each numbered Ag atom in (a) is displayed. The spectrum measured on the Ag atom show YSR excitation compared to the spectrum measured on FeSe. The spectroscopy condition:  $V_{\text{bias}} = 3$  mV and  $I = 50$  pA. Lock-in modulation:  $f = 463.0$  Hz and  $V_{\text{rms}} = 60$   $\mu\text{V}$ .

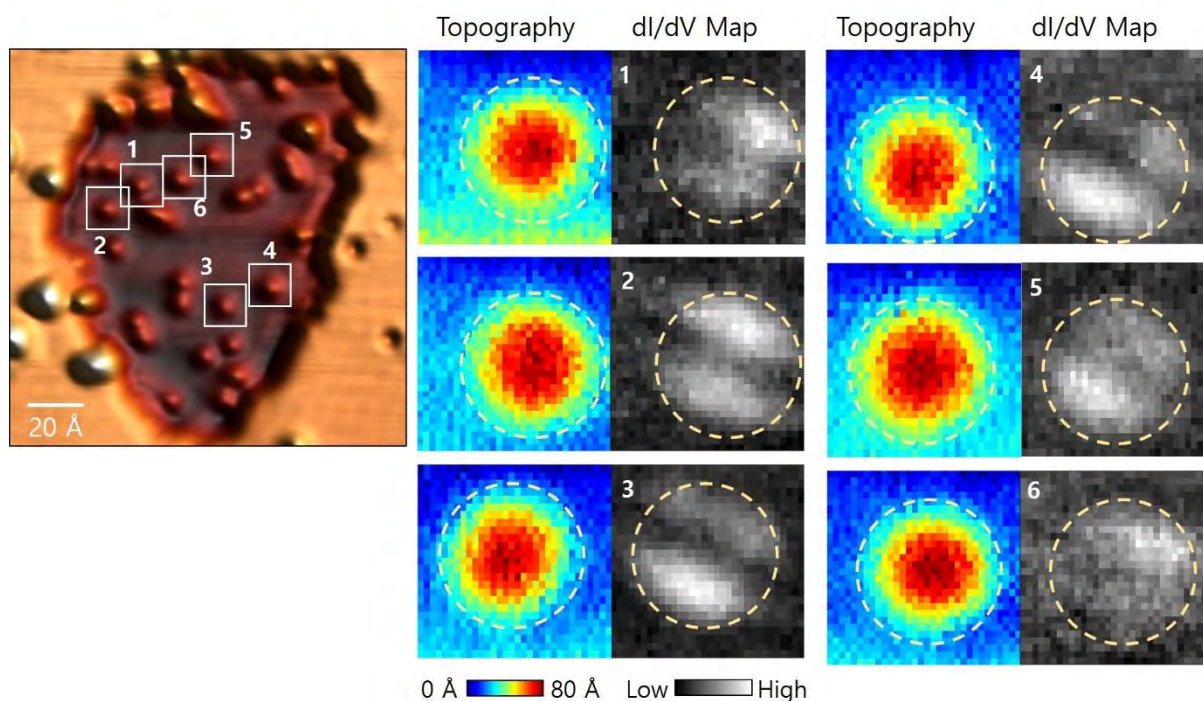


**Figure S9. Magnetic patterns for various Ag atoms on the FeSe.** We measured dI/dV maps at  $E = -1.1$  meV for isolated Ag atoms. The studied Ag atoms are indicated with numbers in the left panel. The topography and simultaneously obtained dI/dV map are displayed in the right panels. Most of Ag atoms exhibit the splitting patterns in dI/dV maps except for the Ag atom labeled with 6. The variation could be because the Ag atoms are not perfectly positioned at the center of Fe lattice.

Spin Angle	Collinear AFM	Néel AFM
45°		
0°		

**Figure S10. Symmetry of Collinear AFM and Néel AFM models with spin angle of 0°.** The collinear AFM model with the spin angle of 0° or 45° is fully consistent with the measured  $dI/dV$  maps in Fig. 3e in the main text in terms of symmetry. The Néel AFM model with the spin angle of 0° does not preserve  $C_2$  symmetry, which is inconsistent with the  $dI/dV$  maps. Furthermore, it maintains a mirror symmetry as indicated by the dashed line in the image, which contradicts the symmetry of the  $dI/dV$  map at  $E = 1.48$  meV. Therefore, the Néel AFM model does not explain the symmetry of the local magnetic moments induced by the Ag impurities in the experiment.

## Note S2. Theory results for local magnetic order around Se centered impurities and FeSe island edges

In this section we expand the theoretical study of local magnetic order around Fe-centered impurity bound states in Ref. S11A to also include Se-centered disorder and edges. These calculations are performed in a similar fashion to that described in detail in Ref. S11A, and therefore we provide only a brief outline here.

We perform self-consistent mean-field calculations in the Hubbard-Hund model using the tight-binding parameters for FeSe derived in Ref. S11B. The interaction parameters are fixed in terms of the Hubbard  $U$  as  $J = J' = U/4$  and  $U' = U - 2J$ .

Orbital selective effects are included by a rescaling of electron creation and annihilation operators  $c_\mu \rightarrow \sqrt{Z_\mu} c_\mu$ , with  $Z_\mu$  the quasiparticle weight factor in the given orbital, yielding an effective model with rescaled orbital-dependent interaction parameters

$$U_{\mu\nu} \rightarrow \sqrt{Z_\mu} \sqrt{Z_\nu} U_{\mu\nu},$$

with similar expressions for  $U', J, J'$ . Based on Ref. S11B. we choose these weights as  $\sqrt{Z_\mu} = 0.2715, 0.9717, 0.4048, 0.9236, 0.5916$  for the five Fe 3d orbitals  $\mu = d_{xy}, d_{x^2-y^2}, d_{xz}, d_{yz}, d_{z^2}$ .

In this model a phase transition to a strongly  $C_2$ -symmetric magnetically ordered bulk phase occurs at a critical  $U_c = 560$  meV. As the Hubbard  $U$  approaches this transition from below, it was previously found that impurity bound states may facilitate local magnetic order [S11A]. In the following we thus fix  $U = 550$  meV just below the critical value, but remark that our results in general apply to an interval of  $U$ , the width of which depends on the type of disorder or impurity potential.

Finally, large-scale real-space calculations are facilitated by employing the Kernel Polynomial method where the electronic Greens function is expanded in a series of orthonormal Chebyshev polynomials [S11C, S11D]. We set the order of this expansion to  $N = 1000$ , use the Lorentz kernel to damp Gibbs oscillations, and iterate self-consistently until convergence of the spin resolved density mean fields  $(n_\uparrow, n_\downarrow)$  is obtained.

We model the Se vacancy as an effective plaquette impurity, i.e. by an onsite potential  $V$  on the four neighboring Fe sites of the vacancy on a given site

$$H_{Se-imp} = V_{Se} \sum_{j,\mu,\sigma} c_{j\mu\sigma}^\dagger c_{j\mu\sigma},$$

where  $V_{Se}$  is the potential applied to the four neighboring Fe sites indexed by  $j$ . Calculations of the induced local magnetic order are performed using such a plaquette impurity in the center of a 12 x 12 supercell.

Our studies of edge magnetism are performed using open boundary conditions in the real-space system. This creates an isolated FeSe island with boundaries determined by the system geometry. In our calculations we modify the original periodic supercell structure to accommodate both (100), (010) and (110) edges on the islands.

Fig. S11 (a-b) displays the result of including a single central plaquette impurity for  $U$  close to the phase boundary. In Fig. S11 (a) we show a zoomed-in real-space plot of the magnetization centered on the impurity site, while Fig. S11 (b) displays the associated 2D Fourier transform. We find that the plaquette impurity induces local magnetic order for a broad range of impurity potentials  $V_{Se}$ . Similar to the point-like impurity, we find that the local magnetic order inherits the structure of the bulk magnetic fluctuations, yielding a strongly non- $C_4$ -symmetric structure of the induced magnetization, as demonstrated by the peaks in the Fourier transform at  $m_z(q) = (\pm \pi, 0)$ .

In Fig. S11 (c-f) we show results for the local magnetic order formed on FeSe island edges when open boundary conditions are imposed in the calculation. In general, we find that as  $U$  is increased from below, magnetic order forms initially on corners of the system, but that closer to the phase boundary magnetization is induced along the entire edge of the system. This is demonstrated for a geometry with long 100 edges in (c) and for 110-type edges in the different geometry in (d). We note that the included orbital selective effects also make the amplitude of the induced magnetization at 100 (extending along  $x$ ) versus 010 (extending along  $y$ ) edges distinct.

Fig S11 (e) shows the linecut of the magnetization in (c) indicated by the dashed grey line transverse to the 100 edge. The magnetization peaks sharply directly on the edge, but a tail of finite magnetization extends into the bulk. In (f) we

show two linecuts taken transverse to the edge through the magnetization of the FeSe island with 110-type edges plotted in Fig. S11 (d). For the staggered 110 edge, the magnetization selectively forms on every second site of the edge, forming a chain conforming to the bulk magnetic order. The linecuts taken transverse to the edge at two neighboring edge sites demonstrates this feature. The linecuts are mirror images of each other, the dashed cut showing the peak in magnetization at the upper edge with an oscillating tail into the bulk, and the cut corresponding to the dotted line has the opposite structure with a peak at the lower edge.

- [S11A] J.H.J. Martiny, A. Kreisel, and B.M. Andersen, *Physical Review B* **99**, 014509 (2019)
- [S11B] A. Kreisel *et al.*, *Physical Review B* **95**, 174504 (2017)
- [S11C] A. Weiße, G. Wellein, A. Alvermann, and H. Fehske, *Rev. Mod. Phys.* **78**, 275 (2006).
- [S11D] L.Covaci, F.M. Peeters, and M. Berciu, *Phys. Rev. Lett.* **105**, 167006 (2010).

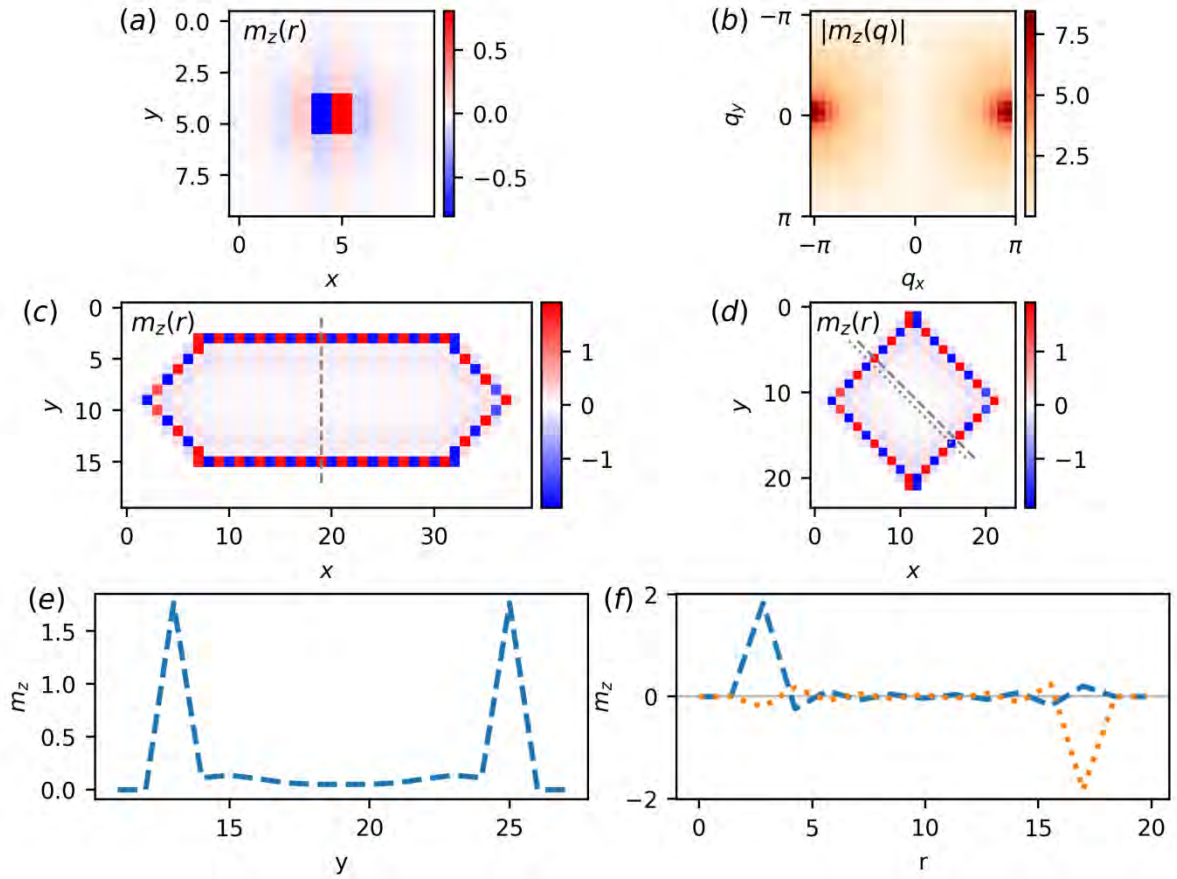


**Figure S11. Theoretical results for local magnetic order near impurity sites and edges.** (a) Zoom of the magnetization nucleated around a plaquette impurity  $V_{se} = 50$  meV. (b) Fourier transform of (a) showing the  $C_2$  structure of the local magnetic order. (c) Edge magnetization on a FeSe island with open boundary conditions and a long 100 edge. (d) Edge magnetization on a different FeSe island with 110-type edges. (e) Linecut of the magnetization for the 100 edge [dashed line in (c)]. (f) Linecuts of the magnetization for the 110 edge [dashed, dotted lines in (d)]. In both geometries the magnetization peaks at the edge with a tail extending into the bulk region.



Technical  
University of  
Denmark

Fysikvej, Building 311  
2800 Kgs. Lyngby  
Tlf. 4525 1700

[www.fysik.dtu.dk](http://www.fysik.dtu.dk)